Petrological and Rheological Controls on Volcanism in Terrestrial Planets

by
Linda Tarbox Elkins Tanton

S.B., S.M. Geology
Massachusetts Institute of Technology, 1987

Submitted to the Department of
Earth, Atmospheric, and Planetary Sciences
in Partial Fulfillment of the Requirements for the Degree of

DOCTOR OF PHILOSOPHY
IN
GEOLOGY AND GEOPHYSICS
AT THE
MASSACHUSETTS INSTITUTE OF TECHNOLOGY

SEPTEMBER 2002

Signature of Author:_____

Department of Earth, Atmospheric, and Planetary Science
June 10, 2002

Certified By:_____

Timothy L. Grove
Professor of Geology
Thesis Co-Supervisor

Certified By:_____

Bradford H. Hager
Cecil and Ida Green Professor of earth Sciences
Thesis Co-Supervisor

Accepted By:_____

Ronald Prinn
Department Chairman

Petrological and Rheological Controls on Volcanism in Terrestrial Planets

by

Linda Tarbox Elkins Tanton

S.B., S.M.
Massachusetts Institute of Technology, 1987

Submitted to the Department of Earth, Atmospheric, and Planetary Sciences
on June 15, 2002, in partial fulfillment of the
Requirements for the Degree of
Doctor of Philosophy in Geology and Geophysics

ABSTRACT

Through experimental petrology and geodynamic modeling, processes of melting under thick lithospheres on the Earth and the moon are investigated. Phase equilibrium experiments were carried out on Apollo 14B and 15C picritic glasses (Chapters 5 and 6) and on a Sierran high-potassium lava (Chapter 1). These, along with petrologic modeling of Cascades high alumina olivine tholeiites (Chapter 4), yield information on depths and pressures of melt generation and constraints on source composition. Geodynamic modeling of lithospheric thinning processes, including delamination under the Siberian flood basalts (Chapter 2), gravitational instabilities in the lunar magma ocean cumulates (Chapter 7), and thinning and convection due to giant meteorite impacts (Chapters 3 and 8), has lead to new models for melt production. These studies together show how lithospheric thinning and unusual mantle compositions can lead to melting without calling on unusual mantle potential temperatures, and can explain the volumes and durations of continental flood basalts and lunar mare basalts.

Thesis Co-Supervisor: Timothy L. Grove
Title: Professor of Geology
Thesis Co-Supervisor: Bradford H. Hager
Title: Cecil and Ida Green Professor of Earth Sciences

Biographical Note

Lindy Elkins Tanton earned her Bachelor's and Master's degrees in geology from MIT in 1987. After her Master's, she worked in business for several years, including jobs at Touche Ross Management Consulting and U.S. News and World Report. She eventually started a business to write business plans for high-tech companies seeking venture funding. While in business, she wrote articles for *Nation's Business* and a book for Entrepreneur Corporation.

After selling the business, she taught math and geology at St. Mary's College of Maryland for two years. In 1997 she returned to MIT for her Ph.D, beginning classes the same day her son began kindergarten. She was awarded a National Defense Science and Engineering fellowship, and then won the Amelia Earhart graduate fellowship from Xonta International for two years.

She lives in Acton with her husband James, son Turner, and a collection of border collies.

Papers published:

Karig, D.E. and L.T. Elkins, Geology of the Cayuga Lake region, *NYSGA Annual Meeting Guidebook*, 1986.

Elkins, Linda T. and Timothy L. Grove, Ternary feldspar experiments and thermodynamic models, *American Mineralogist 75*, 544-559, 1990.

Elkins, L.T., T.L. Grove, J. Delano, V. Fernandez, Origin of lunar ultramafic green glasses: Constraints from phase equilibrium studies, *Geochimica et Cosmochimica Acta 64*, 2339-2350, 2000.

Elkins Tanton, L.T. and Bradford H. Hager, Melt intrusion as a trigger for lithospheric foundering and the eruption of the Siberian flood basalt, *Geophysical Research Letters 27*, 3937-3940, 2000.

Elkins Tanton, L.T., T.L. Grove, and J. Donnelly-Nolan, Hot shallow melting under the Cascades volcanic arc, *Geology 29*, 631-634, 2001.

Elkins Tanton, L.T., J. A. Van Orman, B. H. Hager, and T. L. Grove, Reexamination of the lunar magma ocean cumulate overturn hypothesis: Melting or mixing is required, *Earth and Planetary Science Letters* 196, 239-249, 2002.

Papers in review or preparation:

Elkins Tanton L. T., N. Chatterjee, and T.L. Grove, Constraints on lunar differentiation from the Apollo 15 green picritic glasses, in review at *Meteoritics and Planetary Science.*

Elkins Tanton, L.T. and B. H. Hager, Giant impact craters lead to flood basalts: A viable model, in preparation for submission to *EPSL*, 2002.

Elkins Tanton, L.T., P. Aussillous, J. Bico, D. Quéré, J.W.M. Bush, A laboratory investigation of tektites, in preparation for submission to *Meteoritics and Planetary Science*, 2002.

Elkins Tanton, L.T., B. H. Hager, and T.L. Grove, Magmatic effects of the Lunar Late Heavy Bombardment, in preparation for submission to *Science*, 2002.

Kelly, D.C. and L.T. Elkins Tanton, A possible new tektite strewn field at 5 Ma, in preparation for submission to *Meteoritics and Planetary Science*, 2002.

Acknowledgements

I am immensely grateful to Profs. Tim Grove and Brad Hager for their support, assistance, and encouragement in the face of my broadly ranging interests, for the use of their lab facilities, and for their funding along with the fellowships from the Department of the Navy and Xonta International. How fortunate I am to live in a time when society supports the study of science. I have benefited greatly from the advice and help of my thesis committee, Sam Bowring, Brad Hager, Paul Hess, Tim Grove, and Maria Zuber. I very much appreciated Neel Chatterjee's electron microprobe, mineralogy, and geology expertise, as well as his company in the lab. The interest and time of faculty members from other fields and institutions have helped me significantly and made me feel I am becoming a part of a larger scientific community. Thank you so much, in alphabetical order, to Sam Bowring, Jose Bico, John Bush, John Delano, Julie Donnelly-Nolan, Fred Frey, Paul Hess, Greg Hirth, Clay Kelly, Yan Liang, John Longhi, Marc Parmentier, Wiki Royden, Chip Shearer, Sean Solomon, Rob Van der Hilst, Maria Zuber, and also to the reviewers of the chapters already published. Thanks for all you've done and for your pleasant company, Alison Hearn, Terri Macloon, Jane Shapiro, and Carol Zayotti.

I have been further blessed by some of the finest lab-mates a student could ask for. Thank you for your friendship and support in those crucial first semesters, a permanent bond, Julie Baldwin, Marin Clark, and Karen Viskupic. Your presence has made the department a better place, Sinan Ackiz, Simon Brocklehurst, Clint Conrad, Becky Flowers, Anke Friedrich, Kevin Frye, Marc Hesse, Eric Hetland, Jenny Matzel, Brendan Meade, Stephen Parman, Rebecca Saltzer, and Jessica Warren. A very special, personal thank-you to my good friends, tireless advisors and helpers, and highly valued confidantes, Astrid Holzheid, Kirsten Nicolaysen, Jim Van Orman, and Steven Singletary. And thanks to all of you for putting up with, even welcoming, my beloved collies, Tess and Rue.

It is so necessary and yet so inadequate to thank my family here, for all the love and support and meaning you give me. James, my husband, and Turner, my son, my daily constants and the center of my life. My parents Sally and Len Elkins, and my brother, Jim, and my sister-in-law, Margaret MacNamidhe.

This thesis, for what it is worth, is dedicated to the memory of my brother Tom.

Table of Contents

Introduction

While mid-ocean ridge and island arc volcanism make up the bulk of volcanic flux on Earth, a number of continental volcanic settings offer opportunities to study the continental lithosphere and upper mantle. The mechanisms of melting under and volcanic eruption through continental lithosphere are for the most part poorly understood. In this series of studies we attempt to understand better the composition and dynamics of the continental lithosphere and upper mantle on the Earth and on the early moon through both experimental petrology and geodynamic modeling of melting processes. This thesis is divided into two sections of four chapters each. The first section is devoted to continental magmatism on Earth, and the second, to mare basalt and picritic glass production on the moon.

On the Earth, continental mantle potential temperatures are a matter of debate, but without calling on exceptionally high potential temperatures, creating melt under continents is suppressed by the high pressures under thick continental lithosphere. Our studies indicate that there are processes that can thin lithosphere sufficiently to allow adiabatic melting on adiabats consistent with temperatures found in the oceanic mantle. These processes include melt injection and subsequent lithospheric delamination under the Siberian flood basalts, and the lithospheric thinning effects of giant meteorite impacts.

To create melt, material must be depressurized enough to melt adiabatically, as in the lithospheric thinning processes described, or mantle material may have an unusual composition that enables melting at greater pressures. There is evidence that high-potassium magmas such as those in the central Sierra Nevada are the result of both lithospheric thinning and the availability of small volumes of metasomatized mantle. This metasomatized mantle, thought to consist of phlogopite lherzolite or, in extreme cases, phlogopite clinoproxenite, melts at lower temperatures than nonhydrous lherzolite, and so may be the first melts produced in certain tectonic settings.

On the Moon, millions of cubic kilometers of basalt and related picritic glass beads erupted onto the surface, mainly between 4.0and 3.0 Ga. These basalts lie preferentially in giant impact basins. As with continental magmatism the Earth, questions remain about the depths at which the melts formed and the compositions that melted to create them, as well as any further processes of fractionation or assimilation. To the already extensive collection of studies on various mare basalt and picritic glass compositions, we add phase equilibrium studies on the

Apollo 14B, 15A, and 15C green glasses. By combining evidence from these phase equilibrium studies for lunar lithospheric thicknesses and mantle temperatures with our models for melt production by giant impact, we are able to make a unified theory for mare basalt genesis through the effects of the lunar late heavy bombardment. This theory does not require the wholesale overturn of magma ocean cumulates, and is consistent with the melting depths of the basalts and glasses, as well as with the volumes of basalts seen in the nearside basins.

Section 1: Continental magmatic mechanisms

Chapter 1: Sierran high-potassium magmatism. Based on this and several other studies showing that high-potassium-magmas can be multiply saturated with olivine + clinopyroxene + phlogopite, we conclude that the high-potassium magma WC-1 melted from a phlogopite clinopyroxenite at about 1360 °C and 3.6 GPa. We hypothesize that the phlogopite clinopyroxenite source lay beneath the Sierran lithosphere until delamination some time before the Pliocene, at which time the source material rose into the lithospheric dome and melted adiabatically to produce the high-potassium magmas.

Chapter 2, Siberian flood basalts. A deep, hot, voluminous mantle plume cannot be the cause of the SFB, because of geologic evidence for subsidence during eruption. Without anomalously high temperatures, melting the mantle adiabatically beneath thick continental lithosphere is impossible; the lithosphere must be removed. Our models demonstrate that the lithospheric removal could be controlled by lithospheric rheology, and not by the size or temperature of upwelling beneath it. We suggest that intrusion of a small volume of precursory adiabatic melt into the mantle lithosphere lowers its viscosity and increases its density as the melt freezes into eclogite. Combined with a weak lower crust, this process could result in removal of the mantle lithosphere through shear traction and a Rayleigh-Taylor instability. The Rayleigh–Taylor instability is crucial for creating surface subsidence and a significant increase in the melting column, creating an environment for massive magma genesis. Removal of the mantle lithosphere lengthens the melting column, and the melt volume of the SFB can be produced in less than a million years.

Chapter 3, giant meteorite impacts. We present a model for creation of a flood basalt from a giant impactor striking a relatively thin lithosphere. Mafic magma is produced by immediate in-situ decompression and, for some lithospheric thicknesses and mantle potential temperatures, by

later convective flow in a lithospheric dome that forms under the crater by instantaneous fluid flow of the lithosphere during impact, and by later isostatic uplift. A 300 km radius crater in 75 km thick lithosphere can create 10^6 km^3 of mafic magma in much less than 1 million years from instantaneous in-situ decompression of mantle material with a potential temperature of 1300 °C. Though there is no unequivocal evidence that a giant impactor has struck at the location of any terrestrial flood basalt province, there are impacts, flood basalts, and extinctions that show coincident ages.

Chapter 4, Melting under the Cascades. Analysis of the most primitive, near-anhydrous, high-alumina olivine tholeiites erupted along a 75-km-long, east-west transect across the arc, from near Mount Shasta to east of Medicine Lake volcano, shows hot, shallow melting, no deeper than 66 km. Although the depths of segregation of mantle melts increase from west to east across the arc, and temperatures of origin also rise commensurably, the increase of depth does not parallel the inferred dip of the slab. Rather, the increase in depth of origin parallels modeled mantle corner flow lines.

Section 2: Processes of lunar differentiation

Chapter 5: Apollo 14B picritic glasses. Experimental investigation of the Apollo 14B green glass shows its multiple saturation point with ol + opx to be at 1560°C and 2.3 GPa (approximately 560 km depth in the moon). The compositional variation seen in the Apollo 14B green glasses cannot be explained by fractional crystallization alone, but is well fit by fractional crystallization and concurrent assimilation of cumulates. The data require both a high-Ti and a KREEP assimilant.

Chapter 6: Apollo15 picritic glasses. Phase equilibrium experiments on the most magnesian Apollo 15C green picritic glass composition indicate a multiple saturation point with olivine and orthopyroxene at 1520°C and 1.3 GPa (about 260 km depth in the moon). This composition has the highest Mg# of any lunar picritic glass, and the shallowest multiple saturation point. Experiments on an Apollo 15A composition indicate a multiple saturation point with olivine and orthopyroxene at 1520°C and 2.2 GPa (about 440 km depth in the moon). We confirm the compositional trends reported by Delano (1979, 1986) from his meticulous analysis of the contents of NASA slide 15426,72 through reanalysis of the major element oxides SiO_2, TiO_2,

Al_2O_3, Cr_2O_3, FeO, MnO, MgO, and CaO, and we also obtained data for the trace elements P_2O_5, K_2O, Na_2O, NiO, S, Cu, Cl, Zn and F.

Vesicular rims were found on several of the glass beads. We suggest that these rims are remnants of the fluid that propelled the initial fire fountain eruptions of the picritic glasses.

Petrogenetic modeling confirms that the Apollo 15 A-B-C glass trends could not have been formed by fractional crystallization or any continuous assimilation/fractional crystallization (AFC) process. A simple, consistent model for the Apollo 15 A, B, and C is that the A group formed by congruent melting over a small pressure range, and then an average composition from group A assimilated a separate melt to form the B trend, and a second assimilation process formed the C trend. In this model the assimilants are melted before mixing with the group B and C progenitor glasses, and thus heat and mass transfer are decoupled, in a process similar to one envisioned for some terrestrial systems. A barometer created from multiple saturation points provides a depth estimate of other glasses in the A-B-C trend, and of the depths of assimilation. demonstrates that the Apollo 15 A-B-C trend originated over a depth range of ~460 km to ~260 km.

Chapter 7: Constraints on lunar magma ocean cumulate overturn. There is a long-standing hypothesis that the last fraction of the lunar magma ocean crystallized into a layer of dense, Ti-rich cumulate minerals at shallow depths (~100 km) early in the moon's history. It has been suggested that the cumulates subsequently sank deep into the moon because of gravitational instability. The high-Ti material may have re-erupted from depth, or some or all of it may have remained at shallow depths throughout lunar history. It is found that simple sinking of solidified high-Ti cumulates is unlikely because the temperature at which the cumulates solidify is low, and viscosity under these conditions is very high. It is, however, possible that high-Ti cumulates mixed with a substantial fraction of olivine would have viscosity low enough to allow them to sink as solids. Further, because clinopyroxene and ilmenite melt in a ratio of 2:1, remelted high-Ti cumulates would be negatively buoyant and sink as liquids, percolating downward through the underlying mantle.

Chapter 8: Magmatism from the late heavy bombardment. We present a model for impact-induced volcanism on the moon. Magma can be produced in two stages: first, crater excavation can depressurize the column beneath the crater to the point that material is moved above its

solidus and melts; and second, after excavation the lithosphere rises isostatically, warping the lithosphere-mantle boundary into a dome and initiating convection, in which adiabatic melting can occur. The in-situ decompression melting stage produces by far the largest volume of melt of the two stages and is consistent with the volumes of mare basalt seen in lunar basins. Lunar conditions are such that convection in the lithospheric dome can continue for up to 350 Ma.

The process of impact-induced volcanism can create a variety of magmatic compositions, probably including the aluminous, KREEP, high-Ti, and some of the low-Ti glass and basalts. The impact model results and a compilation of multiple saturation points are consistent with the following lunar conditions at 4.0 – 3.5 Ga: the potential temperature of the lunar mantle at 300 – 500 km depth was about 1450 °C, and the nearside lunar lithosphere is 200 – 300 km thick. The model further implies that deep magmas are picritic glasses, and that mare basalts originated in a cooler lithosphere. This lithosphere was heated and partly melted by impact processes. Only the shallowest mare basalts could not be produced directly by this process; they require the superheat and possibly heat of fusion of stalled, cooling magmas from deeper in the moon.

Ch. 1. Evidence for the formation of Pliocene Sierran high-potassium magmas from deep melting of an olivine-spinel-phlogopite-clinopyroxenite

Abstract

Phase equilibrium experiments have been conducted on a primitive olivine leucitite from the central Sierra Nevada, California. The near-liquidus phase relations of a WC-1 starting material were determined from 1.2 to 3.4 GPa and at temperatures from 1350 °C to 1460 °C in piston-cylinder experiments. The composition with ~2% H_2O is multiply saturated with olivine and clinopyroxene at approximately 2.8 GPa and 1460 °C, and with 6% water phlogopite is stable. Xenoliths carried by other young Pliocene lavas in the vicinity of WC-1 have yielded temperatures of equilibrium of 700 to 900 °C, with one outlier at 1060 °C. These xenoliths support the hypotheses of other researchers that the lower lithosphere under the Sierra Nevada delaminated just prior to the Pliocene, and fluid metasomatized mantle melted to produce the high-potassium Pliocene lavas. We suggest that subduction fluids drive a reaction that consumes garnet + orthopyroxene to create clinopyroxene + phlogopite, explaining the common finding that high-potassium magmas are created by melting phlogopite clinopyroxenites.

Introduction

Small volumes of high-potassium basaltic rocks have been found in varying tectonic settings worldwide. These rocks contain unusual mineralogies (including high-titanium and high-fluorine phlogopites and leucite) and are often highly magnesian, indicating an unusual petrogenesis when compared to higher-volume calc-alkaline or tholeiitic basalts (Figure 1).

Small volumes of high-potassium lavas erupted through the Sierra Nevadan granodiorites during the mid-Miocene, and again during the Pliocene, at about 3.5 Ma. The most primitive lavas contain 12 to 13 wt % MgO, and have Mg#s of 74 to 75 (Mg# = 100*molar Mg/[molar Fe + molar Mg]). These lavas also contain olivine phenocrysts with forsterite contents of 90.8 to 91, indicating that these high-MgO samples are in equilibrium with mantle olivine and represent liquid compositions. They are therefore potential near-primary liquid compositions from mantle melting beneath the Sierras, and provide information on the conditions of the continental mantle.

Classification and tectonic settings of high-K lavas

High-potassium rocks are found in a variety of locations representing different tectonic settings, including the Leucite Hills, Wyoming; the Sweet Grass Hills in Montana and Alberta; West Kimberley, Australia; the East African Rift; in the vicinities of Rome and Naples, Italy; the Colorado Plateau and Wasatch Plateaus; the Sierra Nevada, California; and western Mexico

(e.g., Foley 1992a; Righter 2000; Wannamaker *et al.* 2000, Buhlmann *et al.* 2000, Van Kooten 1980, Conticelli and Peccerillo 1992, Rogers *et al.* 1992, Carmichael *et al.* 1996).

High-potassium rocks have been classified in a number of ways over the past decades. Foley (1992a) emphasizes the continuous nature of the worldwide high-potassium compositional data set. He therefore recommends a classification based on a continuum of compositions among three end members, called lamproites, kamafugites, and plagioleucitites. Lamproites have the least calcium and the most extreme enrichment of incompatible elements and fluorine. They are associated with mild continental extension. Kamafugites have the highest calcium and lowest silica and are associated with continental rifting. Plagioleucitites have the highest aluminum and are associated with collisional settings. Those in the central Sierra fall mainly into Foley's plagioleucitite category, with elements of the lamproites. This classification, though intriguing for its reliance on tectonic setting, is not precise enough to help differentiate among rocks in a single setting.

To classify the high-potassium rocks of the Sierras, we follow the definitions of Farmer *et al.* (2002) and Feldstein and Lange (1999). Sixty-three lavas from the central Sierra Nevada are plotted in Figure 2. Those with lower alkalis, in the basalt to dacite series and the trachybasalt to trachyte series, are named according to part (A) of Figure 2. The higher alkali series, basanite to tephriphonolite, are further subdivided on the basis of potassium content and mineralogy.

High-potassium rocks are often defined according to the K_2O-SiO_2 scheme of Peccerillo and Taylor (1976), shown in part (B) of Figure 2. Lange *et al.* (1993) found, however, that rocks with identical potassium and silica contents (that would cause them to lie in the same place in Figure 2A) could have distinctly different phenocryst assemblages, possibly caused by different water or carbon dioxide contents. Farmer *et al.* (2002) define the high-potassium, low-silica Sierran rocks according to phenocryst and groundmass phases, as shown in Table 1. These differ somewhat from previous classification schemes, including that of Wallace and Carmichael (1989). The rocks we consider in detail in this study are categorized as absarokites, olivine leucitites, and basalts, and the xenoliths considered were carried to the surface in a trachyandesite and in a second, uncategorized host rock.

Tectonic setting of the central Sierra Nevada

Prior to the Miocene, there was active subduction of the Farallon plate to the west of the present Sierra Nevada. Subduction ended in the Miocene. Despite the height of the high Sierras and the size of the batholith, it has been shown through seismic studies that the deepest point to the Moho today is in the western Sierra (~43 km), and the Moho becomes shallower to the east (Jones *et al.*, 1994; Fleidner *et al.*, 1996). Under the central Sierra the Moho lies at about 35 km (Fleidner *et al.*, 1996; Wernicke *et al.*, 1996). Based on these observations, a number of researchers have proposed that the deep lithospheric root created by batholith production has delaminated. It is now thought that the high topography in the Sierras is caused by buoyant asthenospheric upwelling rather than isostatic equilibrium with a deep root.

Ducea and Saleeby have proposed a history for the lithosphere under the Sierras based on thermometry and barometry on crustal and peridotitic xenoliths carried to the surface in lavas. They find that the xenoliths with deep equilibration pressures (corresponding to 35 to 100 km depth) date to 80 to 120 Ma, the age of the most voluminous batholithic emplacement (Figure 3). They propose that the batholith emplacement created at least 70 km of mafic cumulates and residues under the Sierras, forming a thick, cold keel, and implying that the subducting slab had a steep dip under the continent (Ducea and Saleeby, 1998a). They find that xenoliths in younger lavas equilibrated at between 34 and 70 km and 1100 to 1200 °C, indicating an asthenospheric adiabat close to the bottom of the crust, and supporting the hypothesis that the deep keel delaminated and sank between 10 and 3 Ma (Ducea and Saleeby, 1996, 1998c). In further support of the delamination hypothesis, Ducea and Saleeby (1998b) found high-silica glass inclusions in xenoliths found in Pliocene lavas from the central Sierra Nevada, and propose that these glasses were low-percent melts of lower crustal compositions during delamination.

Manley *et al.* (2000) suggest that delamination occurred at 3.5 Ma, based on the sudden pulse of magmatism that provided the rocks used in this study, following the low and fairly constant level of magmatism that had persisted since 13 Ma. The potassic and ultrapotassic, low ε_{Nd} nature of these magmas is also in stark contrast to those that came before, and therefore the petrogenesis of these rocks must be strongly linked to the tectonic events. In further support, Farmer *et al.* (2002) found that only shallow, potassium-rich spinel peridotite xenoliths have the requisite low ε_{Nd} needed to form the Pliocene magmas. Heating and melting this shallow source requires

delamination. Lee *et al.* (2001) find evidence in xenoliths that hot asthenosphere and cold lithosphere were suddenly juxtaposed, demonstrated by high-temperature xenoliths with shallow equilibration pressures (temperatures are given in Figure 3). Though their evidence does not unequivocally indicate that delamination occurred in the Pliocene, the data indicate that if removal occurred in the Miocene, the delamination was only partial, whereas if the delamination occurred in the Pliocene, the entire lithosphere was removed. A partial removal in the Miocene could account for the low level of magmatism in the Sierras, and further removal in the Pliocene could account for the pulse of magmatism at that time.

Experimental and analytic techniques

Electron microprobe analysis of the natural compositions

We analyzed micas and olivines from five primitive lavas, designated WC-1, WC-6, TD-3, TD-8, and TD-14 from Farmer *et al.* (2002). The bulk compositions of these rocks, from Farmer *et al.* (2002), are given in Table 2. According to the classification scheme outlined above, samples TD-3, TD-8, and WC-6 are absarokites, TD-14 is a basalt, and WC-1, with the lowest silica of the group, is an olivine leucitite.

Mineral phases in phlogopite peridotite xenoliths from six Pliocene lavas are also analyzed.

Analyses were performed on the MIT JEOL-JXA-733 Superprobe, using a 10-micron spot size with a 10 nA beam current and an accelerating voltage of 15 kV, for oxide components SiO_2, TiO_2, Al_2O_3, Cr_2O_3, FeO, MnO, MgO, CaO, Na_2O, K_2O, and P_2O_5. For the olivines, only analyses with totals between 98.50 and 101.50 oxide wt % were included in our data set. The CITZAF correction package of Armstrong (1995) using the atomic number correction from Duncumb and Reed, the absorption corrections with Heinrich's tabulation of mass-absorption coefficients, and the fluorescence corrections from Reed was used to reduce the data and obtain a quantitative analyses.

Experiments on synthetic analogs of composition WC-1

From the available primitive Sierran lavas, olivine leucitite sample WC-1 was chosen as a likely candidate to be a primary liquid composition from mantle melting, based on its clean appearance in transmitted light, high bulk Mg# of 74, and analyses of its olivines, as discussed elsewhere in

the paper. A synthetic analog with the bulk composition of WC-1 was prepared from high-purity oxides and ground under ethyl alcohol for 6 hours.

We conditioned the material by pressing the powder into a pellet using Elvanol as a binding agent and hanging the pellet in a one-atmosphere Deltech furnace for 24 hours at 1000°C with an oxygen fugacity corresponding to the iron-wustite buffer. After conditioning, the material was melted to a glass in a piston cylinder apparatus and found to have lost more than half its Na_2O, K_2O, and P_2O_5. Because of the high volatile content of this composition, we then used only unconditioned powder in the subsequent experiments. It was further found that Na_2O had been lost in processing the powder, and an appropriate amount of liquid NaOH was added to make up the deficit. NaOH is strongly hygrophilic and its use resulted in adding ~2% H_2O of the final starting material, calculated by difference in microprobe analyses of experiments containing only glass. The composition of the starting material is shown in Table 2. The near-liquidus phase relations of this WC-1 starting material were determined in experiments from 1.2 to 3.4 GPa (corresponding to about 40 to 115 km depth) and at temperatures from 1350 °C to 1460 °C.

For each experiment ~10 mg of conditioned starting material was packed into a graphite crucible and capped with graphite. The capsule was then fitted into a hole drilled into the end of an MgO cylinder (or, in some cases, placed on top of the MgO cylinder inside an alumina ring), powdered graphite was packed around the capsule, and the assembly positioned in the hot spot of a graphite heater with MgO spacers, using $BaCO_3$ as the pressure medium. The experiments were performed in a 0.5-inch piston-cylinder apparatus. Pressure and temperature calibrations are described in Wagner and Grove (1997).

Runs in the piston cylinder apparatus were pressurized to 0.8 GPa, heated to 865 °C at 100 °C/min, pressurized to 1.5 GPa, heated to the run temperature at 50 °C/min, and then brought to final run pressure. When the final run pressure was less than 2.4 GPa, to obtain crystal-free glass the experiments were temperature- and pressure-quenched by shutting off the power to the furnace and simultaneously dropping the pressure on the experiment to 0.8 GPa. In experiments at pressures above 2.4 GPa, the experiment was ended by turning off the power alone and allowing the experiment to cool. Cooling to 500 °C takes about 11 seconds, and most cases was sufficient to quench thes liquid in the experiments to analyzable glass without the aid of pressure drop.

The experimental charges were sawn in half vertically, mounted in 1" epoxy disks, polished, and carbon-coated. The crystalline phases were analyzed at MIT on a JEOL-JXA-733 Superprobe as described in the previous section. Glasses in the experimental charges were analyzed with a beam diameter of 20 microns, or 10 microns when the size of the glass pool was too small to allow a 20-micron beam. A materials balance calculation was used to estimate phase proportions and to determine whether any oxides had been lost from the experimental charge. The high volatile and high magnesium content of this composition made maintaining perfect isolation of the experimental charge particularly difficult, especially when coupled with the relatively high pressures for the piston cylinder. Whenever the conditions placed the experiment close to the liquidus, the glass would flow through any available crack in the graphite capsule, gaining MgO and losing FeO, Na_2O, K_2O, and P_2O_5. This phenomenon lead, in particular, to fallacious appearances of olivine in experiments that were actually at conditions above the liquidus. Careful examination of the materials balance calculations was necessary, along with multiple repetitions of experiments at the same conditions.

Experiments on WC-1 with added silica and alumina

Because the WC-1 composition is not multiply saturated with orthopyroxene, a further synthetic composition was created to determine how close to orthopyroxene saturation the magma is. These experiments are motivated by the assumption that a primary mantle melt must be in equilibrium with two pyroxenes and olivine, and are intended to challenge the hypothesis that these magmas may have originated from unusual mantle compositions. In this model, a parental magma to WC-1 existed and fractionated alumina- and silica-rich phases to create WC-1. This model composition, WC-1+10%Si+5%Al, was created by adding 10% high purity SiO_2 and 5% Al_2O_3 to the existing WC-1 mix. This composition is listed in Table 2.

WC-1+10%Si+5%Al experiments were performed at 3.3 and 2.5 GPa, to increase the chances of obtaining analyzable results and acceptable mass balances. The experiments were conducted and analyzed as described in the preceeding section.

Experimental and analytic results

Olivine and phlogopite in the natural lavas

Between 7 and 31 olivine core analyses were made in each of the five natural compositions studied, WC-1, WC-6, TD-3, TD-8, and TD-14. The results of these analyses are listed in Table 3. The phenocrystic olivines vary in size up to about a millimeter, and are often euhedral.

The cores of the olivines represent the liquidus olivine of the bulk composition. We calculated the liquidus olivine composition that would be expected for the bulk Mg# of the rock, given an olivine/liquid Fe-Mg KD of between 0.29 and 0.32. If the measured olivine cores match the calculated equilibrium olivine composition, then the bulk rock may be considered a liquid composition. The expected liquidus olivine compositions and the analyses of the natural olivine cores are shown in figure 4, and a backscattered electron image of an olivine in lava WC-1 is shown in figure 5. For all the compositions the expected liquidus olivine compositions lie between Fo 88.7 and Fo 91. Samples WC-1 and WC-6 have the highest expected liquidus olivine forsterite contents, the first indicator of primitiveness. WC-6 and TD-14, however, contain no olivines with forsterite contents within the ranges predicted. These two compositions, therefore, may be cumulate compositions, and are not candidates to be liquid compositions. The other three samples, WC-1, TD-3, and TD-8, are likely primitive liquid compositions.

Between 5 and 20 mica analyses were made in each of the natural samples. The results of these analyses are listed in Table 4. In all the cases the mica analyzed was a phlogopite. The totals obtained varied from 90 to 100 wt%, indicating widely varying water contents among the samples analyzed (water is inferred by difference). The expected total for a phlogopite when water is not analyzed is 96 wt%; the remaining 4% is water. Sample WC-1 had the mica with the greatest water content (lowest analysis total), and sample TD-14 has the highest total. The micas, notably, contain between 6 and 10 wt% TiO_2, and 2.6 and 4.7 wt% F. Table 4 also shows the average phlogopite composition for each sample recast into the chemical formula for phlogopite. The analyses were recalculated on a basis of filled tetrahedral and octahedral sites (8, for these trioctahedral micas), rather than on an oxygen basis, because of unanalyzed water. Between 34 and 51% of the water sites in these micas are taken up by F, P, or Cl rather than water; sample WC-1 has the highest percentage of non-water residents in the water site.

Transects of microprobe analyses were made across several phlogopites from four of the five natural lavas. In all cases, potassium is strongly enriched and sodium slightly enriched at the

rims of the phlogopites, while fluorine, chlorine, and iron remain constant throughout the transect. Silica is slightly enriched at the edges of the grains, and aluminum is depleted at the edges. Titanium is depleted at the edges of all the micas with the exception of those in sample WC-1, in which titanium is somewhat enriched at the edges of the grains. These changes may reflect changes in magma composition during the crystallization of the phlogopites. For example, silica enrichment may occur when less titanium and aluminum are available to take up that site. That fluorine remains constant may reflect either that availability of water is not a limiting factor in crystallizing phlogopite, or that fluorine and water are equally likely to take up the site, and their ratio in the site in that case reflects the ratio of fluorine to water in the bulk composition. Van Kooten (1980) demonstrated, using a plot of fluorine vs. potassium content for whole rock analyses, that the high fluorine content in ultrapotassic rocks must be the result of phlogopite in the source. The high fluorine content of the micas in these Sierran lavas matches the fluorine content found in West Kimberley lamproites (Van Kooten, 1980, and references therein).

Xenoliths

Finding fresh phlogopite to analyze in the xenoliths was hampered by phlogopite decomposition. Much of the phlogopite has decomposed into a fine-grained mass of amphibole and oxides. In each sample, however, there was enough undecomposed phlogopite to obtain analyses. Of the six xenoliths analyzed, four were carried by trachyandesite TD-1, and are designated TD-1-A, TD-1-F, TD-1-G, and TD-1-I. A fifth xenolith was carried by an unclassified flow, and is labeled KVF-1-2-A, and the sixth xenolith was carried by basaltic andesite BK-003, and is designated BK-003-A. Lava samples are named following Farmer *et al.* (2002). All of the xenoliths were small, less than 4 cm in diameter, and all exhibited some level of alteration. TD-1-F, TD-1-G, TD-1-I, and BK-003-A are large-grained (grains on the millimeter scale and larger), while TD-1-A and KVF-1-2-A are finer-grained. Each of the xenoliths contains orthopyroxene, clinopyroxene, and phlogopite. TD-1-A and TD-1-G have no olivine, and TD-1-I has very little olivine. All the xenoliths except TD-1-G contain spinel, and sample KVF-1-2-A has at least three populations of spinels (TD-1-G contained neither spinel not garnet). Analyses of all phases are given in Table 5.

Using the composition of coexisting pyroxenes in the geothermometer QUILF (Anderson *et al.*, 1993), we were able to obtain estimates and errors for temperatures of final equilibration for the xenoliths in this study. These are shown in Figure 3 and Table 5. The temperatures found for these xenoliths, carried by Pliocene lavas, are arguably slightly hotter than temperatures calculated by previous researchers for xenoliths found in Miocene lavas.

An interesting reaction relationship is also found in the xenoliths. Where the large xenolith mineral grains met the magma that carried the xenolith, there was no reaction except when the xenolith grain was orthopyroxene. Each orthopyroxene grain has a thick reaction rim of clinopyroxene+phlogopite±spinel ±olivine, while the clinopyroxene, olivine, and phlogopite grains in the xenolith have no reaction rims (see Figure 6).

WC-1 experiments

The phase diagram for synthetic composition WC-1 is shown in Figure 7. The 29 experiments locate a multiple saturation point with olivine and clinopyroxene on the liquidus at 3.1 GPa (~100 km depth) at 1460°C. Olivine is the liquidus phase from 1 atmosphere pressure to the multiple saturation point. Above the multiple saturation point clinopyroxene is the liquidus phase. The phase relations at about 3.0 GPa have been determined in more detail. Olivine and clinopyroxene are crystallized over a temperature interval of ~15 °C, below which spinel is also a crystallizing phase. The small temperature interval between multiple saturation on the liquidus and the appearance of spinel may indicate that spinel was exhausted from the source during melting. As much as 60 °C below the multiple saturation point, olivine + clinopyroxene + spinel are still the crystallizing phases; orthopyroxene has not appeared. An analog for WC-1 with 6% H_2O was saturated with phlogopite.

The 12 experiments that contained analyzable glass and contained well-grown homogeneous phases were used to calculate crystal–liquid exchange equilibria. The average equilibrium olivine-melt Fe-Mg exchange coefficient, K_D, (where $K_D = [(X_{Fe}^{xtl} * X_{Mg}^{liq})/(X_{Mg}^{xtl} * X_{Fe}^{liq})]$) is 0.29. The average clinopyroxene-melt K_D is 0.28. The conditions and results of the 12 phase experiments for which analyses of multiple phases are available are given in Table 6. Seven other experiments (numbers 1, 2, 3, 4, 18, 19, and 20.2) were above the liquidus, and an additional five experiments (10, 15, 24, 25, and 26) contained recognizable phases but had no analyzable glass. A backscattered electron image of experiment 16 is given in Figure 8.

WC-1 with added silica and alumina experiments

The purpose of adding silica to the WC-1 composition is to attempt to obtain a multiple saturation point with two pyroxenes and olivine, the expected mantle assemblage. Of the five experiments conducted on this composition, none produced orthopyroxene. The run conditions and products for two experiments are listed in Table 6 and a backscattered electron image is shown in Figure 8.

Discussion

Phase equilibrium studies on high-K lava compositions

In the last quarter century approximately a dozen experimental studies have been done on high-potassium rocks. A selection of these studies is summarized in Table 7. The majority of the studies found a multiple saturation point with clinopyroxene + olivine + phlogopite on the liquidus, and a minority also found orthopyroxene, garnet, or spinel. Without two pyroxenes and olivine in multiple saturation, these seemingly primitive rocks are not in equilibrium with a mantle assemblage of minerals, and a spectrum of theories on their provenance have been suggested.

Of the twelve studies reviewed here, four found a combination of conditions and composition that lead to saturation with orthopyroxene. Tatsumi and Koyaguchi (1989) found olivine + orthopyroxene + clinopyroxene + phlogopite in equilibrium with an absarokite with 3% and 5% water, and no CO_2 or graphite in the assemblage. They therefore propose that the absarokite magma melted from a lherzolite at the pressure and temperature of multiple saturation. Hesse (unpublished, personal communication) also found such a mineral assemblage. The other two researchers that found orthopyroxene at multiple saturation appeared to require CO_2 to stabilize it. Edgar and Condliffe (1978) and Edgar *et al.* (1980), in their experiments on an olivine ugandite, obtained multiple saturation points with olivine + clinopyroxene + phlogopite at all water contents up to saturation (except the dry composition, which lacked phlogopite). By changing their volatile mix to 25% H_2O and 75% CO_2, they obtained orthopyroxene at multiple saturation. Sato (1997), in experiments at three water contents in assemblies with graphite in contact with the experimental charge, found the assemblage olivine + orthopyroxene + phlogopite. The effect of CO_2 on orthopyroxene stability has been noted previously; see Foley (1992a) and references therein.

Experimental studies that obtained olivine + clinopyroxene + phlogopite at multiple saturation include this study, Esperanca and Holloway (1987), Righter and Carmichael (1996), Barton and Hamilton (1978, 1979), Edgar and Condliffe (1978), and Edgar *et al.* (1976, 1980). Nicholls and Whitford (1983) and Mitchell (1995) both obtained the assemblage clinopyroxene + garnet + phlogopite. In none of their experiments could Nicholls and Whitford (1983) find any conditions under which the magma was in equilibrium with orthopyroxene. In an attempt to find how far from orthopyroxene saturation their magma was, they added finely ground orthopyroxene to their experimental mix. Experiments with up to 10 wt% added orthopyroxene did not saturate with orthopyroxene; nor did experiments with 10 wt% added orthopyroxene and CO_2 completely replacing water. In that case even the effects of CO_2 could not bring the composition to orthopyroxene saturation.

Where orthopyroxene saturation was not achieved, the researchers concluded that the magmas had melted from mica-olivine-pyroxenites at, or close to, water saturation. Some concluded that mica was exhausted from the residue, and others that mica remained, depending on arguments about fluorine and potassium variation or trace element indicators. Mitchell (1995) accepts previously published theories that the magmas are formed by melting amphibole- or phlogopite-bearing veins within harzburgite (Mitchell and Bergman, 1991; Foley, 1992b). The five studies that failed to obtain garnet at appropriate pressures also raise questions about garnet stability with these strange compositions. (See Table 7.)

Esperanca and Holloway (1987) did study a composition saturated with orthopyroxene, but in addition they state that the "ubiquitous" absence of orthopyroxene on the liquidus of undersaturated magmas can be explained by a series of reactions with orthopyroxene and liquid at high pressure and temperature. In particular they indicate the importance of the reaction

$$\text{phlogopite} + \text{enstatite} \Leftrightarrow \text{forsterite} + \text{liquid}$$

as potentially responsible for eliminating orthopyroxene from metasomatized source regions at pressures from 12 to 20 kbar and temperatures from 1150 to 1200 °C.

Petrologic and other studies on high-K lava compositions

A variety of petrologic and isotopic studies on high-potassium magmas have also come to a hesitant agreement that some high-potassium magmas are the result of melting unusual mantle

assemblies created by metasomatism. Lloyd and Bailey (1975) suggested that high-potassium magmas in Uganda were produced by melting of phlogopite clinopyroxenites. They further suggest that the phlogopite-rich mantle may provide additional buoyancy to the lithosphere in east Africa. Later, Lloyd *et al.* (1985) melted a mantle xenolith from Uganda consisting of clinopyroxene, phlogopite, and minor titanomagnetite, sphene, and apatite, to test the source theory. They found that a 20 – 30% melt of this xenolith at 3.0 GPa and 1175 to 1300 °C closely matched the high-potassium lavas of that area, and concluded that the high-potassium magmas of the region were likely the product of melting phlogopite clinopyroxenites.

Conticelli and Peccerillo (1992) studied potassic magmatism from central Italy, and also concluded that these magmas were the result of melting a phlogopite pyroxenite. The source composition was created by the addition of subduction fluids to an olivine + orthopyroxene + clinopyroxene mantle that remained subsolidus until the cessation of subduction at the time of continental collision. Later extension and heating melted the metasomatized mantle and created the undersaturated magmas. This tectonic scenario is similar to the Sierra Nevada.

Carlson and Nowell (2001) examined potassic magmas from the Colorado Plateau in light of growing evidence for non-peridotitic mantle compositions. They use Re and Os and other isotopic systems to analyze the likelihood that a melt came from a normal peridotite or from a non-peridotitic source. They find that the lowest silica compositions, katungites, are likely melts of mica-clinopyroxenites, and that the trend toward higher-silica minettes reflects increasing involvement of peridotitic wall rock.

Buhlmann *et al.* (2000) finds that the minettes in south Alberta carry numerous phlogopite clinopyroxenite xenoliths. They also find that the xenoliths and all the Albertan and Montanan high-potassium lavas have low ε_{Nd}, ranging from zero to –27. Low ε_{Nd} signatures seem to be ubiquitous among high-potassium magmas; e.g. Wannamaker *et al.*, 2000; Farmer *et al.*, 2002. Buhlmann *et al.* (2000) concludes that the most magnesian minettes were formed by melting clinopyroxene + phlogopite ± olivine at pressures greater than 1.7 GPa, and perhaps as great as 3.0 GPa. Other members of the high-potassium suite were created by fractionating clinopyroxene + phlogopite ± olivine from the most magnesian of the magmas.

Van Kooten (1980) suggested that the Sierran high-potassium magmas formed by melting a phlogopite- and garnet-bearing clinopyroxene-rich upper mantle source at depths of 100 to 125

km. He suggests that clinopyroxene enrichment of the upper mantle occurred as a result of introduction of a partial melt, and a fluid phase that carried Ba, Rb, Sr, K, and water. He notes that phlogopite occurs as both a groundmass phase and a vapor-phase vesicle filling. Where overlapping field relations are available, the lower-potassium lava overlies the high-potassium lava, indicating depletion by melting of a single source. Beard and Glazner (1998) suggest that the Deep Spring Valley lavas (see Figure 2) were formed by mixing between MORB-like magma and a potassic magma formed by melting high-K mantle veins, based on isotopic, trace, and major element variations in the lava compositions.

Foley (1992a) suggests that ultrapotassic lavas are frequently the result of melting a clinopyroxene + phlogopite source. He finds that models for the origin of ultrapotassic magmas by melting of phlogopite-bearing lherzolite are contradicted by the "now extensive" array of liquidus experimental results, and suggests that increasing degrees of CO_2 can lead to orthopyroxene saturation in a magma that is otherwise saturated with mica, clinopyroxene, and water. Foley (1992b) developed a comprehensive model for the origin of ultrapotassic magmas through the melting of clinopyroxene and phlogopite-rich veins in a peridotitic wall rock. In this model, the veins contain the hydrous minerals and any carbonates. He suggests that ultrapotassic magmas are hybrids of melt components derived from the veins and others derived from the wall rock, and that melting in the veins is continuously buffered by either phlogopite or amphibole. Foley (1992b) and Hirschmann and Stolper (1996) find that many olivine-poor mantle lithologies have lower melting temperatures than peridotite.

Source materials for high-potassium Sierran lavas

Because the purpose of this experimental study was to determine the mantle melting conditions and compositions that lead to the production of the high-potassium magmas in the Sierras, it is first necessary to ensure that the starting composition we use is as close to a primary mantle melt as possible. When working with mid-ocean ridge basalts, where the range of available mantle compositions for melting is more apparent, it is simpler to delineate a priori what characteristics a primitive melt should have. One of the traditional tests is for equilibrium with mantle olivine, expected to have a forsterite content of about 91. As described above, based on the olivine analyses made the three samples WC-1, TD-3, and TD-8 are likely primitive liquid compositions if they originated from a source with mantle olivine.

If the magma WC-1 is primary, then its multiple saturation point represents the temperature, depth, and mineral assemblage with which the magma was last in equilibrium; this generally implies the source it melted from. If the magma was not primary, then it may be multiply saturated with the phases it fractionated. In Figures 9, 10, and 11, the bulk compositions used in the experimental studies described above and in this study are plotted in ternary diagrams. In each diagram, the top provides labels to the compositions, and the bottom diagram shows the vectors from WC-1 for adding olivine, clinopyroxene, and phlogopite. Each vector represents adding 20% of the phase. In Figure 9, the olivine + clinopyroxene + quartz pseudoternary, it is apparent how severely undersaturated the magmas are.

The compositions that are saturated with orthopyroxene are marked with empty circles. Three, labeled Hesse, Tatsumi, and Sato, are multiply saturated with mantle phases. The Sato composition is only saturated with orthopyroxene when CO_2 is in the volatile phase. Arima has orthopyroxene saturation but no clinopyroxene. It is interesting to note that the few compositions that did saturate with orthopyroxene do not plot in the same region in any of the ternary projections used here. This reinforces the hypothesis that alumina and silica alone do not control orthopyroxene saturation.

In the olivine + clinopyroxene + quartz pseudoternary projection, the hypothetical magma parental to WC-1 would be close to a composition that is multiply saturated with mantle phases if it had fractionated 20% of clinopyroxene and 20% of olivine. This is an impossible scenario for several reasons. Firstly, the magma likely contained at least 3 to 5% water before eruption (e.g., Feldstein and Lange, 1999), and our experiments indicate that the magma is multiply saturated with phlogopite in wet conditions. Therefore fractionation of only clinopyroxene and olivine is unlikely. Secondly, a parental magma made from WC-1 plus 20% clinopyroxene and 20% olivine would have an Mg# of about 80, and have been precipitating olivines of near pure forsterite, a situation that seems highly unlikely. Lastly, in the other two pseudoternary figures, adding clinopyroxene and olivine will not move the composition close to any composition saturated with orthopyroxene.

These arguments lead us to conclude that magma WC-1 did not fractionate enough liquidus phases that any parental magma it evolved from would have been saturated with orthopyroxene. A second question remains: could this magma have been saturated with orthopyroxene if a large

proportion of its volatiles consisted of CO_2? The experiments reported here were conducted with about 2% H_2O and saturated with graphite, but perhaps the composition requires more water along with CO_2. WC-1 is similar in composition to that used by Nicholls and Whitford (1983), and addition of orthopyroxene and CO_2 was not sufficient to bring the magma into saturation with orthopyroxene. The experiments conducted on the WC-1 composition with added silica and alumina saturated with the same phases that the Nicholls and Whitford (1983) experiments with 2% H_2O had, that is, garnet and clinopyroxene. It is reasonable, then, to hypothesize that the WC-1 composition would behave as the Nicholls and Whitford (1983) composition, and fail to saturate with orthopyroxene.

A second line of evidence that the Sierran magmas did not contain enough volatiles to saturate orthopyroxene before eruption is found in the rims of the xenoliths. Though these xenoliths were not carried by WC-1, they were carried by magmas closely related compositionally and spatially. In every case where an orthopyroxene in a xenolith touched the magma that carried it, the orthopyroxene had a thick reaction rim of clinopyroxene+phlogopite+spinel ±olivine. Xenolithic phlogopites, olivine, and clinopyroxenes had no reaction rim. If the magma had a composition saturated with orthopyroxene, these reaction rims would not have formed. Interestingly, Feldstein and Lange (1999) found only two Sierran high-potassium lavas out of the thirty-eight studied contained any orthopyroxene, and the orthopyroxene found was in a clot surrounded by clinopyroxene.

We therefore conclude that magma WC-1 is close to primary, and that it melted from a fluid-metasomatized source consisting of olivine + clinopyroxene + phlogopite ± spinel in the presence of water. Other magmas in the suite may be related to WC-1 by fractional crystallization of these phases; Wallace and Carmichael (1989) have demonstrated this relationship for high-potassium magmas from western Mexico. This conclusion also implies that the xenoliths carried by related magmas are not examples of the source of the magma, but lithospheric material entrained in the eruption, because the xenoliths all contain two pyroxenes.

Mantle metasomatic reaction textures that create phlogopite and clinopyroxene are common in cratonic peridotite (Erlank *et al.*, 1987) The metasomatism creates both phlogopite, clinopyroxene and spinel through reaction of garnet and orthopyroxene (see their Fig. 2, 3 and 4) Such reaction textures lead to veins and also create interconnected polymineralic textures with

olivine. If such a metasomatized peridotite were melted, the resulting interconnected porous flow network could be created by melting the phlogopite + clinopyroxene + spinel metasomatic zones. In addition to their occurrence in the Kaapvaal craton, phlogopite-clinopyroxenite xenoliths have also been found in a number of localities, including Alberta (Buhlmann *et al.*, 2000), Uganda (Lloyd *et al.*, 1985), and Tanzania (Furman, 1995).

Van Kooten (1980) and others have suggested that a correlation of bulk rock Mg# and potassium, or between potassium or titanium and any incompatible element, would indicate that phlogopite was left in the residuum and buffered the melting reactions that formed the high-K magma. The Sierran suites from Farmer *et al.* (2002) show no correlation between potassium and Mg#, nor between potassium and the rare earth elements. There is, however, a clear positive linear relationship throughout the suite between potassium and barium. Foley (1989) demonstrated that barium and potassium vary inversely in mica through the substitution $Ba^{XII} + Al^{IV} = K^{XII} + Si^{IV}$. There is no clear relationship between whole-rock barium content and potassium in the micas, however. The data does not therefore indicate that phlogopite was buffering the melting reaction that formed the lavas, and may not have been left as a residual phase in the source.

Based on the lack of both orthopyroxene and garnet in many experimental studies, we suggest that the presence of a water-rich subduction fluid reduces the stability of both garnet and orthopyroxene, and makes phlogopite the stable aluminous phase. A metasomatic reaction that describes the transition from garnet lherzolite to spinel-phlogopite-clinopyroxene peridotite is as follows:

$$[CaMg_5]Al_4Si_6O_{24} + Mg_2Si_2O_6 + K_2O = K_2Mg_6Al_2Si_6O_{20}(OH)_4 + MgAl_2O_4 + CaSiO_3$$

mantle garnet + opx + fluid = phlogopite + spinel + cpx

Formation of phlogopite is driven by the presence of of an H_2O-rich, alkali-bearing fluid. A balanced reaction using mantle pyrope which contains 1/6 grossular component reacts with opx to makes an equal molar amount of phlogopite. In addition to phlogopite, reaction products are spinel and one mole of wollastonite, which will combine with the orthopyroxene present in the peridotite, and further deplete the peridotite in orthopyroxene

The fluid envisioned must be rich in the elements K, Rb, Sr, Ce, and Ba, to match the unusual enrichments found in the high-potassium lavas. Because the metasomatized mantle is the result of exchange reactions, and not melting residues or cumulates created by fractional crystallization, this metasomatized mantle will melt to create lavas with Mg#s similar to those of normal peridotite melts, as are seen in the Sierras, and in sample WC-1

Depths and temperatures of melting under the Sierra Nevada at 3.5 Ma

The magma WC-1 was not dry while melting, since it melted from a phlogopite-rich source, nor was it dry when it erupted and crystallized, based on phlogopites in the lava. Since multiple saturation temperatures and pressures are changed by water, the 2% H_2O multiple saturation point does not reflect the point of origin of the natural, wet composition WC-1. Feldstein and Lange (1999) have estimated that the magma held 3 – 5% water before eruption, and the water content could have been higher earlier in the magma's ascent.

Researchers are in agreement that addition of water lowers the temperature of multiple saturation. Figure 12 shows the effect of water on the temperatures and pressures of melting of the high-potassium magma phase equilibrium experiments described in Table 7. The experiments that were conducted on the same composition with varying water content are connected with lines. These are also shown as grey lines in Figure 13. Righter and Carmichael (1996) found that at 1.5 GPa, ~5 wt. % water depresses the liquidus by 100 °C. This is roughly in agreement with the results of Tatsumi and Koyaguchi (1989), whose experiments on an absarokite from Japan using three different water contents demonstrated water saturation suppresses the multiple saturation point by 140 °C and 0.7 GPa. Sato (1997) states that 6 to 12% water lowers the liquidus 100 °C at 5.0 GPa. These results are interestingly similar to the results of Gaetani and Grove (1998), who showed that the liquidus of an anhydrous depleted MORB mantle source is lowered 150 °C at 5% H_2O, and Baker, Grove, and Price showed that the liquidus of a primitive Cascades magma is lowered 170 °C with addition of 6% H_2O.

Though all the studies show that water decreases the temperature of multiple saturation, there is less agreement on the effect of pressure. In general, as seen in Figures 12 and 13, the pressure of multiple saturation is increased by addition of water. Only Nichols and Whitford (1983) show a decrease in the pressure of multiple saturation with the addition of water. This strange result may be an artifact of their analysis of experimental results, or it may be a true effect of the

unusual compositions studied; the movement of multiple saturation to lower pressures with the addition of water is considered anomalous until replicated by other researchers.

If the results of Tatsumi and Koyaguchi (1989) are applied to the absarokite used in this study, then the multiple saturation point of the 2% H_2O WC-1 composition from this study moves to approximately 1360 °C and 3.6 GPa when water-saturated. This hypothetical water-saturated multiple saturation point is in agreement with the estimates Van Kooten (1980) made for Sierran ultrapotassic basanites, estimated to have a source at 100 to 125 km depth (temperature was unconstrained). This implies that the water-saturated magma was created from its source at a potential temperature of about 1320 °C.

Melting of Pliocene high-potassium magmas under the Sierras was therefore deep but not unusually hot. In Figure 13, the multiple saturation points of high-potassium magmas are compared to temperatures and depths of melting in other tectonic regimes. To first order, continental arc magmas and MORB magmas are produced at similar pressures and temperatures. The high-potassium magmas are produced at an astonishingly wide range of pressures, but at low temperatures because of their high water content. This is consistent with the low volumes in which they are produced: if temperatures in the melting region were higher, then the unusual mantle mineral assemblages that produce the high-potassium magmas would be exhausted and larger-volume melts with more normal basaltic compositions would be created.

Both Farmer *et al.* (2002) and Lee *et al.* (2001) have suggested that warm asthenospheric upwelling into the space that the delaminated lithosphere under the Sierras had recently occupied triggered the small-volume high-potassium magmatic activity in the Pliocene. Though conductive heating of a lithospheric source by upwelling asthenosphere is possible, conductive heating is an inefficient and unlikely mechanism to trigger melting. We suggest that mantle that had been previously metasomatized by subduction fluids lay at some depth beneath the lithosphere, at a pressure too high to allow melting. When the lower lithosphere delaminated, this mantle, veined with phlogopite-clinopyroxenite, flowed upward into the void in the lower lithosphere (material would be pulled into the void left by the sinking delaminated material, and the dome in the lithosphere will drive a small convection cell in that place (Elkins Tanton and Hager, 2000)). The phlogopite component of the material will significantly lower its viscosity and facilitate flow. This material can then melt adiabatically as it reaches its solidus close to the

bottom of the lithosphere, and the high-potassium magmas will migrate through the remaining lithosphere to erupt. Hypothesizing that the phlogopite-clinopyroxenite source remained deeper in the mantle until delamination also explains why it was not available to melt in the Miocene.

Conclusion

Based on the many studies showing multiple saturation with olivine + clinopyroxene + phlogopite, and prior evidence for this in the Sierras, we conclude that the high-potassium magma WC-1 melted from a phlogopite-clinopyroxenite. The 2% H_2O composition is multiply saturated at 3.1 GPa and 1460 °C, and we suggest that the water-saturated multiple saturation point was at 1360 °C and 3.6 GPa. This wet multiple saturation point can be regarded as the depth and pressure of last equilibration of the magma with the metasomatized, phlogopite-clinopyroxenite source it melted from.

We hypothesize that the phlogopite-clinopyroxenite source lay beneath the Sierran lithosphere until delamination some time before the Pliocene, at which time the source material rose into the lithospheric dome and melted adiabatically to produce the high-potassium magmas.

These lavas also carried xenoliths to the surface. Based on QUILF thermometry and barometry on six such xenoliths, we find that four of them record cool, upper-lithospheric conditions, perhaps reflecting the upper lithosphere shortly after delamination.

We further hypothesize that subduction fluids drive a reaction that converts garnet + orthopyroxene to clinopyroxene + phlogopite, creating a phlogopite-clinopyroxenite from a mantle lherzolite while maintaining overall Mg#. Such a source is consistent with experimental results, bulk compositions, and xenolith/lava reaction relationships found in the Sierras.

Acknowledgements

Many thanks to Lang Farmer for his samples and guidance, and to Lang, Marc Hesse, and Steven Singletary's excellent company in the field. The advice, encouragement, and experimental expertise of Steven Singletary was invaluable to the progress of this research. This research was supported by an NSF grant.

References

Anderson D.J., D.H. Lindsley, P.M. Davidson (1993) QUILF: A PASCAL program to assess equilibria among Fe-Mg-Ti oxides, pyroxenes, olivines, and quartz. *Computers Geosciences* **19**, 1333-1350.

Arima M. and A.D. Edgar (1983) A high pressure experimental study on a magnesian-rich leucite-lamproite from the West Kimberley area, Australia: petrogenetic implications. *Contrib. Min. Pet.* **84** 228-234.

Armstrong, J.T. (1995) CITZAF – A package of correction programs for the quantitative electron microbeam x-ray-analysis of thick polished materials, thin-films, and particles. *Microbeam Anal.* **4** 177-200.

Baker M.B., T.L. Grove, R. Price (1994) Primitive basalts and andesites from the Mt. Shasta region, N. California: products of varying melt fraction and water content. *Contrib. Min. Pet.* **118** 111-129.

Barton M. and D.L. Hamilton (1978) Water-saturated melting relations of 5 kilobars of three Leucite Hills lavas. *Contrib. Min. Pet.* **66** 41-49.

Barton M. and D.L. Hamilton (1979) The melting relationships of a madupite from the Leucite Hills, Wyoming, to 30 kb. *Contrib. Min. Pet.* **69** 133-142.

Beard B.L. and A.F. Glazner (1998) Petrogenesis of isotopically unusual Pliocene olivine leucitites from Deep Springs Valley, California. *Contrib. Min. Pet.* **133** 402-417.

Buhlmann A.L., P. Cavell, R.A. Burwash, R.A. Creaser, R.W. Luth (2000) Minette bodies and cognate mica-clinopyroxene xenoliths from the Milk River area, southern Alberta: records of a complex history of the northernmost part of the Archaen Wyoming craton. *Can. J. Earth Sci.* **37** 1629-1650.

Carlson R.W. and G.M. Nowell (2001) Olivine-poor sources for mantle-derived magmas: Os and Hf isotopic evidence from potassic magmas of the Colorado Plateau. *Geochem. Geophys. Geosys.* 2.

Carmichael I.S.E., R.A. Lange, J.F. Luhr (1996) Quaternary minettes and associated volcanic rocks of Mascota, western Mexico: a consequence of plate extension above a subduction modified mantle wedge. *Contrib. Min. Pet.* **124** 302-333.

Conticelli S. and A. Peccerillo (1992) Petrology and geochemistry of potassic and ultrapotassic volcanism in central Italy: petrogenesis and inferences on the evolution of mantle sources. *Lithos* **28** 221-240.

Deer W.A., R.A. Howie, J. Zussman (1966) *An introduction to the rock forming minerals.* Longman , Burnt Mill, England.

Ducea M. and J. Saleeby (1996) Buoyancy sources for a large, unrooted mountain range, the Sierra Nevada, California: Evidence from xenolith thermobarometry. *J. Geophys. Res.* **101** 8229-8244.

Ducea M. and J. Saleeby (1998a) The age and origin of a thick mafic-ultramafic keel from beneath the Sierra Nevada batholith. *Contrib. Min. Pet.* **133** 169-185.

Ducea M. and J. Saleeby (1998b) Crustal recycling beneath continental arcs: silica-rich glass inclusions in ultramafic xenoliths from the Sierra Nevada, California. *Earth Planet. Sci. Lett.* **156** 101-116.

Ducea M. and J. Saleeby (1998c) A case for delamination of the deep batholithic crust beneath the Sierra Nevada, California. *Int'l Geology Rev.* **40** 78-93.

Edgar A.D., E. Condliffe (1978) Derivation of K-rich ultramafic magmas from a peridotitic mantle source. *Nature* **275** 639-640.

Edgar A.D., D.H. Green, W.O. Hibberson (1976) Experimental petrology of a highly potassic magma. *J. Pet.* **17** 339-356.

Edgar A.D., F.E. Lloyd, D. Vukadinovic (1994) The role of fluorine in the evolution of ultrapotassic magmas. *Min. Pet.* **51** 173-193.

Edgar A.D., E. Condliffe, R.L. Barnett, G.J. Shirran (1980) An experimental study of an olivine ugandite magma and mechanisms for the formation of its K-enriched derivatives. *J. Pet.* **21** 475-497.

Eggins S.M. (1992) Petrogenesis of Hawaiian tholeiitesd 1. Phase equilibria constraints. *Contrib. Min. Pet.* **110** 387-397.

Elkins Tanton, L.T. and Bradford H. Hager (2000) Melt intrusion as a trigger for lithospheric foundering and the eruption of the Siberian flood basalt. *Geophysical Research Letters 27* 3937-3940.

Elkins Tanton, L.T., T.L. Grove, and J. Donnelly-Nolan (2001) Hot shallow melting under the Cascades volcanic arc. *Geology* **29** 631-634.

Erlank A.J., F.G. Waters, C.J. Hawkesworth, S.E. Haggerty, H.L. Allsopp, R.S. Rickard and M. Menzies (1987) Evidence for mantle metasomatism in peridotite nodules from the Kimberley Pipes, South Africa. *In* M.A. Menzies and C.J. Hawkesworth, eds., *Mantle Metasomatism*, Academic Press, New York, pp. 221 – 311.

Esperanca S. and J.R. Holloway (1987) On the origin of some mica-lamprophyres: experimental evidence from a mafic minette. *Contrib. Min. Pet.* **95** 207-216.

Farmer G.L., A.F. Glazner, C.R. Manley (2002) Did lithospheric delamination trigger late Cenozoic potassic volcanism in the southern Sierra Nevada, California? *GSA Bulletin* **114** in press.

Feldstein S.N. and R.A. Lange (1999) Pliocene potassic magmas from the Kings River region, Sierra Nevada, California. Evidence for meting of a subduction-modified mantle. *J. Pet.* **40** 1301-1320.

Fliedner M.M., S. Ruppert, Southern Sierra Nevada Continental Dynamics Working Group (1996) Three-dimensional crustal structure of the southern Sierra Nevada from seismic fan profiles and gravity modeling. *Geology* **24** 367-370.

Foley S.F. (1989) Experimental constraints on phlogopite chemistry in lamproites: 1. The effect of water activity and oxygen fugacity. *Eur. J. Mineral.* **1** 411-426.

Foley S. (1992a) Petrological characterization of the source components of potassic magmas: geochemical and experimental constraints. *Lithos* **28** 187-204.

Foley S. (1992b) Vein-plus-wall-rock melting mechanisms in the lithosphere and the origin of potassic alkaline magmas. *Lithos* **28** 435-453.

Furman T. (1995) Melting of metasomatized subcontinental lithosphere: undersaturated mafic lavas from Rungwe, Tanzania. *Contrib. Min. Pet.* **122** 97-115.

Gaetani G.A. and T.L. Grove (1998) The influence of water on melting of mantle peridotites. *Contrib. Min. Pet.* **131** 323-346.

Grove T.L. (2000) Origin of Magmas. *In* Sigurdsson, H., ed. *Encyclopedia of Volcanoes.* Academic Press. San Diego CA, 1417 pp.

Grove T.L., S.W. Parman, J.C. Dann (1999) Conditions of magma generation for Archaen komatiites from the Barberton Mountainland, South Africa. *In.* Yingwei Fei, ed. *Mantle petrology: Field observations and high pressure experimentation: A tribute to Francis R. (Joe) Boyd.* Geochemical Society Special Publication No. 6.

Hirschmann M.M. and E.M. Stolper (1996) A possible role for garnet pyroxenite in the origin of the "garnet signature" in MORB. *Contrib. Min. Pet.* **124** 185-205.

Jones C.H., H. Kanamori, S.W. Rocker (1994) Missing roots and mantle "drips": Regional P_n and teleseismic arrival times in the southern Sierra Nevada and vicinity, California. *J. Geophys. Res.* **99** 4567-4601.

Kinzler, R.J., and Grove, T.L. (1992) Primary magmas of mid-ocean ridge basalts 1. Experiments and methods: *J. Geophys. Res.* **97** 6885–6906.

Klein E.M. and C.H. Langmuir (1987) Global correlations of ocean ridge basalt chemistry with axial depth and crustal thickness. *J. Geophys. Res.* **92** 8089-8115.

Lange R.A., I.S.E. Carmichael, P.R. Renne (1993) Potassic volcanism near Mono basin, California: Evidence for high water and oxygen fugacities inherited from subduction. *Geology* **21** 949-952.

Lee C.-T., R.L. Rudnick, G.H. Brimhall Jr. (2001) Deep lithospheric dynamics beneath the Sierra Nevada during the Mesozoic and Cenozoic as inferred from xenolith petrology. *Geochem. Geophys. Geosys.* **2.**

Le Maitre R.W. ed. (1989) *A classification of igneous rocks and glossary of terms.* Blackwell Scientific, Oxford. 193 p.

Lloyd F.E. and D.K. Bailey (1975) Light element metasomatism of the continental mantle: the evidence and the consequences. *Phys. Chem. Earth* **9** 389-416.

Lloyd F.E., M. Arima, A.D. Edgar (1985) Partial melting of a phlogopite-clinopyroxenite nodule from south-west Uganda: an experimental study bearing on the origin of highly potassic continental rift volcanics. *Contrib. Min. Pet.* **91** 321-329.

Manley C.R., A.F. Glazner, G.L. Farmer (2000) Timing of volcanism in the Sierra Nevada of California: Evidence for Pliocene delamination of the batholithic root? *Geology* **28** 811-814.

Mitchell R.H. (1995) Melting experiments on a sanidine phlogopite lamproite at 4-7 GPa and their bearing on the sources of lamproite magma. *J. Pet.* **36** 1455-1474.

Mitchell R.H. and S.C. Bergman (1991) *Petrology of Lamproites.* Plenum, New York. 447 pp.

Modreski D.J. and A.L. Boettcher (1972) the stability of phlogopite + enstatite at high pressures: A model for micas in the interior of the earth. *Am. J. Sci.* **272** 852-869.

Nicholls I.A. and D.J. Whitford (1983) Potassium-rich volcanic rocks of the Muriah complex, Java, Indonesia: products of multiple magma sources? *J. Volcan. Geo. Res.* **18** 337-359.

Peccerillo A. and S.R. Taylor (1976) Geochemistry of Eocene calc-alkaline volcanic rocks from Kastamonu area, northern Turkey. *Contrib. Min. Pet.* **68** 63-81.

Righter K. (2000) A comparison of basaltic volcanism in the Cascades and western Mexico: compositional diversity in continental arcs. *Tectonophysics* **318** 99-117.

Righter K. and I.S.E. Carmichael (1996) Phase equilibria of phlogopite lamprophyres from western Mexico: biotite-liquid equilibria and P-T estimates for biotite-bearing igneous rocks. *Contrib. Min. Pet.* **123** 1-21.

Rogers N.W., C.J. Hawkesworth, Z.A. Palacz (1992) Phlogopite in the generation of olivine-melilites from Namaqualand, South Africa and implications for element fractionation processes in the upper mantle. *Lithos* **28** 347-365.

Sato K. (1997) Melting experiments on a synthetic olivine lamproite composition up to 8 GPa: Implications to its petrogenesis. *J. Geophys. Res.* **102** 14751-14764.

Tatsumi Y. and T. Koyaguchi (1989) An absarokite from a phlogopite lherzolite source. *Contrib. Min. Pet.* **102** 34-40.

Tatsumi Y., Y. Furukawa, S. Yamashita (1994) Thermal and geochemical evolution of the mantle wedge in the northeast Japan arc: 1. Contribution from experimental petrology. *J. Geophys. Res.* **99** 22275-22283.

Van Kooten (1980) Mineralogy, petrology, and geochemistry of an ultrapotassic basaltic suite, Central Sierra Nevada, California, U.S.A. *J. Pet.* **21** 651-684.

Wallace P. and I.A.S. Carmichael (1989) Minette lava and associated leucitites from the Western Front of the Mexican Volcanic Belt: petrology, chemistry, and origin. *Contrib. Min. Pet.* **103** 470-492.

Wagner T. P. and Grove T. L. (1997) Experimental constraints on the origin of lunar high-Ti ultramafic glasses. *Geochim. Cosmochim. Acta* **61** 1315–1327.

Wagner T.P. and T.L. Grove (1998) Melt/harzburgite reaction in the petrogenesis of tholeiitic magma from Kilauea volcano, Hawaii. *Contrib. Min. Pet.* **131** 1-12.

Wannamaker P.E., J.B. Hulen, M.T. Heizler (2000) Early Miocene lamproite from the Colorado Plateau tectonic province, Southeastern Utah, USA. *J. Volcan. Geotherm. Res.* **92** 175-190.

Wernicke B., R. Clayton, M. Ducea, C.H. Jones, S. Park, S. Ruppert, J. Saleeby, J.K. Snow, L. Squires, M. Fleidner, G. Jiraceck, R. Keller, S. Klemperer, J. Luetgert, P. Malin, K. Miller, W. Mooney, H. Oliver, R. Phinney (1996) Origin of high mountains in the continents: the southern Sierra Nevada. *Science* **271** 190-193.

Table and figure captions

Table 1. Classification of high-potassium, low-silica extrusive igneous rocks, after Farmer *et al.* (2002).

Table 2. Bulk compositions in oxide wt % for the five natural compositions of Sierran high-K lavas discussed in this paper (Farmer *et al.*, 2002), and the synthetic starting compositions used in experiments.

Table 3: Average electron microprobe olivine compositions from five Sierran high-K lavas in oxide wt %. Reported values are averages of N analyses. Two-sigma population errors are shown (two sigma standard deviation divided by the square root of the number of analyses), in units of the last significant digit of the oxide wt%. The highest and lowest Mg# analyses are given to show the range of compositions.

Table 4: Average electron microprobe phlogopite compositions from five Sierran high-K lavas in oxide wt %. Reported values are averages of N analyses. Two-sigma population errors are shown (two sigma standard deviation divided by the square root of the number of analyses), in units of the last significant digit of the oxide wt%. Mica analyses are converted into mineral formulae on the basis of 11 oxygens. Sites and expected contents are after Deer *et al.* (1966). All the micas have significant percentages of their hydroxyl sites taken up by fluorine.

Table 5. Phases in six metasomatized xenoliths carried to the surface by lavas in the King's Canyon volcanic field analyzed by electron microprobe. Reported values are averages of N analyses. Major elements in oxide wt% and their standard deviations are given, in units of the last significant digit of the oxide wt%. Mg# is calculated as (molar MgO/(molar MgO + molar FeO)). Temperatures with errors are shown from QUILF thermometry based on two pyroxenes (Anderson *et al.*, 1993).

Table 6. Conditions and products of experiments. Pressure is GPa, temperature in °C, run times in hours. Sum of squared residuals resulting from multiple linear regression of analyzed phases against starting compositions is given as R^2, and elements most responsible for residual are listed. Phase proportions are also the results of linear regression. Run product compositions are given in oxide wt%. Glass analyses are reported as analyzed, and renormalized to 100%. Reported values are averages of N analyses. Number after oxide is 1 standard deviation on the average and is in units of the last significant digit of the oxide wt%.

Table 7. A summary of phase equilibrium studies of high-potassium lavas. Bulk compositions are listed in wt %, normalized without H_2O or CO_2, which is listed in a separate column. Liquidus or near-liquidus phases are shown, a mark indicating the presence of the phase. Ol = olivine; C = clinopyroxene; Op = orthopyroxene; G = garnet; S = spinel; P = phlogopite. Garnet is expected at pressures over about 2.2 GPa; "na" in the garnet column indicates no experiments were performed at those pressures. Experiments with graphite in contact with the experiment are marked in the "C" column; CO_2 may be involved in orthopyroxene stability. Multiple saturation points are listed in GPa and °C. Those with question marks are interpreted by the authors of this study. Note that only about a third of the experiments have near-liquidus orthopyroxene, and that garnet is often absent at its stability pressures.

Figure 1. High-potassium rocks from several localities compared to average ocean island basalt, mid-ocean ridge basalt, and island arc basalts in a K_2O vs. TiO_2 variation diagram, making

the anomalously high-potassium nature of these rocks clear. Kings and San Jaoquin volcanic field data from Farmer *et al.* (2002); Basin and Range and Deep Spring Valley lava compositions from Beard and Glazner (1998) and references therein. A box marks the composition WC-1 used for the experiments in this study.

Figure 2. Primitive extrusive igneous rock classification schemes. (A) Total NaO plus K_2O vs. SiO_2 (scheme of Le Maitre, 1989), and (B) K_2O vs. SiO_2 (scheme of Peccerillo and Taylor, 1976). References for rock compositions as for Figure 1. A box marks the composition WC-1 used for experimentation in this study.

Figure 3: Equilibration temperatures for xenoliths from Pliocene and Miocene lavas. Data from Ducea and Saleeby (1998c); filled squares: Lee *et al.* (2001); triangles (empty triangles are from rim compositions), and this study, filled circles. Temperatures of multiple saturation from this study, 2% H_2O, empty square; hypothetical water-saturated point, hatchured square.

Figure 4. Analyzed and calculated equilibrium olivine analyses for Sierran lavas. Circles are olivine core analyses (see Table 4), and bars show expected equilibrium olivine compositions, assuming KD2 from 0.29 to 0.32. Three of the rocks are liquid compositions, and two (TD-14 and WC-6), are probably cumulates. WC-1 is used in phase equilibrium experiments in this study.

Figure 5. Backscattered electron image of an olivine phenocryst in lava WC-1. Groundmass is fine-grained and vesicular; olivine composition is Fo 90.5 at center.

Figure 6. Backscattered electron images of the edges of the xenolith carried in lava TD-1. In (A), a large clinopyroxene grain from the xenolith is in contact with lava TD-1 with no reaction rim. In (B), an orthopyroxene from the xenolith has a wide reaction rim separating it from the lava. The reaction rim consists of clinopyroxene, spinel, and a hydrous potassium-rich phase, either amphibole or phlogopite. In every xenolith examined, any orthopyroxenes found in contact with the lava had wide reaction rims consisting of clinopyroxene+phlogopite or amphibole ± olivine ±spinel. Other phases lack reaction rims.

Figure 7. Phase equilibrium experiments on synthetic analog of Sierran olivine leucitite WC-1. Experiment numbers are marked. The filled oval marks

Figure 8. Backscattered electron images of experimental run products for experiments 16 and SiAl 5.

Figure 9. Bulk compositions for the high-potassium lava experimental studies from Table 7 shown in a olivine-clinopyroxene-quartz pseudoternary projections. Note that in the olivine-clinopyroxene-quartz figure, the olivine and clinopyroxene axes are extended past 100%, into silica-undersaturated space. At the top, the compositions are labeled according to their authors in Table 7, with the exception of two compositions from this study: WC-1 and WC-1 + 10%Si + 5% Al. Compositions with orthopyroxene as a liquidus or near-liquidus phase are shown as empty circles; those with no orthopyroxene as a run product are shown as filled triangles. Note the extreme silica undersaturation of many of these compositions, but that compositions with orthopyroxene are both saturated and undersaturated. Vectors represent 20% addition of clinopyroxene, phlogopite, and olivine, as marked, to bulk composition WC-1. Additive phases are from liquidus, near-multiple saturation point experiments 16 and 20.2 from this study. It has been suggested that some bulk compositions lack orthopyroxene saturation because they had fractionated liquidus phases.

Figure 10. Bulk compositions and assimilation vectors as in Figure 9, shown in an olivine-clinopyroxene-plagioclase pseudoternary projection. Note that it is not possible to move the undersaturated bulk compositions closer to the orthopyroxene-saturated compositions by any combination of addition of these phases.

Figure 11. Bulk compositions and assimilation vectors as in Figure 9, shown in an olivine-clinopyroxene-potassium feldspar pseudoternary projection. In this projection, phlogopite addition is required to move the composition WC-1 toward orthopyroxene multiple saturation, in contradiction to Figs. 9 and 10.

Figure 12. High-potassium lava multiple saturation points from Table 7, showing the changes in multiple saturation with addition of water. Experiments done with varying water contents on the same bulk composition are shown linked with lines.

Figure 13. Pressures (depths) and temperatures of mantle melting in different tectonic regimes. Mid-ocean ridge magma genesis conditions are shown with dotted line: Kinzler and Grove (1992), Grove (2000), and Klein and Langmuir (1987). Continental arc magmatism is shown with hatchured bars: Cascades high-alumina olivine tholeiites from Elkins Tanton *et al.* (2001), the northeast Japanese arc from Tatsumi *et al.* (1994), dry and wet Cascades melts from Baker *et al.* (1994), and a komatiite multiple saturation point from Grove *et al.* (1999). Conditions of melting under Hawaii from Wagner and Grove (1998) and Eggins (1992). Multiple saturation points of high-K lavas shown with filled circles, results from this study, Edgar and Condliffe (1978), and Edgar *et al.* (1976, 1980), Barton and Hamilton (1978, 1979), Arima and Edgar (1983), Nicholls and Whitford (1983), Esperanca and Holloway (1987), Tatsumi and Koyaguchi (1989), Mitchell (1995), Righter and Carmichael (1996), Sato (1997). Vectors connect multiple saturation points for the same composition with different water contents. The vector of Tatsumi and Koyaguchi is applied to the Sierran composition from this study, to estimate the water-saturated multiple saturation point. An approximate mantle solidus, plagioclase, spinel, and garnet phase volumes are shown, as well as approximate adiabats that correspond to the 2% water and water saturated Sierran high-potassium lava compositions.

Table 1. Classification of high-potassium, low-silica extrusive igneous rocks (after Farmer *et al.*, 2002)

Rock name	phenocryst phases	groundmass phases	Notes
Absarokite	olivine, augite	plagioclase	
Shoshonite	olivine, augite	plagioclase	Absarokite and shoshonite are differentiated by bulk K_2O and SiO_2 (Fig. 2)
Olivine leucitite	olivine, augite	leucite, plagioclase	
Minette	olivine, augite, phlogopite	plagioclase	

Table 2. Bulk compositions

	H_2O	SiO_2	TiO_2	Al_2O_3	Cr_2O_3	FeO	MnO	MgO	CaO	Na_2O	K_2O	P_2O_5	Mg#
Natural compositions													
WC-1		44.77	1.25	12.71	0.08	8.70	0.17	13.93	10.68	2.17	4.20	1.34	74.04
WC-6		45.49	1.09	12.30	0.07	7.96	0.16	14.66	11.22	2.97	2.89	1.19	76.64
TD-3		46.73	1.46	10.93	0.07	9.16	0.16	12.89	10.34	3.77	3.16	1.33	71.49
TD-8		45.71	1.22	11.77	0.06	8.74	0.18	12.75	10.10	3.21	4.24	2.02	72.22
TD-14		48.51	0.89	13.44	0.10	9.19	0.17	13.67	9.94	2.62	1.01	0.47	72.60
Synthetic experimental materials													
WC-1 exp. starting material	2.00	44.40	1.19	12.91	0.13	8.73	0.16	14.23	11.61	2.39	3.15	1.10	74.39
WC-1 with 10% silica and 5% alumina	2.00	47.47	1.02	13.39	0.12	7.97	0.15	13.83	11.28	2.32	1.53	0.92	75.56
WC-1 with 6% H2O	6.00	44.40	1.19	12.91	0.13	8.73	0.16	14.23	11.61	2.39	3.15	1.10	74.39

Table 3. Olivine cores from natural compositions

Sample		N	SiO_2	TiO_2	Al_2O_3	Cr_2O_3	FeO	MnO	MgO	CaO	NiO	Tot	Mg#
WC-1	Average	31	40.1	0.00	0.00	0.01	10.5	0.18	49.2	0.15	0.39	100.54	89.3
	2 s pop. st. dev. (wt%)		1			1	5	3	4	1	2		
	Highest Mg# analysis		40.0	0.00	0.00	0.02	9.0	0.12	50.1	0.12	0.48	99.81	90.8
	Lowest Mg# analysis		39.6	0.00	0.00	0.05	14.3	0.37	46.6	0.19	0.28	101.27	85.3
WC-6	Average	7	39.0	0.00	0.04	0.04	15.0	0.39	45.3	0.18	0.25	100.19	84.4
	2 s pop. st. dev. (wt%)		6		2	1	6	3	7	2	8		
	Highest Mg# analysis		39.2	0.01	0.03	0.03	14.6	0.40	45.0	0.15	0.22	99.54	84.6
	Lowest Mg# analysis		39.0	0.00	0.03	0.02	15.7	0.39	44.9	0.23	0.15	100.42	83.6
TD-3	Average	14	40.1	0.00	0.03	0.03	10.8	0.14	48.7	0.12	0.37	100.30	88.9
	2 s pop. st. dev. (wt%)		2		2	1	6	2	5	2	7		
	Highest Mg# analysis		40.7	0.00	0.02	0.03	9.6	0.09	49.6	0.12	0.51	100.69	90.2
	Lowest Mg# analysis		39.4	0.01	0.15	0.00	13.3	0.24	46.5	0.23	0.10	99.87	86.2
TD-8	Average	9	40.0	0.00	0.03	0.03	12.3	0.27	47.8	0.17	0.29	100.86	87.4
	2 s pop. st. dev. (wt%)		2		1	1	9	5	8	5	5		
	Highest Mg# analysis		40.3	0.00	0.02	0.04	10.7	0.21	49.4	0.08	0.34	101.08	89.1
	Lowest Mg# analysis		39.4	0.01	0.05	0.01	15.2	0.39	45.4	0.21	0.23	100.93	84.2
TD-14	Average	12	39.2	0.00	0.04	0.04	16.2	0.41	44.1	0.19	0.24	100.43	82.9
	2 s pop. st. dev. (wt%)		2		1	1	8	4	5	2	3		
	Highest Mg# analysis		39.7	0.00	0.07	0.04	13.0	0.34	45.1	0.21	0.32	98.84	86.1
	Lowest Mg# analysis		39.2	0.00	0.04	0.03	17.7	0.53	42.9	0.23	0.18	100.78	81.2

Table 4. Mica from natural compositions

Sample	N	SiO_2	TiO_2	Al_2O_3	Cr_2O_3	FeO	MnO	MgO	CaO	Na_2O	K_2O	P_2O_5	Cl	F	Tot	Mg#
WC-1	Average phlog. 20	33.3	8.8	13.6	0.03	7.1	0.06	15.8	0.02	0.77	7.0	0.7	0.14	3.7	90.98	80.0
	2 s (wt%)	6	3	2	1	2	1	2	1	7	4	2	2	3		
WC-6	Average phlog. 19	35.5	9.2	13.5	0.16	8.2	0.09	16.7	0.1	0.88	8.0	1.0	0.03	2.6	95.86	78.4
	2 s (wt%)	4	4	2	4	2	1	4	2	7	3	0	1	1		
TD-3	Average phlog. 5	37	8	14	0.4	8	0.12	18	0.05	0.58	8	0.1	0.02	3.4	97.32	79.7
	2 s (wt%)	2	3	1	7	2	3	3	3	6	1	1	2	7		
TD-8	Average phlog. 14	36	9.9	13.7	0.02	7.4	0.09	17.2	0.02	1.01	7.6	0.0	0.03	3.7	96.35	80.5
	2 s (wt%)	1	4	5	1	3	1	7	1	8	6	0	1	1		
TD-14	Average phlog. 15	38.5	6.2	13.4	0.26	6.5	0.07	20.5	0.09	0.77	8.8	1.0	0.07	4.0	100.20	85.0
	2 s (wt%)	2	3	2	1	1	1	3	1	5	2	0	2	1		

	Chemical Formula							
	Site:	Z	Z	Y	X	Hyd.	Hyd.	**Total**
	Contents:	Si	Al	remain	Na,K	P,Cl,F	H_2O	
						analyzed	by diff.	
Sample	Expected ions:	**3**	**1**	**3**	**1**		**2**	**10**
WC-1	average	2.73	1.27	3.0	0.85	1.0	1.0	9.9
	1 s stand. dev.	5	5	1	6	2	2	1
WC-6	average	2.70	1.30	2.87	0.91	0.68	1.32	9.77
	1 s stand. dev.	4	4	3	4	5	5	6
TD-3	average	2.8	1.2	3.1	0.9	0.8	1.2	10.0
	1 s stand. dev.	1	1	1	1	2	2	2
TD-8	average	2.8	1.2	3.04	0.90	0.90	1.10	9.94
	1 s stand. dev.	1	1	1	8	4	4	8
TD-14	average	2.85	1.15	3.06	0.94	1.01	0.99	10.00
	1 s stand. dev.	4	4	3	5	5	5	5

Table 5. Sierra Nevada xenoliths

Sample	phase	N	SiO_2	TiO_2	Al_2O_3	Cr_2O_3	FeO	MnO	MgO	CaO	Na_2O	K_2O	P_2O_5	NiO	Cl	F	Total	Mg#	T [C]	+/-
TD-1-A	Opx.	7	56.93	0.132	1.23	0.42	8.11	0.191	32.63	1.41	0.00						100.90	87.7	1068	36
	Cpx.	15	54.27	0.00	1.53	0.31	4 6 3	0.131	18.53	20.83	0.0						100.10	87.7		
	Phlog.	8	38.09	2.72	14.67	0.84	6.59	0.042	21.09	0.021	0.746	8 1	0.12 0		0.04 3	4 2	97.04	85.1		
	Spin.	1	0.30	6.77	12.68	1.74	64.08	0.12	5.57	0.01				0.23			91.50	13.4		
	Ulvosp.	3	0.064	35 19	0.6 4	1.5 2	50 18	0.189	5.4 8	0.1 1				0.5 4			93.13	16.3		
TD-1-F	Oliv.	22	40.28	0.03 0	0.00	0.00	13.9 7	0.15 1	47 1	0.04 1							101.17	85.7	819	55
	Opx.	14	56.11	0.12 0	2.1 1	0.21 1	8.9 1	0.14 1	32.9 2	0.5 2	0.00						100.87	86.9		
	Cpx.	2	53.63	0.29 4	2.7 2	0.50 1	3.55 4	0.09 4	16.6 2	23.0 1	0.62 8						100.99	89.3		
	Phlog.	4	39.42	1.89 8	15.9 2	0.98 5	5.7 2	0.04 2	22.6 2	0.00	0.9 2	8 1				5 1	100.15	87.6		
	Ulvosp.	4	0.0	62.46	1.3 1	1.66 9	23.4 6	0.00	8.4 2	0.00							97.00	39.0		
TD-1-G	Opx.	9	55.22	0.09 1	3.1 2	0.23 2	9.7 6	0.21 1	32.0 2	0.6 1	0.00						101.03	85.5	828	66
	Cpx.	20	53.02	0.25 3	3.5 2	0.35 5	4.3 2	0.12 1	16.4 2	22.5 3	0.68 2						100.99	87.2		
	Phlog.	11	38.22	1.7 2	16.5 2	0.31 4	6.4 3	0.02 2	21.1 4	0.00	0.60 4	9.2 2	0.12 0		0.04 2	1.7 9	95.75	85.5		
TD-1-I	Oliv.	2	40.06	0.00	0.00	0.03 2	14.2 2	0.16 5	46.4 4	0.12 1	0.00			0.24 0			101.17	85.4	834	92
	Opx.	22	55.71	0.06 1	2.0 9	0.58 2	6.7 1	0.14 1	34.5 9	0.0	0.00						99.66	90.2		
	Cpx.	6	53.75	0.20 7	2.3 5	0.6 2	3.5 2	0.07 2	17 5 5	21.9 9	0.59 6						100.47	89.9		
	Phlog.		small, highly altered, unanalyzable																	
	Chrom.	1	0.1	3.30	5.15	31.84	46.9	0.25	5.9	0.18				0.22			93.80	18.3		
	Magnet	1	0.1	1.68	2.69	0.78	87.1	0.18	1.8	0.04				0.29			94.56	3.5		
	Spin.	1	0.0	0.50	25.53	21.29	32.4	0.24	15.3	0.05				0.27			95.58	45.6		
KVF-1-2-A	Oliv.	13	40.32	0.00	0.00	0.00	11.2 3	0 19 2	47.7 5	0.13 1	0.13 5						99.60	88.4	958	17
	Opx.	5	56.29	0.16 7	1.4 3	0.31 9	10.0 8	0.22 1	31.8 3	1.1 3	0.00						101.15	85.1		
	Cpx.	11	53.64	0.38 3	1.5 2	0.6 2	4.2 2	0.12 1	17.8 2	22.3 1	0.30 5						100.71	88.3		
	Phlog..	4	38.53	2.4 3	14.5 4	1.0 2	6.1 5	0.05 2	22.1 3	0.02 1	0.92 6	8.9 1	0.12 0		0.02 1	4 1	98.64	86.6		
	Spin.	2	0.04 1	4.1 5	13.2 7	23 4	48 2	0.35 1	9.4 2	0.00				0.29 1			98.42	25.9		
	Spin.	3	0.00	1.42 9	9 1	43 2	34 4	0.32 2	9 1	0.4 1				0.13 4			97.71	32.3		
	Spin.	1	0.00	4.08	5.02	14.00	64.42	0.34	6.60	0.01				0.31			94.78	15.4		
	Spin..	1	0.00	43.83	0.11	1.52	43.75	0.19	3.49	0.00				0			92.89	12.4		
	Mag.	1	0.04	4.33	2.72	3.66	79.32	0.26	2.58	0.03	0.48			0.31			93.73	5.5		
BK-003-A	Opx.	8	57.84	0.03 1	0.8 3	0.19 7	6.5 2	0.17 2	35.3 3	0.3 1	0.00						101.23	90.6	788	64
	Cpx.	7	54.96	0.2 1	1.1 9	0.38 8	2.8 8	0.11 3	18.2 6	23 2	0.5 2						101.26	92.0		
	Spin	1	0.07	0.73	14.36	44.96	27.28	0.24	12.36	0.02				0.25			100.27	44.7		

(other phases in BK-003-A not analyzed)

Table 6. Experimental conditions and results

Starting composition: WC-1 with 2% water

Run	P	T	t	R^2	Prop.	phase	N	SiO_2	TiO_2	Al_2O_3	Cr_2O_3	FeO	MnO	MgO	CaO	Na_2O	K_2O	P_2O_5	Total	K_D
5	1.2	1390	4.5	0.37	98	glass	3	43.33	1.267	13.01	0.000	8.81	0.152	13.22	11.72	2.72	3.261	1.31	98.54	
					2	olivine	8	40.45	0.011	0.091	0.181	9.52	0.141	50.34	0.443	0.000	0.000	0.000	101.05	0.29
6	1.2	1370	4.5	0.03	94	glass	5	43.82	1.187	13.336	0.143	8.53	0.172	11.985	12.138	2.51	3.36	1.37	98.33	
					5	olivine	5	39.837	0.011	0.082	0.152	10.11	0.163	48.53	0.423	0.000	0.000	0.000	99.17	0.29
					1	spinel	2	2.33	0.663	34.43	34.83	12.194	0.171	18.34	0.602	0.000	0.000	0.000	103.42	
7	1.2	1350	1.0	0.14	94	glass	6	43.72	1.179	13.128	0.203	8.467	0.171	12.11	11.62	2.319	3.047	1.22	97.03	
				Ca	5	olivine	3	39.73	0.023	0.081	0.152	10.21	0.161	48.176	0.442	0.000	0.000	0.000	98.85	0.30
					1	spinel	2	0.282	0.691	321	37.18	12.14	0.192	18.16	0.188	0.000	0.000	0.000	100.81	
8	2.1	1400	0.8	2.06	101	glass	4	43.72	1.12	12.52	0.243	8.73	0.152	14.057	10.539	2.32	3.145	2.22	98.72	
				Ca, P	-1	olivine	6	41.22	0.11	0.103	0.205	9.22	0.112	50.12	0.433	0.012	0.000	0.000	101.39	0.29
9	2.0	1420	0.8	1.18	100	glass	2	43.44	1.184	12.73	0.161	8.44	0.131	13.94	11.33	2.32	3.204	2.13	98.79	
				Cr, Fe, P	0	olivine	4	41.02	0.048	0.11	0.156	9.62	0.144	50.04	0.483	0.000	0.000	0.000	101.50	0.32
11	2.4	1410	1.5	1.05	87	glass	8	43.23	1.199	13.61	0.173	8.65	0.172	11.39	11.03	3.25	2.92	0.738	96.21	
				Ca, Na, K, P		renorm		44.9	1.24	14.1	0.18	9.0	0.18	11.8	11.5	3.3	3.0	0.76	100.00	
					6	olivine	6	40.466	0.042	0.22	0.143	9.84	0.102	48.58	0.78	0.000	0.000	0.000	99.95	0.27
					7	cpx	6	51.16	0.374	7.15	1.32	3.42	0.052	16.94	19.03	0.738	0.000	0.000	99.85	0.26
12	2.6	1430	2.0	0.54	91	glass	6	43.73	1.407	13.71	0.171	8.52	0.133	12.92	11.22	2.62	3.177	0.709	98.06	
				Al, Fe, P		renorm		44.5	1.43	14.0	0.17	8.6	0.13	13.2	11.4	2.6	3.23	0.71	100.00	
					3	olivine	3	40.63	0.011	0.130	0.142	9.71	0.173	49.439	0.423	0.000	0.000	0.000	100.63	0.30
					6	cpx	3	51.42	0.343	7.71	1.064	3.42	0.131	17.24	18.74	0.913	0.000	0.000	100.75	0.30
13	2.1	1430	4.0	1.88	98	glass	5	42.91	1.21	12.856	0.222	8.22	0.181	13.468	12.71	2.225	2.935	1.025	97.90	
				Si, Fe, Ca		renorm		43.8	1.2	13.13	0.22	8.4	0.18	13.75	13.0	2.27	2.99	1.04	100.00	
					2	olivine	3	40.71	0.030	0.141	0.181	9.11	0.151	49.987	0.453	0.000	0.000	0.000	100.66	0.30
14	2.0	1440	0.6	0.35	99	glass	4	43.34	1.269	12.387	0.288	8.82	0.184	13.73	11.54	2.11	3.12	0.85	97.42	
				Al, Fe, Na, P		renorm		44.5	1.29	12.71	0.29	9.1	0.18	14.1	11.8	2.2	3.2	0.8	100.00	
					1	olivine	7	39.94	0.022	0.122	0.161	9.71	0.152	49.04	0.442				99.42	0.31
16	2.8	1440	4.0	1.88	92	glass	5	42.03	1.32	12.81	0.184	9.05	0.174	12.54	11.73	31	3.565	0.22	96.17	
				Fe, Ca, Na, P		renorm		43.6	1.3	13.3	0.19	9.4	0.18	13.0	12.1	3	3.70	0.2	100.00	
					3	olivine	9	40.25	0.021	0.114	0.153	10.33	0.142	48.53	0.454				99.88	0.29
					5	cpx	6	49.88	0.328	81	1.21	3.21	0.12	16.04	19.95	0.825			99.63	0.28
				Quench		mica	3	35.69	2.474	17.14	0.033	17.85	0.123	121	0.42	0.64	9.85		95.41	7.22

17	2.0	1450	0.8		2.61	99	glass	5	43.39	2.56	13.23	0.000	9.05	0.21	13.64	12.26	2.22	3.138	1.12	100.30	
				Si, Ti, Ca		1	olivine	5	41.57	0.011	0.102	0.171	8.92	0.212	49.36	0.412	0.00	0.00	0.00	100.56	0.27
27	3.3	1460	2.6		7.80	59	glass	3	40.16	1.92	12.98	0.034	10.02	0.152	9.46	7.67	3.93	6.45	1.917	94.09	
							renorm		42.6	2.0	13.66	0.03	10.6	0.16	10.0	8.0	4.2	6.8	2.03	100.00	
						38	cpx	4	49.96	0.62	10.38	0.52	2.87	0.094	15.06	203	1.14			100.73	0.18
						2	spinel	2	0.73	0.325	644	2.98	8.62	0.084	243	0.17				100.00	0.34

Experiments with recognizable phases but unanalyzable glass

10	2.4	1430	1.5	glass, olivine
15	3.1	1440	1.0	glass, olivine, cpx, spinel
24	3.3	1450	1.3	glass, olivine, cpx
25	3.3	1430	2.0	glass, olivine, cpx, spinel
26	3.3	1410	2.8	glass, olivine, cpx, spinel

Experiments above the liquidus

1	1.2	1450	3.0
2	1.2	1450	3.0
3	1.2	1430	4.0
4	1.2	1410	3.5
18	3.2	1460	1.0
19	2.8	1460	2.5
20.2	3.0	1460	2.5

Table 6 continued. Starting composition: WC-1 + 10% SiO_2 + 5% Al_2O_3

Run	P	T	t	R^2	Prop.	phase	N	SiO_2	TiO_2	Al_2O_3	Cr_2O_3	FeO	MnO	MgO	CaO	Na_2O	K_2O	P_2O_5	Total	K_Ds
5	2.5	1400	3.5	2.64	60	glass	8	45.66	1.12	16.02	0.103	7.84	0.134	10.27	9.25	2.41	2.24	0.771	95.54	
				Fe, Na		renorm		47.7	1.2	16.7	0.10	8.2	0.14	10.7	9.6	2.5	2.3	0.81	100.00	
					6	garnet	5	41.64	0.270	23.54	0.72	8.15	0.20	19.65	6.72	00			100.68	0.54
					34	cpx	6	51.28	0.262	81	0.434	4.64	0.071	17.45	17.15	1.075			100.45	0.34
6	2.5	1370	6.0	2.45	37	glass	7	48.13	1.31	16.21	0.094	7.74	0.133	7.658	7.81	2.899	2.91	0.883	95.44	
				Fe, Na		renorm		50.4	1.3	16.9	0.09	8.0	0.14	8.02	8.2	3.03	3.0	0.92	100.00	
					20	garnet	6	41.33	0.64	23.14	0.41	91	0.21	18.96	7.04	00			100.80	0.49
					43	cpx	4	52.31	0.352	7.84	0.304	5.42	0.085	16.82	16.35	1.31			100.70	0.32

Table 7. Comparison of studies

	H_2O	CO_2	SiO_2	TiO_2	Al_2O_3	Cr_2O_3	FeO	MnO	MgO	CaO	Na_2O	K_2O	P_2O_5	Mg#	Near-liquidus phases: Ol	C	Op	G	S	P	C	MSP: P	T
This study Olivine leucitite WC-1	2.00		44.40	1.19	12.91	0.13	8.73	0.16	14.23	11.61	2.39	3.15	1.10	74.39	•	•			•		•	3.1	1460
WC-1 with 10% silica and 5% alumina	2.00		47.47	1.02	13.39	0.12	7.97	0.15	13.83	11.28	2.32	1.53	0.92	75.56		•		•			•		
WC-1 wet	6.00		44.40	1.19	12.91	0.13	8.73	0.16	14.23	11.61	2.39	3.15	1.10	74.39	•	•			•	•			
Edgar et al. (1976)																							
Biotite mafurite, Toro Ankole, Uganda	0.00		43.13	5.37	8.40	0.20	8.08	0.00	16.00	10.83	0.81	7.19	0.00	77.92	•						•		
Biotite mafurite, Toro Ankole, Uganda	5.00		43.13	5.37	8.40	0.20	8.08	0.00	16.00	10.83	0.81	7.19	0.00	77.92	•	•				•		3.3	1300
Biotite mafurite, Toro Ankole, Uganda	>15		43.13	5.37	8.40	0.20	8.08	0.00	16.00	10.83	0.81	7.19	0.00	77.92	•	•				•			
Edgar et al. (1978, 1980)																							
Olivine ugandite, Toro Ankole, Uganda	0.00		44.16	1.86	9.95	0.16	10.87	0.17	20.38	8.78	1.56	1.75	0.37	76.97	•	•			•		•		
Olivine ugandite, Toro Ankole, Uganda	5.00		44.16	1.86	9.95	0.16	10.87	0.17	20.38	8.78	1.56	1.75	0.37	76.97	•	•			•	•			
Olivine ugandite, Toro Ankole, Uganda	15.00		44.16	1.86	9.95	0.16	10.87	0.17	20.38	8.78	1.56	1.75	0.37	76.97	•	•			•	•		3.5	1200
Olivine ugandite, Toro Ankole, Uganda	sat.		44.16	1.86	9.95	0.16	10.87	0.17	20.38	8.78	1.56	1.75	0.37	76.97	•	•			•	•			
Olivine ugandite, Toro Ankole, Uganda	3.75	11.25	44.16	1.86	9.95	0.16	10.87	0.17	20.38	8.78	1.56	1.75	0.37	76.97		•	•	•		•		3.0	1300
Barton and Hamilton (1978, 1979)																							
Orendite A1770, Leucite Hills, Wyoming	1.23		58.31	2.73	10.95	0.04	3.74	0.06	6.78	3.65	1.28	12.45	0.00	76.39	•	•		na		•		4.5	1100
Wyomingite A1745, Leucite Hills, WY	3.59		53.99	2.47	12.25	0.00	5.10	0.08	7.78	6.45	0.92	10.96	0.00	73.12	•	•		na		•		1	1130
Madupite A1805, Leucite Hills, WY	2.89		48.10	2.55	8.67	0.04	6.41	0.17	12.18	13.13	0.82	7.94	0.00	77.20	•	•		•		•		0.7	1250
Nicholls and Whitford (1983)																							
Leucite basanite, Muriah, Indonesia	2.00		45.17	1.26	13.62	0.00	9.39	0.17	10.39	13.27	2.60	3.10	1.02	66.35		•		•				3.3	1300
Leucite basanite, Muriah, Indonesia	5.00		45.17	1.26	13.62	0.00	9.39	0.17	10.39	13.27	2.60	3.10	1.02	66.35		•		•		•		3.2	1200
Leucite basanite, Muriah, Indonesia	10.00		45.17	1.26	13.62	0.00	9.39	0.17	10.39	13.27	2.60	3.10	1.02	66.35		•		•		•		3.1	1120
Leucite basanite, Muriah, Indonesia	sat.		45.17	1.26	13.62	0.00	9.39	0.17	10.39	13.27	2.60	3.10	1.02	66.35		•		•		•		3	1050
Mitchell (1995)																							
Phlog. lamproite, Leucite Hills, WY	0.72		58.03	2.57	10.82	0.00	3.66	0.91	6.53	3.21	1.29	11.60	1.39	76.09		•		•		•	•	>5.0	1600?
Righter and Camichael (1996)																							
Phlog. lamprophyre MAS4a, W. Mex.	0.99		50.42	1.79	13.00	0.00	7.50	0.14	9.74	7.84	2.96	5.29	1.31	69.83	•	•		na		•		2	1120
Phlog. lamprophyre MAS49, W. Mex.	0.50		54.26	1.78	14.00	0.00	4.86	1.64	5.41	6.94	3.37	6.35	1.39	66.47	•	•		na		•		0.5	1100
Esperanca and Holloway (1987)																							
Minette BPR-6, Buell Park, Arizona	4.37		51.02	2.10	10.91	0.00	8.00	0.12	10.25	9.41	2.14	5.05	1.01	69.56	•	•			•	•	•	2.0?	1200?
Tatsumi and Koyaguchi (1989)																							
Absarokite, Katamata, Japan	3.32		49.81	1.71	17.55	0.00	7.10	0.16	9.69	7.92	1.73	3.56	0.77	70.86	•	•	•	na		•		1.4	1230
Absarokite, Katamata, Japan	5.08		49.81	1.71	17.55	0.00	7.10	0.16	9.69	7.92	1.73	3.56	0.77	70.86	•	•	•	na		•		1.7	1170
Sato (1997) lamproite	6.00		46.08	3.49	4.34	0.00	8.79	0.00	27.54	5.30	0.43	4.02	0.00	84.81	•		•	•		•	•	5.3	1370
lamproite	9.00		46.08	3.49	4.34	0.00	8.79	0.00	27.54	5.30	0.43	4.02	0.00	84.81	•		•	•		•	•	5.8	1350
lamproite	11-12		46.08	3.49	4.34	0.00	8.79	0.00	27.54	5.30	0.43	4.02	0.00	84.81	•		•	•		•	•	5.8	1370
Arima and Edgar (1983)																							
Wolgidite MN4, West Kimberley, Aus.	3.22	0.93	51.22	7.94	3.15	0.00	7.96	0.09	16.51	4.37	0.95	7.80	0.00	78.70	•		•			•		1.5	1150
Wolgidite MN4, West Kimberley, Aus.	13.00	0.84	51.22	7.94	3.15	0.00	7.96	0.09	16.51	4.37	0.95	7.80	0.00	78.70	•	•	•		•	•		2.3	1100

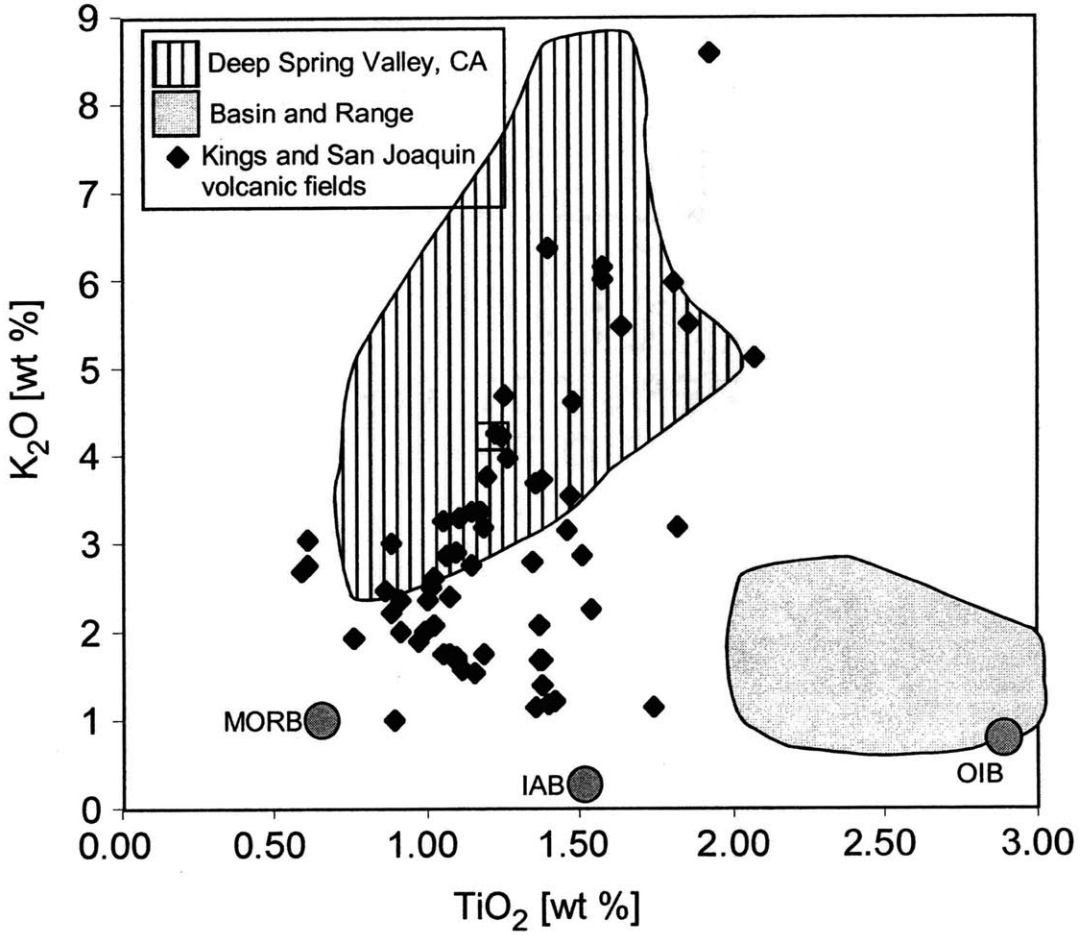
Deep Spring Valley, CA
Basin and Range
Kings and San Joaquin volcanic fields
MORB
IAB
OIB
K_2O [wt %]
TiO_2 [wt %]
0
1
2
3
4
5
6
7
8
9
0.00
0.50
1.00
1.50
2.00
2.50
3.00

Figure 1

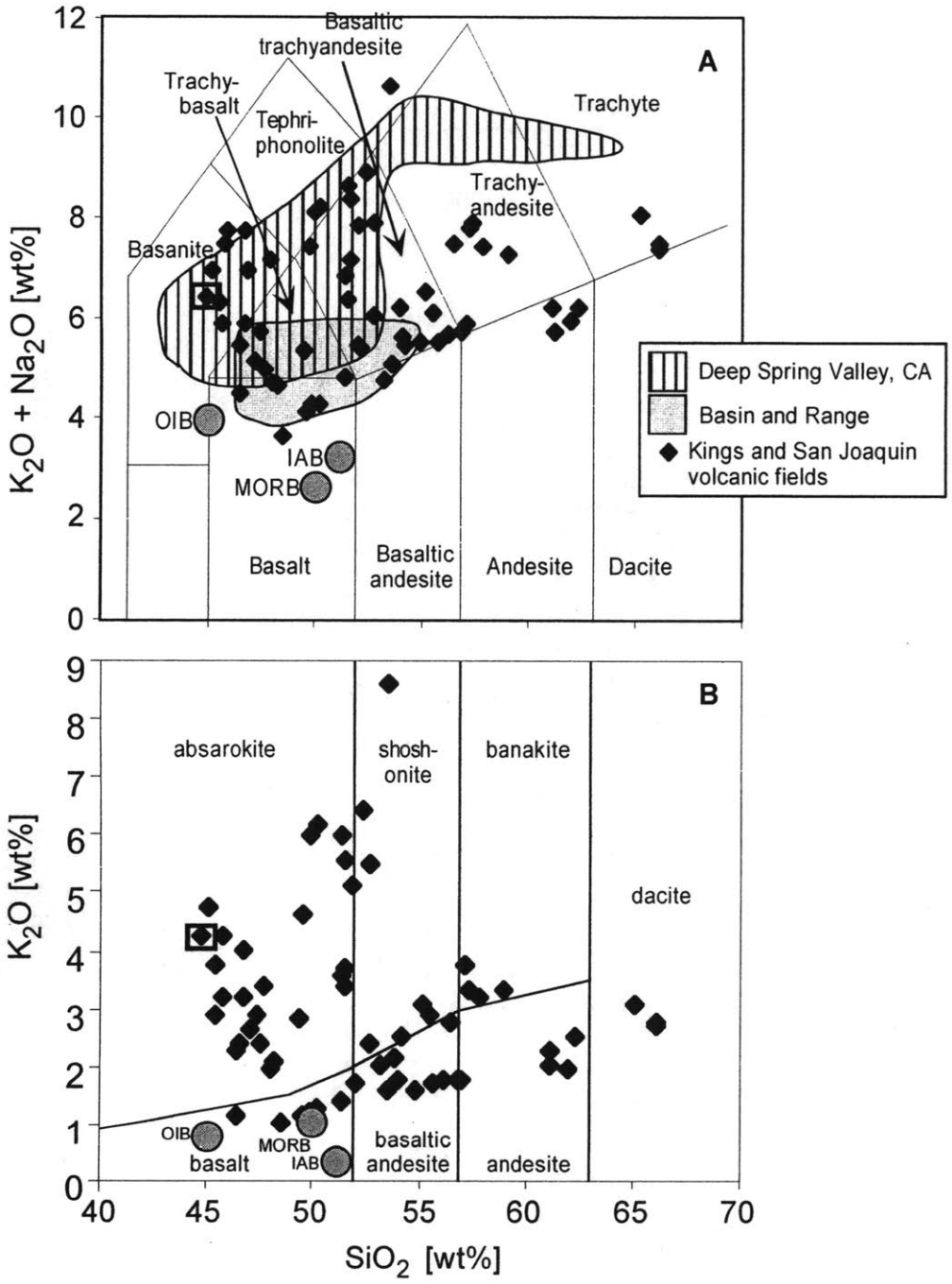
A
Basaltic trachyandesite
Trachy-basalt
Tephri-phonolite
Trachyte
Trachy-andesite
Basanite
OIB
IAB
MORB
Basalt
Basaltic andesite
Andesite
Dacite
Deep Spring Valley, CA
Basin and Range
Kings and San Joaquin volcanic fields
$K_2O + Na_2O$ [wt%]
B
absarokite
shosh-onite
banakite
dacite
basalt
basaltic andesite
andesite
K_2O [wt%]
SiO_2 [wt%]

Figure 2

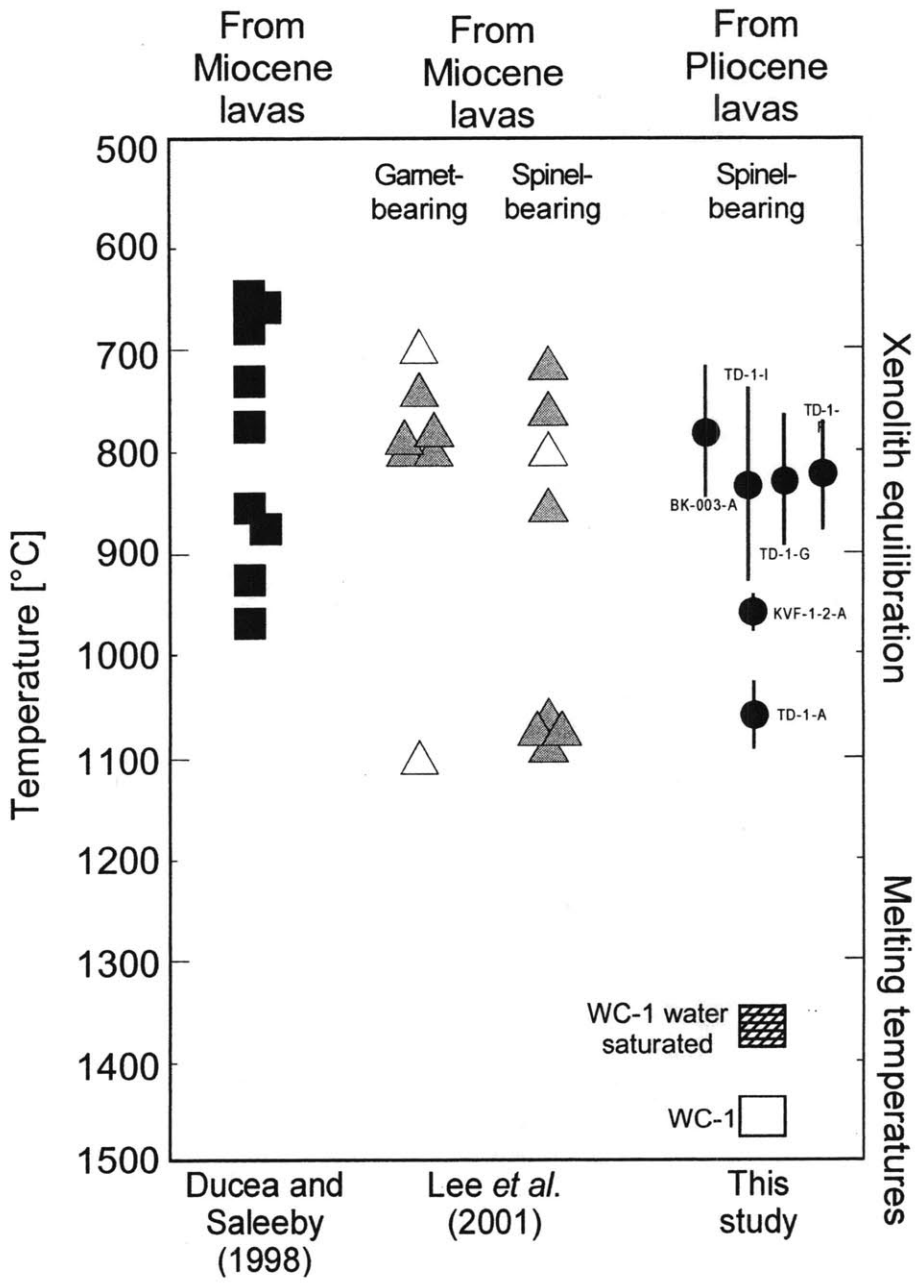
From Miocene lavas
From Miocene lavas
From Pliocene lavas
Garnet-bearing
Spinel-bearing
Spinel-bearing
Temperature [°C]
500
600
700
800
900
1000
1100
1200
1300
1400
1500
TD-1-I
TD-1-
BK-003-A
TD-1-G
KVF-1-2-A
TD-1-A
WC-1 water saturated
WC-1
Xenolith equilibration
Melting temperatures
Ducea and Saleeby (1998)
Lee et al. (2001)
This study

Figure 3

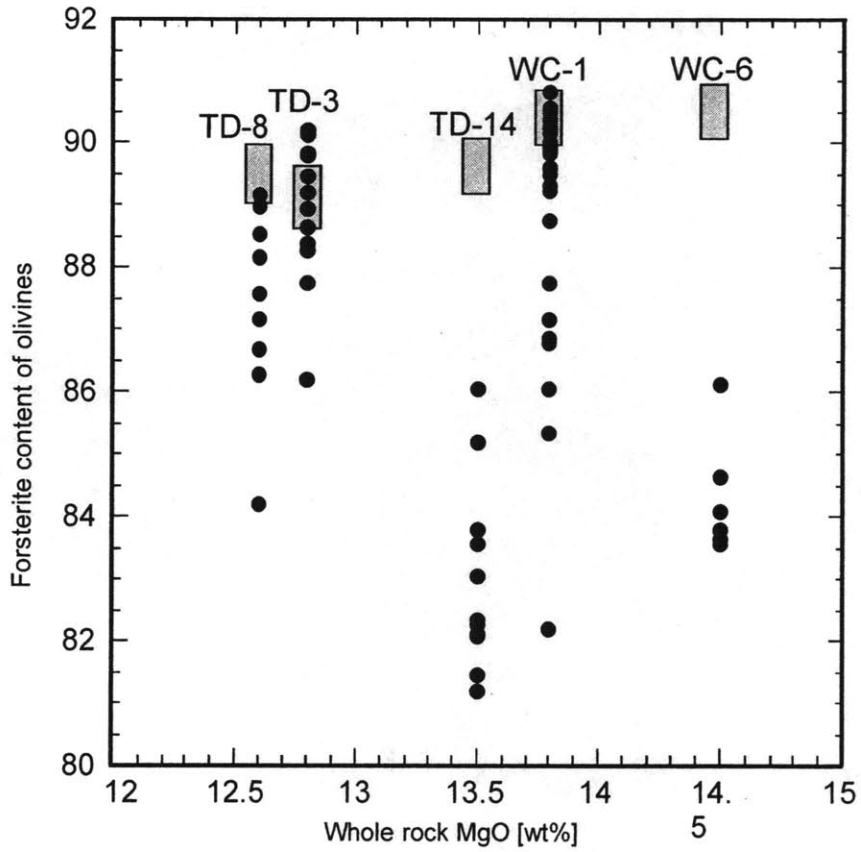
92
90
88
86
84
82
80
Forsterite content of olivines
TD-8
TD-3
TD-14
WC-1
WC-6
12
12.5
13
13.5
14
14.5
15
Whole rock MgO [wt%]

Figure 4

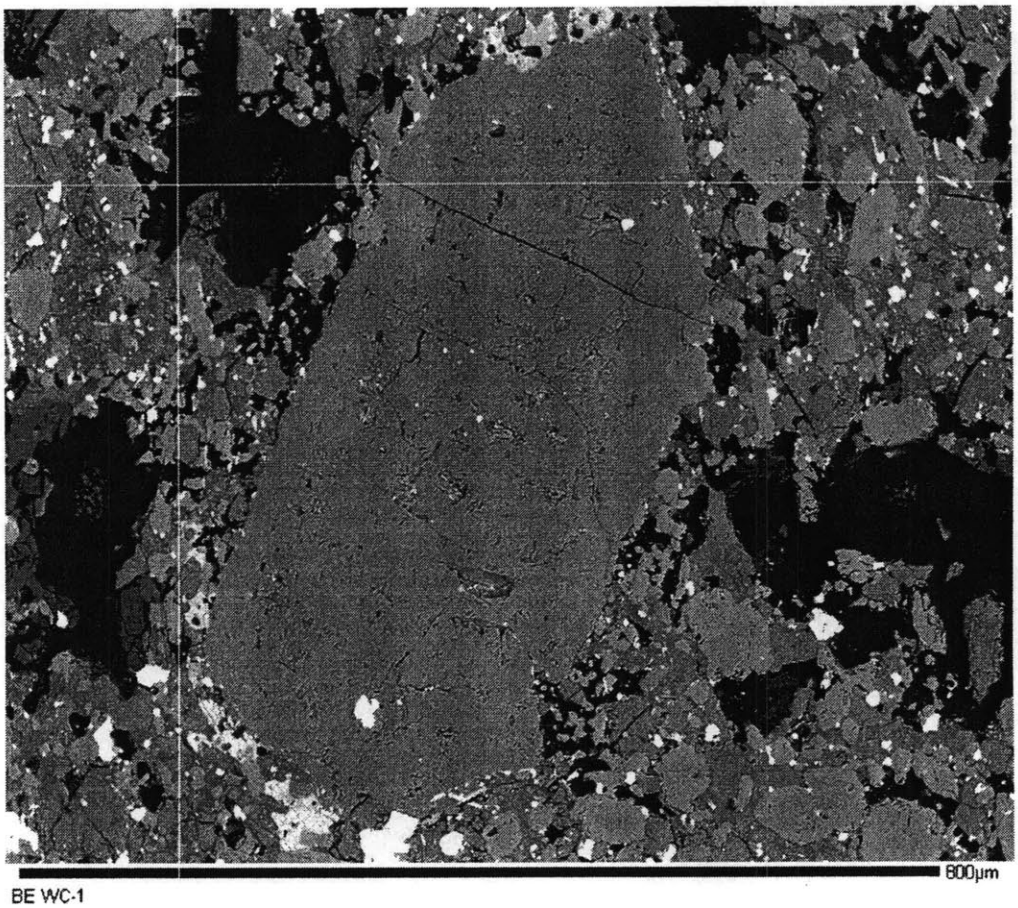

Lava WC-1 with olivine phenocryst, Fo 90.5 at center

Figure 5

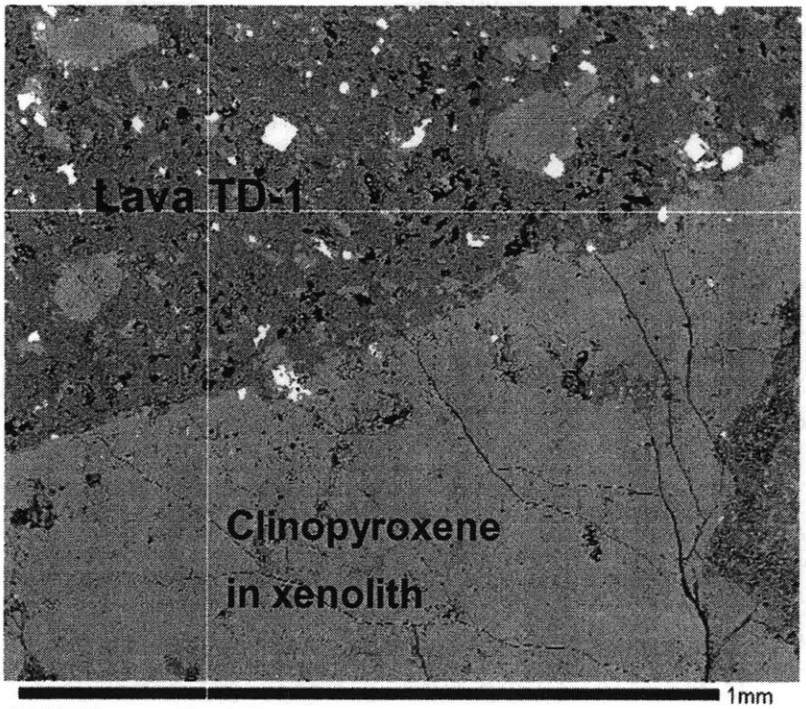

CL TD-1-F no reaction rim by cpx

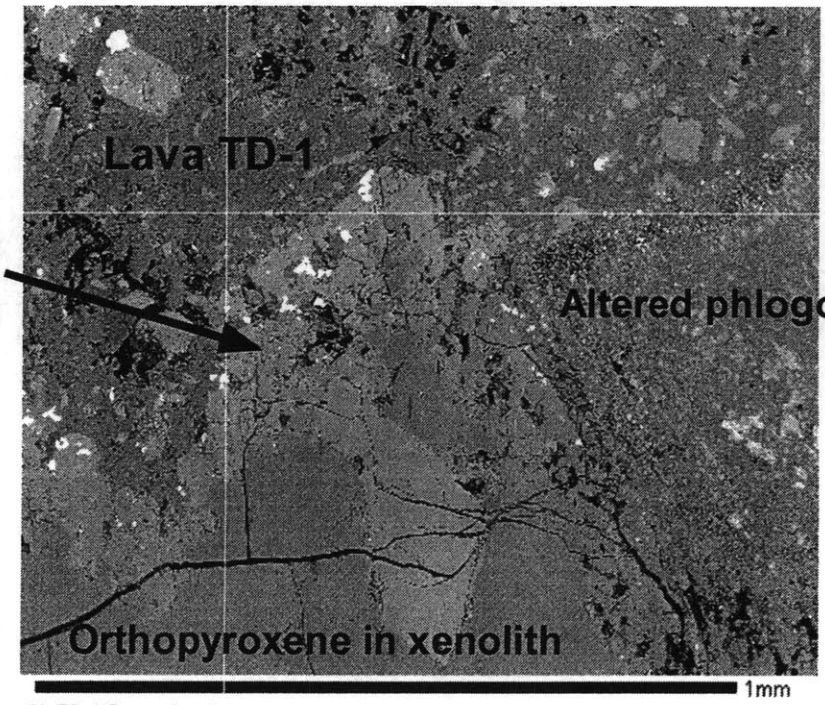

CL TD-1-F reaction rim on opx

Xenolith TD-1-F

Figure 6

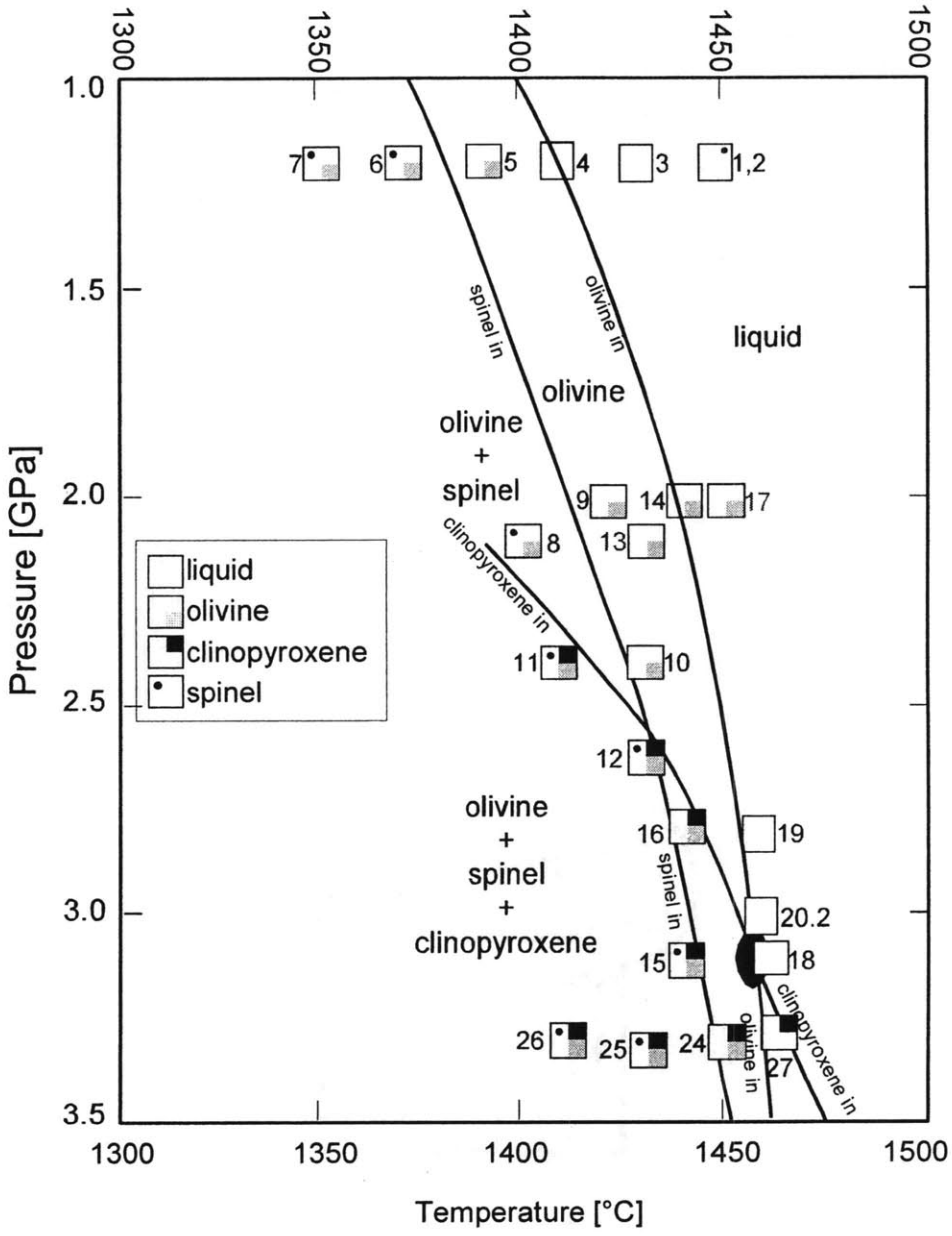
1300
1350
1400
1450
1500
1.0
1.5
2.0
2.5
3.0
3.5
Pressure [GPa]
Temperature [°C]
liquid
olivine
clinopyroxene
spinel
spinel in
olivine in
clinopyroxene in
liquid
olivine
olivine + spinel
olivine + spinel + clinopyroxene
1,2
3
4
5
6
7
8
9
10
11
12
13
14
15
16
17
18
19
20.2
24
25
26
27

Figure 7

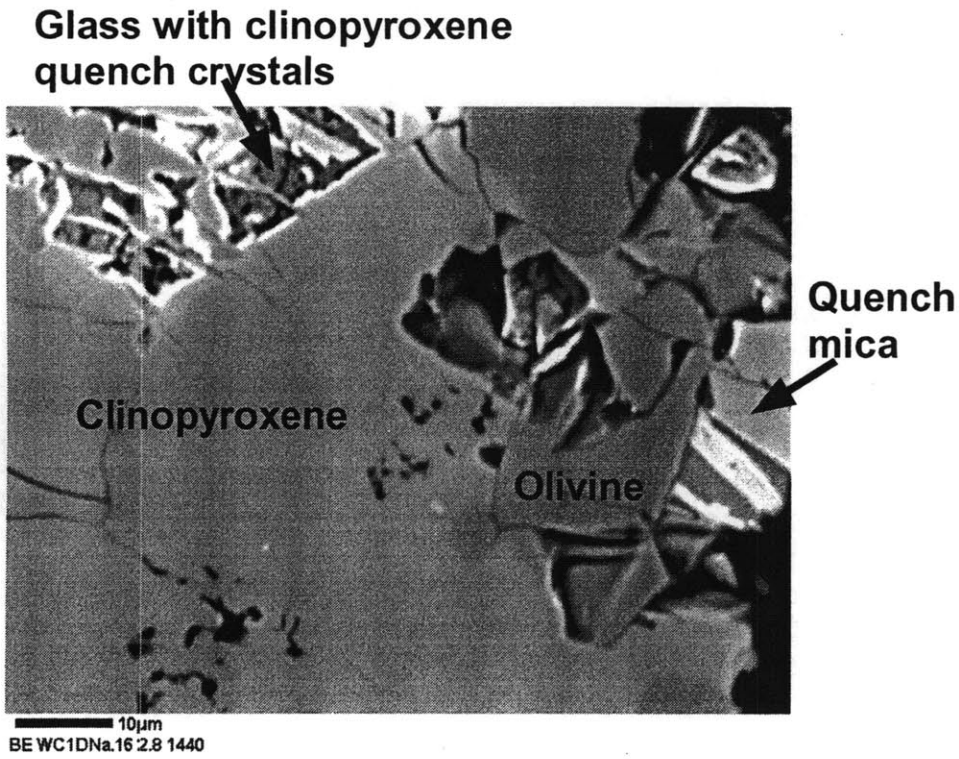

Experiment 16, 2.8 GPa, 1440 °C
WC-1 starting material

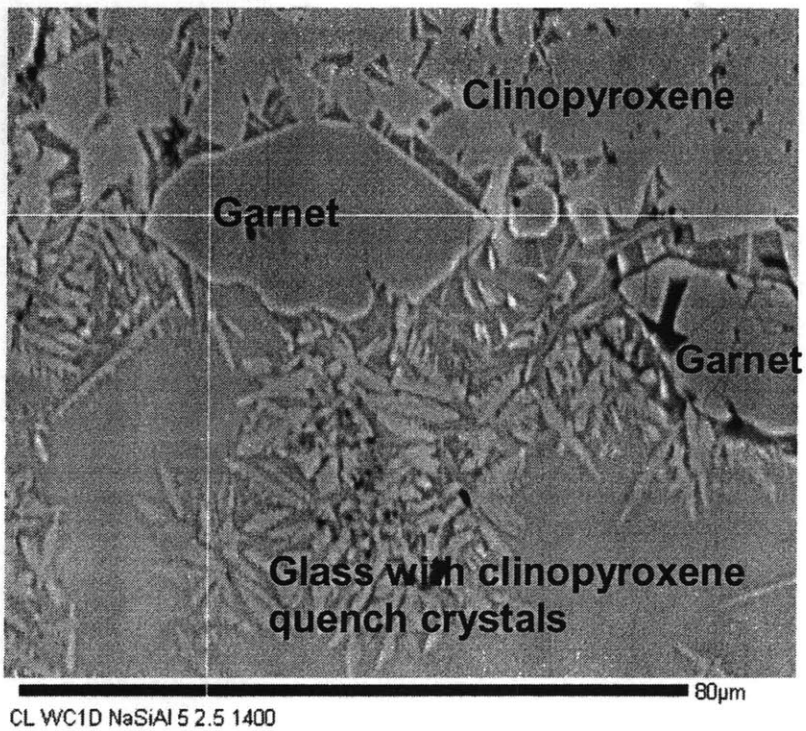

Experiment SiAl5, 2.5 GPa, 1400 °C
WC-1+10%Si+5%Al starting material

Fig. 8

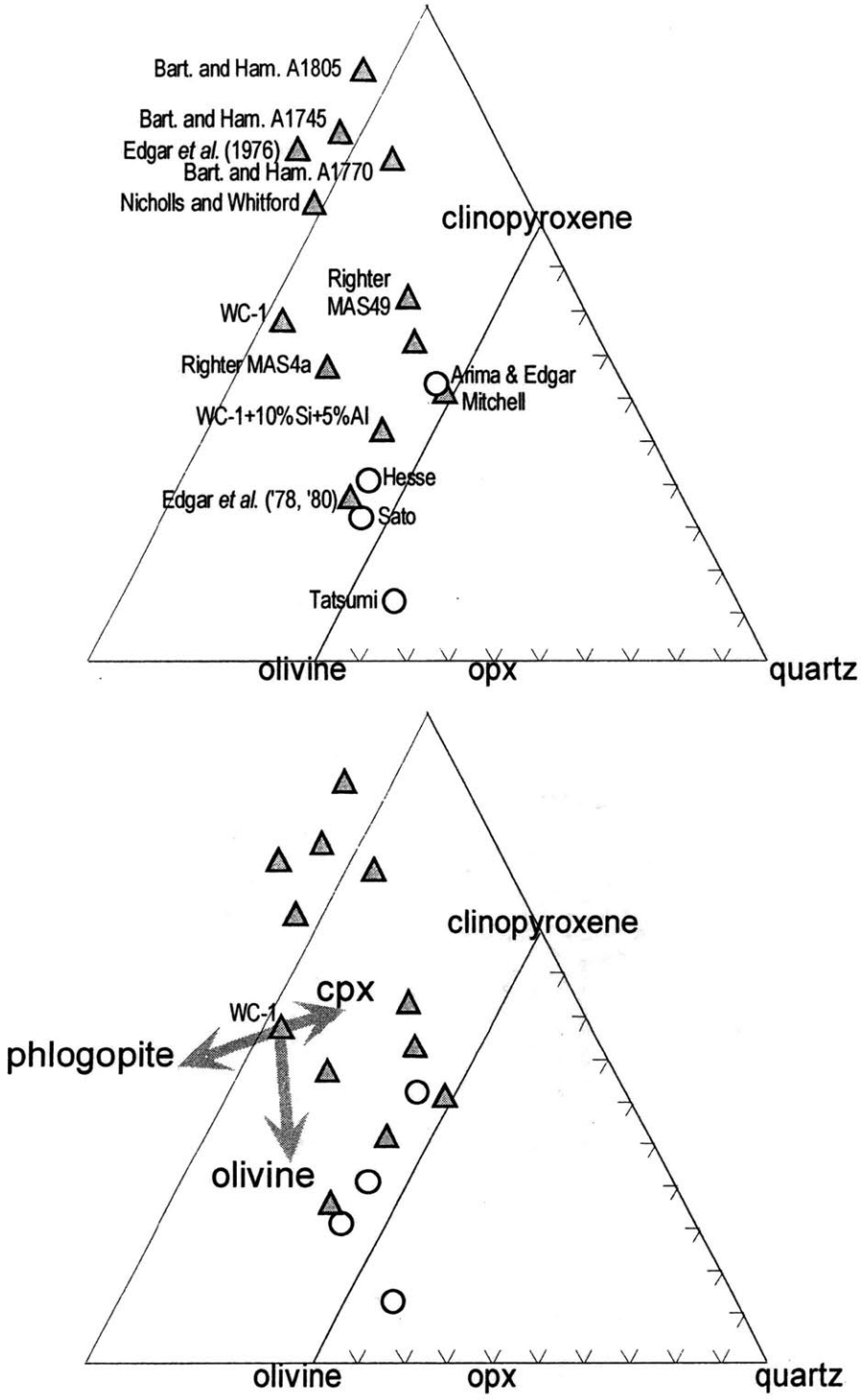
Bart. and Ham. A1805
Bart. and Ham. A1745
Edgar et al. (1976)
Bart. and Ham. A1770
Nicholls and Whitford
clinopyroxene
Righter
MAS49
WC-1
Righter MAS4a
Arima & Edgar
Mitchell
WC-1+10%Si+5%Al
Hesse
Edgar et al. ('78, '80)
Sato
Tatsumi
olivine
opx
quartz
clinopyroxene
cpx
WC-1
phlogopite
olivine
olivine
opx
quartz

Figure 9

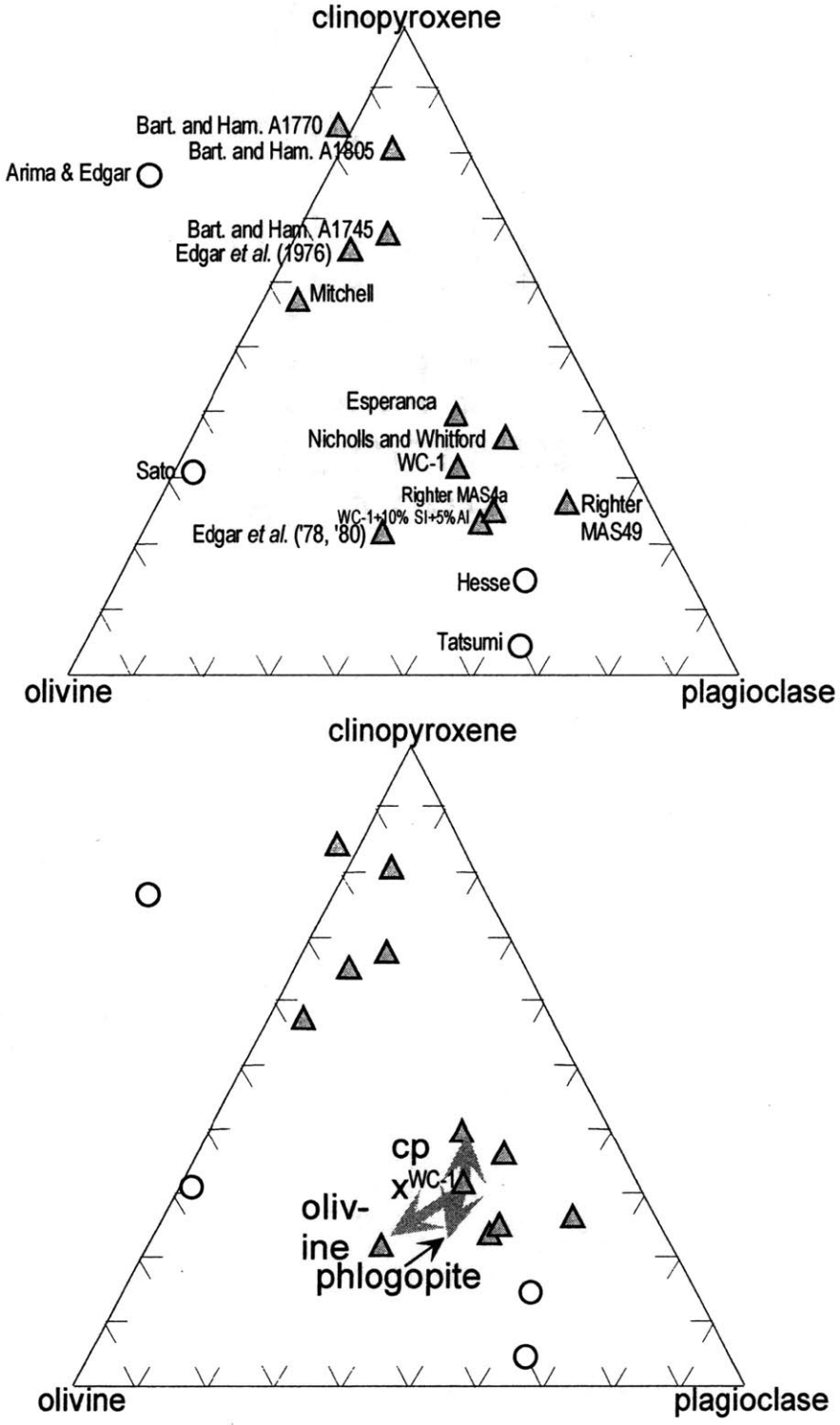
clinopyroxene
Bart. and Ham. A1770
Bart. and Ham. A1805
Arima & Edgar
Bart. and Ham. A1745
Edgar et al. (1976)
Mitchell
Esperanca
Nicholls and Whitford
WC-1
Sato
Righter MAS4a
WC-1+10% Si+5% Al
Righter MAS49
Edgar et al. ('78, '80)
Hesse
Tatsumi
olivine
plagioclase
clinopyroxene
cp
x
WC-1
oliv-
ine
phlogopite
olivine
plagioclase

Figure 10

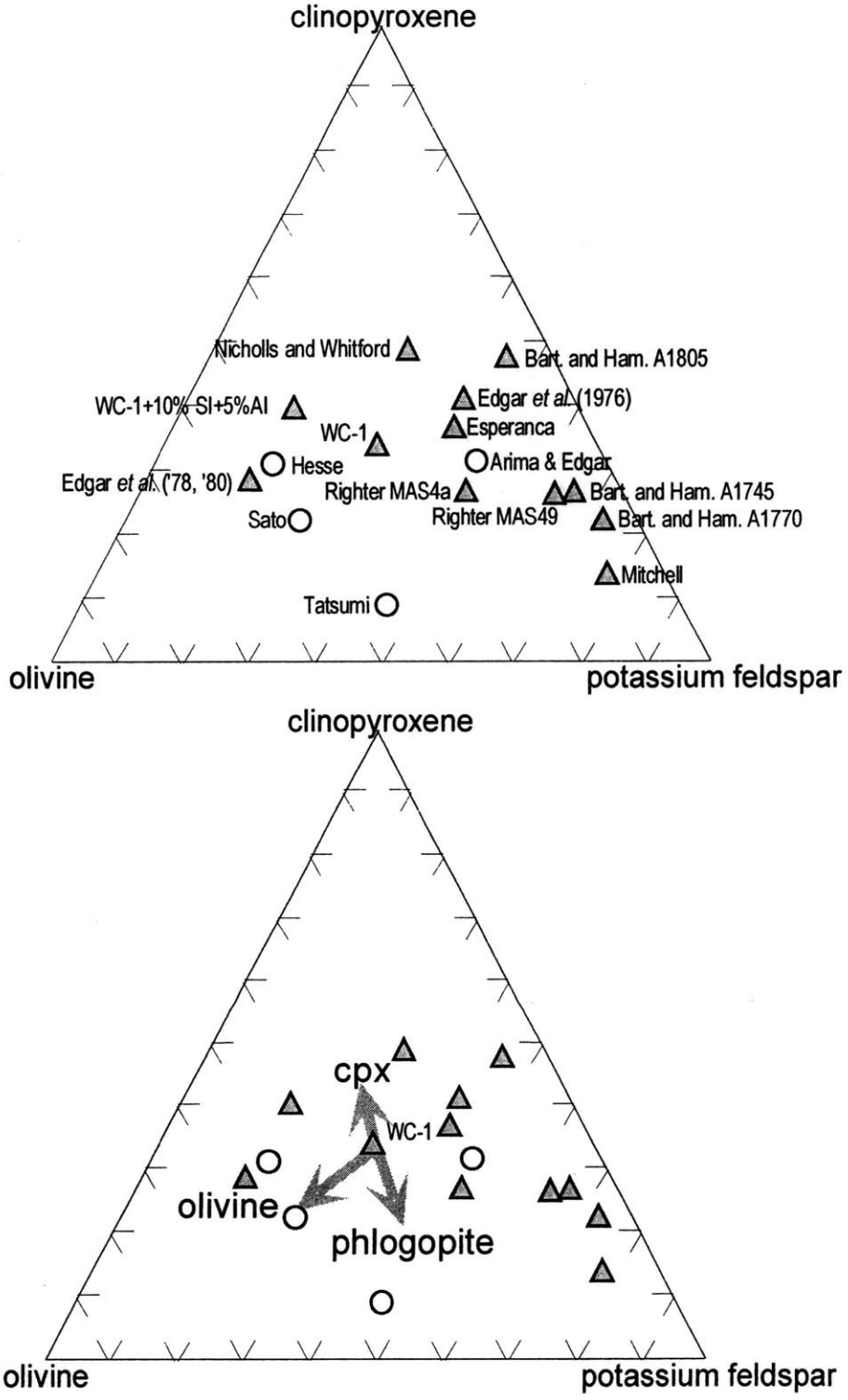
clinopyroxene
Nicholls and Whitford
Bart. and Ham. A1805
WC-1+10% SI+5%AI
Edgar et al. (1976)
Esperanca
WC-1
Hesse
Arima & Edgar
Edgar et al. ('78, '80)
Righter MAS4a
Bart. and Ham. A1745
Sato
Righter MAS49
Bart. and Ham. A1770
Mitchell
Tatsumi
olivine
potassium feldspar
clinopyroxene
cpx
WC-1
olivine
phlogopite
olivine
potassium feldspar

Figure 11

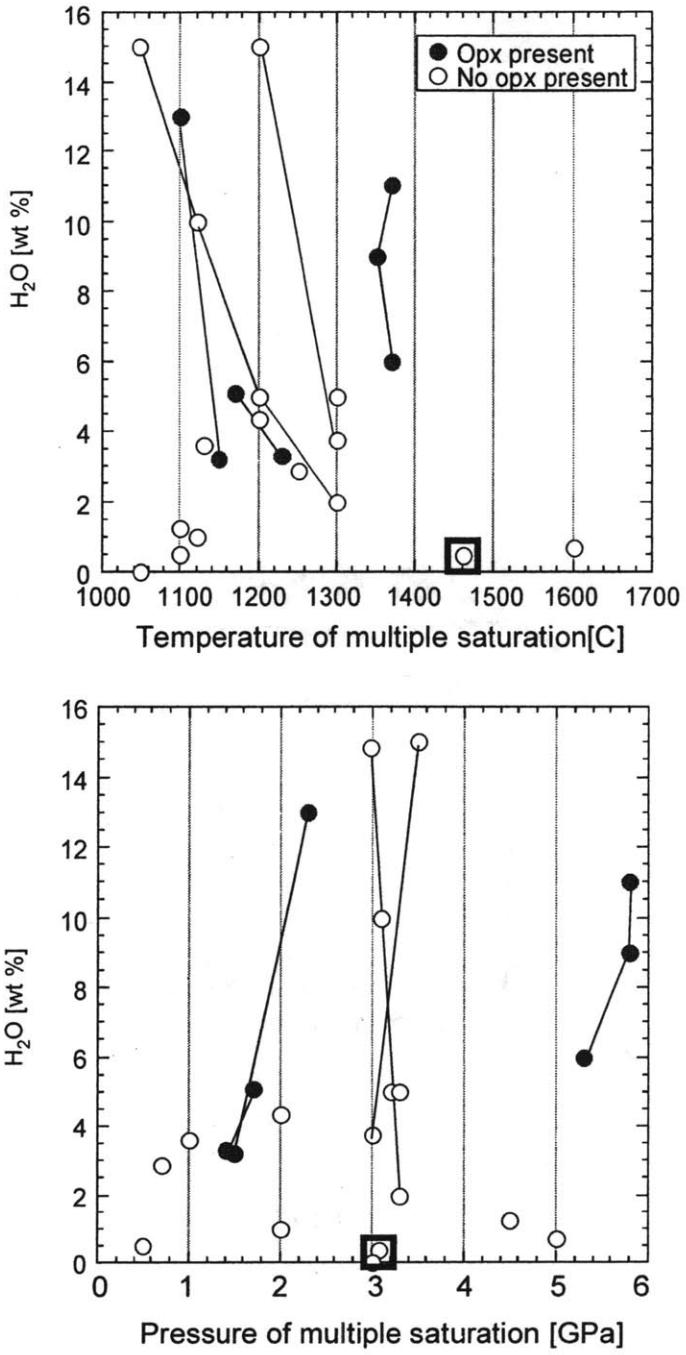
Opx present
No opx present
H2O [wt %]
Temperature of multiple saturation[C]
Pressure of multiple saturation [GPa]

Figure 12

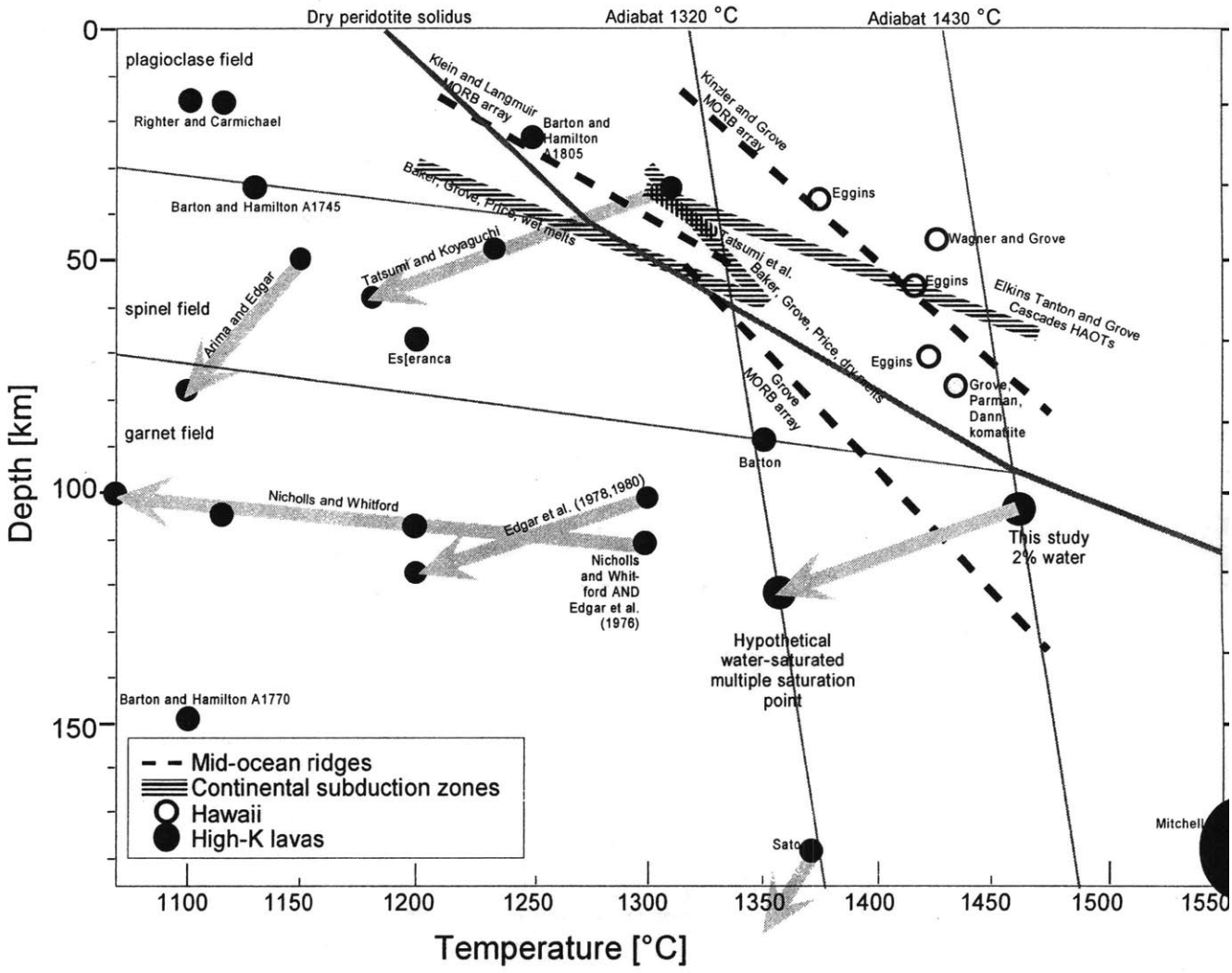
Dry peridotite solidus
Adiabat 1320 °C
Adiabat 1430 °C
plagioclase field
spinel field
garnet field
Depth [km]
Temperature [°C]
Righter and Carmichael
Barton and Hamilton A1745
Barton and Hamilton A1770
Barton and Hamilton A1805
Klein and Langmuir MORB array
Kinzler and Grove MORB array
Grove MORB array
Baker, Grove, Price, wet melts
Tatsumi and Koyaguchi
Tatsumi et al.
Baker, Grove, Price, dry melts
Arima and Edgar
Es[eranca
Eggins
Wagner and Grove
Eggins
Elkins Tanton and Grove
Cascades HAOTs
Eggins
Grove, Parman, Dann komatiite
Batton
Nicholls and Whitford
Edgar et al. (1978,1980)
Nicholls and Whitford AND Edgar et al. (1976)
This study 2% water
Hypothetical water-saturated multiple saturation point
Mid-ocean ridges
Continental subduction zones
Hawaii
High-K lavas

Figure 13

Ch. 2. Melt intrusion as a trigger for lithospheric foundering and the eruption of the Siberian flood basalts

Elkins Tanton, L.T. and Bradford H. Hager, Melt intrusion as a trigger for lithospheric foundering and the eruption of the Siberian flood basalt, *Geophysical Research Letters 27*, 3937-3940, 2000.

Abstract

Any viable model of the Siberian flood basalt (SFB) eruption must provide for a massive pulse of magma, initially erupted below sea level. We propose as a triggering mechanism a limited precursory melt that intrudes and heats the mantle lithosphere, lowering its viscosity, and increasing its density as the melt freezes into eclogite. This warm, dense mantle lithosphere is then removed via a Rayleigh-Taylor instability that creates surface subsidence. Removal of the mantle lithosphere lengthens the melting column, and the melt volume of the SFB can be produced in less than a million years. The model is permissive of the existing geologic data for the SFB, which rule out a traditional hot, deep mantle plume. Numerical models demonstrate that the ability of a mantle upwelling to remove lithosphere is dependent primarily upon the lithospheric rheology, not on the temperature or size of the upwelling.

Introduction

In the prevailing model for flood basalt formation, developed by *Richards et al.* [1989] and others, a hot plume rises from the core-mantle boundary and melts adiabatically. In most models, the plume is unusually hot, beyond the range of petrological evidence [e.g., *Farnetani and Richards*, 1994; *Moore et al*, 1998, 1999]. Without excessive temperatures, no melting occurs because the plume cannot move upward far enough to cross its solidus. The buoyancy of such a plume head would cause surface uplift from 1 km [*Monnereau et al.*, 1993] to more than 4 km [*Farnetani and Richards*, 1994]. The inability of a plume to breach the lower lithosphere is a major drawback of the plume model. Researchers have noted that it is almost impossible, even with exceptionally high temperature, for a plume to displace or erode the cold lower lithosphere [e.g., *Farnetani and Richards*, 1994; *Ribe and Christensen*, 1994; *Moore et al.*, 1998].

Other researchers have investigated alternatives to the plume model. Noting that most continental flood basalts occur at the edges of ancient cratons, *King and Anderson* [1998] examined a model for convection at a step-increase in lithospheric depth. They found that for certain initial conditions, warm mantle could flow from under the continent and melt, and they assume that the resulting magma could be erupted through tensional dikes. The initial conditions assumed are highly unstable, however, and unlikely to have developed in a convecting mantle, begging the question of the triggering mechanism. *White and McKenzie* (1989) require a mantle

upwelling of only 100 to 200°C above ambient mantle temperature, and note that thin lithosphere enables adiabatic melting, that igneous intrustions may not reach the surface, and that these intrusions may create density anomalies. They require complete rifting, however, to create flood basalts.

We propose a new model for the formation of flood basalts that is consistent with the geological constraints on the emplacement of the SFB and that overcomes many of the problems with previous models. Our mechanism lengthens the melting column by removing mantle lithosphere through a Rayleigh–Taylor instability, allowing mantle material to rise far enough to melt adiabatically. For relatively thin lithosphere such as that at the edge of a continent, the melting column would be long enough for substantial magma production.

Geologic Constraints on the Siberian Flood Basalts

The SFB were erupted onto the Siberian craton over about one million years at the Permo-Triassic boundary, coeval with the largest extinction in Earth history [*Renne and Basu*, 1991; *Bowring et al.*, 1998]. With a total section thickness of 6500 m and a volume of more than 3 x 10^6 km^3 [*Renne et al.*, 1995], the SFB are one of the largest of the large igneous provinces.

The SFB are underlain by the sedimentary Tunguska Series, covering 10^6 km^2, including the world's largest coal basin [*Lightfoot et al.*, 1990]. The unconformity between the sediments and the volcanics is erosional [*Czamanske et al.*, 1998]. Marine fossils are found through the first 1100 m of the flows [*Fedorenko et al.*, 1996], and there are pillow structures and fossilized tree trunks, particularly in the lowest few hundred meters of the section near Noril'sk (V. Fedorenko, personal communication). Thus the Siberian craton was originally near sea level, was uplifted, resulting in the unconformity, and then returned to sea level before eruption of the flood basalts. The uplift must have been short-lived, since it is constrained by the late-Permian sediments below and the 250 Ma SFB above, but its height is not constrained. Ongoing subsidence maintained the craton surface at sea level throughout the eruption of over 1 km of basalts. No existing plume model allows subsidence to below sea level before and during eruption of the basalts, ruling out a traditional plume head as the source [*Fedorenko et al.* , 1996; *Czamanske et al.*, 1998].

Model for Formation of the SFB

We have developed a model for the generation of the SFB that honors the important geological constraints. The model is sketched in Figure 1. The SFB were erupted onto an area with a long pre- and post-eruptional history of lithospheric thinning [*Sengor*, 1984; *Lightfoot et al.*, 1990]. We assume a total lithospheric thickness of 60 km, with 30 km of crust underlain by 30 km of depleted mantle lithosphere. Densities are estimated by calculating high-pressure modes of natural and experimental bulk compositions. The initial mantle lithosphere has a density of 3250 kg/m^3 and is highly viscous. The fertile mantle below it has a density of 3310 kg/m^3. Both the viscosity of the mantle and the viscosity of the crust are crucial. *Carter and Tsenn* [1987] concluded that mechanically weak zones could develop below 10 km in continental crust. Given the hot model geotherm, the lower half of the model crust (15 to 30 km depth) might well be mechanically weak.

We propose that the initiation of the SFB was triggered by a weak convective upwelling. We adopt a mantle upwelling potential temperature of 1480°C, the approximate upper limit of oceanic mantle temperatures [*Kinzler and Grove,* 1992]. (This upwelling, which would have caused the modest uplift that resulted in the pre-SFB erosional unconformity, is consistent with plume tail models, but not plume head models.) For dry mantle at 1480°C, adiabatic melting is limited to depths shallower than about 90 km [*Hirth and Kohlstedt*, 1996], and the mantle material would melt about 10% before it hits the lithosphere [*Kinzler*, 1997]. The initial 10% melt is not sufficient in volume to create the SFB, but it could act as a catalyst to allow the removal of the mantle lithosphere. Given the assumed temperature of the mantle upwelling, even with such a thin initial lithosphere, additional lithosphere must be removed to allow significant melting volumes. The novel feature of our model is that this lithosphere is removed via a Rayleigh-Taylor instability. A damp mantle source, or alternative composition, could increase the melting column, but there is currently no compelling evidence in Siberia that such conditions existed [*Braun et al.,* 2000*; Hirschmann et al.,* 1999]. If conditions for additional melt production did exist under Siberia, then our model could be revised with a lower mantle temperature, which would in turn allow more subsidence.

We postulate that the 10% melt intrudes the mantle lithosphere as dikes. We assume that the intruding melt freezes in the mantle lithosphere. An amount corresponding to intrusion of two batches of 10% melt (a volume about 1/7 of the mantle lithosphere it intrudes) would raise the temperature of the mantle lithosphere by about 170°C from the superheat of the melt and the heat

of fusion when the melt solidifies [e.g., *Lister*, 1991]. This would lower lithospheric viscosity by about two orders of magnitude. When the dike material solidifies as eclogite, the lithospheric density would rise to about 3340 kg/m^3, and that of the underlying depleted mantle would fall to 3280 kg/m^3, creating a gravitational instability (e.g., *Ringwood and Green*, 1966). The diked lithosphere could now be sheared to the side or sink by Rayleigh-Taylor instability, depending on the strength of the upwelling and the density and rheology of the lithosphere.

When the mantle lithosphere is removed, the melting column of the adiabatically rising mantle is doubled from 30 km to 60 km. The resulting melt fraction is increased from approximately 10% to 20% [e.g., *White and McKenzie*, 1989]. If the footprint of the SFB mantle is 400 km by 400 km and the convective upwelling moves at 10 cm/yr, then the melt volume of the SFB can be produced in less than one million years by a continuously replenished melt column. After melt extraction the residual mantle is less dense and therefore prone to underplate the crust. We propose that the residual mantle fills in the space previously occupied by the mantle lithosphere, shortening the melting column, occluding melt transport, and ending eruption. This mechanism may explain the anomalous high-velocity seismic zones under present-day Noril'sk [*Pavlenkova et al.*, 1996], and may be the explanation for the short duration of most flood basalt events. If the mantle underplating is 60 km in depth and 170°C hotter than the undisturbed geotherm, then post–eruptional uplift of about 300 m could result. Uplift before and after eruption is consistent with this model and not contradicated by geological evidence. During cooling the uplift would subside.

Numerical Models

To test the viability of our conceptual model, we use a version of the finite element code ConMan [*King et al.*, 1990] that includes compositionally, as well as thermally driven convection [equations given in *van Keken et al.*, 1997]. The thermal buoyancy is determined by the Raleigh number, $Ra = (\rho g \alpha \Delta T h^3)/(\eta \kappa)$. The negative buoyancy of the diked lithosphere is controlled by the compositional Rayleigh number, $Rac = (\Delta \rho g h^3)/(\eta \kappa) = Ra[\Delta \rho/(\rho \alpha \Delta T)]$. The value of negative buoyancy for the diked lithosphere is calculated from densities corrected for composition, pressure, and temperature.

The viscosity law used depends on stress, temperature, and depth:

$$\eta = \eta_o \left[\frac{\sigma_o}{\sigma}\right]^2 \exp\left[\frac{E+vz}{R(T+T_o)} - \frac{E+vz_o}{R(1+T_o)}\right] \quad (1)$$

where η_0 , σ_0 , T_0 , and z_0 are reference values, E is the activation energy, and v scales viscosity to depth, with a total viscosity change across the mantle in the model of 30. Although not included in most previous treatments, the stress-dependent viscosity law is crucial because it facilitates removal of the diked lithosphere (also see *Keen and Boutilier*, 2000). A list of key variables follows: height and width of model box (h) = 200 km; reference mantle density (ρ) = 3300 kg/m$^{3;}$ reference viscosity (η) = 1.00E+20 Pas; thermal expansivity (α) = 3.00E-05 /°; thermal diffusivity (κ) = 1.00E-06 m^2/s; number of elements in model box, in each dimension (e) = 66.

A template for all model runs was created by running the model with Ra = Rac = 0 until the box had cooled to the depth of the base of the mantle lithosphere. Because we do not model the melt migration process, the mantle lithosphere is simply overlain by a second composition and higher temperature to model the dike intrusion. This intrusion is modeled as the sum of a half cosine wave in x with a maximum at the left side of the box, falling to zero by 100 km in the x direction, and a half cosine wave in z, with a maximum at the bottom of the mantle lithosphere, falling to zero vertically in z over 30 km. The maximum amount of intruded dike material is 20%.

We have run a large suite of models, but present in detail only those that are successful in explaining the SFB. In models with hot upwelling material impinging on a uniform, high-strength crust, with or without diked lithosphere, very little lithosphere is removed, even with a stress-dependent viscosity law. Without the weak lower crust, traction from the convection cell cannot shear the mantle lithosphere, and cooling immobilizes the diked portion before a Rayleigh-Taylor instability can develop. Weak lower crust is necessary to allow a convection cell to remove diked lithosphere and lengthen the melting column.

In successful models, the lower half of the crust, between 15 km and 30 km depth and across the entire width of the model box, is given an initial viscosity lower than background. If this initial viscosity is three orders of magnitude lower than background, the diked lithosphere is rapidly sheared to the side before any Rayleigh-Taylor instability can develop. If the viscosity of the

lower crust is ten to one hundred times less than background, some diked material is sheared to the side and some falls as a Rayleigh-Taylor instability, the melting column is doubled, and results are consistent with the circumstances of the SFB. In general, shear removal of the mantle lithosphere creates topographic uplift, and Rayleigh-Taylor removal creates subsidence.

In the most successful model (lower crustal viscosity 100 times less than background), by about 1.1 Ma the diked lithosphere has been stretched into a band about 185 km wide, but the hot mantle has only been able to rise to about 50 km depth. Then, shortly after 3 Ma, the remaining diked lithosphere drops straight down the upwelling axis as a Rayleigh-Taylor instability (see Figure 2). At time zero topography at the model's axis is depressed by about 50 m. As the diked lithosphere begins to shear to the side, the axial topography rises slightly, to 50 m. During the brief period of uplift, little or no magma eruption would have occurred because the upwelling has not yet risen above 60 km depth. The diked lithosphere soon begins to drop by Rayleigh-Taylor instability, and pulls the topography back down to a minimum at 120 m below the undisturbed zero value (see Figure 2). Scaling may allow creation of subsidence equivalent to what is seen in Siberia. The topographic signature during eruption would be of subsidence.

Conclusions

A deep, hot, voluminous mantle plume cannot be the cause of the SFB, because of geologic evidence for subsidence during eruption. High mantle temperatures cause surface uplift. Without anomalously high temperatures, melting the mantle adiabatically beneath thick continental lithosphere is impossible; the lithosphere must be removed. Our models demonstrate that the lithospheric removal could be controlled by lithospheric rheology, and not by the size or temperature of upwelling beneath it.

Given the necessity of a modest upwelling, there are few models left to explain the SFB. Some triggering mechanism must be responsible for the rapid development and abrupt end of flood basalt events, and in the SFB, eruption must be accompanied by subsidence

We have proposed a novel mechanism for the triggering of massive flood basalt eruptions and demonstrated its dynamic viability. We suggest that continents ride over existing modest upwellings, and when the upwellings reach lithosphere thin enough, they create a small amount of adiabatic melting. Intrusion of this adiabatic melt into the mantle lithosphere, combined with a weak lower crust, could result in removal of the mantle lithosphere through shear traction and a

Rayleigh-Taylor instability. The Rayleigh–Taylor instability is crucial for creating surface subsidence and a significant increase in the melting column, creating an environment for massive magma genesis.

Acknowledgments. Clint Conrad was tirelessly helpful with the modeling code. Tim Grove, Wiki Royden, Don Anderson, and Sam Bowring supplied insightful comments and conversations, and two anonymous reviewers helped us to refine our arguments. The American Museum of Natural History kindly lent us samples from their collection, and this work was partly paid for by a National Defense Science and Engineering Graduate fellowship and by NSF grant EAR 9905779.

References

Bowring, S.A., D.H. Erwin, Y.G. Jin, M.W. Martin, K. Davidek, W. Wang, U-Pb zircon geochronology and the tempo of the end-Permian mass extinction, *Science, 280*, 1039-1045, 1998.

Braun, M.G., G. Hirth, and E.M. Parmentier, The effects of deep damp melting on mantle flow and melt generation beneath mid-ocean ridges, *Earth Planet. Sci. Lett., 176*, 339-356, 2000.

Carter, N.L. and M.C Tsenn, Flow properties of continental lithosphere, *Tectonophysics, 136*, 27-63, 1987.

Czamanske, G.K., A.B. Gurevitch, V. Fedorenko, and O. Simonov, Demise of the Siberian plume: Paleogeographic and paleotectonic reconstruction from the prevolcanic and volcanic record, North-central Siberia, *Int. Geology Rev., 40*, 95-115, 1998.

Farnetani, C.G. and M. A. Richards, Numerical investigations of the mantle plume initiation model for flood basalt events, *J. Geophys. Res., 99*, 13,813-13,833, 1994.

Fedorenko, V.A., P.C. Lightfoot, A.J. Naldrett, G.K. Czamanske, C.J. Hawkesworth, J.L. Wooden, D.S. Ebel, Petrogenesis of the flood-basalt sequence at Noril'sk, North-central Siberia, *Int. Geology Rev,. 38*, 99-135, 1996.

Harry, D.L. and W.P. Leeman, Partial melting of melt metasomatized subcontinetnal mantle and the magma source potential of the lower lithosphere, *J. Geophys. Res., 100*, 10255–10269, 1995.

Hirschmannn, M.M., P.D. Asimow, M.S. Ghiorso, and E.M. Stolper, Calculation of peridotite partial melting from thermodynamic models of minerals and melts. III. Controls on isobaric melt production and the effect of water on melt production, *J. Pet., 40,* 831-851, 1999.

Hirth, G. and D.L. Kohlstedt, Water in the oceanic upper mantle: implications for rheology, melt extraction and the evolution of the lithosphere, *Earth Planet. Sci. Lett., 144*, 93-108, 1996.

Keen, C.E. and R.R. Boutilier, Interaction of rifting and hot horizontal plume sheets at volcanic margins, *J. Geophys. Res., 105*, 13375-13387, 2000.

King, S.D. and D.L. Anderson, Edge-driven convection, *Earth Planet. Sci. Lett., 160*, 289-296, 1998.

King, S.D., A. Raefsky and B.H. Hager, ConMan: Vectorizing a finite element code for incompressible two-dimensional convection in the Earth's mantle, *Phys. Earth Planet. Inter., 59*, 195-207, 1990.

Kinzler, R.J. and T.L. Grove, Primary magmas of mid-ocean ridge basalts 2. Applications, *J. Geophys. Res., 97*, 6907-6926, 1992.

Kinzler, R., Melting of mantle peridotite at pressures approaching the spinel to garnet transition: Application to mid-ocean ridge basalt petrogenesis, *J. Geophys. Res., 102*, 853-874, 1997.

Lightfoot, P.C., A.J. Naldrett, N.S. Gorbachev, W. Doherty, and V.A. Fedorenko, Geochemistry of the Siberian Trap of the Noril'sk area, USSR, with implications for the relative contributions of crust and mantle to flood basalt magmatism, *Contrib. Mineral. Petrol., 104*, 631-644, 1990.

Lister, J.R., Steady solutions for feeder dykes in a density-stratified lithosphere, *Earth Planet. Sci. Lett., 107*, 233-242, 1991.

Monnereau, M., M. Rabinowicz, and E. Arquis, Mechanical erosion and reheating of the lithosphere: A numerical model for hotspot swells, *J. Geophys. Res., 98*, 809-823, 1993.

Moore, W.B., G. Schubert, and P. Tackley, Three-dimensional simulations of plume-lithosphere interaction at the Hawaii swell, *Scienc,e 279*, 1008-1011, 1998.

Moore, W.B, G.Schubert, and P.J. Tackley, The role of rheology in lithospheric thinning by mantle plumes, *Geophys. Res. Lett., 26*, 1073-1076, 1999.

Pavlenkova, N.I., G.A. Pavlenkova, and L.N. Solodilov, High velocities in the uppermost mantle of the Siberian craton, *Tectonophysics, 262*, 51-65, 1996.

Renne, P.R and A.R. Basu, Rapid eruption of the Siberian traps flood basalts a the Permo-Triassic boundary, *Science, 253*, 176-179, 1991.

Renne, P.R, Z. Zichao, M.A. Richards, M.T. Black, and A.R. Basu, Synchrony and causal relations between Permian-Triassic boundary crises and Siberian flood volcanism, *Science, 269*, 1413-1416, 1995.

Ribe, N.M. and U.R. Christensen, Three-dimensional modeling of plume-lithosphere interaction, *J. Geophys. Res., 99*, 669-682, 1994.

Richards, M.A., R.A. Duncan, and V.E. Courtillot, Flood basalts and hot-spot tracks: Plume heads and tails, *Science, 246*, 103-107, 1989.

Ringwood, A.E., and M.C. Green, An experimental investigation of the gabbro–eclogite transformations and some geophysical implications, *Tectonophysics, 3*, 383-427, 1966

Sengor, A.M.C., The Cimmeride orogenic system and the tectonics of Eurasia, *Geol. Soc. Am. Special Paper 195*, 1984.

van Keken, P.E., S.D. King, H. Schmeling, U.R. Christensen, D. Neumeister, and M.-P. Doin, A comparison of methods for the modeling of thermochemical convection, *J. Geophys. Res., 102*, 22477-22495, 1997.

White, R. And D. McKenzie, Magmatism at rift zones: The generation of volcanic continential margins and flood basalts, *J. Geophys. Res., 94*, 7685–7729, 1989.

Table and Figure Captions

Figure 1. Cartoon of the continental volcanism model. Step 1 shows a mantle upwelling melting to a small extent and emplacing dikes in the mantle lithosphere. The numerical models in this paper address step 2, in which the diked lithosphere is removed to allow a longer melt column and magma emplacement through the crust shown in step 3. Step 4 is a possible mechanism for ending flood volcanism. Shown are the solidus for dry mantle after *Hirth and Kohlstedt* [1996], and an adiabat for mantle at 1480°C.

Figure 2. Top figure: Surface topographical expression from the numerical model. At time zero (dashed line) the axial topography is at about -70m; at 800,000 years (solid line) it has risen to about 20 m, and by 4.3 Ma (bold line) it has fallen to -120 m. Bottom figure: The numerical models of composition, temperature, and velocity field. Dashed lines are 10% temperature gradients. The shaded areas show concentration of diked mantle lithosphere, with the darkest representing 20% dike material and the palest 4% dike material. The left edge of the box has reflection symmetry. The model is shown at 3.9 Ma, demonstrating Rayleigh-Taylor instability concurrent with shear removal of diked lithosphere. The lines delineating crustal and lithospheric layers are as in Figure 1, step 2.

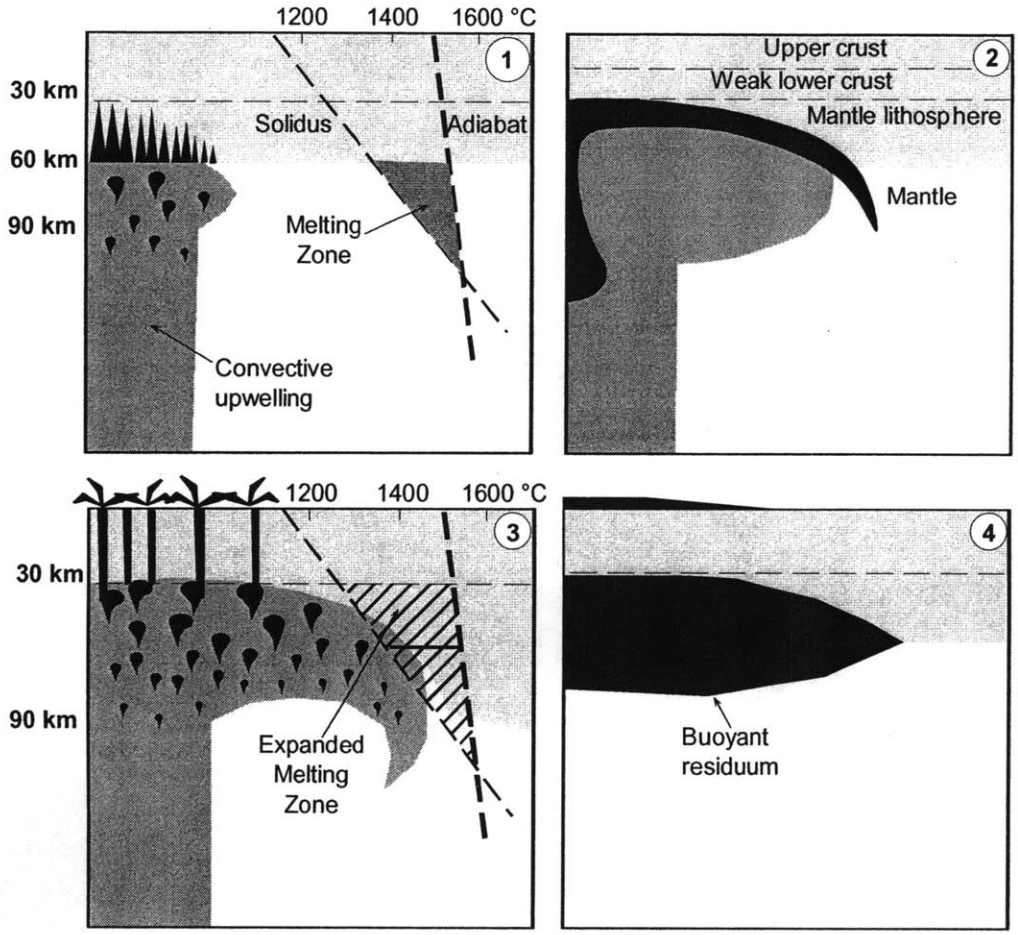
1200
1400
1600 °C
1
30 km
60 km
90 km
Solidus
Adiabat
Melting
Zone
Convective
upwelling
Upper crust
Weak lower crust
Mantle lithosphere
2
Mantle
1200
1400
1600 °C
3
30 km
90 km
Expanded
Melting
Zone
4
Buoyant
residuum

Figure 1

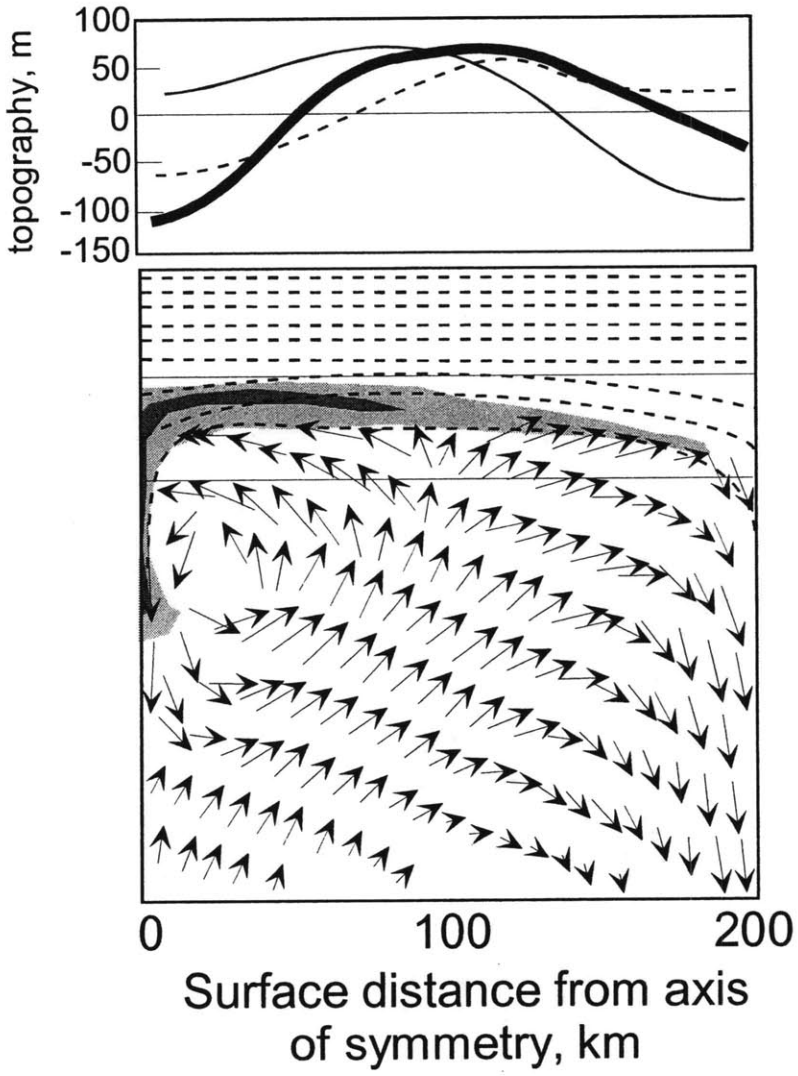
100
50
0
-50
-100
-150
topography, m
0
100
200
Surface distance from axis
of symmetry, km

Figure 2

Ch. 3. Giant meteorite impacts can cause flood basalts: A viable mechanism

Abstract

We present a model for creation of a flood basalt from a giant impactor striking a relatively thin lithosphere. A 300 km radius crater in 75 km thick lithosphere can create 10^6 km^3 of magma from instantaneous in-situ decompression of mantle material with a potential temperature of 1300 °C. For some lithospheric thicknesses and potential temperatures, subsequent adiabatic melting in mantle convection beneath the lithosphere at the site of the impact can create additional magma. Though there is no unequivocal evidence that a giant impactor has struck at the location of any terrestrial flood basalt province, there are coincident ages of impacts, flood basalts, and extinctions. This model provides an internally consistent explanation for the formation of several flood basalt provinces, including the Siberian and Deccan.

Introduction

Because several pairs of extinctions and flood basalts have ages that are statistically indistinguishable, researchers have hypothesized that extinctions may be partly or entirely caused by environmental changes brought on by the eruption of flood basalts (continental provinces having more than about 10^5 km^3 of extrusive igneous rocks) (Rampino, 1987). Notable coincidences of extinctions and flood basalts occur at the Cretaceous-Tertiary boundary (the Deccan flood basalts), during the Toarcian (the Karoo/Ferrar province), at the end of the Norian (the Central Atlantic Magmatic Province, or CAMP), at the end of the Changxingian (the Siberian flood basalts), and during the Guadelupian (the Emeishan basalts). Though current dates show coincidences within errors, better age constraints are needed to confirm even the possibility of a causal relationship (see caption to figure 1 for references). (See Figure 1.)

Flood basalt provinces traditionally have been attributed to hot mantle plumes rising from deep in the mantle and injecting adiabatically-produced melt through the lithosphere (e.g., Richards *et al.*, 1989). There is little empirical evidence that supports this model. Satisfactory models have been made to explain large volumes of melt at rifting margins, such as the Parana/Etendeka, Yemen/Ethiopia, CAMP, Karoo/Ferrar, Brito-Arctic, and Madagascar provinces (Leitch *et al.*, 1998; White and McKenzie, 1989), but flood basalts in non-rifting areas (such as the Siberian, Columbia, Deccan, Rajmahal, and Emeishan flood basalt provinces) are not well characterized by existing models (see Elkins Tanton and Hager, 2000, for further discussion).

Continental flood basalts, including those not associated with rifting, occur at the edges of continents, and not in their centers, we believe, because of the difficulty of bringing mantle

material above its solidus under the great depth of continental keels. Any model for continental flood basalts, therefore, must work at the edge of continental cratons, in lithosphere about 50 to 100 km thick. Numerous investigators have suggested that giant impacts could trigger flood basalt eruptions, but little evidence exists for such an event, and no feasible mechanism has been suggested (Rampino, 1987; Negi *et al.*, 1993; Kaihu *et al.*, 2001).

Since the first suggestions of Alvarez *et al.* (1980) that an extraterrestrial impact caused the extinction at the Cretaceous-Tertiary boundary, researchers have been searching for evidence of impacts coincident with extinctions, and increasing numbers of horizons with elevated iridium, shocked quartz, and other indicators have been found. (See Table 1.) Thus far, there are five unequivocal matches of ejecta evidence with a sizeable known crater, most involving tektites, and several lesser examples. The major examples are at 1.07 Ma (the Ivory Coast tektites and Bosumptwi crater; Gentner *et al.*, 1970), at 14.7 Ma (the Moldavite tektites and Ries crater; Fleischer *et al.*, 1965; Delano and Lindsley, 1982), at 35.5 Ma (the North American and Siberian strewn fields, and the Chesapeake Bay and Popigai craters, respectively; Glass *et al.*, 1986; Koeberl *et al.*, 1996; Glass and Koeberl, 1999; Whitehead *et al.*, 2000), and at 65 Ma (a world-wide ejecta layer of shocked minerals, spherules, and iridium, associated with Chicxulub crater, Smit *et al.*, 1992, Grieve, 1997).

Beyond these proven cases there is little ejecta evidence for major impacts. Not only does impact ejecta appear to be ephemeral in the geologic record, but efforts to locate it are relatively new and techniques are improving. There is an intense search for impact evidence simultaneous with flood basalts, with some success. There is some evidence for a crater underneath or close to the Deccan flood basalts themselves (Basu *et al.*, 1985; Negi *et al.*, 1993). Becker *et al.* (2001) reported evidence for a large impact at the time of the Siberian flood basalts based on trapped helium and argon in fullerines, but the finding is controversial and remains to be replicated by another laboratory. Xu *et al.* (1985) report high iridium at the Permian boundary, but this measurement is strongly contested by Orth *et al.* (1990). Kaihu *et al.* (2001) report a large sulfur and strontium excursion and impact-metamorphosed mineral grains coincident with the end-Permian. They interpret these findings as indicative of a 30 to 60 km asteroid strike, creating a crater with a radius from 300 to 600 km. There is a report of shocked minerals at 200 Ma (Bice *et al.*, 1992), the time of the Central Atlantic Magmatic Province. Rampino and Haggerty (1996) report evidence for

high iridium levels at 200 Ma. Despite these intriguing reports, unequivocal evidence for simultaneous occurrences of giant impacts and flood basalts has not been found on Earth.

Beyond the controversy over both the existence of impact evidence and the coincidence of dates among ejecta, extinctions, and flood basalts, there has been skepticism about the possibility of a causal relationship between giant impacts and flood basalts (e.g., Melosh, 2000). No successful quantitative model has been presented. We describe here a reasonable mechanism for the formation of volumes of magma equivalent to flood basalts by a giant impact on thin continental lithosphere.

Models

There are three stages in the impact process that can create melt: 1. Initial cosmic speed impact causes shock melt; 2. Excavation of crustal material from the impact site can cause instantaneous decompression melting in a column beneath the impact site; and 3. Development of a dome in the lithosphere-asthenosphere boundary, either through instantaneous liquid flow of the shocked lithosphere or through later isostatic rebound, induces convection due to the horizontal temperature gradient at the edges of the dome, and upwelling mantle material in these convective cells can potentially melt adiabatically. (See Figure 2.)

Constraints on lithospheric thickness and mantle temperature

As in any model addressing flood basalts, bringing the required volume of mantle material above its solidus is the heart of the modeling problem. The higher the mantle potential temperature, the deeper mantle melting can begin, and the larger the resulting melt fraction and volume of magma. Similarly, if the lithosphere is thin, asthenospheric material can be decompressed to lower pressures and more easily melt. We define the lithosphere as material cooler than 1000 °C, and the asthenosphere as all underlying material. We model craters 50, 100, 200, and 300 km in excavation radius in continental lithospheres 50, 75, 100, and 125 km thick. We do not model any impacts that would completely remove the lithosphere. Though the results of such an impact would no doubt be catastrophic, they would not follow necessarily the process we are modeling.

This model does not rely on unusual asthenospheric temperatures to allow melting. For a 50 km lithosphere, melt exists in the mantle below it for potential temperatures greater than about 1250 °C. We therefore suggest that using an asthenospheric potential temperature higher than 1250 °C is

unrealistic if there was no previous evidence for magmatic activity at the site of impact (though it has been suggested that some amount of melt exists in the upper mantle at all times; see Anderson *et al.*, 1992). For a lithosphere 75 km thick, 1300 °C is the highest mantle potential temperature that does not produce melt, and for lithospheres 100, 125, and 150 km thick a potential temperature of 1350 °C is used. Higher mantle potential temperatures significantly increase melt volumes, but are considered unrealistic. See Figure 3 for the lithospheric and asthenosphere model used in this study.

Crater models

The evolution of the shape of craters, from the first seconds after impact through isostatic rebound thousands of years after impact, is controversial. Because material excavated from the crater is thrown farther than any possible radius of inward flow, thinning of the lithosphere and depressurization of the underlying mantle will result regardless of the magnitude of lateral crater collapse. This simple assumption removes some of the controversy over the possibility of instantaneous lateral resurge filling the crater and disallowing in-situ melting; if the mass has been ejected from the crater, then a mass deficiency exists for the lithosphere in the region of the crater, and our modeled processes will proceed.

The ejecta argument probably would not be as effective in the case of an oceanic impact. The rapid resurge of a wall of water back into the crater, perhaps carrying with it sediment and breccia, is likely to largely refill the crater and decrease the amount of depressurization. It is thought that this process rapidly refilled Chicxulub (Ebbing *et al.*, 2001).

Our crater models are based on the models of O'Keefe and Ahrens (1999, 1993) and Cintala and Grieve (1998); see Figure 4. The maximum depth of excavation equals 0.15R, where R is the radius of excavation. The value 0.15R is also the maximum isostatic uplift of the bottom of the lithosphere under the crater. The radius of the final crater, including outer ring structures, is about 1.9R.

The complex crater depth profile (D_C) of O'Keefe and Ahrens (1999) is closely fitted by the following expression, where R is the radius of excavation of the crater, and r is the radial distance from the center of the crater, all in km:

$$D_C = R\left(\frac{0.2r^3}{R^3} + \frac{0.022}{\frac{r}{R}+0.1} - 0.22\right) \quad (1)$$

When integrated, this fitted profile yields the following expression for excavated crater volume, V:

$$V_C = 0.11\pi R^3 \quad (2)$$

This excavated volume is matched by the total ejecta volume obtained by integrating the following expression for ejecta blanket thickness, D_E, as a function of distance from the crater's outer edge:

$$D_E = \frac{0.34R^{4\,24}}{r^{3.5}} \quad (3)$$

The crater depth profile is used in both the in-situ decompression melting model and the formation of the lithospheric dome for subsequent convective melting.

The resulting volumes are in agreement with the ejecta law given in Housen, Schmidt and Holsapple (1983), and crater profiles are roughly in agreement with Melosh (1989) and Grieve and Cintala (1992).

Impactor size and energy

Assuming that impacts excavate one hundred times their own mass (e.g., Melosh, 1989), the average upper lithospheric density is 2500 kg/m^3, and the volume of the initial crater is given as equation 2, the mass and therefore the radius of impactor required to create the modeled craters can be calculated. To create a crater with a 50 km radius, depending on the mass and speed of the impactor, an impactor with radius of 3 - 5 km is required. To create a crater with 300 km radius, an impactor with 15 - 25 km radius is required.

Modeling impact energy simply as $\frac{mv^2}{2}$ (where m = impactor mass and v = impactor velocity), and assuming impactors will strike at between 10 and 40 km/sec (Steel, 1998), the energy of impact for the modeled craters varies between 10^7 and 10^{10} Mt (10^{22} to 10^{26} J). It has been estimated that

impacts of this size should occur about once every 100 Ma, suggesting that 5 or 6 such events should exist in the Phanerozoic record (Grieve and Shoemaker, 1994).

Modeling melt volumes

Stage 1: Shock melt from impact

The first stage of melting, shock melting from the energy of impact, was not modeled here. A 300-km radius crater makes about 10^5 km^3 of shock melt, and a 100-km radius crater about 10^4 km^3 of melt, between 1% and 10% of the volume required to make a flood basalt province (Pierozzo, Vickery, and Melosh, 1997; Tonks and Melosh, 1993). Because the crust is compositionally distinct from the mantle, shock melts are generally compositionally distinct from adiabatic mantle melts, and would not be mistaken for them, and so are not included in this study.

Stage 2: In-situ decompression melting

At the time of impact, material at the impact site is ejected, and within a certain additional radius, material is melted (shock melt) or disrupted and heated by shock. In giant craters the volume of material heated but not melted may be considerable, but this heating process is not considered in this model. For simplicity, a conductive geotherm through the lithosphere culminating at an adiabatic asthenosphere is assumed to remain in place after excavation.

Excavation of the crater reduces pressure beneath the crater by an amount equal to the lithostatic pressure of the material excavated. The greatest pressure release is over the interval from 20% to 40% of the radius of excavation, and pressure release declines to zero at the crater rim (and pressure can increase outside the rim due to new deposits). This lowering of pressure effectively moves the solidus deeper into the material, in some cases causing it to cross the geotherm and create melt. This melting mechanism is shown in Figure 5. A general equation for in-situ decompression melt was created by integrating the area of intersection between the solidus and geotherm around the axis of symmetry of the crater. The parameters used in the equations are given in Table 2.

A critical parameter is β, the melt fraction per degree between solidus and liquidus. This can be calculated using C_p, the heat capacity of the silicates, and H_f, the heat of fusion of the silicates, as follows:

$$\beta = \frac{df}{dT} = \frac{C_P}{H_f} = 0.003 \tag{4}$$

Based on this $\frac{df}{dT}$ and the maximum decompression created by any impact modeling, the maximum melt percent of a parcel of mantle in the in-situ melting model is 15%. In fertile mantle peridotite, melting about 20% is generally required to exhaust clinopyroxene and change the melting productivity (Walter, 1998; Kinzler and Grove, 1992). With 15% the maximum melt produced in these models, it is not a bad assumption to use a constant $\frac{df}{dT}$.

The geotherm is modeled as a straight, conductive profile through the lithosphere from the surface to the adiabatic potential temperature at the base of the lithosphere, and as an adiabat through the mantle. The solidus is approximately that of Hirschmann (2000). The following expressions describe the geotherm in the lithosphere, which is conductive, and in the mantle, where it is adiabatic:

$$Lithospheric\_geotherm = T_A = z\left(\frac{T_p}{d} + a\right) \tag{5}$$

$$Mantle\_geotherm\_(adiabatic) = T_B = az + T_p \tag{6}$$

A solidus for mantle material can be expressed as follows, and subsequently as it appears following excavation of the crater:

$$Solius = sz + s_o \tag{7}$$

$$Solidus\_following\_crater\_excavation = T_C = s(z + D_C) + s_o \tag{8}$$

Where the expression for the crater profile, D_C, is given by equation 1 above.

The integration is performed in two parts, one from the intersection of the solidus and the adiabat (z_l, where equation T_B equals equation T_C) upward to the base of the lithosphere (where the geotherm changes slope and becomes conductive), and the second from the base of the lithosphere to the intersection between the solidus and the conductive geotherm (z_u, where equation T_A equals equation T_C). The maximum temperature interval of melting between the solidus and geotherm is found over the interval from 0.2 to 0.4 of the radius of excavation. As the radius increases toward the edge of the crater the solidus effectively moves up, following the crater floor, and the melting interval decreases. See Figures 2 and 3 (process and lithosphere diagrams). The final equation for in-situ melt is given as:

$$F = 2\pi\beta\left[\int_{d}^{z_l}\int_{0}^{R} r\left(T_B - T_C\right)drdz + \int_{z_u}^{d}\int_{0}^{R} r\left(T_A - T_C\right)drdz\right] \tag{9}$$

This equation for F is easily integrated, and the result is an equation for in-situ melt as a function of R, d, s, a, s_o, and T_p.

Because silicic crustal materials have, in general, a lower-temperature solidus than do mafic mantle materials, it is tempting to use their solidus in calculating intersections with the geotherm in the lithosphere. If a great percentage of the lithosphere is made up of silicic materials it is possible to melt crustal materials through in-situ depressurization. This process may be important in the formation of ore bodies such as Sudbury's, but crustal melting is not modeled in this paper.

Stage 3: Adiabatic melting in convection currents

The excavated crater profile shown in Figure 3 is not in isostatic equilibrium; the thinned lithosphere has a gravitational driving force to rise and form a dome in the lithosphere-mantle boundary. The process of forming a dome may occur virtually instantaneously, when the lithosphere behaves as a liquid due to the intense shock of the impact. Alternatively, the lithosphere may rebound isostatically over approximately the next 10^4 years.

Domes under lunar impact basins have been clearly demonstrated in lunar gravity modeling (Weiczorek and Phillips, 1999; Neumann *et al.*, 1996), but they have not been demonstrated on the Earth. There are a number of possible reasons for the lack of evidence for terrestrial lithospheric domes. First, the smallest lunar basins that show domes are about the size of the very largest

terrestrial impacts yet recognized. On the moon, domes are present for basins that range in size from Imbrium to Smythii. Imbrium has a radius of excavation of about 350 km and Smythii about 80 km; Chicxulub, on Earth, had an excavation radius of about 50 km (Weiczorek and Phillips, 1999; Neumann *et al.*, 1996; Pilkington *et al.*, 1994; Morgan *et al.*, 1997). If domes are formed by instantaneous fluid flow of shocked lithosphere, then it is possible that the process requires basin-forming impacts larger than that of Chicxulub. Alternatively, domes may have formed in the largest terrestrial impacts but were obliterated by later dynamic processes. Buoyant residuum from in-situ melt will fill the lithospheric dome and end convective melt. The buoyant residuum, combined with possible long-term lateral middle-crustal flow and cooling and thickening of the lithosphere, could obscure any original lithospheric dome from detection by seismic surveys.

We suggest that terrestrial lithospheric domes will form by nearly instantaneous flow combined with later isostatic compensation for giant impacts in thin lithospheres. All the impacts modeled in this study (with the exception of the 50 km-radius crater in 150 km thick lithosphere) penetrate or disrupt through shock the entire thickness of the lithosphere. Therefore all the impacts modeled are expected to create significant lithospheric flow and create at least a partial lithospheric dome. Based on analysis of the shape and size of the central uplift feature in the Vredefort impact structure, Henkel and Reimold (1998) calculated that the viscosity of the crust during initial deformation was about 10^{12} Pas. This is at least ten orders of magnitude less than normal crustal viscosity, and about seven orders of magnitude less viscous than the aesthenosphere. This is strong support for immense volumes of rock involved in liquid flow at the time of giant impact. Later, as the in-situ decompression melts erupt, the thinned, weakened lithosphere may subside. This would be consistent with the critical geological observation that both the Siberian and the Emeishan basalts were subsiding while erupting (Fedorenko *et al.*, 1996; Thompson *et al.*, 2001).

When the lithospheric dome has formed, it necessarily creates a horizontal temperature gradient across its edges, which provides a driving force for convection. Adiabatic melting may occur in the resulting convective cells, depending on the depth and temperature of the mobilized mantle materials. This third melting stage begins as soon as immediately after the time of impact and, at latest, on the order of 10^4 years after impact.

The convection is calculated numerically using a spherical axisymmetric version of the finite element code ConMan (King *et al.*, 1990), called NewScam, and any resulting melt is calculated

with a post-processor routine using the parameters listed in Table 2. We ran a large suite of test models to ensure that the code was correctly calculating the convective flow, and to ensure that the grid had sufficient resolution to avoid numerical defects.

Thermal convection is governed by the Rayleigh number:

$$Ra = \frac{\rho g \alpha \Delta T h^3}{\eta_o \kappa} \tag{10}$$

where α is thermal expansivity, κ is thermal diffusivity, ρ is a characteristic density, ΔT is the temperature change over the model box, h is a characteristic length and η_o is a reference viscosity. Viscosity is first calculated using the following temperature-dependent law:

$$\eta_{nonN.} = \eta_o \exp\left(\frac{E + vz}{T + T_o} - \frac{E + vz_o}{1 + T_o}\right) \tag{11}$$

where η_o, z_o, and T_o are reference values for viscosity, depth, and temperature, respectively; E is the activation energy, set such that a 100°C change in mantle temperature creates a factor of ten change in viscosity, and v is the reference volume, set such that a 33 kb change in pressure also creates a factor of ten change in viscosity. The second invariant of the stress tensor is given as:

$$Secinv = 0.5\left(\sigma_{rr}^2 + \sigma_{\tau\tau}^2 + \sigma_{\Phi\Phi}^2\right) + \sigma_{r\tau}^2 \tag{12}$$

If the second invariant of the stress tensor is non-zero, then viscosity is recalculated using the following two non-Newtonian laws in this order:

$$\eta_{stress} = \left(\frac{\sigma_o^2}{2(Secinv)^2}\right)^{0.25} \qquad \text{Stress-weighting law} \tag{13}$$

$$\eta = \eta_{stress}\left(\frac{\sigma_o^{0.66}\ \eta_{nonN}^{0.33}}{2(Secinv)^{0.66}}\right)^{0.75} \qquad \text{Strain-weighting law} \tag{14}$$

where σ_0 is the reference value for stress. A list of key variables is given in Table 2.

A starting condition for each model runs was created by using an erfc cooling law to make a cooled lithosphere of the required thickness with a lithospheric dome with maximum uplift equal to 0.15 times the crater excavation radius.

Results

Stage 1: In-situ decompression melting

In-situ decompression melt is the largest, and, for most parameters, the only contributor to melt created by giant terrestrial impacts.

Table 3 lists the total melt produced in the model. Volumes of melt consistent with flood basalt provinces are created by large impacts in thin lithospheres, without resorting to mantle potential temperatures that would create extant melt before impact (these conditions are shaded in the table). The impact-generated mafic mantle melts originate from the lowest part of the lithosphere to depths as great as 140 km. The range of the melting interval is also listed in Table 2. This depth of melting is unusual for terrestrial processes; melting in mid-ocean ridge environments, for example, begins at about 50 km. The depths of origin, however, are strongly dependent upon the degree of isostatic compensation of the crater. If a high lithospheric dome forms by instantaneous fluid flow, then the melting interval will be shallow, as determined by the depth of the bottom of the lithosphere. If the crater retains its maximum excavation depth because little instantaneous doming occurs, then the melting interval will be commensurately deeper, though the volumes of melt produced will be identical. The melting depths listed in Table 2 are calculated for craters with no dome formation. In the case of maximum instantaneous dome formation, the melting columns will be made shallower by the excavation depth, equal to 0.15 times the excavation radius of the crater.

Stage 2: Adiabatic melting in convection currents

To test the theory of convective melting under rebounded craters, we have run numerical models assuming lithospheric domes of the maximum height formed under the crater. From the start of each of the numerical model runs, mantle material flows upward in the center of the dome and flows out and down at the edges. As convection continues, the strongest upward currents move toward the edges of the dome, and a matching eddy outside the dome may form. Cooling thickens the lithosphere and convection currents are forced more deeply into the mantle. The strong

downward-flowing limb of the cell at the rim of the dome may eventually pull material from the edge of the dome consisting of cool upper aesthenosphere or the warmest lowest lithosphere. In most models, a Rayleigh-Taylor instability forms in the center of the mantle dome and drops off by about 10 Ma after impact.

Though in lunar models the convective stage produces small volumes of melt over a long period of time, in terrestrial models only the thinnest lithosphere with the hottest mantle produces convective melt (Elkins Tanton *et al.*, 2002). In other models, convection proceeds but fails to bring material to shallow enough depths to produce melt. The models demonstrate that even in the ideal case of maximum dome formation, very little or no melt is produced in the resulting convection cells for Earth.

Discussion

There is no unequivocal evidence that any flood basalt province on Earth has ever been caused by a giant impact. However, the parameters of the models discussed in this paper are consistent with terrestrial conditions.

As Argon dating techniques have improved (Baker *et al.*, 1996), the estimated duration of flood basalt eruptions have shortened. The Siberian and Deccan flood basalts are thought to have occurred in one million years or less (Bowring *et al.*, 1998; Baksi, 1994), but others had longer durations. The Columbia flood basalts had a peak of eruption over about a million years, but continued to erupt over 11 million years (Hooper and Hawkesworth, 1993). The lingering volcanism is a result of the process of formation of the volcanic province, and should be recreated by the model. A successful flood basalt model, then, is required to create on the order of 10^6 km^3 of magma in less than a million years. In the cases of the Siberian and Emeishan provinces, the model must allow subsidence during eruption, and in the case of the Columbia, produce lingering eruptions for about 10 Ma.

Figure 6 shows a comparison of melt volumes and eruption durations of flood basalt provinces and model results. The models in which melt was only created by in-situ depressurization produce all their magma in a very brief time, and the volumes and durations fit the Siberian, Deccan, Emeishan, and Rajmahal provinces. Models in which later convection produces melt have longer durations of eruption, and fit the Columbia flood basalts in volume and duration.

The three largest known craters on Earth, Chicxulub, Sudbury, and Vredefort, on the other hand, do not have flood basalts associated with them. Sudbury and Vredefort both struck thick continental lithosphere, and were relatively small compared to those modeled in this study: each had an estimated excavation radius of 50 to 70 km (scaling from O'Keefe and Ahrens, 1999 and 1993, applied to data from Grieve and Therriault, 2000). Craters this size produce little or no mafic magma in lithospheres thicker than 75 km, according to our model results. Therefore based on this study we would expect no basaltic magmatism from either impact (though crustal melting from depressurization may have been significant in both cases and will be addressed elsewhere).

Chicxulub, the youngest and freshest of the large terrestrial impacts, had an excavation radius of about 50 km (Pilkington *et al.*, 1994; Morgan *et al.*, 1997). It struck shallow ocean, which presumably lay over relatively thin lithosphere. Though the crater is the smallest size modeled in this study, if the lithosphere it struck was thin, Chicxulub would have been a reasonable candidate to create not a flood basalt, but about 1,000 km^3 of magma. There is, however, no known magmatism associated with Chicxulub. Deep seismic reflection studies carried out by Snyder *et al.* (1999) show that there is no dome under Chicxulub. The shapes and positions of collapsed blocks and thrust faults under the crater indicate little or no fluid lithospheric flow during the initial cratering process. Their results, along with those of Pilkington *et al.* (1994) and Morgan *et al.* (1997), indicate that the cavity of Chicxulub is filled with breccia. We therefore agree with Ebbing *et al.* (2001) that resurge must have nearly instantaneously filled Chicxulub with material, removing any possibility of in-situ decompression melting, and also of the formation of a lithospheric dome to force mantle convection.

Conclusions

A giant meteorite impact in thin lithosphere is a viable mechanism for creating a flood basalt province on Earth. Mafic magma is produced by immediate in-situ decompression and by later convective flow in a lithospheric dome that forms under the crater by instantaneous fluid flow of the lithosphere during impact, and by later isostatic uplift. Volumes and durations of existing flood basalt provinces are well fit by melt production in these models. Though there is no unequivocal evidence that giant impacts have created flood basalt provinces on Earth, researchers continue to search for impact evidence coincident with flood basalt formation. Such evidence is apparent on the Moon, where mare basalts fill large impact basins. Basins of this age and size have been

obliterated on the Earth through processes of plate tectonics and erosion, but the possibility remains of craters obscured beneath existing flood basalt provinces. The largest visible craters, Chicxulub, Sudbury, and Vredefort are not large enough to create flood basalts according to our model. This model for giant impact is applicable to other terrestrial planets, in particular, Venus and Mars.

Acknowledgments

This work was supported by a National Defense Science and Engineering graduate fellowship, and an Amelia Earhart graduate fellowship. The authors thank Marc Parmentier for rewarding conversations on mechanisms of melting.

References

Alvarez L.W., W. Alvarez, F. Asaro, H.V. Michel (1980) Extraterrestrial cause of the Cretaceous-Tertiary extinction. *Science* **208** 1095-1008.

Anderson D.L., T. Tanimoto, Y.-s. Zhang (1992) Plate tectonics and hotspots: The third dimension. *Science* **256**, 1645-1651.

Baker J., L. Snee, M.A. Menzies (1996) A brief Oligocene period of volcanism in Yemen; implications for the duration and date of continental flood volcanism at the Afro-Arabian triple junction. *Earth Planet. Sci. Lett.* **138**, 39-55

Baksi A.K. (1994) Geochronological studies on whole-rock basalts, Deccan Traps, India: evaluation of the timing of volcanism relative to the K-T boundary. *Earth Planet. Sci. Lett.* **121**, 43-56.

Baksi A.K. (1995) Petrogenesis and timing of volcanism in the Rajmahal flood basalt province, northeastern India. *Chem. Geology* **121**, 73-90.

Barrera E. (1994) Global environmental changes preceding the Cretaceous-Tertiary boundary: Early-late Maastrichtian transition. *Geology* **22**, 877-880.

Basu A.R., S. Chatterjee, D. Rudra (1985) Shock-metamorphism in quartz grains at the base of the Deccan Traps: Evidence for impact-triggered flood basalt volcanism at the Cretaceous-Tertiary boundary. *EOS Transactions* **69**, 1487.

Becker L., R.J. Poreda, A.G. Hunt, T.E.Bunch, M. Rampino (2001) Impact event at the Permian-Triassic boundary: Evidence from extraterrestrial noble gases in fullerines. *Science* **291**, 1530-1533.

Bice D.M., C.R. Newton, S. McCauley, P.W. Reiners, C.A. McRoberts (1992) Shocked quartz at the Triassic-Jurassic boundary in Italy. *Science* **255**, 443-446.

Bowring S.A., D.H. Erwin, Y.G. Jin, M.W. Martin, K. Davidek, W. Wang (1998) U-Pb zircon geochronology and the tempo of the end-Permian mass extinction. *Science* **280**, 1039-1045.

Bratt S.R., S.C. Solomon, J.W. Head, C.H. Thurber (1985) The deep structure of lunar basins: Implications for basin formation and modification. *J. Geophys. Res.* **90**, 3049-3064.

Chernet T., W.K. Hart, J.L. Aronson, R.V. Walter (1998) New age constraints on the timing and tectonism in the northern Main Ethiopian Rift – southern Afar transition zone (Ethiopia). *J. Volcanology Geothermal Res.* **80**, 267-280.

Cintala M.J. and R.A.F. Grieve (1998) Scaling impact melting and crater dimensions: Implications for the lunar cratering record. *Meteor. Planet. Sci.* 33, 889-912.

Coffin M.F. and O. Eldholm (1994) Large igneous provinces: Crustal structure, dimensions, and external consequences. *Rev. Geophys.* **32** 1-36.

Courtillot V. (1990) Deccan volcanism at the Cretaceous-Tertiary boundary: past climatic crises as a key to the future? *Palaeo*^{3} **189**, 291-299.

Dalrymple G.B., G.K. Czamanske, V.A. Fedorenko, O.N. Simonov, M.A. Lanphere, A.P. Likhachev (1995) A reconnaissance $^{40}Ar/^{39}Ar$ geochronologic study of ore-bearing and related rocks, Siberian Russia. *Geochim. Cosmochim. Acta* **59**, 2071-2083.

Deckart K., G. Feraud, H. Bertrand (1997) Age of Jurassic continental tholeiites of French Guyana, Surinam and Guinea: Implications for the initial opening of the Central Atlantic Ocean. *Earth Planet. Sci. Lett.* **150**, 205-220.

Delano, J.W. and D.H. Lindsley, D.H. (1982) Chemical systematics among the moldavite tektites. *Geochim. Cosmochim. Acta* **46**, 2447-2452.

Digby J.M. and W.D. Goodfellow (1990) Geological and biological consequences of giant impacts. *Ann. Rev. Earth Planet. Sci.* **18**, 123-171.

Duncan R.A., P.R. Hooper, J.Rehacek, J.S. Marsh, A.R. Duncan (1997) The timing and duration of the Karoo igneous event, southern Gondwana. *J. Geophys. Res.* **102**, 18127-18138.

Ebbing J., P. Janle, J. Koulouris, B. Milkereit (2001) 3D gravity modelling of the Chicxulub impact structure. *Planet Space Sci.* **49**, 599-609.

Elkins Tanton, L.T. and B.H. Hager (2000) Melt intrusion as a trigger for lithospheric foundering and the eruption of the Siberian flood basalt. *Geophys. Res. Lett.* **27**, 3937-3940.

Elkins Tanton. L.T., B.H. Hager, T.L. Grove (2002) Magmatic effects of the lunar late heavy bombardment. Submitted to *Science.*

Fedorenko V.A., P.C. Lightfoot, A.J. Naldrett, G.K. Czamanske, C.J. Hawkesworth, J.L. Wooden, D.S. Ebel (1996) Petrogenesis of the flood-basalt sequence at Noril'sk, North-central Siberia, *Int. Geology Rev.* **38**, 99-135.

Fleischer R.L., P.B. Price, R.M. Walker (1965) On the simultaneous origin of tektites and other natural glasses. *Geochim. Cosmochim. Acta* **29**, 161-166.

Fowell S.J., B. Cornet, P.E. Olsen (1994) Geologically rapid Late Triassic extinctions: Palynological evidence from the Newark Supergroup. *GSA Special Paper* **288**, 197-206.

Gentner W., B.P. Glass, D. Storzer, G.A. Wagner (1970) Fission track ages and ages of deposition of deep-sea microtektites. *Science* **168** 359-361.

Glass B.P. and C. Koeberl (1999) Ocean Drilling Project Hole 689B spherules and upper Eocene microtektite and clinopyroxene-bearing spherule strewn fields. *Met. Planet. Sci.* **34**, 179-208.

Glass B.P., C.M. Hall, D. York, (1986) $^{40}Ar/^{39}Ar$ laser-probe dating of North American tektite fragments from Barbados and the age of the Eocene-Oligocene boundary. *Chem. Geol.* **59**, 181- 186.

Grieve R.A.F. (1997) Extraterrestrial impact events: the record in the rocks and the stratigraphic column. *Palaeo*^{3} **132** 5-23.

Grieve R.A.F. and M.J. Cintala (1992) An analysis of differential impact-melt crater-scaling and implications for the terrestrial impact record. *Meteoritics* **27** 526-538.

Grieve R.A.F. and E.M. Shoemaker (1994) The record of past impacts on earth. In Gehrels, Tom, ed. *Hazards due to Comets and Asteroids* U. of Arizona, 417-462.

Grieve R.A.F. and A. Therriault (2000) Vredefort, Sudbury, Chicxulub: Three of a kind? *Ann. Rev. Earth Planet. Sci.* **28** 305-338.

Hallam A. (1992) Phanerozoic sea-level changes. Columbia Univ. Press, NY.

Hames W.E., P.R. Renne, C. Ruppel (2000) New evidence for geologically instantaneous emplacement of earliest Jurassic Central Atlantic magmatic province basalts on the North American margin. *Geology* **28** 859-862.

Henkel H. and W.U. Reimold (1998) Integrated geophysical modelling of a giant, complex impact structure: anatomy of the Vredefort Structure, South Africa. *Tectonophysics* 287 1-20.

Hirschmann M.M. (2000) Mantle solidus: Experimental constraints and the effects of peridotite composition. *Geochemistry, Geophysics, Geosystems* **1**.

Holser W.T., M. Magaritz, R.L. Ripperdan (1995) Global isotopic events. In Walliser, Otto H., ed. *Global Events and Event Stratigraphy in the Phanerozoic* Springer Verlag, p. 63-88.

Hooper P.R. (1997) The Columbia River flood basalt province: Current status. In Macdougall JD, ed. *Continental Flood Basalts* Kluwer, p. 1-27.

Hooper P.R. and C.J. Hawkesworth (1993) Isotopic and geochemical constraints on the origin abd evolution of the Columbia River Basalt. *J. Pet.* **34**, 1203-1246.

Housen K.R., R.M. Schmidt and K.A. Holsapple (1983) Crater ejecta scaling laws: Fundamental forms based on dimensional analysis. *J. Geophys. Res.* **88**, pp 2485-2499.

Hsu K.J. and J. McKenzie (1990) Carbon-isotope anomalies at era boundaries: Global catastrophes and their ultimate cause. *GSA Special Paper* **247**, 61-70.

Hsu K.J., H. Oberhansli, J.Y. Gao, S. Sun, H.H. Chen, U. Krahenbuhl (1985) Strangelove ocean before the Cambrian explosion. *Nature* **316**, 809-811.

Kaiho K., Y. Kajiwara, T. Nakano, Y. Miura, H. Kawahata, K. Tazaki, M. Ueshima, Z. Chen, G.R. Shi (2001) End-Permian catrastrophe by a bolide impact: Evidence of a gigantic release of sulfur from the mantle. *Geology* **29**, 815-818.

Kamo S.L., G.K. Czamanske, T.E. Krough (1996) A minimum U-Pb age for Siberian flood basalt volcanism. *Geochimica et Cosmochimica Acta* **60**, 3505-3511.

Katz M.E., D.K. Pak, G.R. Dickens, K.G. Miller (1999) The source and fate of massice carbon input during the latest Paleocene thermal maximum. *Science* **286**, 1531-1533.

King, S.D., A. Raefsky, B.H. Hager (1990) ConMan: Vectorizing a finite element code for incompressible two-dimensional convection in the Earth's mantle, *Phys. Earth Planet. Int,* **59** 195-207.

Kinzler R.J. and T.L. Grove (1992) Primary magmas of mid-ocean ridge basalts 1. Experiments and methods. *J. Geophys. Res.* **97**, 6885-6906.

Koeberl C., C.W. Poag, W.U. Reimold, D. Brandt, (1996) Impact origin of the Chesapeake Bay structure and the source of the North American tektites. *Science* **271**, 1263-1266.

Kyte F.T. (1988) The extraterrestrial component in marine sediments: description and interpretation, *Paleoceanography* **3** 235-247.

Leitch A.M., G.F. Davies, M. Wells (1998) A plume head melting under a rifting margin. *Earth Planet. Sci. Lett.* **161**, 161-177.

Marzoli A., P.R Renne, E.M. Piccirillo, M. Ernesto, G.Bellieni, A. De Min (2000) Extensive 200-Million-year-old continental flood basalts of the Central Atlantic Magmatic Province. *Science* **284**, 616-618.

Meighan I.G., A.G. McCormick, D. Gibson, J.A. Gamble, I.J. Graham (1988) Rb-Sr isotopic determinations and the timing of Tertiary central complex magmatism in Northeast Ireland; In Morton A.C., L.M. Parson, eds. *Early Tertiary volcanism and the opening of the Northeastern Atlantic.* Geological Society, London, Special Publication **39**, 349-360.

Melosh H.J. (2000) Can impacts induce volcanic eruptions? Abstract in proceedings of ``Catastrophic Events and Mass Extinction: Impacts and Beyond" Vienna, July 9-12.

Melosh, H.J. (1989) *Impact cratering: A geological process*, Oxford University Press, Oxford and New York, 245 pp.

Menzies M., J. Baker, G. Chazot, M. Al'Kadazi (1997) Evolution of the Red Sea volcanic margin, western Yemen. *In* Large Igneous Provinces: Continental, Oceanic, and Planetary Flood Volcanism. John J. Mahoney and Millard F. Coffin eds. American Geophysical Union monograph 100, Washington DC. 29-44.

Minor D.R. and S.B. Mukasa (1997) Zircon U-Pb and hornblende ^{40}Ar-^{39}Ar ages for the Dufek layered mafic intrusion, Antarctica: Implications for the age of the Ferrar large igneous province. *Geochim. Cosmochim. Acta* **61**, 2497-2504.

Montanari A., F. Asaro, H. Michel, J. Kennett (1993) Iridium anomalies of Late Eocene age at Massignano (Italy), and ODP Site 689B (Maud Rise, Antarctic), *Palaios* **8**, 420-437.

Morgan J., M. Warner, Chicxulub Working Group (1997) Size and morphology of the Chicxulub impact crater. *Nature* **390** 472-476.

Mussett A.E. (1986) $^{40}Ar/^{39}Ar$ step heating ages of the Tertiary igneous rocks of Mull, Scotland. *J. Geol. Soc. London* **143**, 887-896.

Negi J.G., P.K. Agrawal, O.P. Pandey, A.P. Singh (1993) A possible K-T boundary bolide impact site offshore near Bombay and triggering of rapid Deccan volcanism. *Phys. Earth Planet. Int.* **76**, 189-197.

O'Keefe, J.D. and T.J. Ahrens (1993) Planetary cratering mechanics. *J. Geophys. Res.* **98**, 17011-17028.

O'Keefe, J.D. and T.J. Ahrens (1999) Complex craters: Relationship of stratigraphy and rings to impact conditions. *J. Geophys. Res.* **104**, 27,091-27,104.

Orth C.J., M. Attrep, L.R. Quintana (1990) Iridium abundance patterns across bio-event horizons in the fossil record, *GSA Special Paper* **247**, 45-59.

Palfy J. and P.L. Smith (2000) Synchrony between Early Jurassic extinction, oceanic anoxic event, and the Karoo-Ferrar flood basalt volcanism. *Geology* **28**, 747-750.

Pearson D.G., C.H. Emeleus, S.P. Kelley (1996) Precise $^{40}Ar/^{39}Ar$ age for the initiation of Paleogene volcanism in the Inner Hebrides and its regional significance. *J. Geol. Soc. London* **153**, 815-818.

Pierozzo E., A.M. Vickery and H.J. Melosh (1997) A reevalution of impact melt production. *Icarus* **127**, 408-423.

Pilkington M., A.R. Hildebrand, C. Ortiz-Aleman (1994) Gravity and magnetic field modeling and structure of the Chicxulub Crater, Mexico. *J. Geophys. Res.* **99**, 13147-13162.

Pringle M.S. (1994) $^{40}Ar/^{39}Ar$ geochronology of Mid-Cretaceous Indian Ocean basalts: Constraints on the origin of large flood basalt provinces. AGU Fall Meeting abstract #V32A-13, p. 728.

Rampino M.R. (1987) Impact cratering and flood-basalt volcanism. *Nature* **327**, 468.

Rampino M.R. and B.M. Haggerty (1996) The "Shiva Hypothesis": Impacts, mass extinctions, and the galaxy. *Earth Moon Planets* **72**, 441-460.

Raup D.W. and J.J. Sepkoski Jr. (1986) Periodic extinction of families and genera. *Science* **231**, 833-836.

Ray J.S. and K. Pande (1999) Carbonatite alkaline magmatism associated with continental flood basalts at stratigraphic boundaries: Cause for mass extinctions. *Geophys. Res. Lett.* **26**, 1917-1920.

Renne P.R. (1995) Excess ^{40}Ar in biotite and hornblende from the Noril'sk 1 intrusion, Siberia: implications for the age of the Siberian Traps. *Earth Planet. Sci. Lett.* **131**, 165-176.

Renne P.R. and A.R Basu (1991) Rapid eruption of the Siberian Traps flood basalts at the Permo-Triassic boundary. *Science* **253**, 176-179.

Renne P.R., J.M. Glen, S.C. Milner, A.R. Duncan (1996) Age of Etendeka flood volcanism and associated intrusions in southwestern Africa. *Geology* **24**, 659-662.

Renne P.R., Z. Zichao, M.A. Richards, M.T. Black, A.R. Basu (1995) Synchrony and causal relations between Permian-Triassic boundary crises and Siberian flood volcanism. *Science* **253**, 1413-1416.

Richards M.A., R.A. Duncan, V.E. Courtillot (1989) Flood basalt and hot-spot tracks - plume heads and tails. *Science* **246**, 103-107.

Sepkoski J.J. Jr. (1994) Extinctions and the fossil record. *Geotimes* **39**, 15-17.

Sinton C.W., R.A. Duncan, M. Storey, J. Lewis, J.J. Estrada (1998) An oceanic flood basalt province within the Caribbean plate. *Earth Planet. Sci. Lett.* **155**, 221-235.

Smit, J., Alvarez, W., Montanari, A., Swinburne N., Van Kempen, T.M., Klaver, G.T., Lustenhouwer, W.J. (1992) "Tektites" and microkrystites at the Cretaceous Tertiary boundary: Two strewn fields, one crater? *Proc. Lunar Planet. Sci Conf.* **22**, 87-100.

Snyder D.B., R.W. Hobbs, Chicxulub Working Group (1999) Ringed structural zones with deep roots formed by the Chicxulub impact. *J. Geophys. Res.* **104** 10743-10755.

Stanley S.M. and X. Yang (1994) A double mass extinction at the end of the Paleozoic era. *Science* **266**, 1340 - 1344.

Steel D. (1998) Distributions and moments of asteroid and comet impact speeds upon the Earth and Mars. *Planet. Space Sci.* **46** 473-478.

Stewart K., S. Turner, S. Kelly, C. Hawkesworth, L. Kirstein, M. Mantovani (1996) 3-D ^{40}Ar-^{39}Ar geochronology in the Parana continetnal flood basalt province. *Earth Planet. Sci. Lett.* **143**, 95-109.

Storey M., J.J. Mahoney, A.D. Saunders, R.A. Duncan, S.P. Kelley, M.F. Coffin (1995) Timing of hot spot-related volcanism and the breakup of Madagascar and India. *Science* **267**, 852-855.

Stothers R.B. (1993) Flood basalts and extinction events. *Geophys. Res. Letters* **20**, 1399-1402.

Thompson G.M., J.R. Ali, X.Y. Song, D.W. Jolley (2001) Emeishan basalts, SW China: reappraisal of the formation's type area stratigraphy and a discussion of its significance as a large igneous province. *J. Geological Soc. London* **158**, 593-599.

Tonks W.B. and H.J. Melosh (1993) Magma ocean formation due to giant impacts. *J. Geophys. Res.* **98**, 5319-5333.

Torsvik T.H., R.D. Tucker, L.D. Ashwal, E.A. Eide, N.A. Rakotosolofo, M.J. de Wit (1998) Late Cretaceous magmatism in Madagascar: Paleomagnetic evidence for a stationary Marion hot spot. *Earth Planet. Sci. Lett.* **164**, 221-232.

Turner S., M. Regelous, S. Kelley, C. Hawkesworth, M. Mantovi (1994) Magmatism and continental breakup in the south Atlantic: high precision $^{40}Ar/^{39}Ar$ geochronology. *Earth Planet. Sci. Lett.* **121**, 333-348.

Upton B.G.J., C.H. Emeleus, D.C. Rex, M.F. Thirlwall (1995) Early Tertiary magmatism in Northeast Greenland. *J. Geol. Soc. London* **152**, 959-964.

Venkatasan T.R., A. Kumar, K. Gopalon, A.I. Al Mukhamedov (1997) ^{40}Ar-^{39}Ar age of Siberian basaltic volcanism. *Chem. Geology* **138**, 303-310.

Venkatasan T.R., K. Pande, K. Gopalan (1993) Did Deccan volcanism pre-date the Cretaceous/Tertiary transition? *Earth Planet. Sci. Lett.* **119**, 181-189.

Vonhof H.B., J. Smit, H. Brinkhuis, A. Montanari, A.J. Nederbragt (2000) Global cooling accelerated by early late Eocene impacts? *Geology* **28**, 687-690.

Walter M.J. (1998) Melting of garnet peridotite and the origin of komatiite and depleted lithosphere. *J. Pet.* **39**, 29-60.

Wang K., C.J. Orth, M. Attrep, B.D.E. Chatterton, H.G. Hou, H.H.J. Geldsetzer (1991) Geochemical evidence for a catastrophic biotic event at the Frasnian/Famennian boundary in South China. *Geology* **19**, 776-779.

Wang, K, M. Attrep, C.J. Orth (1993) Global iridium anomaly, mass extinction, and redox change at the Devonian-Carboniferous boundary. *Geology* **21**, 1071-1074.

White R. and D. McKenzie (1989) Magmatism at rift zones: The generation of volcanic continential margins and flood basalts, *J. Geophys. Res.* **94**, 7685–7729.

Whitehead, J., D.A. Papanastassiou, J.G. Spray, R.A.F. Grieve, G.J. Wasserburg, (2000) Late Eocene impact ejecta: geochemical and isotopic connections with the Popigai impact structure. *Earth Planet. Sci. Lett.* **181**, 473-487.

Wieczorek M.A. and R.J. Phillips (1999) Lunar multiring basins and the cratering process. *Icarus* 139, 246-259.

Xu D.-Y., S.L. Ma, Z.F. Chai, X.Y. Mao, Y.Y. Sun, Q.W. Zhang, Z.Z. Yang(1985) Abundance variation of Iridium and trace elements at the Permian/Triassic boundary at Shangse in China. *Nature* **314**, 154-156.

Zhou M.I., J. Milpas, X.Y. Song, P.T. Robinson, A.K. Kennedy, M. Sun, G. Thompson, D. Yan, C.J. Zhong (2001) SHRIMP zircon geochronology of the Emeishan large igneous province (SW China): implications for double mass extinctions in the late Permian. 11th Goldschmidt Conference, Virginia, Abstract #3519.

Zumbo V., G. Feraud, H. Bertrand, G. Chazot (1995) $^{40}Ar/^{39}Ar$ chronology of the Tertiary magmatic activity in Southern Yemen during the early Red Sea-Aden rifting. *J. Vol. Geoth. Res.* **65**, 265-279.

Table and Figure Captions

Table 1. Indications of impact in the geologic record.

Table 2. Parameters used in in-situ and convective melt calculations.

Table 3. Melt volume totals for all stages of melt production. For stage 1, in-situ decompression melting, the in-situ melt totals are shaded if the mantle potential temperatures are high enough that a melt fraction would exist beneath the lithosphere before impact. These conditions are considered unrealistic.

Figure 1. Timeline showing dates of flood basalts, oceanic igneous provinces, extinctions, evidence for impacts, and other indicators linked with extinctions. For continental flood basalts, the total volume and duration is shown, along with the peak of eruptive flux. Similar information is presented for the oceanic igneous provinces, without eruptive peaks. Extinctions, iridium anomalies, and mineral indicators for impact are shown by date. Symbols for sea level regressions and carbon isotope excursions indicate the relative size of the event. Within the constraints of current known ages, there are possible time coincidences between extinctions and continental flood basalt eruptive peaks at the Maastrichtian, the Toarcian, Norian, Changxingian, and Guadelupian. There are possible mineral indicators for impact known at three of these extinctions: the Maastrichtian, Norian, and the Changxingian. Note in addition that there are no coincidences between extinctions and oceanic igneous provinces.

References:

Flood basalts: Columbia: Hooper and Hawkesworth, 1993; Hooper, 1997.

Yemen/Ethiopia: Venkatasan *et al.*, 1993; Zumbo *et al.*, 1995; Baker *et al.*, 1996;Chernet *et al.*, 1998.

Brito-Arctic: Mussett, 1986; Meighan *et al.*, 1988; Upton *et al.*, 1995; Pearson *et al.*, 1996.

Deccan: Courtillot, 1990; Venkatasan *et al.*, 1993; Baksi, 1994; Ray and Pande, 1999.

Madagascar: Storey *et al.*, 1995; Torsvik *et al.*, 1998.

Rajmahal: Pringle, 1994; Baksi, 1995.

Parana/Etendeka: Turner *et al.*, 1994; Stewart *et al.*, 1996; Renne *et al.*, 1996.

Karoo/Ferrar: Minor and Mukasa, 1997; Duncan *et al.*, 1997.

CAMP: Deckert *et al.*, 1997; Marzoli *et al.*, 2000; Hames *et al.*, 2000.

Siberia: Renne and Basu, 1991; Dalrymple *et al.*, 1995; Renne, 1995; Renne *et al.*, 1995; Kamo *et al.*, 1996; Venkatasan *et al.*, 1997; Bowring *et al.*, 1998.

Emeishan: Zhou *et al.*, 2001.

Extinctions: Raup and Sepkoski, 1986; Stothers, 1993; Fowell *et al.*, 1994; Sepkoski, 1994; Stanley and Yang, 1994; Renne *et al.*, 1995; Bowring *et al.*, 1998; Katz *et al.*, 1999; Hames *et al.*, 2000; Palfy and Smith, 2000.

Oceanic igneous provinces: Coffin and Eldholm, 1994; Sinton *et al.*, 1998.

Carbon isotope excursions: Hsu and McKenzie, 1990; Wang *et al.*, 1991; Barrera, 1994; Holser *et al.*, 1995; Vonhof *et al.*, 2000.

Iridium anomalies: Hsu *et al.*, 1985; Xu, 1985; Orth *et al.*, 1990; Montanari *et al.*, 1993; Wang *et al.*, 1993; Grieve, 1997; Kyte, 1988.

Impact indicators: Basu *et al.*, 1985; Kyte, 1988; Bice *et al.*, 1992; Grieve and Shoemaker, 1994; Rampino and Haggerty, 1996; Grieve, 1997; Becker *et al.*, 2001; Kaiho *et al.*, 2001.

Sea level regressions: Digby and Goodfellow, 1990; Hallam, 1992.

Figure 2. Schematic description of melt production by giant impact. Each image shows a cross-section through the moon from the surface to the cumulate mantle, and from the axis of impact

on the left to an arbitrary distance on the left. The melt-producing steps modeled in this study are: 1. In-situ decompression melting following crater excavation, and 2. Adiabatic decompression melting in convective currents under a lithospheric dome.

Figure 3. Thermal and compositional model used in melt volume calculations for both in-situ decompression and convective melting. For in-situ decompression melting, lithospheric thicknesses of 50, 75, 100, and 125 km are also used, with mantle potential temperatures of 1250, 1300, and 1350 °C. In numerical modeling of convective melt under the crater, lithospheric thicknesses of 50, 100, and 150 km are used.

Figure 4. Model of crater profiles used in melt modeling, showing the radius of excavation R, the radius at which stratigraphy is turned 90° (R_{st}), the radius of impactor penetration (R_p), the depth of excavation (d_{ex}), and the depth of melting (d_m). Adapted from O'Keefe and Ahrens (1999, 1993) and Cintala and Grieve (1998). D_C, the crater profile given by Eq. 1, is shown in the bold line on the left side of the diagram.

Figure 5. The process of in-situ decompression melting. Excavation of the crater leaves the geotherm in place, but moves the solidus deeper into the Earth because of depressurization in the column under the excavated crater (arrow at top). The movement of the solidus creates a larger melting interval between the solidus and geotherm. Mass defecit in the crater area is shown as an excavated crater for simplicity, but is likely to be a combination of excavated crater with lithospheric dome.

Figure 6. Comparison of model results with terrestrial flood basalt provinces. Total melt production for all stages of modeling are given in diamonds. Total volumes and durations of terrestrial flood basalts are given in circles (references as in Figure 1). Provinces that are not associated with complete rifting are outlined in black. The melt production from craters with 300 km excavation radii fits the eruptive volumes and durations found at the Siberian and Deccan provinces. Models in which later convective melting is significant fit provinces with longer eruptive histories, such as the Columbia.

Table 1. Indications of impact in the geologic record

Location	Age	Error (±)	Type	Suspected crater	Reference
Austral-Asian strewn field	0.71	0.10	tektites	unknown	Grieve and Shoemaker, 1994; Kyte, 1988
Darwin	0.74	0.04	glass spherules	unknown	Grieve and Shoemaker, 1994
Guatemala	0.8		tektites	unknown	Grieve, 1997
Ivory Coast	1.07		tektites	Bosumtwi	Gentner *et al.*, 1970
Urengoite (Russian)	>1		tektites		Grieve and Shoemaker, 1994
N. Pacific	2.2		tektites	unknown	Grieve, 1997
Moldavite	14.7	0.70	tektites	Ries	Fleischer *et al.*, 1965
Libya	28.5	1.30	glass spherules		Grieve and Shoemaker, 1994
N. America	35.7		tektites	Chesapeake Bay	Glass *et al.*, 1986; Koeberl *et al.*, 1996
N. America	38		tektites	Chesapeake Bay	Kyte, 1988
N. America	38		clinopyroxene spherules	Chesapeake Bay	Kyte, 1988
Siberia	35.7		tektites and spherules	Popigai	Glass and Koeberl, 1999; Whitehead *et al.*, 2000
U.S. E. Coast	35		impact wave deposits	Chesapeake Bay	Grieve and Shoemaker, 1994
Italy	35.7		shocked quartz	unknown	Grieve, 1997
Haiti	65.01	0.08	tektites	Chikxulub	Grieve and Shoemaker, 1994
Global	65		tektites, shocked quartz	Chikxulub	Smit *et al.*, 1992; Grieve, 1997
India, under Deccan	Maastrichtian		shocked quartz	unknown	Basu *et al.*, 1985
Italy	200		shocked quartz	unknown	Bice *et al.*, 1992
China, Japan	251.4		fullerines with extraterrestrial component	unknown	Becker *et al.*, 2001
			sulfur	unknown	Kaiho *et al.*, 2001
Qidong, S. China	365		tektites	Lake Taihu?	Grieve and Shoemaker, 1994
Belgium	365		tektites	Charlevoix or Siljan	Grieve and Shoemaker, 1994

Table 2. Parameters used in melt volume calculations

Constants used in melt volume calculations		
s	slope of solidus	3.0 °/km
h_o	maximum crater excavation depth = 0.15R	km
R	radius of excavation of the crater	50, 100, 200, 300 km
s_o	solidus temperature at 1 atmosphere	1120°
T_p	mantle potential temperature	1250, 1300, or 1350 °C
d	lithospheric thickness	50, 75, 100, 125, or 150 km
a	slope of the adiabat	0.33 °/km
C_P	heat capacity of silicates	1256.1 J/°kg
H_f	heat of fusion of silicates	418,700 J/kg
β	frac. of melt produced per deg. above solidus	0.003 df/dT
Variables used in in-situ melt volume calculations		
z	depth, 0 at original land surface	km
r	radial distance from crater center	km
$D_C(r)$	crater excavation depth	km
$T_A(z)$	geotherm in the lithosphere	°
$T_B(z)$	geotherm in mantle	°
$T_C(z)$	solidus after crater excavation	°
z_u	where T_A and T_C cross: shallowest limit of melt region	km
z_l	where T_B and T_C cross: deepest limit of melt region	km
F	volume of melt	km^3
Constants used in numerical modeling of convection		
h	height and width of model box	500 km
ρ	reference mantle density	3300 kg/m^3
ΔT	temperature across the model box	1250, 1300 or 1350 °C
η_o	reference viscosity	10^{20} Pas
α	thermal expansivity	3×10^{-5} /°
σ_o	reference stress	1.6×10^{13} Pa
κ	thermal diffusivity	10^{-6} m^2/s
e	number of elements in model box, in each dimension	120
Ra	Rayleigh number	1.5×10^6

Table 3. Melt volumes produced in models

		Mantle T_p 1250		Mantle T_p 1300		Mantle T_p 1350				
lith thick	crater radius	In-situ Melt	Melting	In-situ Melt	Melting	In-situ Melt	Convective Melt	TOTAL Melt	Melting	Duration of melt
d	r_o	volume	column	volume	column	volume	volume	volume	column	prod.
[km]	[km]	[km^3]		[km^3]		[km^3]	[km^3]	[km^3]		[Ma]
50	50	1.1E+03	49 - 57 km	9.4E+03		1.7E+04	8.60E+03	2.59E+04		12
	100	2.2E+04	48 - 66 km	8.9E+04		1.5E+05	3.60E+04	1.90E+05		9
	200	3.9E+05	46 - 82 km	9.2E+05		1.4E+06	1.70E+05	1.62E+06		7
	300	2.0E+06	44 - 100 km	3.8E+06		5.6E+06	8.40E+05	6.44E+06		5
75	50	0		4.4E+02	75 - 76 km	7.0E+03				
	100	0		8.2E+03	73 - 84 km	7.0E+04				
	200	9.0E+04		2.5E+05	70 - 100 km	7.8E+05				
	300	5.6E+05		1.6E+06	67 - 118 km	3.4E+06				
100	50	0		0		0				
	100	0		0		6.3E+03			99 - 103 km	
	200	0		1.5E+05		1.6E+05			95 - 120 km	
	300	0		4.7E+05		1.2E+06			91 - 137 km	
125	50	0		0		0				
	100	0		0		0				
	200	0		0		0				
	300	0		0		5.0E+05			121 - 137 km	

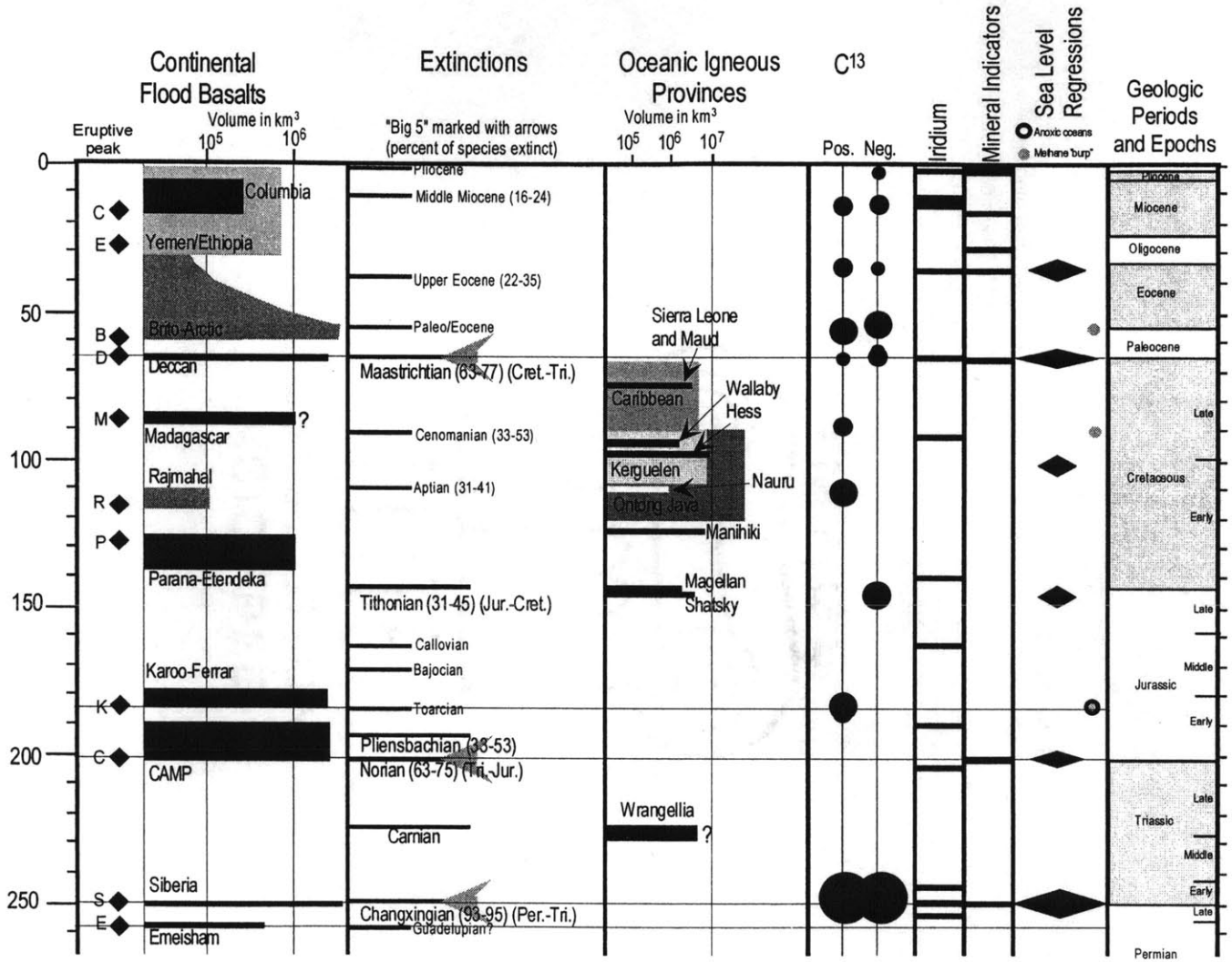
Continental Flood Basalts
Eruptive peak
Volume in km3
10^5
10^6
Extinctions
"Big 5" marked with arrows (percent of species extinct)
Oceanic Igneous Provinces
Volume in km3
10^5
10^6
10^7
C13
Pos.
Neg.
Iridium
Mineral Indicators
Sea Level Regressions
Anoxic oceans
Methane 'burp'
Geologic Periods and Epochs
0
50
100
150
200
250
C
E
B
D
M
R
P
K
C
S
E
Columbia
Yemen/Ethiopia
Brito-Arctic
Deccan
Madagascar
?
Rajmahal
Parana-Etendeka
Karoo-Ferrar
CAMP
Siberia
Emeisham
Pliocene
Middle Miocene (16-24)
Upper Eocene (22-35)
Paleo/Eocene
Maastrichtian (63-77) (Cret.-Tri.)
Cenomanian (33-53)
Aptian (31-41)
Tithonian (31-45) (Jur.-Cret.)
Callovian
Bajocian
Toarcian
Pliensbachian (33-53)
Norian (63-75) (Tri.-Jur.)
Carnian
Changxingian (93-95) (Per.-Tri.)
Guadelupian?
Sierra Leone and Maud
Caribbean
Wallaby
Hess
Kerguelen
Nauru
Ontong Java
Manihiki
Magellan
Shatsky
Wrangellia
?
Miocene
Oligocene
Eocene
Paleocene
Late
Cretaceous
Early
Late
Middle
Jurassic
Early
Late
Triassic
Middle
Early
Late
Permian

Figure 1

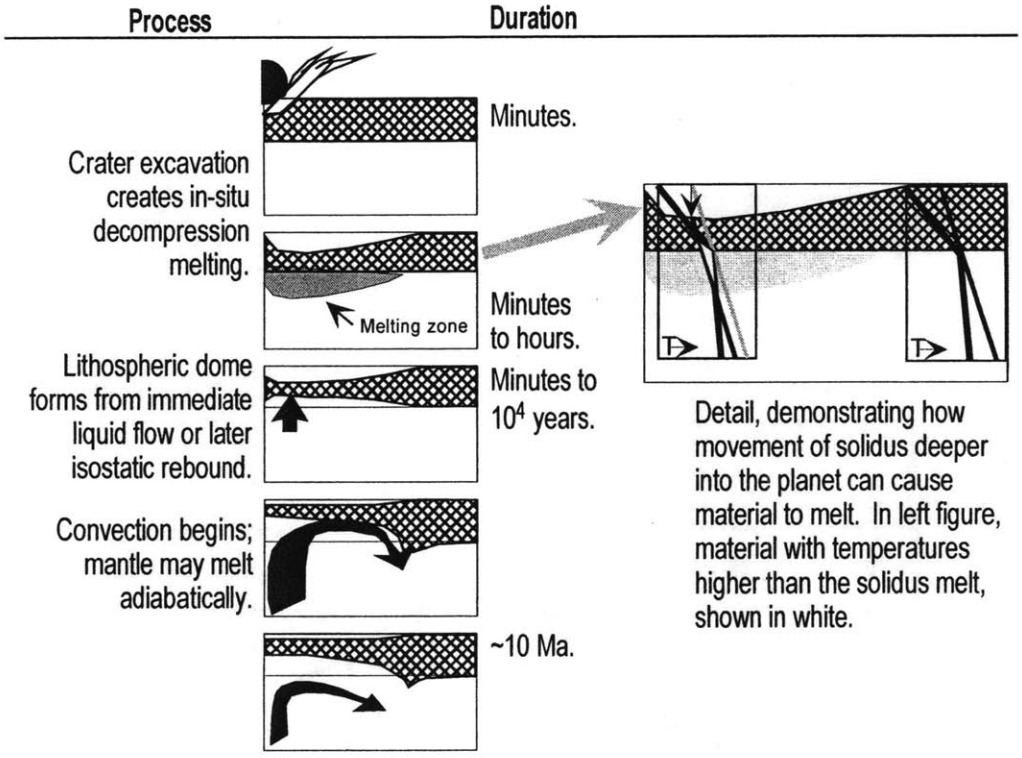
Process
Duration
Minutes.
Crater excavation creates in-situ decompression melting.
Melting zone
Minutes to hours.
Lithospheric dome forms from immediate liquid flow or later isostatic rebound.
Minutes to 10^4 years.
Convection begins; mantle may melt adiabatically.
~10 Ma.
T
T
Detail, demonstrating how movement of solidus deeper into the planet can cause material to melt. In left figure, material with temperatures higher than the solidus melt, shown in white.

Figure 2

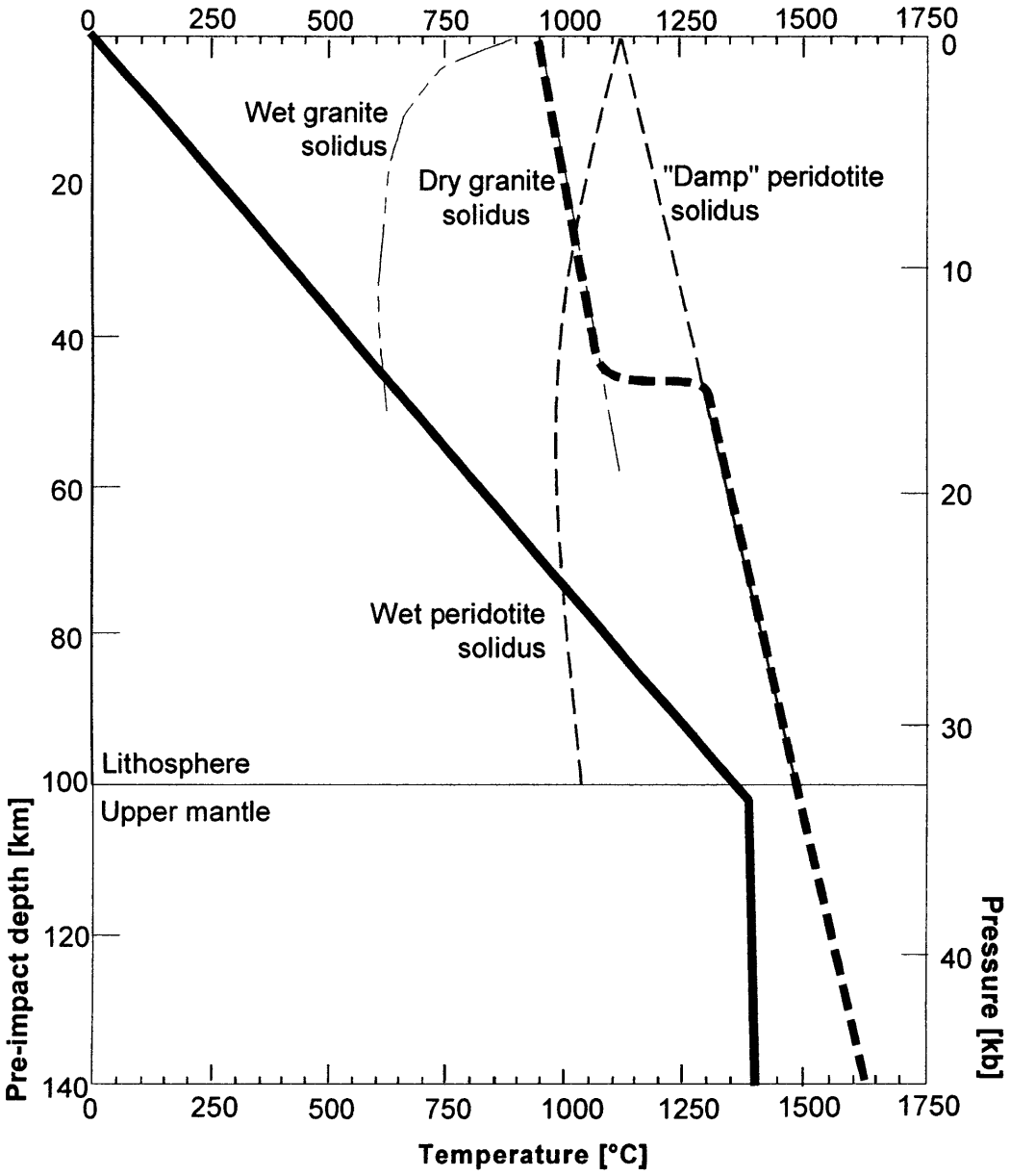
0
250
500
750
1000
1250
1500
1750
Wet granite solidus
Dry granite solidus
"Damp" peridotite solidus
Wet peridotite solidus
Lithosphere
Upper mantle
20
40
60
80
100
120
140
0
10
20
30
40
Pre-impact depth [km]
Pressure [kb]
Temperature [°C]

Figure 3

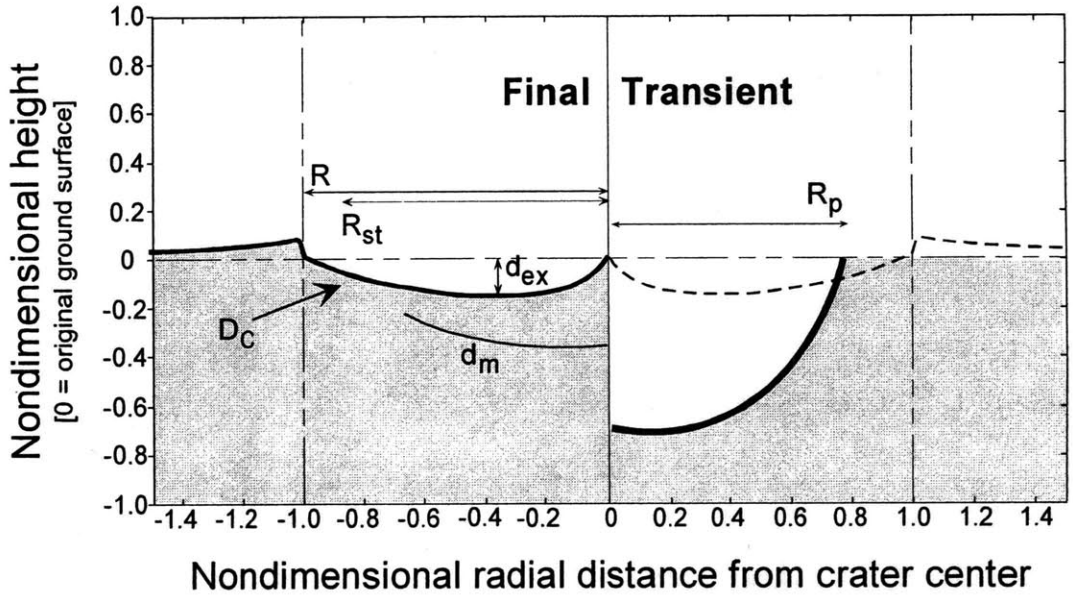
Final
Transient
R
R_{st}
R_p
d_{ex}
D_C
d_m
Nondimensional height
[0 = original ground surface]
Nondimensional radial distance from crater center
1.0
0.8
0.6
0.4
0.2
0
-0.2
-0.4
-0.6
-0.8
-1.0
-1.4 -1.2 -1.0 -0.8 -0.6 -0.4 -0.2 0 0.2 0.4 0.6 0.8 1.0 1.2 1.4

Figure 4

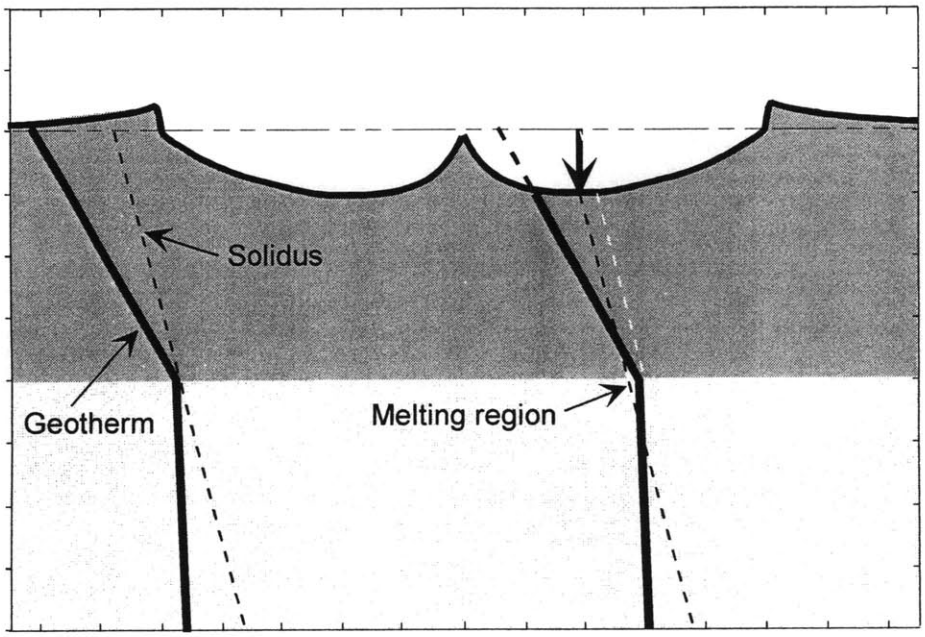

Before excavation:
no existing melt

After excavation:
Geotherm remains in place
while material is depressurized

Figure 5

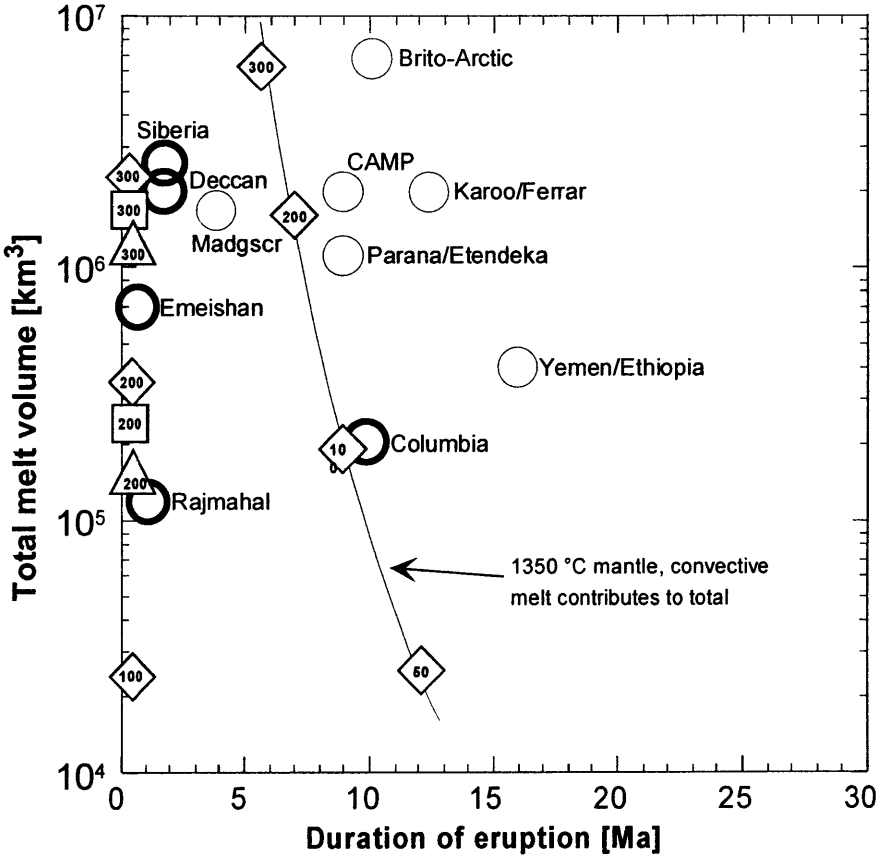
Total melt volume [km³]
Duration of eruption [Ma]
Brito-Arctic
Siberia
Deccan
CAMP
Karoo/Ferrar
Madgscr
Parana/Etendeka
Emeishan
Yemen/Ethiopia
Columbia
Rajmahal
1350 °C mantle, convective
melt contributes to total
MODELS, Mantle T_p:
50 km lithosphere, 1250 and1350 °C
75 km lithosphere, 1300 °C
100 km lithosphere, 1350 °C
Numbers in symbols denote crater excavation radii
CONTINENTAL FLOOD BASALTS:
Bold = not associated with complete rifting

Figure 6

Ch. 4. Hot, shallow mantle melting under the Cascades volcanic arc

Elkins Tanton, L.T., T.L. Grove, and J. Donnelly-Nolan, Hot shallow melting under the Cascades volcanic arc, *Geology 29*, 631-634, 2001.

Abstract

Melting occurs at progressively greater depths and higher temperatures from west to east across the Cascades volcanic arc in northern California, as demonstrated by compositional variations observed in high-alumina olivine tholeiites. The lavas studied erupted from seven vents defining a 75-km-long, east-west transect across the arc, from near Mount Shasta to east of Medicine Lake volcano. The increase in melting depth across the arc parallels modeled isotherms in the mantle wedge, and does not parallel the inferred dip of the slab. The depth of mantle melting at which the high-alumina olivine tholeiites were created is about 36 km at the western end of the transect and 66 km at the eastern end. The very high temperatures of dry melting so close to the crust indicate a transitory condition of the mantle.

Introduction

Quaternary volcanism in the Cascades arc in northern California produced lavas with a wide compositional range. Modern Mount Shasta has been built of four major eruptive episodes, from 120 ka to ca. 2 ka, and includes both dry and wet magmas (Baker *et al.*, 1994). Medicine Lake volcano has erupted throughout the past 500 k.y. (Donnelly-Nolan, 1988), producing both near-anhydrous, high-alumina olivine tholeiites and hydrous, subduction-related calc-alkaline basalts (Kinzler *et al.*, 2000).

The lavas chosen for study are near-anhydrous, Quaternary high-alumina olivine tholeiites, all younger than 500 ka, and closely associated in time and space with Mount Shasta and Medicine Lake volcanoes. Lavas analyzed are from the following seven units, from west to east: basalts of Whaleback–Deer Mountain saddle, Tennant, Giant Crater, Yellowjacket Butte, Mammoth Crater, Tionesta, and Damons Butte. The seven vent areas lie in a transect ~75 km long (Fig. 1). These vents each produced 2–5 km^3 of magma during brief eruptions (~100 yr, Champion and Donnelly-Nolan, 1994). The lavas of the seven units are aphanitic to fine-grained (some are diktytaxitic) and equi-granular to microporphyritic with < 2% olivine and plagioclase microphenocrysts 0.3 to 0.5 mm in size, and likely represent liquid compositions.

The Mg#s of the lavas range to 71 (where Mg# = [mol% MgO/(mol% MgO + mol% FeO)]). The compositional range is wide even when the data set is confined to lavas with Mg#s higher than 60: FeO in these more primitive lavas ranges from 6.8 to 10.5 wt% (Fe_2O_3 was not

measured separately), MgO from 8.0 to 10.5 wt%, SiO_2 from 47.2 to 50.5 wt%, CaO from 9.5 to 12.5 wt%, K_2O from 0.1 to 0.4, and Al_2O_3 from 16.0 to 19.5 wt%. Rb content varies from ~1 to 20 ppm, and Sr ranges from 150 to 450 ppm (Table 1).

The fractional crystallization and mantle melting models applied here require dry magmas. Preeruptive water contents have been determined from melt inclusion studies and are generally <0.25 wt% (Sisson and Layne, 1993; Anderson, 1973). A few high-alumina olivine tholeiites, however, have Sr contents near the high end of the range for Cascades high-alumina olivine tholeiites. In these lavas K_2O and Rb are low while Sr is elevated relative to that of the other lavas. Crustal contamination will lead to lower Sr abundance (Baker *et al.*, 1991) and higher K_2O and Rb abundances. At Medicine Lake, elevated Sr has been demonstrated to be a proxy for the presence of an H_2O-rich slab fluid component (see Kinzler *et al.*, 2000, Fig. 10) and suggestive of hydrous melting, not a proxy for crustal contamination.

For the purpose of calculating the conditions of formation, only the lava compositions with Mg#s > 60 are considered. Limiting the compositions to Mg# > 60 left between 7 and 60 analyses available for each unit (note that the higher SiO_2, lower Mg# samples are typically found at or near the vent, while the most primitive lavas are typically erupted late and tube-fed to distal locations; also, it is interesting that there is a general trend from higher Mg#s in the west to lower Mg#s in the east).

Depths of fractional crystallization

The effects of fractional crystallization and crustal assimilation must be removed from even the most primitive lava composition to reconstruct a model primary mantle melt, from which pressure and temperature of formation can be calculated. Our selection of seven units with primitive lavas yielded lava compositions that experienced fractional crystallization of only olivine and plagioclase. This relatively simple fractional crystallization history is used to infer a model primary magma.

Using the technique of Yang *et al.* (1996), we calculated the positions of the boundaries defining the olivine, plagioclase, and clinopyroxene primary phase volumes in the olivine-plagioclase-clinopyroxene pseudoternary. Compositions from all the vents plot along their predicted olivine and plagioclase saturation boundaries, indicating olivine plus plagioclase fractionation under near-anhydrous conditions (e.g., Fig. 2).

Grove *et al.* (1992) demonstrates that pressure variation has little effect on the position of the olivine + plagioclase saturation boundary. The major effect of increasing pressure is to move the olivine + plagioclase + clinopyroxene boundary down toward the olivine + plagioclase join at nearly constant proportions of olivine to plagioclase. We infer a maximum pressure for fractional crystallization by calculating olivine + plagioclase + clinopyroxene saturation points for each composition at a range of pressures, and finding the location of the lavas with respect to these multiple saturation points.

Because the olivine + plagioclase + clinopyroxene multiple saturation point is pressure sensitive, and the lavas have undergone only olivine + plagioclase fractionation, a maximum fractionation pressure can be estimated, but fractional crystallization at lower pressures cannot be excluded. The maximum possible fractionation pressure is given by the lava composition and the multiple saturation point that have the highest clinopyroxene content (between 8 and 10 kbar in Fig. 2 for all seven units). If the pressure at which fractional crystallization occurred were any higher, the lava compositions would cluster at the multiple saturation point and show compositional variability that indicated olivine + plagioclase + clinopyroxene·crystallization. Since the compositional variations in the lava suites indicate olivine + plagioclase fractionation, fractional crystallization must have occurred at a pressure below that where clinopyroxene was a stable phase with liquid + olivine + plagioclase. Fractional crystallization of olivine + plagioclase thus could have occurred at any pressure lower than the maximum estimated pressure.

Using this method, we calculated the highest pressure at which fractional crystallization of olivine + plagioclase could have occurred for each of the vents. The compositions from all seven units show that fractional crystallization could not have begun any deeper than 12 kbar, or about 36 km depth, which corresponds to the base of the crust in this area (Fuis *et al.*, 1987; Zucca *et al.*, 1986). Fractional crystallization of olivine + plagioclase could have occurred at shallower depths, but at no greater depth than the base of the crust.

Pressures and temperatures of mantle melting

To estimate the pressures and temperatures of mantle melting we first calculate a model primary magma, the progenitor of the high-alumina olivine tholeiites from each vent. Using the most primitive composition from each unit (Table 1), we added equilibrium olivine and plagioclase to the lava composition in the proportion necessary to keep the liquid on the olivine + plagioclase

cosaturation boundary. These proportions are predicted in the Yang *et al.* (1996) model. For all the vents, the predicted ratio (Yang *et al.*, 1996) was close to 71 wt% plagioclase and 29 wt% olivine. The olivine and plagioclase are added in 2% increments at the 71:29 ratio, recalculating the equilibrium composition after each increment, until the resulting magma is in equilibrium with mantle olivine having a forsterite component of 89 mol%, approximately that of the mantle. This is the model primary magma. The compositions required addition of from 4 to 35 wt% olivine + plagioclase to bring them into equilibrium with mantle olivine.

The assumption that these liquids were saturated with only olivine + plagioclase is based on three lines of reasoning. 1) All of the high-alumina olivine tholeiites that have been examined show compositional and petrographic evidence for olivine + plagioclase saturation. 2) We explored models that assume that the primitive magmas had just reached olivine + plagioclase saturation, and prior crystallization involved only olivine. When olivine alone is added to produce a liquid that is in equilibrium with forsterite 89 mantle olivine, the model primary liquid compositions yield pressure estimates at crustal, not mantle, depths, and their compositions are not similar to the primary magma compositions predicted by the Kinzler and Grove (1992) model. 3) The addition of the phases that are present in the primitive lavas (olivine + plagioclase) is sufficient to bring the liquid to a composition in equilibrium with a mantle peridotite residue.

Using the algorithm of Kinzler and Grove (1992) for spinel-lherzolite melting and the compositions of the model primary magmas, we calculated pressures and temperatures of mantle melting. There is an increase in maximum calculated pressure from west to east across the arc corresponding to nearly a doubling in depth of the origin of the magma, from 12 kbar (about 36 km depth) in the west to 22 kbar (about 66 km depth) in the east. Temperatures likewise increase across the arc, from 1300 °C in the west to 1450 °C in the east (Fig. 3). Bartels *et al.* (1991) found, through phase equilibrium experiments, that a high-alumina olivine basalt from Giant Crater is in equilibrium with spinel lherzolite at 1290 °C and 11 kbar, in agreement with our results (see also Bacon *et al.*, 1997).

The Kinzler and Grove (1992) model is calibrated for dry melting. While we chose the most primitive, driest magmas, results for two of the samples indicated the influence of fluid as the analysis proceeded: the basalts of Tennant and Yellowjacket Butte. The parental magmas from

these lava flows that were used for the model primary melt calculation have elevated Sr values of ~350 ppm. These elevated Sr values strongly suggest a slab fluid component. The Kinzler and Grove (1992) temperature algorithm returns anomalously high temperatures for the model primary magmas of these slightly hydrous compositions. These two vents are shown with gray symbols in Figures 3 and 4 to differentiate them from the other, near-anhydrous compositions.

Implications for mantle corner flow

Although the pressures of mantle melting increase across the arc from west to east, they do not conform to the dip of the slab as inferred tomographically by Harris *et al.* (1991). The descending slab is ~100 km beneath Mount Shasta and 200 km beneath Medicine Lake volcano, and so falls 100 km deeper over the distance of the transect. The depth of mantle melting at which the high-alumina olivine tholeiites were created, by comparison, is ~36 km at the western edge of the transect and 66 km at the eastern edge, and so has descended only 30 km across the transect.

The increase in the pressure of mantle melting parallels the corner flow lines in the mantle wedge calculated by Furukawa (1993). The temperatures of mantle melting, however, are anomalously high for their proximity to the crust (Figs. 3 and 4). These results imply that magma between 1300–1450 °C is entering the lower crust, and that mantle material at these temperatures is passing beneath it.

If mantle at this temperature remained in steady-state contact with the lithosphere at 36 km, then within 1 Ma the bottom of the crust would have melted upward ~6 km, depending on composition (for example, Mareschal and Bergantz, 1990). Mantle above 1300 °C and 36 km should, moreover, be partially melted. The predicted crustal melt volumes indicated (6–7 km^3 per square km on the surface) are not seen on the surface, nor inferred from seismic data (Zucca *et al.*, 1986). We are forced to conclude, therefore, that the high-temperature mantle is in transient contact with the crust.

Baker *et al.* (1991) show that more than 50 % of the Giant Crater series lavas were produced by a combination of processes whereby mantle melts intrude the shallow crust, assimilate crustal material, and mix with previous injections in variable amounts. The Giant Crater lava field preserves 6 distinctive eruptive episodes, and each successive eruption contains less crustal contamination. The last eruptive phase is a near-pristine near-primary mantle melt that does not

contain a crustal component. The Giant Crater lavas were erupted ~10,000 years before present over a time span of ~30 years (Champion and Donnelly-Nolan, 1994). The eruptive flux was sustained over a time that allowed crustally contaminated melts to be cleared out from the magma plumbing system and primitive high-alumina olivine tholeiites to be delivered to the surface. After the Giant Crater eruption, Medicine Lake volcano experienced a 6,000 year gap in magmatic activity (Donnelly-Nolan, 1988). Although we do not have a precise time chronology for all seven eruptive units it is likely that they also represent short-lived events separated by long time intervals. Therefore, magma supply to the Mt. Shasta – Medicine Lake region has been episodic and the persistence of hot mantle near the base of the crust should be viewed as a transitory phenomenon punctuated by long periods of quiescence accompanied by cooling of shallow mantle.

Conclusions

Analysis of the most primitive, near-anhydrous, high-alumina olivine tholeiites erupted along a transect across the Cascades volcanic arc, northern California, shows that the magmas underwent fractional crystallization of olivine + plagioclase no deeper than the base of the crust, and originated from mantle melts at 36 to 66 km depth and 1300 to 1450 °C, increasing from west to east across the arc. Although the depths of segregation of mantle melts increase from west to east across the arc, and temperatures of origin also rise commensurably, the increase of depth does not parallel the slab dip. Rather, the increase in depth of origin parallels modeled mantle corner flow lines. To match eruptive cycles and avoid creation of questionably high volumes of crustal melt, these high temperatures must be transitory at the base of the crust.

Acknowledgements

The authors thank Fred Anderson, Charlie Bacon, and Brad Hager for helpful conversations and comments, and George Bergantz and Paul Hess for thoughtful reviews. This work was supported by the National Science Foundation and by a National Defense Science and Engineering Graduate Fellowship.

References

Anderson, A.T., Jr., 1973, The before-eruption water content of some high-alumina magmas: Bulletin of Volcanology v. 37, p. 530-552.

Bacon, C.R., Bruggman, P.E., Christiansen, R.L., Clynne, M.A., Donnelly-Nolan, J.M., and Hildreth, W., 1997, Primitive magmas at five cascades volcanic fields: Melts from hot, heterogeneous sub-arc mantle: Canadian Mineralogist v. 35, p. 397–423.

Baker, M.B., Grove, T.L., Kinzler, R.J., Donnelly-Nolan, J.M., and Wandless, G.A., 1991, Origin of compositional zonation (high-alumina basalt to basaltic andesite) in the Giant Crater lava field, Medicine Lake volcano, northern California: Journal of Geophysical Research v. 96, p. 21,819-21,842.

Baker, M.B., Grove, T.L., and Price, R., 1994, Primitive basalts and andesites from the Mt. Shasta region,. N. California: products of varying melt fraction and water content: Contributions to Mineralogy and Petrology, v. 118, p. 111-129.

Bartels , K.S., Kinzler, R.J., and Grove, T.L., 1991, High pressure phase relations of primitive high-alumina basalts from Medicine Lake volcano, northern California: Contributions to Mineralogy and Petrology, v. 108, p. 253–270.

Blakely, R.J., Christiansen, R.L., Guffanti, M., Wells, R.E., Donnelly-Nolan, J.M., Patrick Muffler, L.J., Clynne, M.A., and Smith, J.G., 1997, Gravity anomalies, Quaternary vents, and Quarternary faults in the southern Cascade Range, Oregon and California: Implications for arc and backarc evolution: Journal of Geophysical Research, v. 102, p. 22,513-22,527.

Champion, D.E., and Donnelly-Nolan, J.M., 1994, Duration of eruption at the Giant Crater lava field, Medicine Lake volcano, California, based on paleomagnetic secular variation: Journal of Geophysical Research, v. 99, p. 15,595-15,604.

Donnelly-Nolan, J.M., 1988, A magmatic model of Medicine Lake volcano, California: Journal of Geophysical Research, v. 93, p. 4412-4420.

Furukawa, Y., 1993, Magmatic processes under arcs and formation of the volcanic front: Journal of Geophysical Research, v. 98, p. 8309-8319.

Fuis, G.S., Zucca, J.J., Mooney, W.D., and Milkereit, B., 1987, A geologic interpretation of seismic-refraction results in northeastern California: Geological Society of America Bulletin, v. 98, p. 53–65.

Grove, T.L., Kinzler, R.J., and Bryan, W.B., 1992, Fractionation of mid-ocean ridge basalt (MORB), *in* Morgan J.P., Blackman, D.K. and Sinton, J.M. eds., Mantle Flow and Melt Generation at Mid-Ocean Ridges: Geophysical Monograph 71, American Geophysical Union, Washington, D.C., p. 281 – 310.

Harris, R.A., Iyer, H.M., and Dawson, P.B., 1991, Imaging the Juan de Fuca plate beneath southern Oregon using teleseismic P-wave residuals: Journal of Geophysical Research, v. 96, p. 19,879–19,889.

Kinzler, R.J., Donnelly-Nolan, J.M., and Grove, T.L., 2000, Late Holocene hydrous mafic magmatism at the Paint Pot Crater and Callahan flows, Medicine Lake Volcano, N. California and the influence of H_2O in the generation of silicic magmas: Contributions to Mineralogy and Petrology, v. 138, p. 1–16.

Kinzler, R.J., and Grove, T.L., 1992, Primary magmas of mid-ocean ridge basalts 1. Experiments and methods: Journal of Geophysical Research, v.97, p. 6885–6906.

Mareschal, J.-C., and Bergantz, G., 1990, Constraints on thermal models of the Basin and Range province: Tectonophysics, v. 174, p. 137–146.

Sisson, T.W. and Layne, G.D., 1993, H_2O in basalt and basaltic andesite glass inclusions from four subduction-related volcanoes: Earth and Planetary Science Letters, v. 117, p. 619-635.

Zucca, J.J., Fuis, G.S., Milkereit, B., Mooney, W.D., and Catchings, R.D., 1986, Crustal structure of northeastern California: Journal of Geophysical Research, v. 9, p. 7359–7382.

Yang, H-J., Kinzler, R.J., and Grove, T.L., 1996, Experiments and models of anhydrous, basaltic olivine-plagioclase-augite saturated melts from 0.001 to 10 kbar: Contributions to Mineralogy and Petrology, v. 124, p. 1–18.

Table and Figure Captions

Table 1. Compositions used from each basalt unit. Analysis of whole rocks was done at the U.S. Geological Survey laboratories at Lakewood, Co and Menlo Park, CA. Oxides have been recalculated to 100 wt%; elements are in ppm.

Figure 1. Study area. Areas in Cascades arc with vents younger than 2 Ma are shaded. Transect from this paper is marked with darker rectangle (after Blakely *et al.*, 1997, plate 2.).

Figure 2. Magnified corner of pseudo-ternary diagram of olivine-plagioclase-clinopyroxene, with data from Tionesta. Three cosaturation boundaries are shown, with locations for points of multiple saturation at 1 atm, 4, 8, and 10 kbar. These lavas cocrystallized olivine and plagioclase no deeper than 10 kbar, or ~33 km.

Figure 3. Temperatures and pressures of mantle melting for seven basalt units, shown with west on left. Tennant and Yellowjacket Butte are gray because we believe their results are anomalous due to addition of slab fluid. Temperature is shown with hachured symbols; pressure and depth are shown with solid symbols. Kinzler and Grove (1992) demonstrated that these algorithms have a pressure error of ±2.5 kbar and a temperature error of ±25 °C, as shown by the error bars.

Figure 4. Cross section across arc. Position of slab is from Harris *et al.* (1991) and thickness of crust is from Zucca *et al.* (1986). Tennant and Yellowjacket Butte are gray because we believe their results are anomalous due to addition of slab fluid. Squares show maximum depth of fractionation of olivine and plagioclase, and solid circles show mantle melting depth.

Table 1. Compositional data from each unit.

Basalt Unit	Sample	Mg#	SiO_2	Al_2O_3	FeO	MgO	CaO	Na_2O	K_2O	TiO_2	P_2O_5	MnO	Rb	Sr	Y	Zr	Nb	Ba	Ni	Cu	Zn	Cr
Whaleback–Deer Mtn	83-43	70.1	50.70	17.70	7.06	9.30	10.72	3.06	0.28	1.06	0.11	0.00										
Tennant	1634	64.3	48.31	18.76	9.02	9.13	10.89	2.61	0.13	0.89	0.10	0.16	9	354	29	74	5	121	136	65	65	185
Giant Crater	82-72f	69.6	47.69	18.54	8.20	10.52	12.02	2.16	0.07	0.59	0.06	0.15	1	180	17	48	2	29	245	135	44	180
Mammoth Crater	840M	66.4	48.65	18.02	8.65	9.61	11.21	2.66	0.16	0.77	0.10	0.16	2	268	20	69	2	79	159	95	53	225
Yellowjacket Butte	1788M	65.3	50.39	18.48	7.81	8.23	10.60	2.83	0.43	0.89	0.18	0.15	9	390	20	92	8	250	110	84	54	220
Tionesta	1629	67.0	48.16	18.26	8.71	9.92	11.44	2.47	0.10	0.72	0.06	0.15	0	217	18	58	0	80	212	97	58	177
Damons Butte	1630	62.4	47.83	17.89	9.68	8.99	11.25	2.76	0.22	1.07	0.14	0.17	0	304	24	85	7	115	147	114	67	164

Note: Units are listed from west to east.

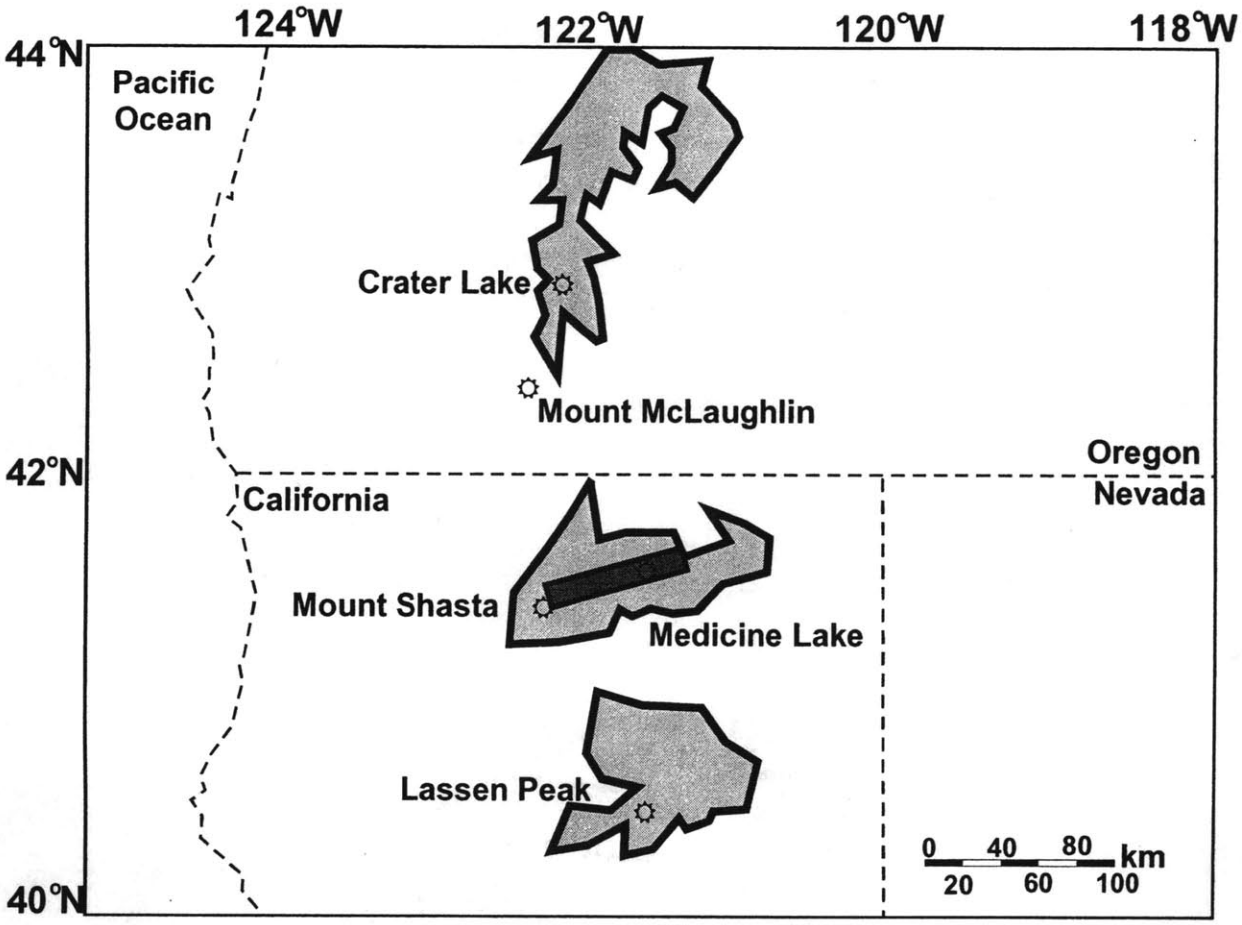
124°W
122°W
120°W
118°W
44°N
42°N
40°N
Pacific Ocean
Crater Lake
Mount McLaughlin
Oregon
Nevada
California
Mount Shasta
Medicine Lake
Lassen Peak
0 40 80 km
20 60 100

Figure 1

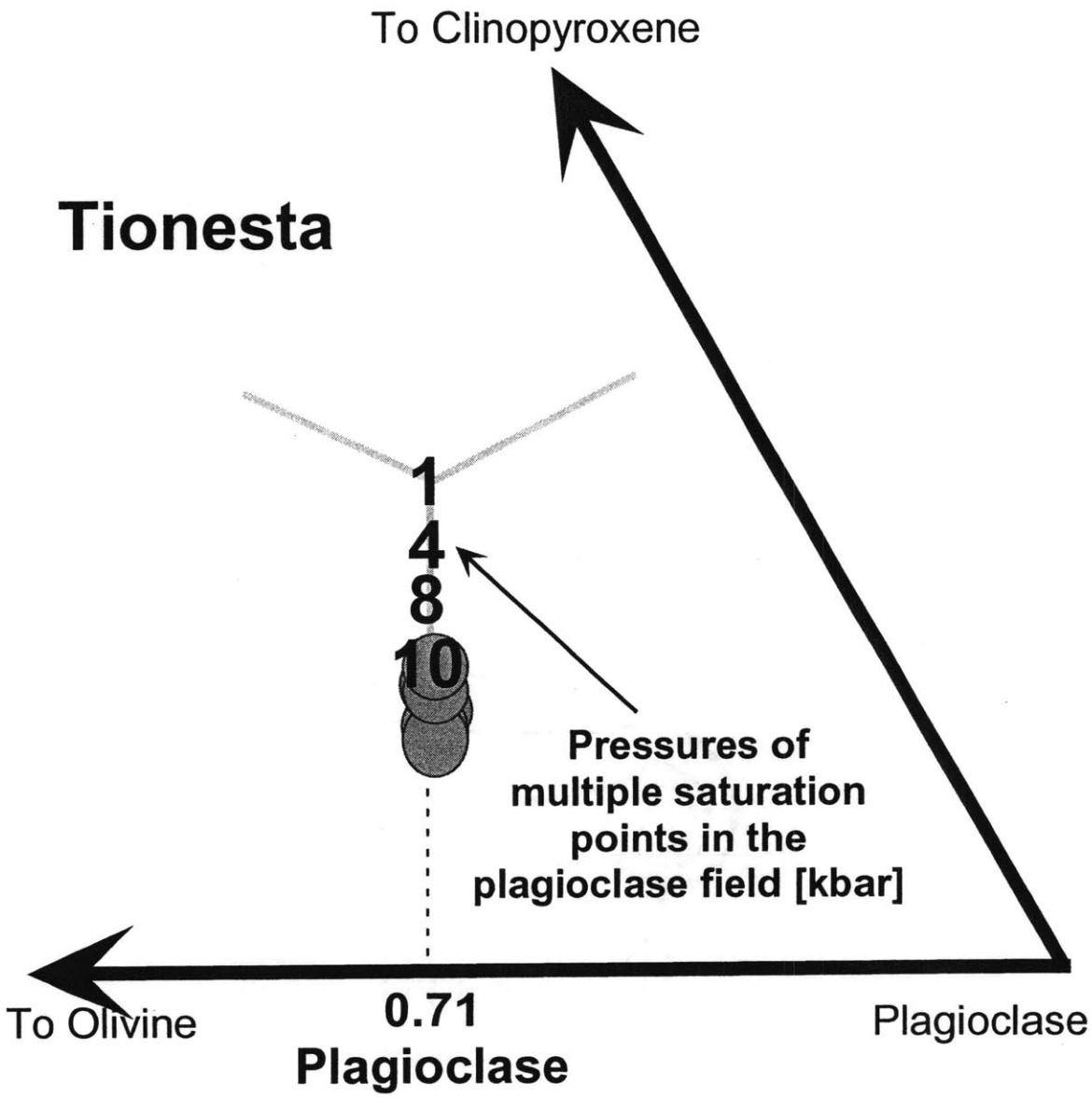
To Clinopyroxene
Tionesta
1
4
8
10
Pressures of multiple saturation points in the plagioclase field [kbar]
To Olivine
0.71
Plagioclase
Plagioclase

Figure 2

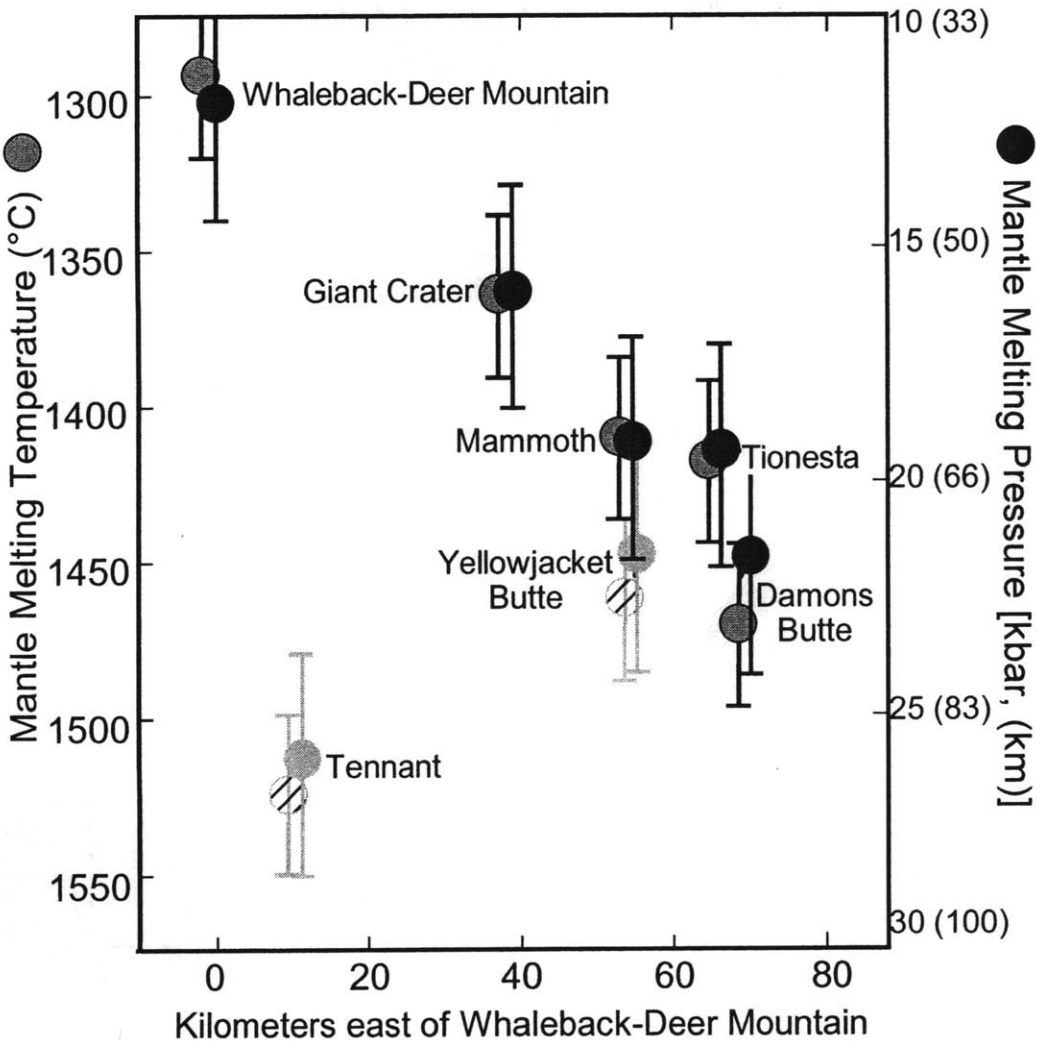
Whaleback-Deer Mountain
Giant Crater
Mammoth
Tionesta
Yellowjacket Butte
Damons Butte
Tennant
1300
1350
1400
1450
1500
1550
Mantle Melting Temperature (°C)
10 (33)
15 (50)
20 (66)
25 (83)
30 (100)
Mantle Melting Pressure [kbar, (km)]
0
20
40
60
80
Kilometers east of Whaleback-Deer Mountain

Figure 3

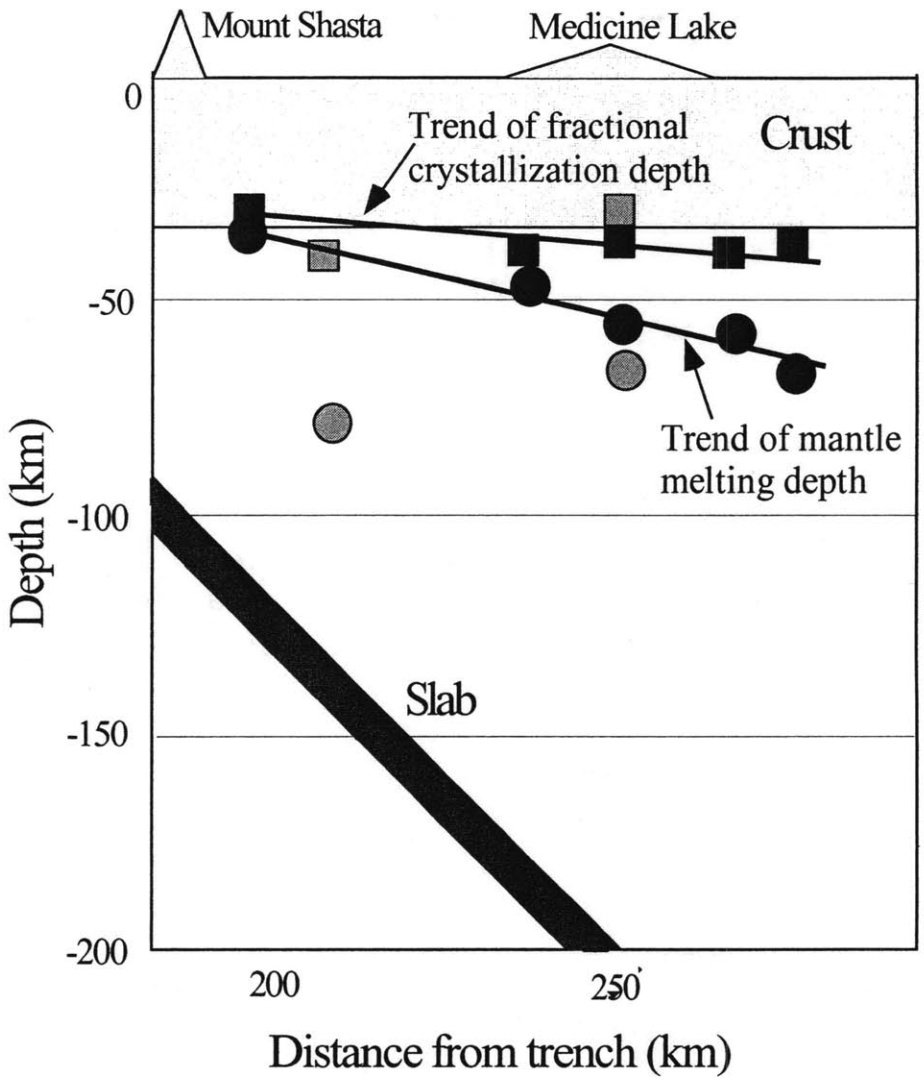
Mount Shasta
Medicine Lake
0
-50
-100
-150
-200
Depth (km)
Trend of fractional crystallization depth
Crust
Trend of mantle melting depth
Slab
200
250
Distance from trench (km)

Figure 4

Ch. 5. Origin of lunar ultramafic green glasses: Constraints from phase equilibrium studies

Elkins, L.T., T.L. Grove, J. Delano, V. Fernandez, Origin of lunar ultramafic green glasses: Constraints from phase equilibrium studies, *Geochimica et Cosmochimica Acta 64*, 2339-2350, 2000.

Abstract

Phase equilibria experiments on an Apollo 14B green glass composition are used to develop a petrogenetic model for the Apollo 14B green glasses. New compositional data for the Apollo 14B green glasses are presented, which replace the original data set of Delano (1986). Near-liquidus phase relations of the 14B green glass are determined from 1.3 to 2.7 GPa and 1380 to 1570°C. The liquidus is saturated with olivine to 2.4 GPa and orthopyroxene above 2.4 GPa. A multiple saturation point with olivine and orthopyroxene occurs at 1560°C and 2.4 GPa. Crystallization on the ol + opx saturation boundary involves 40 wt% ol and 60 wt% opx, and occurs over a 140°C interval before cpx appears at a reaction boundary. Crystallization/melting models are developed to reproduce the compositional variations displayed by the Apollo 14B glasses using these phase equilibrium constraints. Fractional crystallization alone cannot account for the observed variation in the major element abundance of the Apollo 14B green glasses. Assimilation is also necessary, in particular, to fit variations in TiO_2, FeO, Na_2O and Al_2O_3. The 14B glasses show evidence of simultaneous high-Ti assimilation and fractional crystallization of olivine, followed by simultaneous KREEP assimilation and olivine fractionation. The data requires the high-Ti assimilant to be at a greater depth than the KREEP assimilant, but only constrains the total assimilation/fractional crystallization process to occur between approximately 2.3 and 0.5 GPa. Assimilation of a high-Ti cumulate within this depth range is consistent with an overturn/hybrid mantle remelting model. Highlands crust assimilation is precluded for the Apollo 14B green glasses.

Introduction

Lunar ultramafic glasses show a tremendous compositional variability, and understanding their formation mechanisms will place boundary conditions on both the early thermal history and chemical structure of the moon, from about 4.3 to 4.5 Ga, when the magma ocean cooled and solidified to create differentiated chemical reservoirs. The ultramafic glasses were produced by remelting of these reservoirs during a later period, 3.3 to 3.5 Ga, when the magmas erupted (e.g. Delano, 1986; Papike et al, 1998).

There are currently two models for the origin of the ultramafic glasses. Ringwood and Kesson (1976) and Hess and Parmentier (1995) suggest that between 4.6 and 4.4 Ga an initially molten moon differentiated into a layered cumulate, of which approximately the last 5% consisted of dense high-Ti compositions and a final residual liquid, the "ur-KREEP", all of which solidified high in the cumulate pile. The high density of the Ti-rich cumulates caused them to sink and

overturned the cumulate pile into density-stratified layers. During a later episode, a hybrid source region at 400 to 500 km depth consisting of a mixture of high-Ti cumulates plus ol + opx cumulates (or, alternatively, primitive mantle materials) were remelted to produce high-Ti ultramafic magmas. This model could produce the low-Ti glass magmas, but its limitations for producing the very high- TiO_2 ultramafic glasses have been discussed (Circone and Agee, 1996; Wagner and Grove, 1997).

An alternative formation model calls on a primitive, low-Ti ultramafic magma, such as a green glass generated by deep melting, to rise from the deep lunar interior and assimilate layered cumulates at shallower depths to create the compositional variability observed in the glasses. This model was proposed by Hubbard and Minear (1975), and has since been supported by ilmenite and diopside dissolution experiments showing that black glasses can be made from shallow assimilation by a green glass composition parent magma. This work focuses on the compositional variability displayed in Apollo 14 green glasses. These glasses were chosen for study because they are among the most primitive green glasses. The results are consistent with the production of the compositional variation observed in the Apollo 14B green glasses at elevated pressure by fractional crystallization of olivine combined with assimilation of both high-Ti lunar magma ocean cumulates and a KREEP component.

Experimental and analytic techniques

Electron Microprobe Re-analysis of the Apollo 14B Green Glasses

The compositions of the Apollo 14B green glasses were first reported in Delano (1986). A re-analysis of the glass compositions is presented here. The Apollo 14B green glasses were analyzed using a JEOL 733 Superprobe at Rensselaer Polytechnic Institute, Troy, New York. The analytical method used was modified after Hanson *et al.* (1996). Glass analyses were done with a 15 keV, approximately 70 nA beam current of approximately 10 micron diameter. The oxide components SiO_2, Al_2O_3, FeO, MgO, CaO, TiO_2, Cr_2O_3, MnO, Na_2O, and K_2O were measured.

Each glass spot analysis was divided into three sequential measurement stages. Within each stage five elements were measured, one by each of the probe's five spectrometers. In the first stage Al_2O_3, TiO_2, Cr_2O_3, Na_2O, and K_2O were each measured for 550 seconds. Next, Al_2O_3,

MgO, CaO, TiO_2, and Cr_2O_3 were each measured for 300 seconds. Finally, SiO_2, Al_2O_3, FeO, MgO, and MnO were measured for 300 seconds.

Minimum detection limits and standard deviations are presented in Table 1.

Working standards were selected from within the set of Apollo 14B green glasses being analyzed. These standards were analyzed six times per working session. The percentage difference between the working standard analyses for a given day and the "true" (average) composition of these glasses was used as the correction factor for all glass data obtained that day.

Experiments on a Synthetic Analog of an Apollo 14B Composition

The near-liquidus phase relations of a synthetic analog of the Apollo 14B green glass (Delano, 1986) were determined in experiments from 1.3 to 2.7 GPa (corresponding to 260 to about 600 km depth in the moon) and at temperatures from 1380°C to 1570°C. The composition of the synthetic analog starting composition is shown in Table 2. The specific 14B green glass synthesized for these experiments is among the most primitive in this group, and was chosen because of its high Mg# (Mg# = molar [Mg/(Mg+Fe)]) and low Ti content. The synthetic analog of this glass was prepared from high-purity oxides and ground under ethyl alcohol for 6 hours. The powdered mix was then pressed into a pellet using Elvanol as a binding agent, hung on a 0.004" Pt wire, and conditioned in a one-atmosphere Deltech furnace for 24 hours at 1000°C at an oxygen fugacity corresponding to the iron-wustite buffer.

For each experiment about 10 mg of conditioned starting material was packed into a graphite crucible, capped with graphite, and welded into a Pt outer capsule. Before welding, graphite powder was placed between the crucible and the capsule at each end, to prevent any leaks through pressure-induced cracks in the crucible from touching the Pt capsule. The capsule was then fitted into an MgO sleeve and positioned in the hot spot of a graphite heater with MgO spacers, using $BaCO_3$ as the pressure medium. The experiments were performed in a 0.5 inch piston-cylinder apparatus. Pressure and temperature calibrations are described in Wagner and Grove (1997).

Runs were pressurized to 1.0 GPa, heated to 865°C at 100°C/min, pressurized to 1 to 3 GPa less than final pressure (depending on final pressure), heated to the run temperature at 50°C/min, and then brought to final pressure after equilibrating at the run temperature for an hour. The very

high Mg content of these experiments created a low-viscosity glass which is prone to growing clinopyroxene crystals upon quenching at the end of the experiment. To obtain crystal-free glass, the experiments were temperature- and pressure-quenched by shutting off the power to the furnace and simultaneously dropping the pressure on the experiment to 0.8 GPa.

The range of experimental temperatures spanned the liquidus and subliquidus phase volumes. All observed primary phases were analyzed at MIT on a JEOL 733 Superprobe, and a materials balance calculation was used to estimate phase proportions and to determine whether Fe had been lost from the experimental charge. Fe loss occurs primarily when the graphite crucible forms cracks, which act as melt conduits and allow the melt to come in contact with the Pt outer capsule.

Experimental and Analytic Results

Microprobe Analysis of the Apollo 14B Green Glasses

Thirty-one Apollo 14B green glasses were analyzed. All glasses were devoid of crystals. Analytic precision is greatly improved over the 1981 data set, and major element trends are tighter and better defined. The new analyses are shown in Table 3 and plotted in Figs. 3, 4, and 5a – f.

Experimental Results

The phase diagram for the Apollo 14B glass is shown in Fig. 1. The 44 experiments locate a multiple saturation point with olivine (ol) and orthopyroxene (opx) on the liquidus at 2.4 GPa (~560 km lunar depth) at 1560°C. Olivine is the liquidus phase from 1 atm and ~1440°C to the multiple saturation point at 2.4 GPa and 1560°C. Above the multiple saturation point orthopyroxene is the liquidus phase. The phase relations at 2.3 GPa have been determined in detail. After a brief interval of ol crystallization, ol and opx are crystallized over a temperature interval of ~120°C, where a reaction point is encountered for opx + liq = ol + sub-calcic augite (cpx). At the pressure of multiple saturation, ol and opx are crystallized over a temperature interval of ~140°C before the reaction point is encountered.

The 11 experiments (out of 44 total) that contained quench crystal-free glass, mass-balanced with the starting composition, and contained well-grown homogeneous phases, were used to calculate crystal–liquid exchange equilibria. The equilibrium olivine-melt Fe-Mg exchange coefficient,

K_D, (where $K_D = [(X_{fe}^{xtl} * X_{Mg}^{liq})/(X_{Mg}^{xtl} * X_{Fe}^{liq})]$) is 0.37. This higher K_D is approximately in agreement with the results of Kushiro and Walter (1998), who found that K_D varied primarily with composition, as a function of degree of polymerization, and not primarily with temperature or pressure. The NBO/T polymerization calculation for our composition places its K_D at the peak of the Kushiro and Walter curve, though our experimental K_Ds are slightly higher. The orthopyroxene-melt and clinopyroxene-melt KDs are both 0.36. Similar K_Ds were obtained by Chen and Lindsley (1983) on an ultramafic glass composition.

At 2.3 GPa, four experiments in the ol + opx phase volume from 1430°C and 1480°C were successful: experiments B29, B36, B37, and B44. At 2.3 GPa experiment B33 at 1550°C is in the ol + liq phase volume, as is B31 at 1520°C. The existence of these two experiments shows that, at 2.3 GPa, the bulk composition is close to the multiple saturation point. There are also three experiments at 2.3 GPa near the opx + liq = ol + sub-calcic augite (cpx) reaction point. These experiments, B32, B34, and B35, contain liq + ol + opx + cpx and range in temperature from 1400°C to 1430°C. Phases, compositions, conditions, and mass balance results for these experiments are shown in Tables 4 and 5.

The experimental data were used to calculate a liquid line of descent for fractional crystallization or melting at 2.4 GPa. At 2.4 GPa a cooling liquid of the experimental mass composition passes the liquidus directly into the liq + ol + opx phase volume. By plotting the experimental data in an ol-cpx-qtz pseudoternary projection, the experimental trend can be numerically fitted with a model fractionation path. The experimental liquids closely match the modeled liquids residual from 2% increments of fractionally crystallizing 60 wt% opx and 40 wt% ol. These phases co–crystallize until F = 0.71 (where F = fraction of liquid remaining). Continued crystallization involves the reaction point with cpx. Thus, at 2.4 GPa there is an ol + opx cotectic that ends in a reaction boundary.

The experimentally produced liquids are shown on an ol-cpx-qtz pseudoternary projection in Fig. 2. This figure shows all acceptable experiments at 2.3 GPa and the bulk starting composition. Fig. 2 also shows the 60 wt% opx plus 40 wt% ol liquid line of descent from the experimental starting material with the experiments from the opx-ol-glass phase volume.

Discussion

The Multiple Saturation Point and Other Constraints

The multiple saturation point on the liquidus of the Apollo 14B green glass in this study, 2.4 GPa and 1560°C, is the highest temperature point of multiple saturation yet found for an Apollo glass of any composition, and the second-highest pressure (the Apollo 15 red glass is multiply saturated at 2.5 GPa) (Wagner and Grove, 1997; Delano, 1980). The multiple saturation point has been postulated to represent the temperature and pressure of the liquidus assemblage from which the melt was segregated (Delano, 1986); if this is the case, then the Apollo 14B originated at 560 km depth. Hess and Parmentier (1995) suggest in their model that the lunar mantle does consist of olivine + orthopyroxene at 560 km, in agreement with our phase diagram.

Because so little is known about the early evolution of the interior of the moon, there are several potential models for the melting process which formed the parental green glasses. The parental glasses may have been formed by melting in an upwelling region, or by batch melting in a stationary hot source. These melts may be polybaric or polythermic in their origins, or both, or they may each originate from one temperature and pressure. Longhi (1992) modeled the formation of green glasses as polybaric fractional melting, similar to Kinzler and Grove's (1992) model for terrestrial MORBs. Formation by melting an ol + opx residue has also been proposed by a number of researchers (e.g. Delano, 1986; Longhi, 1992). If the Apollo 14B green glass of this study was formed by polybaric fractional melting, then the multiple saturation point simply represents a mean of melts formed at both greater and shallower depths than the 560 km multiple saturation point. As shown below, the compositional variation exhibited by the 14B green glasses does not follow that expected for fractional melting involving an ol + opx residue.

We could try to model the compositional variability as melting trends, but for reasons which should become clear we prefer the fractional crystallization and assimilation model. The phase constraints demonstrated by these experiments and the compositional data do not require that the Apollo 14B green glass parental melt was formed at the multiple saturation point, but only that the melt is available at some depth below 0.5 GPa to crystallize olivine in the ol + liquid phase volume. These results do not preclude the possibility that the glass is a result of polybaric fractional melting.

A Fractional Crystallization Model for Apollo 14B Green Glasses

Terrestrial basalts almost invariably undergo some fractional crystallization on their way to the surface from depth, and this process has been proposed to explain some trends in the lunar glasses (e.g., Delano, 1986). Because the Apollo 14B green composition chosen for experiments is saturated with ol + opx at its point of multiple saturation, this assemblage is the natural starting point for modeling fractional crystallization in these glasses.

When plotted on an ol-cpx-qtz pseudoternary the Apollo 14B green glasses do not parallel the ol + opx saturation boundary defined by the 2.3 GPa experiments (Fig. 3; also shown in an ol-cpx-plag pseudoternary in Fig. 4). The glass compositions move directly away from olivine, indicating removal of olivine as the only fractionating phase. About 14% of the bulk glass magma must be fractionated as olivine to match the observed data trend.

This result is in contradiction with the appearance of the 1981 data: when the 1981 data was plotted on the pseudoternary, the Apollo 14B glasses showed an ol + opx fractionation trend, followed by an ol alone fractionation trend. The new analyses at Rensselaer Polytechnic have significantly tightened the SiO_2 variance, and eliminated the ol + opx signature, which we must now view as an analytical artifact. Under the model created with the 1981 data, high-pressure ol + opx fractionation was constrained to have occurred deeper than 400 km in the moon, and the model was therefore in strong support of the high-Ti cumulate overturn model. The model presented here, based on the new Apollo 14B data set, constrains assimilation to have accurred between about 0.5 GPa and the point of multiple saturation, or between 100 and 560 km depth.

To model the Apollo 14B green glass data set as liquids residual from fractional crystallization or melting of olivine, a starting composition had to be chosen. It is clear that the primitive Apollo 14B glass composition used in these experiments is not the single primitive progenitor for the entire Apollo 14B green glass group. There are several glasses at approximately the same high Mg#, forming a range of major element compositions at the same Mg# and indicating, if they are derived from a single source (beyond analytic uncertainty), that the original primitive melt fraction has a higher yet Mg# and is not in the Apollo data set. This variation at the high Mg# end of the data exists for almost all the Apollo glass groups.

Our hypothesis for the origin of the Apollo 14B glasses assumes that all glasses within a group are related. As a starting point for modeling liquid lines of descent, a composition was created

by averaging the three A14B compositions at the high Mg#, blunt end of the data set. This average composition was renormalized without Cr_2O_3 and MnO (as were all the lunar data) because our model does not take into consideration these elements. This results in a slight offset between the data used in our model and the original microprobe data. This averaged starting composition has an Mg# of 63.9 and is listed in Table 2. The model trajectories, nonetheless, are not meant to perfectly describe all the data, but rather to encompass the data and describe possible processes.

All liquid lines of descent were modeled by 2% increments of crystallization, by calculating the equilibrium ol composition at each increment, using the experimentally-determined equilibrium olivine-melt Fe-Mg K_D of 0.37. The resulting liquid was then used to calculate the composition of the next increment of solid to be removed.

To match the Apollo 14B data as plotted in the ol-cpx-qtz pseudoternary (Fig. 3), the liquid line of descent is the result of 7 increments 2% olivine crystallization (a total of 14% crystallization).

The modeled crystallization path is shown for Al_2O_3, CaO, FeO, Na_2O, SiO_2, and TiO_2 vs. Mg# in Fig. 5a - f, along with the compositional variation in the Apollo 14B green glass. It is clear from the compositional trends in these variation diagrams that while olivine fractionation is required by the data in the pseudoternary projection, an additional process is required to explain the compositional variability observed in the Apollo 14B green glasses. The finding that fractional crystallization alone cannot explain the compositional variations seen is in agreement with Delano and Fernandes, 1998.

Fractionation and Assimilation Models for the Apollo 14B Green Glasses

The assimilation models

Assimilation is the next mechanism to consider. From the immediate rise in the TiO_2 abundances of the Apollo 14B glasses in Fig. 5f it is plausible that assimilation occurred along with fractional crystallization. This assimilation and fractional crystallization (AFC) model takes the existing olivine fractional crystallization model from above and adds an assimilant at each 2% increment.

Two possible assimilants must be considered. The first is KREEP, hypothetically the final dregs of the lunar magma ocean, thought to have remained just under the anorthosite crust of the moon.

The KREEP composition used is from Warren and Wasson (1979). The second is a high-Ti cumulate, which has been proposed to have been reshuffled deep into the lunar interior after differentiation. The most likely high-Ti cumulate composition is made up of clinopyroxene and ilmenite. These phases are the equilibrium solidus phases in experiments on a synthetic high-Ti cumulate. The high-Ti assimilant used in this model is 80 wt% cpx and 20 wt% ilmenite (Snyder et al, 1992). Both assimilant compositions are given in Table 2.

Both the TiO_2 and Al_2O_3 data have trends which suggest a change in assimilant composition (all trends discussed in this subsection are seen in Figs. 5a – f). To match the steep TiO_2 increase at high Mg#s the first assimilant must have been higher in Ti than KREEP. We combine the first step of olivine fractionation with assimilation of a high-Ti cpx + ilm cumulate to match the observed TiO_2 variation.

While a high-Ti assimilant is required to match the initial slope of the TiO_2 data, the high-Ti assimilant is inadequate to describe the subsequent variation in TiO_2, FeO, and Na_2O, in particular. Below an Mg# of approximately 63, the TiO_2 data levels out, FeO falls, and Al_2O_3 and Na_2O rise. All these changes are consistent with switching from a high-Ti assimilant to a KREEP assimilant. The high-Ti assimilant, for example, can only raise the FeO content of the resulting magma, never let it fall. Similarly, the high-Ti component cannot raise the Al_2O_3 and Na_2O adequately while allowing TiO_2 to rise as slowly as it does. After the first assimilation step with the high-Ti assimilant, therefore, we combine fractional crystallization of olivine with KREEP assimilation.

The AFC two-step model is then 14% fractional crystallization of olivine combined in its first 2% with a 1.6 wt% assimilation of the high-Ti cumulate, and combined thereafter with assimilation of KREEP at the same ratio of 0.8 wt% KREEP assimilated per 2.0 wt% of olivine fractionated (Fig. 5a - f and Table 6). For comparison, a path of olivine fractionation with only a KREEP assimilant is also included, to show more clearly the necessity of the high-Ti cumulate.

A concern with modeling the Apollo 14B data as described here is that two trends appear in the major element variation diagrams for FeO, Al_2O_3, and Na_2O, while the major element variation diagram for TiO_2 shows only one trend, that of AFC (Fig. 5a – f). In the TiO_2 variation diagram, the data are closely described as two line segments of differing slope, meeting at an Mg# of

about 63. It is not possible to devise an assimilation, fractional crystallization, or melting model which, at a given Mg#, creates two trends in some elements and only one in others.

In the FeO, Al_2O_3, and Na_2O variation diagrams, the trend of olivine fractionation alone is largely defined by two data points: numbers 29 and 31 as numbered in Table 3. These two data points also lie outside the general trend in the SiO_2 variation diagram, but here they do not conform to the olivine fractionation trend. We suggest that, given the high analytical precision of the new microprobe analyses, these two samples may have undergone a different process prior to eruption than did the others in the data set. Beyond this concern over the two data points, the AFC model presented here is a good fit for the Apollo 14B green glass data.

The AFC process in the moon

Two possible paths for the AFC model in P-T space are shown in Fig. 6. The point of multiple saturation is shown as the starting point. The constraints on the path from this study are: (1) all fractionation occurs within the olivine + liquid phase volume, and (2) high-Ti cumulate is assimilated before KREEP. There are no constraints from this study on the depth at which assimilation and fractional crystallization begin, but it is assumed that they are concurrent processes, that is, that the heat from fractional crystallization is required to melt the assimilant.

The KREEP assimilant is proposed to sit at the base of the anorthosite crust (e.g. Ringwood and Kesson, 1976), and since our model requires simultaneous ol fractionation and KREEP assimilation, we show this process close to the surface. At low pressure, the magma is constrained to erupt above its liquidus (the Apollo 14B glasses analyzed did not contain any crystals). Because of the shallow slope of the liquidus at low pressures, the KREEP assimilation step must have occurred at about 0.5 GPa. Had it been any shallower, the resulting magma would have had to retain all its heat to remain above its liquidus for eruption. It is physically reasonable to assume the magma ascended along an adiabat.

The high-Ti assimilation, conversely, is only constrained to have occurred between the point of multiple saturation and 0.5 GPa. The two paths shown in Fig. 6 are end-members of this possible depth range. If the high-Ti cumulate was assimilated at depths significantly below that of the KREEP assimilant, a mechanism must be found for stalling the magma's ascent and allowing it to cool and fractionate. There is no point in its ascent, until it hits the base of the

anorthosite crust, that the green glass magma is denser than its surroundings, so some other mechanism has to be called upon.

The small amount of assimilant modeled is consistent with the heat budget available for melting. In general, heat for assimilation can be provided by the heat of fusion during fractional crystallization, and by cooling of superheat in the melt. Either or both of the assimilant steps may have had superheat in addition to heat of fusion, but to arrive at the most conservative answer we assume only heat of fusion is available. The R value of this assimilation stage must therefore be below unity (where R = [wt% assimilated/wt% fractionated]). The amount of assimilant in the model was chosen to recreate the major element variation in the Apollo 14B glasses, initially without regard to R value. In all steps, however, the R value is 0.8.

Additional evidence for assimilation

The two-step AFC model is consistent with the observed major element oxide data (Fig. 5a - f), with the lunar models of Kesson and Ringwood (1976) and Shearer et al (1990), as well as with the observed REE abundances and KREEP assimilation estimates of Shearer et al (1990). Two distinct compositions of residuum have been proposed as assimilants in the literature. Kesson and Ringwood (1976) proposed that the first residuum assimilant, dense ilmenite + pyroxene - bearing cumulates, sank into the underlying cumulate pile after solidification and differentiation of the lunar mantle, leaving the less dense final residuum, the KREEP, high in the lunar interior just under the anorthosite crust.

Shearer *et al.* (1990) point out the elevated REE signature and strong negative Eu anomaly in the 14B glasses. They interpret this as the signature of KREEP assimilation, which would raise other REE abundances without raising Eu, as Eu would have been previously preferentially incorporated into the plagioclase in the anorthosite crust and thus depleted in the KREEP component. In Shearer *et al.*'s assimilation-fractional crystallization model a deep lunar mantle composition hybridized from sunken high-Ti cumulates and in situ ol + opx cumulates melts and rises into the shallow KREEP zone, where additional assimilation takes place.

Shearer *et al.* proposed a KREEP component in the Apollo 14B glasses of about 6 to 10%. Our two-step AFC model incorporates a maximum of 9.6% KREEP to match A14B major element trends, in good agreement with Shearer *et al.*'s REE model. Their least KREEP-contaminated Apollo 14B composition plots at the high Mg#, least fractionated end of the Apollo 14B

compositional variation trend. Their most KREEP-enriched composition plots at the low Mg#, most fractionated end of the A14B trend, matching our model's increasing KREEP component with decreasing Mg#.

Conclusion

Experimental investigation of the Apollo 14B green glass shows its multiple saturation point with ol + opx to be at 1560°C and 2.3 GPa (approximately 560 km depth in the moon). Based on a fit to the experimental data, the saturation boundary with ol + opx involves co–crystallization of ol and opx in the proportions 40 wt% ol and 60 wt% opx.

The compositional variation seen in the Apollo 14B green glasses cannot be explained by fractional crystallization alone, but is well fit by fractional crystallization and concurrent assimilation of cumulates. Apollo 14B green glasses require both a high-Ti cumulate and a KREEP component of assimilation to create their major element oxide trends: they are modeled by fractional crystallization of olivine with simultaneous assimilation first of high-Ti cpx + ilm cumulate, then of a KREEP component. The Apollo 14B glasses are precluded from anorthite assimilation by their negative Eu anomalies.

Acknowledgements

This research was supported by NASA grant NAG–5–4768. The authors thank J. Longhi for an exceptionally careful and thoughtful review, and A. Holzheid for her kind help with the experimental apparatus.

References

Chen H. K. and Lindsley D. H. (1983) Apollo 14 very low titanium glass: Melting experiments in iron-platinum alloy capsules. *J. Geophys Res* **88**, B335–342.

Delano J.W. (1980) Chemistry and liquidus phase relations of Apollo 15 red glass: Implications for the deep lunar interior. *Proc. 11th Lunar Planet. Sci. Conf.*, 251–288.

Delano J. W. (1986) Pristine lunar glasses: criteria, data, and implications. *Proc. 16th Lunar Planet. Sci. Conf.*, D201–D213.

Delano J. W. (1990) Buoyancy-driven melt segregation in the Earth's moon: I. Numerical results. *Proc. 20th Lunar Planet Sci. Conf.*, 3–12.

Delano J.W. and V.A. Fernandes (1998) Deep–seated magmatic processes reflected by compositional trends within Apollo 14 green glasses. *Lunar Planet. Sc. XXIX*, p. 1177–1178.

Hanson B., J. W. Delano, and D.J. Lindstrom (1996) High pressure analysis of hydrous rhyolitic glass inclusions in quartz phenocrysts using electron microprobe and INAA. *American Mineralogist* **81**, 1249-1262.

Hess P. C. and Parmentier E. M. (1995) A model for the thermal and chemical evolution of the moon's interior: Implications for the onset of mare volcanism. *Earth Planet. Sci. Lett.*, **134**, 501–514.

Hubbard N.J. and J. W. Minear (1975) A chemical and physical model for the genesis of lunar rocks: Part II Mare basalts. *Lunar Sci* .**VI**, 405–407.

Kinzler R.J. and T.L Grove (1992) Primary magmas of mid-ocean ridge basalts 2. Applications. *J. Geophys. Res.* **97**, 6907–6926.

Kushiro I. and Walter M. J. (1998) Mg–Fe partitioning between olivine and mafic–ultramafic melts. *Geophys. Res. Lett.* **25**, 2337–2340.

Longhi J. (1992) Origin of picritic green glass magmas by polybaric fractional fusion. *Proc. 22nd Lunar Planet. Sci.*, 343-353.

Papike J. J., Ryder G., and Shearer C. K. (1998) Lunar Samples. In *Planetary Materials, Reviews in Mineralogy Volume 36.* 5-1–5-224. Mineralogical Society of America.

Ringwood A. E. and Kesson S. E. (1976) A dynamic model for mare basalt petrogenesis. *Proc. 7th Lunar Sci. Conf.*, 1697–1722.

Shearer C. K., Papike J.J., Simon S. B., Galbreath K.C., Shimizu N., Yurimoto Y., and Sueno S. (1990) Ion micorprobe studies of REE and other trace elements in Apollo 14 'volcanic' glass beads and comparison to Apollo 14 mare basalts. *Geochim. Cosmochim. Acta.* **54**, 851–867.

Snyder G. A., Taylor L. A., Neal C. R. (1992) A chemical model for generating the sources of mare basalts: Combined equilibrium and fractional crystallization of the lunar magmasphere. *Geochim. Cosmochim. Acta.* **56**, 3809–3823.

Wagner T. P. and Grove T. L. (1997) Experimental constraints on the origin of lunar high-Ti ultrmafic glasses. *Geochim. Cosmochim. Acta* **61**, 1315–1327.

Warren, P.H. and J.T. Wasson (1979) The origin of KREEP. *Rev. Geophys. Space Phys.* **17**, 73-88.

Table and Figure Captions

Table 1. The ten oxides measured by electron microprobe from the Apollo 14B green glass samples, minimum detection limits in ppm, and standard deviations (1 σ) for measurements given in Table 3.

Table 2. Starting materials used in experiments and in models. Oxide values in wt%. Composition of Apollo 14B green glass synthetic analog used for experiments from Delano (1986). Clinopyroxene and ilmenite compositions from Van Orman and Grove (personal communication). KREEP composition from Warren and Wasson (1979).

Table 3. Compositions of thirty-one Apollo 14B green glasses analyzed by electron microprobe. Oxide values in wt%.

Table 4. Conditions and results of experiments on Apollo 14B green glass synthetic analog.

Phase proportions determined by multiple linear regression of analyzed phases (Table 5) against starting composition (Table 2).

Table 5. Composition of run products in experiments on Apollo 14B green glass synthetic analog. Oxide values in wt%. Reported value is average of N points, number after oxide is 1 standard deviation on the last significant digit of the oxide value.

Table 6. The AFC petrogenetic model for the Apollo 14B green glasses, involving fractional crystallization of olivine combined with two assimilants. See text for details and Figures 5a - f.

Figure 1. Phase diagram of Apollo 14B green glass synthetic analog. Experiment numbers are given. Data from unpublished experiments in addition to those from Table 4 (circled numbers).

Figure 2. Pseudoternary projection of glasses from successful Apollo 14B green glass synthetic analog experiments at 2.3 GPa, showing the calculated 40 wt% ol + 60 wt% opx saturation boundary from starting material composition.

Figure 3 Magnified ol - cpx - qtz ternary projection of Apollo 14B green glasses showing olivine fractionation trend.

Figure 4 Magnified ol - cpx - plag ternary projection of Apollo 14B green glasses showing olivine fractionation trend.

Figure 5. AFC models: Major element oxide variation diagrams for the Apollo 14B green glasses plotted against Mg#. Modeled fractionation and assimilation paths are shown: "ol frac." is a path of 14% olivine fractionation alone; "ol + KREEP" is a path of 14% ol fractionation and KREEP assimilation starting at R = 0.9 and ending at R = 0.5; "ol + 2 assim." is the preferred path discussed in the paper. The two assimilant path begins with a step of ol fractionation and high-Ti assimilation, followed by six steps of ol fractionation and KREEP assimilation. In particular the TiO_2 trends which are not described by fractionation alone or by KREEP assimilation alone are described by the two assimilant model. See Tables 2 and 6 for compositions and amounts of assimilants. The two data points discussed in the text, numbers 29 and 31, are marked.

Figure 6. Two possible paths of liquid evolution in P-T space which fit the constraints on the Apollo 14B green glasses: only olivine is fractionated; magma moves along an approximate adiabat when not cooling in situ; assimilation is simultaneous with fractionation; the high-Ti

assimilant came before the KREEP assimilant; the entire process occurred between about 2.3 and 0.5 GPa; and the magma erupted above its liquidus.

Table 1. Electron microprobe oxide measurements.

.

Oxide	Minimum Detection Limit	1 Standard Deviation (± wt%)
SiO_2	49	0.30
TiO_2	74	0.02
Al_2O_3	61	0.04
Cr_2O_3	22	0.02
FeO	73	0.20
MnO	68	0.05
MgO	31	0.06
CaO	51	0.04
Na_2O	28	0.04
K_2O	49	0.005

Table 2. Bulk compositions.

	SiO_2	TiO_2	Al_2O_3	Cr_2O_3	FeO	MnO	MgO	CaO	Na_2O	K_2O	Total	Mg#
Experimental Apollo 14B green glass starting composition	44.71	0.45	7.13	0.54	19.76	0.24	19.06	8.03	0.06	0.03	100	63.2
Apollo 14B initial liquid for modeled liquid lines of descent	45.38	0.43	7.20	0.00	19.31	0.00	19.20	8.29	0.16	0.03	100	63.9
Cpx for cumulate assimilation modeling	48.17	1.45	3.07	0.00	28.76	0.00	8.92	9.62	0.00	0.00	100	35.6
Ilm for cumulate assimilation modeling	0.05	52.13	0.51	0.00	45.30	0.00	1.65	0.36	0.00	0.00	100	6.1
Deep high-Ti assimilant 80 wt% cpx and 20 wt% ilm	38.50	11.64	2.55	0.00	32.09	0.00	7.46	7.76	0.00	0.00	100	29.3
KREEP assimilant	48.64	1.69	16.85	0.00	10.73	0.00	10.73	9.65	0.87	0.84	100	64.1

Table 3. Apollo 14B green glass compositions.

No.	Sample No.	SiO_2	TiO_2	Al_2O_3	Cr_2O_3	FeO	MnO	MgO	CaO	Na_2O	K_2O	TOT.	Mg#
1	14307, 45 #18	45.09	0.45	7.26	0.49	19.05	0.26	18.94	8.26	0.15	0.03	100.00	63.9
2	14307, 45 #40	45.41	0.71	7.55	0.50	19.18	0.27	17.47	8.70	0.18	0.04	100.00	61.9
3	14307, 45 #45	46.11	0.77	8.46	0.45	18.75	0.26	15.67	9.17	0.26	0.09	100.00	59.8
4	14307, 45 #20	45.60	0.74	8.43	0.45	18.87	0.26	16.25	9.07	0.25	0.08	100.00	60.6
5	14307, 48 #32	45.87	0.80	8.69	0.45	18.78	0.25	15.50	9.29	0.26	0.10	100.00	59.5
6	14307, 48 #52	45.06	0.53	7.31	0.50	19.15	0.26	18.60	8.38	0.17	0.04	100.00	63.4
7	14307, 48 #71	45.07	0.42	7.11	0.49	19.12	0.26	19.12	8.22	0.15	0.04	100.00	64.1
8	14307, 48 #75	45.31	0.69	7.59	0.50	19.22	0.27	17.51	8.68	0.18	0.04	100.00	61.9
9	14307, 49 #9	45.27	0.71	7.64	0.49	19.34	0.26	17.40	8.67	0.19	0.04	100.00	61.6
10	14307, 49 #38	45.12	0.72	7.65	0.50	19.46	0.27	17.38	8.68	0.19	0.04	100.00	61.4
11	14307, 49 #42AAA	44.96	0.42	7.07	0.49	19.31	0.26	19.09	8.22	0.16	0.04	100.00	63.8
12	14307, 49 #43	45.23	0.60	7.37	0.49	19.25	0.26	18.17	8.39	0.19	0.04	100.00	62.7
13	14307, 49 #48	45.08	0.59	7.30	0.49	19.27	0.25	18.43	8.38	0.17	0.04	100.00	63.0
14	14307, 49 #49	45.14	0.73	7.67	0.50	19.34	0.27	17.33	8.78	0.20	0.04	100.00	61.5
15	14307, 49 #56	45.11	0.67	7.52	0.50	19.25	0.26	17.90	8.57	0.18	0.04	100.00	62.4
16	14307, 49 #59	45.02	0.52	7.25	0.49	19.30	0.26	18.59	8.36	0.16	0.04	100.00	63.2
17	14307, 49 #77	45.21	0.39	7.16	0.48	19.16	0.26	18.78	8.31	0.20	0.05	100.00	63.6
18	14307, 49 #80	45.07	0.38	7.18	0.49	19.33	0.25	18.83	8.28	0.15	0.04	100.00	63.5
19	14307, 49 #88	45.43	0.71	8.02	0.45	19.06	0.25	17.01	8.77	0.24	0.06	100.00	61.4
20	14307, 36 #12	45.63	0.75	8.43	0.44	19.02	0.24	16.17	8.99	0.25	0.08	100.00	60.2
21	14307, 36 #19	45.20	0.73	7.64	0.49	19.32	0.26	17.37	8.74	0.19	0.04	100.00	61.6
22	14307, 36 #32	45.39	0.77	8.29	0.45	18.95	0.24	16.68	8.94	0.23	0.06	100.00	61.1
23	14307, 36 #85	45.13	0.74	7.72	0.49	19.49	0.26	17.02	8.80	0.29	0.05	100.00	60.9
24	14307, 36 #92	46.23	0.65	8.17	0.52	19.30	0.25	15.46	9.17	0.18	0.06	100.00	58.8
25	14307, 36 #102	45.14	0.77	8.09	0.49	19.33	0.25	16.85	8.83	0.21	0.04	100.00	60.8
26	14307, 41 #16	45.22	0.70	7.42	0.49	19.35	0.26	17.64	8.66	0.21	0.04	100.00	61.9
27	14307, 41 #41	45.22	0.70	7.84	0.44	19.20	0.25	17.29	8.77	0.23	0.06	100.00	61.6
28	14307, 41 #50	45.34	0.83	7.87	0.49	19.53	0.27	16.29	9.15	0.19	0.04	100.00	59.8
29	14307, 41 #88	45.20	0.71	7.48	0.48	19.38	0.27	17.54	8.72	0.18	0.04	100.00	61.7
30	14307, 41 #110	45.26	0.75	7.57	0.48	19.48	0.27	17.16	8.82	0.18	0.04	100.00	61.1
31	14307, 41 #137	44.67	0.66	7.30	0.48	19.21	0.26	18.85	8.36	0.18	0.04	100.00	63.6

Table 4. Conditions and results of experiments on Apollo 14B green glass synthetic analog.

Run	Pressure GPa	Temperature °C	Duration hours	Phases present	Proportions	Sum of sq. residuals
B-1	1.3	1450	25	gl, ol	83:17	0.2
B-3	2.8	1550	23	gl, ol, opx	94: 9: -3	0.0
B-29	2.3	1430	22	gl, ol, opx	84:10:6	2.4
B-31	2.3	1520	5	gl, ol	88:12	2.2
B-32	2.3	1420	20	gl, ol, opx, cpx	38:14:-1:49	0.0
B-33	2.3	1550	5	gl, ol	96:4	0.5
B-34	2.3	1430	5	gl, ol, opx, cpx	56:10:-3:37	0.0
B-35	2.3	1400	7	gl, ol, opx, cpx	52:17:14:17	0.2
B-36	2.3	1450	5	gl, ol, opx	78:5:17	0.4
B-37	2.3	1480	6	gl, ol, opx	80:6:14	2.5
B-44	2.3	1470	5	gl, ol, opx	73:5:22	0.5

Table 5. Phase compositions from A14B experiments.

Run #	phase	N	SiO_2	TiO_2	Al_2O_3	Cr_2O_3	FeO	MnO	MgO	CaO	Na_2O	K_2O	Total	K_Ds
B-1	glass	17	45.7[5]	0.52[2]	8.4[2]	0.56[3]	19.2[3]	0.25[3]	14.4[6]	9.5[2]	0.09[2]	0.04[1]	98.66	
	olivine	7	38.6[2]	0.01[1]	0.09[1]	0.33[2]	19.5[2]	0.18[2]	41.3[3]	0.34[2]	0.02[1]	0.00[0]	100.38	0.35
B-3	glass	13	45.4[2]	0.49[1]	7.62[7]	0.56[2]	19.5[2]	0.26[2]	17.0[2]	8.68[6]	0.06[2]	0.03[0]	99.50	
	olivine	10	39.0[4]	0.00[1]	0.10[1]	0.30[2]	17.7[1]	0.14[2]	43.2[4]	0.29[2]	0.00[0]	0.00[0]	100.76	0.36
	opx	9	55.0[5]	0.04[1]	2.1[3]	0.77[9]	10.8[1]	0.15[2]	29.6[3]	1.66[5]	0.00[0]	0.00[0]	100.24	0.32
B-29	glass	20	44.1[6]	0.66[3]	9.0[2]	0.41[1]	19.3[3]	0.29[3]	16.0[3]	10.6[1]	0.10[7]	0.04[1]	100.37	
	olivine	4	39.3[6]	0.02[2]	0.10[2]	0.19[2]	19.0[4]	0.22[2]	41.8[8]	0.34[3]	0.00[0]	0.00[0]	100.89	0.37
	opx	6	53.9[5]	0.06[1]	3.7[3]	0.86[6]	11.8[5]	0.17[2]	28.0[5]	2.5[5]	0.00[0]	0.00[0]	100.99	0.35
B-31	glass	15	43.8[3]	0.55[3]	8.8[3]	0.52[3]	20.6[3]	0.27[3]	15.8[2]	9.5[2]	0.09[8]	0.03[1]	99.93	
	olivine	6	39.3[4]	0.01[1]	0.09[1]	0.25[1]	18.8[6]	0.21[2]	42.0[7]	0.32[2]	0.00[0]	0.00[0]	100.99	0.34
B-32	glass	17	40.6[6]	1.03[5]	10.5[3]	0.24[4]	24.3[5]	0.28[2]	11.8[4]	10.5[4]	0.16[9]	0.08[1]	99.37	
	olivine	5	37.7[3]	0.03[1]	0.17[8]	0.11[2]	26.6[2]	0.28[3]	35.6[3]	0.41[1]	0.00[0]	0.00[0]	100.89	0.36
	opx	4	53.2[2]	0.14[2]	4.3[5]	1.3[2]	13.3[4]	0.20[2]	27[1]	3[1]	0.00[0]	0.00[0]	101.59	0.24
	cpx	4	50.9[5]	0.2[1]	6.3[3]	0.76[6]	14.5[2]	0.20[3]	20.3[4]	8.3[2]	0.00[0]	0.00[0]	101.47	0.35
B-33	glass	23	45.4[4]	0.44[2]	7.59[9]	0.54[2]	19.3[5]	0.24[2]	18.1[3]	8.4[2]	0.05[6]	0.03[1]	100.05	
	olivine	6	40.1[3]	0.01[1]	0.08[2]	0.24[4]	16.3[3]	0.18[2]	44.2[5]	0.25[2]	0.00[0]	0.00[0]	101.43	0.35
B-34	glass	6	43.3[8]	0.90[5]	10.4[4]	0.31[4]	21.7[2]	0.29[2]	13.5[4]	10.0[1]	0.01[4]	0.05[1]	100.46	
	olivine	5	37.8[3]	0.04[1]	0.14[1]	0.13[1]	24.7[5]	0.24[1]	36.9[5]	0.42[2]	0.00[0]	0.00[0]	100.38	0.42
	opx	6	51.9[3]	0.08[2]	6.1[5]	0.77[5]	15.0[2]	0.16[3]	24.4[3]	2.5[1]	0.00[0]	0.00[0]	100.82	0.38
	cpx	5	51.8[2]	0.10[1]	5.5[4]	0.86[3]	14.0[2]	0.19[3]	20.7[3]	7.8[2]	0.00[0]	0.00[0]	100.90	0.42
B-35	glass	3	44[2]	1.03[1]	10.2[7]	0.37[3]	20[1]	0.27[3]	11[3]	12[1]	0.00[0]	0.06[1]	98.95	
	olivine	4	37.6[1]	0.05[1]	0.18[6]	0.13[2]	26.8[6]	0.24[3]	35.4[4]	0.43[1]	0.00[0]	0.00[0]	100.77	0.40
	opx	11	51.7[4]	0.11[2]	6.4[6]	0.71[6]	15.4[4]	0.17[2]	23.4[4]	2.5[2]	0.00[0]	0.00[0]	100.32	0.35
	cpx	9	51.4[4]	0.15[3]	6.0[3]	0.72[3]	14.6[4]	0.19[2]	19.4[3]	8.5[5]	0.00[0]	0.00[0]	100.84	0.40
B-36	glass	5	43.4[9]	0.73[5]	9.1[3]	0.39[3]	19.8[4]	0.24[2]	15.2[5]	10.1[4]	0.04[5]	0.04[1]	99.03	
	olivine	5	38.2[3]	0.02[2]	0.12[2]	0.15[2]	21.5[3]	0.21[2]	38.5[3]	0.41[2]	0.00[0]	0.00[0]	99.11	0.43
	opx	6	52.6[3]	0.06[1]	4.7[4]	0.85[6]	13.0[1]	0.14[2]	25.3[2]	2.48[7]	0.00[0]	0.00[0]	99.15	0.39
B-37	glass	10	42.8[3]	0.66[3]	9.3[2]	0.39[2]	19.2[5]	0.23[2]	14.7[2]	11.1[2]	0.13[7]	0.04[1]	98.63	
	olivine	7	39.1[3]	0.02[1]	0.13[2]	0.19[2]	19.8[1]	0.20[2]	40.6[6]	0.35[2]	0.00[0]	0.00[0]	100.37	0.37
	opx	7	53.7[6]	0.05[1]	3.9[4]	0.96[9]	11.9[2]	0.14[4]	27.1[2]	2.44[9]	0.00[0]	0.00[0]	100.23	0.34
B-44	glass	15	42.7[4]	0.66[3]	9.36[9]	0.33[3]	20.5[2]	0.28[3]	14.0[4]	11.1[1]	0.11[4]	0.04[1]	99.01	
	olivine	8	37.9[5]	0.04[1]	0.11[1]	0.22[2]	20.0[3]	0.22[2]	41.9[6]	0.40[1]	0.00[0]	0.00[0]	100.91	0.37
	opx	7	53.6[6]	0.06[1]	4.0[5]	1.0[2]	12.6[3]	0.17[1]	26.9[4]	2.51[7]	0.01[1]	0.00[0]	100.65	0.34

Table 6. The AFC petrogenetic model for the Apollo 14B green glasses.

	Step 1		Steps 2 – 7	
Fractionating assemblage	ol:	100%	ol:	100%
% fractionation	ol:	2.0%	ol:	12.0%
% assimilation	high-Ti:	1.6%	KREEP:	9.6%
R		0.8		0.8

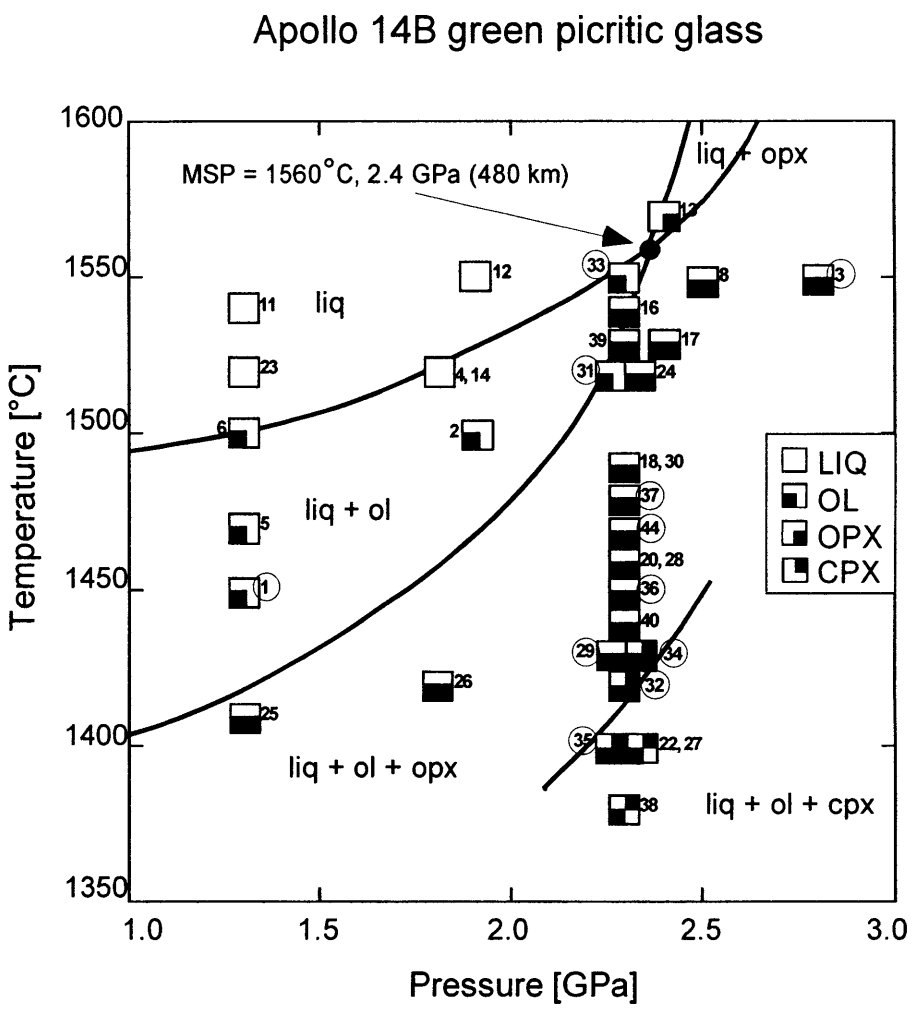
Apollo 14B green picritic glass
MSP = 1560°C, 2.4 GPa (480 km)
liq + opx
liq
liq + ol
liq + ol + opx
liq + ol + cpx
LIQ
OL
OPX
CPX
Temperature [°C]
Pressure [GPa]
1600
1550
1500
1450
1400
1350
1.0
1.5
2.0
2.5
3.0

Figure 1

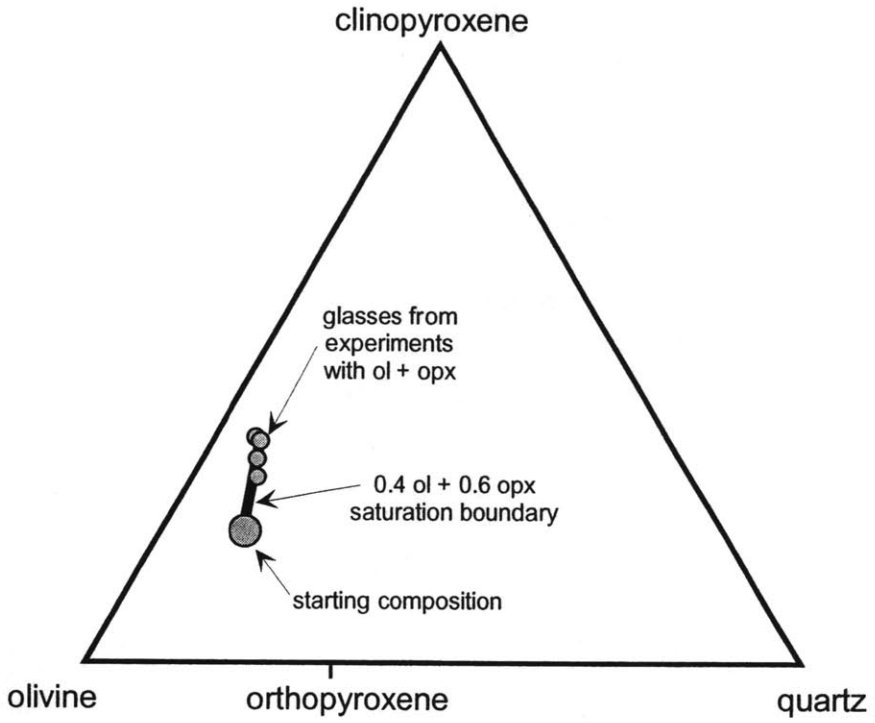
Olivine + orthopyroxene
2.3 GPa experiments
clinopyroxene
glasses from
experiments
with ol + opx
0.4 ol + 0.6 opx
saturation boundary
starting composition
olivine
orthopyroxene
quartz

Figure 2

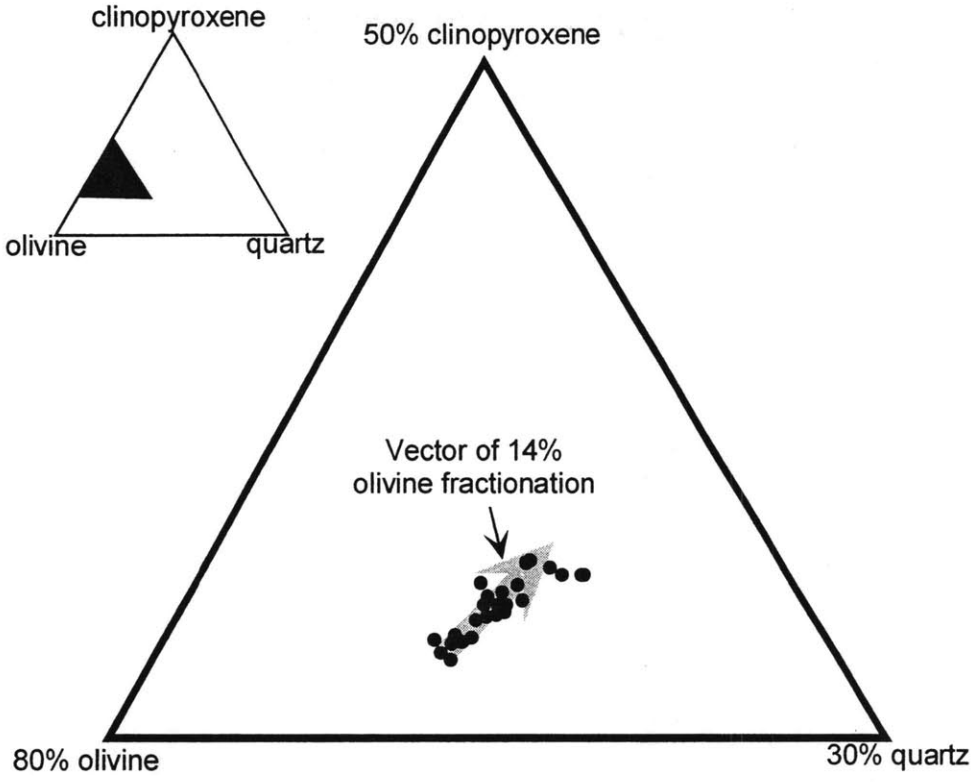
clinopyroxene
olivine
quartz
50% clinopyroxene
Vector of 14%
olivine fractionation
80% olivine
30% quartz

Figure 3

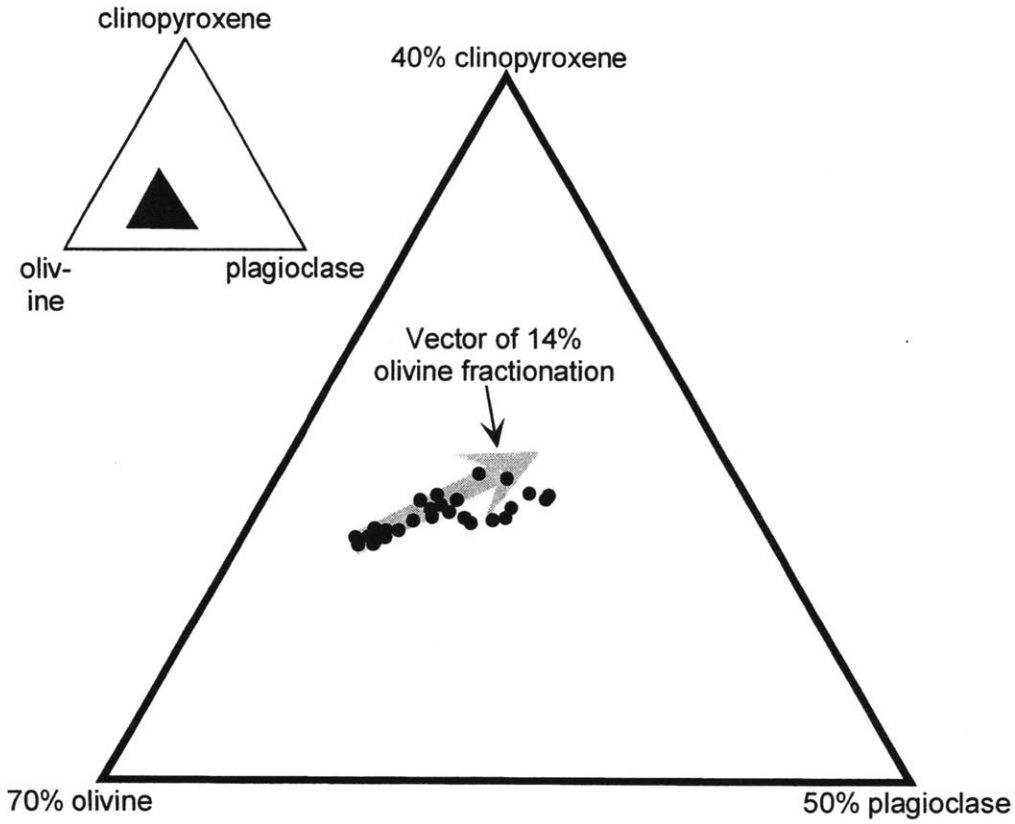
clinopyroxene
oliv-
ine
plagioclase
40% clinopyroxene
Vector of 14%
olivine fractionation
70% olivine
50% plagioclase

Figure 4

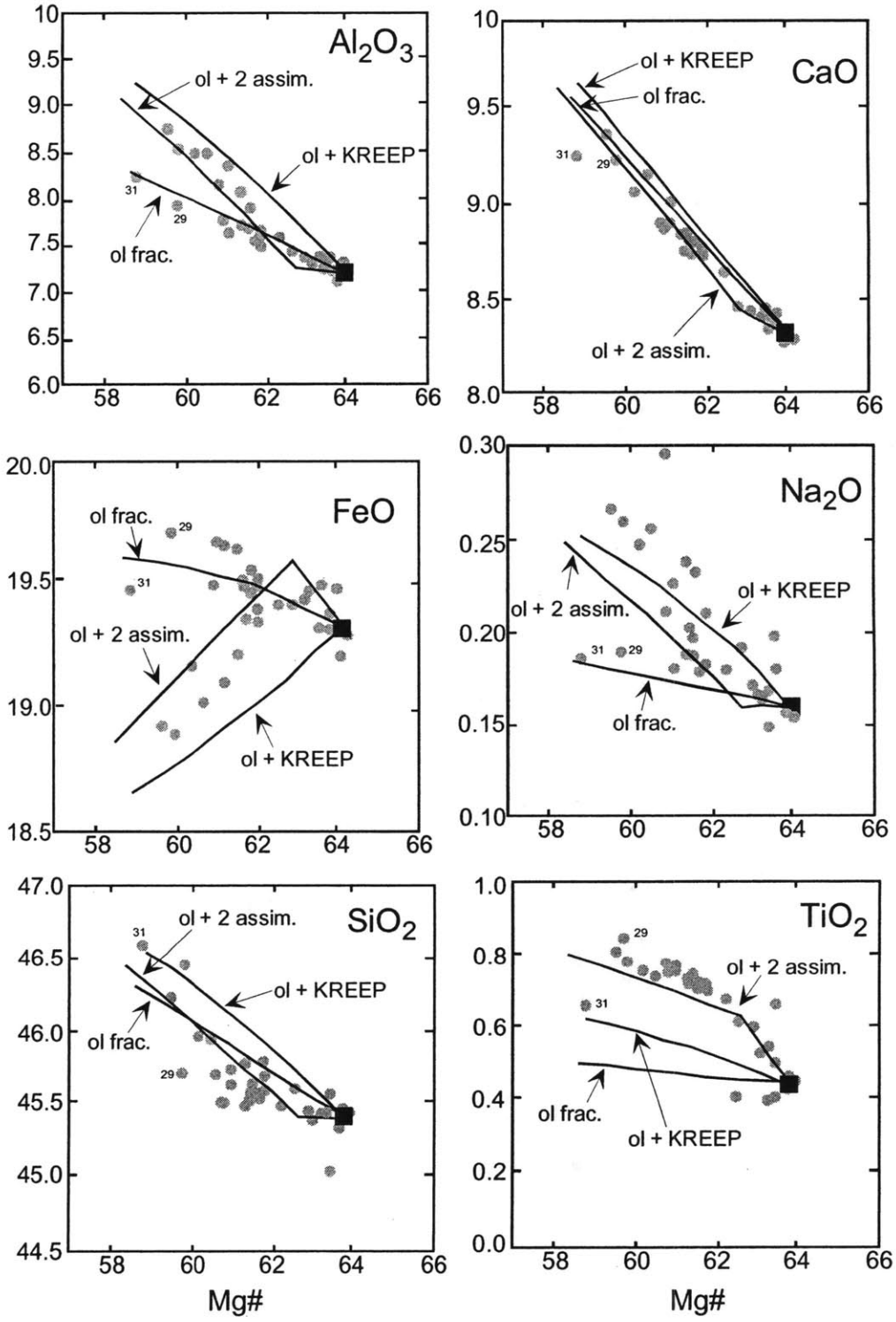
Al2O3
ol + 2 assim.
ol + KREEP
ol frac.
31
29
CaO
ol + KREEP
ol frac.
ol + 2 assim.
FeO
ol frac.
ol + 2 assim.
ol + KREEP
Na2O
ol + 2 assim.
ol + KREEP
ol frac.
SiO2
ol + 2 assim.
ol + KREEP
ol frac.
TiO2
ol + 2 assim.
ol frac.
ol + KREEP
Mg#
Mg#

Figure 5

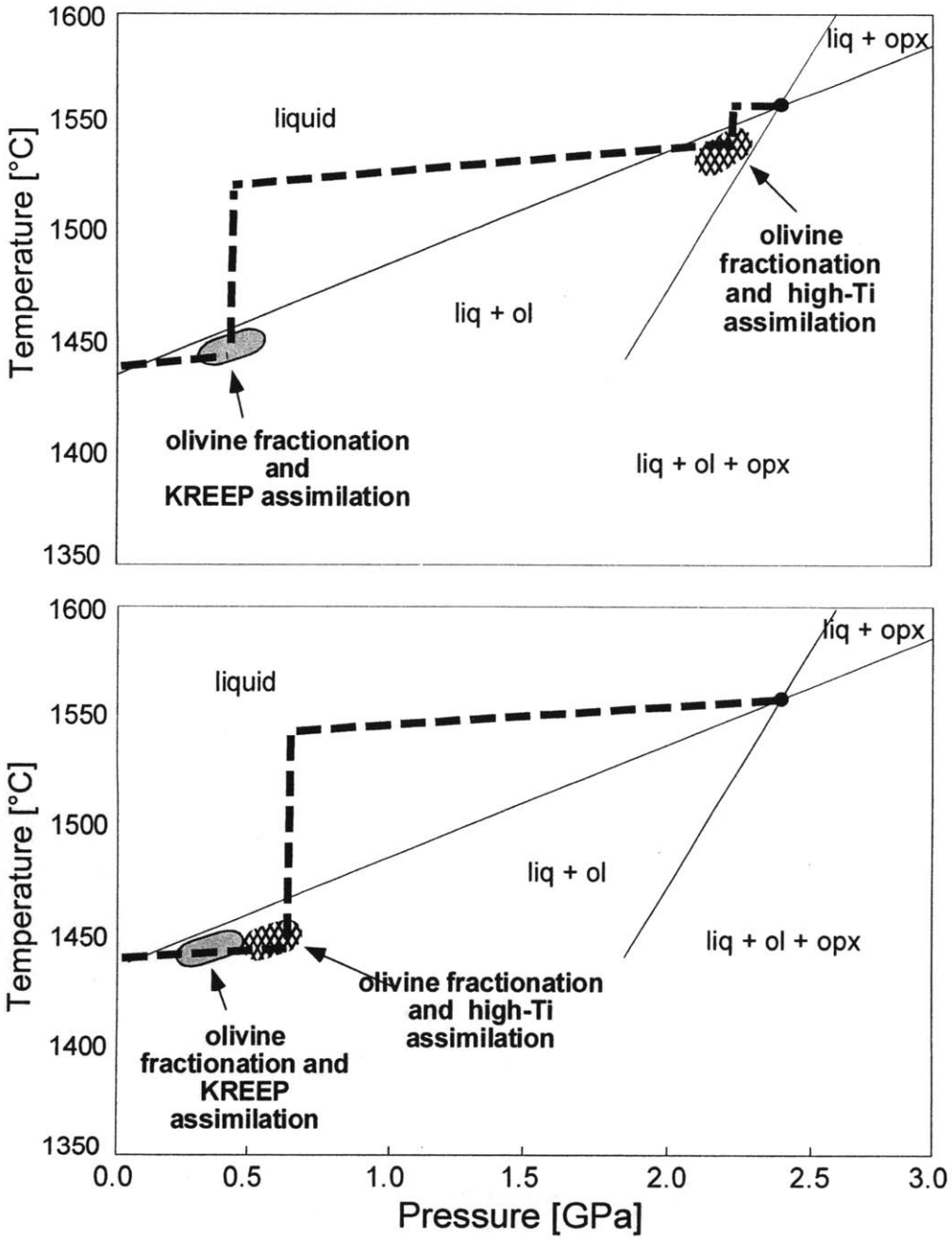
1600
1550
1500
1450
1400
1350
Temperature [°C]
liquid
liq + opx
liq + ol
olivine fractionation and high-Ti assimilation
olivine fractionation and KREEP assimilation
liq + ol + opx
0.0
0.5
1.0
1.5
2.0
2.5
3.0
Pressure [GPa]

Figure 6

Ch. 6. Constraints on lunar differentiation from the Apollo 15 green picritic glasses

Abstract

Phase equilibrium experiments on the most magnesian Apollo 15C green picritic glass composition indicate a multiple saturation point with olivine and orthopyroxene at 1520°C and 1.3 GPa (about 260 km depth in the moon). This composition has the highest Mg# of any lunar picritic glass, and the shallowest multiple saturation point. Experiments on an Apollo 15A composition indicate a multiple saturation point with olivine and orthopyroxene at 1520°C and 2.2 GPa (about 440 km depth in the moon). Garnet is close to the liquidus in the Apollo 15A at pressures above 2.0 GPa. The importance of the distinctive compositional trends of the Apollo 15 groups A, B and C picritic glasses merits their reanalysis with modern electron microprobe techniques. We confirm the compositional trends reported by Delano (1979, 1986) from his meticulous analysis of the contents of NASA slide 15426,72 through reanalysis of the major element oxides SiO_2, TiO_2, Al_2O_3, Cr_2O_3, FeO, MnO, MgO, and CaO, and we also obtained data for the trace elements P_2O_5, K_2O, Na_2O, NiO, S, Cu, Cl, Zn and F.

Vesicular rims were found on several of the glass beads. These rims are high in S and Ni, but otherwise compositionally similar to the green glasses. We suggest that these rims are remnants of the fluid that propelled the initial fire fountain eruptions of the picritic glasses.

Petrogenetic modeling confirms that the Apollo 15 A-B-C glass trends could not have been formed by fractional crystallization or any continuous assimilation/fractional crystallization (AFC) process. The B and C glass compositional trends cannot have been formed by batch or incremental melting of an olivine + orthopyroxene source or any other homogeneous source, though the A glasses may have been formed by congruent melting over a small pressure range at depth. The B compositional trend is well modeled by starting with an intermediate A composition and assimilating a shallower, melted cumulate, and the C compositional trend is well modeled by a second assimilation event involving a melted cumulate. These assimilants may have come from the same source at about 260 km depth, or from separate sources over a depth range. The assimilation process envisioned for the group B and C trend is one in which heat and mass transfer were separated in space and time. In an initial intrusive event a picritic magma crystallized and provided heat to melt magma ocean cumulates. In a later replenishment event the picritic magma mixed with the melted cumulate, creating the compositional trends in the green glass data set, ascended to the lunar surface and erupted as a fire fountain. A barometer created from multiple saturation points provides a depth estimate of other glasses in the A-B-C trend, and of the depths of assimilation. This barometer demonstrates that the Apollo 15 A-B-C trend originated over a depth range of ~460 km to ~260 km within the moon.

Introduction

Lunar ultramafic glasses have tremendous compositional variability. Understanding their formation mechanisms will place boundary conditions on both the early thermal history and chemical structure of the moon, from about 4.5 to 4.3 Ga, when the magma ocean cooled and

solidified to create differentiated chemical reservoirs, and on later lunar history, from 3.3 to 3.5 Ga, when the magmas melted from the differentiated reservoirs and erupted (e.g. Delano, 1986; Papike *et al*, 1998). The Apollo 15 glasses were erupted onto the lunar surface at 3.5 Ga (Meyer, 1975) in what most investigators agree was a gas-propelled fire fountain eruption.

Wood *et al.* (1970), Smith *et al.* (1970), and Taylor and Jakes (1974) suggested that between 4.6 and 4.4 Ga an initially molten moon differentiated into a layered cumulate, of which approximately the last 5% consisted of dense high-Ti compositions and a final residual liquid, the "ur-KREEP", all of which solidified high in the cumulate pile. Some researchers believe that the high density of the Ti-rich cumulates may have caused them to sink and overturn the cumulate pile into density-stratified layers (e.g., Ringwood and Kesson, 1976; Hess and Parmentier, 1995), while others suggest that rheological constraints would make wholesale overturn unlikely (e.g., Elkins Tanton *et al.*, 2002). During a later episode (post-4.0 Ga), a hybrid source region at 250 to 500 km depth consisting of olivine + orthopyroxene cumulates (or, alternatively, primitive mantle materials), possibly mixed with high-Ti cumulates and adulterated with intercumulus liquids that failed to escape during original magma ocean crystallization, were remelted to produce the picritic glass magmas.

This work focuses on the compositional variability displayed in Apollo 15 green glasses, groups A, B, and C, as defined by Delano (1986). The Apollo 15C green glass has the highest Mg# of any picritic glass yet found on the moon (Mg# = molar [Mg/(Mg + Fe)]). The compositional trends of the Apollo 15 A-B-C green glasses are distinctive and span a broad range of compositions; they vary in Mg# from 60.6 to 67.4 (MgO from 17.1 to 18.6 wt. %), in SiO_2 from 45.5 to 48.5 wt. %, and in FeO from 20 to 16 wt. %. The processes that created these trends will necessarily shed light on the thermal and compositional conditions in the moon's mantle.

Because little is known about the early evolution of the interior of the moon, there are several potential models for the processes that formed the parental green glasses, the progenitors of the compositional trends seen in each picritic glass group (Fig. 1), and the compositional trends themselves. In the discussion section below we critique the application of these models to the Apollo 15 A, B, and C trends. Based on compositions and multiple saturation points, a number of models can be ruled out without making any assumptions about the phases present in the lunar mantle.

By reanalyzing with wavelength-dispersive spectrometry on an electron microprobe the same glass beads that Delano (1986) did from sample 15426,72, we confirm and in some cases further constrain the narrowness of the trends, we more precisely determine the minor oxide and some trace element contents of specific beads, and we thereby obtain more constraints on models of formation of the green glasses.

The Apollo 15 Preliminary Examination Team first described the green glass beads in 1972 (Apollo 15 PET, 1972). Delano analyzed the Apollo 15 picritic glasses in 1978 and 1979 at the Australian National University in Canberra using energy-dispersive spectrometry on an electron microprobe. Delano's analyses were meticulous and have formed the basis of many of the subsequent petrologic studies of the picritic glasses (1979, 1986). Delano kindly lent us his photos, data, and notes from the original analyses, so we were able to reanalyze the exact beads, and compare the analyses directly.

Experimental and Analytic Methods

Experiments on a Synthetic Analog of an Apollo 15C Composition

The near-liquidus phase relations of a synthetic analog of the highest Mg# Apollo 15C green glass (Delano, 1986) were determined in experiments from 1 atmosphere to 2.0 GPa (corresponding to near surface to about 400 km depth in the moon) and at temperatures from 1350°C to 1550°C. The composition of the synthetic analog starting composition is shown in Table 1. The specific green glass chosen defines the extreme high Mg# end of the Apollo green glass trends, and, therefore, of all the lunar picritic glasses. The synthetic analog of this glass was prepared from high-purity oxides and ground under ethyl alcohol for 6 hours. The powdered mix was then pressed into a pellet using Elvanol as a binding agent, hung on a 0.004" Pt wire, and conditioned in a one-atmosphere Deltech furnace for 24 hours at 1000°C at an oxygen fugacity corresponding to the iron-wustite buffer.

For each experiment about 10 mg of conditioned starting material was packed into a graphite crucible and capped with graphite. The capsule was then fitted into a hole drilled into the end of an MgO cylinder, powdered graphite was packed around the capsule, and the assembly positioned in the hot spot of a graphite heater with MgO spacers, using $BaCO_3$ as the pressure medium. The experiments were performed in a 0.5-inch piston-cylinder apparatus. Pressure and temperature calibrations are described in Wagner and Grove (1997). In previous experiments

(e.g., Elkins *et al.* 2000) the graphite capsule had been welded into a Pt sleeve before placement in the MgO spacers. We found that manufacturing the assembly without Pt reduced cracking of the graphite capsule and iron loss in these very low-volatile compositions.

Runs in the piston cylinder apparatus were pressurized to 0.8 GPa, heated to 865°C at 100°C/min, pressurized to 0.1 to 0.3 GPa less than final pressure (depending on final pressure), heated to the run temperature at 50°C/min, and then brought to final run pressure. The very high Mg content of these experiments creates a low-viscosity glass that is prone to growing clinopyroxene crystals upon quenching at the end of the experiment. To obtain crystal-free glass, the experiments were temperature- and pressure-quenched by shutting off the power to the furnace and simultaneously dropping the pressure on the experiment to 0.8 GPa. Using this technique resulted in analyzable glass unmodified by disequilibrium pyroxene crystals in about 95% of experiments, where without this technique only about 25% of experiments contained analyzable glass.

The range of experimental temperatures spanned the liquidus and subliquidus phase volumes. The experimental charges were mounted in 1" epoxy disks, polished, and carbon-coated. The crystalline phases were analyzed at MIT on a JEOL-JXA-733 Superprobe at an accelerating voltage of 15 kV, beam current of 10 nA, and beam diameter of 1 micron. Glasses in the experimental charges were analyzed with a beam diameter of 10 microns. The CITZAF correction package of Armstrong (1995) using the atomic number correction from Duncumb and Reed, the absorption corrections with Heinrich's tabulation of mass-absorption coefficients, and the fluorescence corrections from Reed was used to reduce the data and obtain a quantitative analyses. A materials balance calculation was used to estimate phase proportions and to determine whether Fe had been lost from the experimental charge. The results of these materials balance calculations are reported in Table 2 as the R^2, the sum of squared residuals, and as phase proportions.

Experiments on a Synthetic Analog of an Apollo 15A Composition

The near-liquidus phase relations of a synthetic analog of an Apollo 15A green glass (Delano, 1986) were determined in experiments from 1 atmosphere to 2.5 GPa and at temperatures from 1400°C to 1570°C at SUNY Stonybrook in 1978 (see also Grove and Vaniman, 1978, for phase relations at one atmosphere). The composition of the synthetic analog starting composition is

shown in Table 1. The synthetic analog of this glass was prepared from high-purity oxides and ground under ethyl alcohol for 6 hours. The resulting mix was melted at one atmosphere in an iron capsule sealed in an evacuated silica tube to produce a glass starting material.

Experiments were performed in both iron capsules and graphite capsules. Experimental techniques are described in Grove and Vaniman (1978). The experiments were performed in a 0.5-inch piston-cylinder apparatus.

The range of experimental temperatures spanned the liquidus and subliquidus phase volumes. The experimental charges were mounted in 1" epoxy disks, polished, and carbon-coated. The crystalline phases were analyzed at SUNY Stonybrook on an ARL-EMX-SM microprobe using the data correction procedures of Bence and Albee (1968) with the modifications of Albee and Ray (1970). A materials balance calculation was used to estimate phase proportions and to determine whether Fe had been lost from the experimental charge. The results of these materials balance calculations are reported in Table 3 as the R^2, the sum of squared residuals.

Experiments on a possible cumulate source composition for assimilation

It became apparent in the petrogenetic modeling process that an aluminous assimilant was required to create the trends of the Apollo 15 A, B, and C glasses, as described below. We carried out some melting experiments on a possible depleted cumulate composition, in order to examine the possibility that a melt from that cumulate could be responsible for the trends seen in the Apollo 15 B and C glasses.

A synthetic mix was made of equal percentages of pigeonite, olivine, and plagioclase of the compositions predicted by a magma ocean crystallization model of Longhi (personal communication) at approximately 300 km depth in the moon. The bulk composition of this mix is given in Table 1.

Piston cylinder experiments were conducted in the same manner as those described in section 2.1, at pressures of 1.3 and 2.0 GPa and temperatures from 1350°C to 1500°C. These experiments were analyzed on the electron microprobe as described in section 2.1.

Reanalysis of green glasses of sample 15426,72

The polished thin section 15426,72 was obtained from the Lunar Sample Curator at the Johnson Space Center through the NASA CAPTEM sample program.

Before each analysis session, the MIT JEOL-JXA-733 Superprobe was calibrated with primary standards and then secondary standards were analyzed, as listed in Table 4. The two final secondary standards are anhydrous glasses that have been characterized at the MIT lab and are used regularly for high-precision glass analysis. Both the anhydrous glass standards were reproduced within 1-σ error limits of the analyses after primary calibration and adjustments made to the calibration after analyzing the DJ35 secondary standard. Secondary standard ALV-1690-20 and 70-002 are mid-ocean ridge basalt (MORB) glasses that have been analyzed extensively by electron microprobe at MIT (Grove *et al.*, 1990, Table 4). Analysis of the green glasses themselves was further calibrated among sessions by comparing the repeated analysis of two glass beads, designated by Delano as 31A and 131A.

Each glass bead was analyzed five times with a 10-micron beam spot size, using a 10 nA beam current and an accelerating voltage of 15 kV, for oxide components SiO_2, TiO_2, Al_2O_3, Cr_2O_3, FeO, MnO, MgO, CaO, Na_2O, K_2O, and P_2O_5. Only glass analyses with totals between 99.00 and 101.00 oxide wt % were included in our data set. During a separate analysis session we measured the trace elements Ni, S, Cl, Cu, Zn, and F. Again five separate analyses of each bead were done, with a 10 micron spot size but a 200 nA beam current and counting times up to 300 seconds. The data were reduced and corrected as described in section 2.1.

Table 5 lists the counting times for each oxide and element component, 1-σ standard deviations from microprobe counting times, minimum detectable levels, and population standard errors for single glass beads based on 5 replicate analyses from microprobe counting statistics.

Experimental and Analytic Results

The Apollo 15C Composition

The phase diagram for the Apollo 15C glass is shown in Fig. 2. The 18 experiments locate a multiple saturation point with olivine and orthopyroxene on the liquidus at 1.3 GPa (~260 km lunar depth) at 1520°C. Olivine is the liquidus phase from 1 atmosphere pressure and ~1380°C to the multiple saturation point at 1.3 GPa and 1520°C. Above the multiple saturation point orthopyroxene is the liquidus phase. The phase relations at 1.3 GPa have been determined in detail. Olivine and orthopyroxene are crystallized over a temperature interval of ~140°C, where a reaction point is encountered.

The 18 experiments that contained quench crystal-free glass, mass-balanced with the starting composition, and contained well-grown homogeneous phases, were used to calculate crystal–liquid exchange equilibria. The average equilibrium olivine-melt Fe-Mg exchange coefficient, K_D, (where $K_D = [(X_{Fe}^{xtl} * X_{Mg}^{liq})/(X_{Mg}^{xtl} * X_{Fe}^{liq})]$) is 0.34. The average orthopyroxene-melt K_D is 0.31. The conditions and results of the 13 phase equilibrium experiments for which analyses of multiple phases are available are given in Table 2 (the other experiments, numbers 1, 2, and 4 at one atmosphere and 2 and 16 at higher pressures, were above the liquidus).

The Apollo 15A Composition

The phase diagram for the Apollo 15A glass is shown in Fig. 3. The 21 experiments locate a multiple saturation point with olivine and orthopyroxene on the liquidus at 2.2 GPa (~440 km lunar depth) at 1520°C. Olivine is the liquidus phase at pressures lower than that of the multiple saturation point (2.2 GPa). Above the multiple saturation point orthopyroxene is the liquidus phase.

The 7 experiments that contained quench crystal-free glass, mass-balanced with the starting composition, and contained well-grown homogeneous phases, were used to calculate crystal–liquid exchange equilibria. The average equilibrium olivine-melt Fe-Mg exchange coefficient, K_D, is 0.36. The conditions and results of phase equilibrium experiments are given in Table 3.

The cumulate melting experiments

The pressures and temperatures of the cumulate melting experiments were chosen to reflect the mantle conditions implied by the phase equilibrium studies, that is, depths from 260 to 400 km, and temperatures near the multiple saturation temperature of about 1500°C.

Under these conditions the cumulate composition was largely melted. The liquidus of this cumulate composition is at about 1450°C at 1.5 GPa, and at about 1500°C at 2.0 GPa. Olivine was the liquidus phase, followed by clinopyroxene, and neither plagioclase nor spinel nor any other aluminous phase was stable on or near the liquidus. Without a stable aluminous phase, the aluminum content in the melt could never be low enough to form the assimilant needed for the trends of the Apollo 15 B and C. These experiments do, however, give useful information about cumulate melting behavior that will be used to constrain the mechanisms of formation of the

Apollo 15 A, B, and C trends. Conditions and experimental products for the cumulate melting experiments are given in Table 6.

Reanalysis of slide 15426,72

From the Apollo 15 group A, Delano analyzed 82 separate beads, and we reanalyzed 75 of the same beads. From group B, Delano analyzed 53 beads and we reanalyzed 37. From group C, Delano analyzed 8 beads and we reanalyzed 7. The missing beads were either located in lunar sample 15427, which we did not obtain, or had been plucked from the edges of sample 15426,72 during polishing that was done by researchers after Delano's analyses and before we obtained the slide. Delano's photos allowed relocation of the exact beads that were previously analyzed, if they still existed on the slide. In total, Delano analyzed 143 beads and we reanalyzed 119. In addition, we analyzed soil materials surrounding some of the glass beads.

The individual glass beads vary in size from about 50 to 350 microns in diameter. Almost all are spherical or close to spherical, or are broken fragments of what were apparently spheres. A few of the beads have dumbbell shapes. Almost all the glass beads analyzed were homogeneous, showing no crystals, and no systematic compositional variation across the beads (several detailed transects of beads were taken to confirm this). A very few beads showed distinctive thin vesicular rims, and are discussed below.

Our major element reanalysis confirmed the work Delano had done with the electron microprobe at the Australian National University for the oxides SiO_2, TiO_2, Al_2O_3, Cr_2O_3, FeO, MnO, MgO, CaO, and NiO (See Fig. 4 a-g and i and Appendix 1). In Delano (1986), Na_2O and K_2O were not detected; S abundances for some Apollo 15 green glasses are reported in Delano *et al.* 1994. We also obtained data for P_2O_5, K_2O, Na_2O, S, Cu, and Cl, and found that there is no measurable Zn or F in the interiors of these beads. See Fig. 4 a-k and Appendix 1 for complete data. The compositional trends from Delano's data have the same attitudes and largely the same variation at a given MgO as our reanalyses have. Strikingly, though, the MIT and Delano trends are offset from each other (Fig. 5 a-d), in particular those of calcium and aluminum (see discussion section).

Discussion

Compositional trends in the Apollo 15 A, B, and C green glasses

The A glasses have the smallest range of Mg#, from 60.7 to 61.6. The B glasses have the largest Mg# range, from 61.5 to 66.5, and the C glasses stretch from 65.8 to 67.6 (Fig. 6). Largely on the basis of the continuity in Mg#, the A, B, and C trends have been thought of together, and have been discussed as arising from a continuous process. When viewed in certain major element variation diagrams, in particular FeO vs. Mg# (Fig. 6b), the A, B, and C groups look like a single continuous linear trend. Other compositional variation diagrams, in particular FeO vs. MgO (Fig. 4e), show that the A trend is not collinear with the beginning of the B trend; in fact, the B trend initiates from the center of the A trend (see Fig. 6 and compare to Fig. 4). The correct geometry of the trends seems to be: the A trend is not collinear with the B trend, though the B trend may begin at its low MgO end with one of the A compositions, while the high-MgO end of the B trend and the low MgO end of the C trend are coincident in all compositional projections.

The A group has a small compositional range when compared to the B and C groups, though it is the most abundant glass type found at the Apollo 15 site. The C group, with only 7 data points, forms a roughly linear array in all compositional projections. The B group appears to be roughly linear throughout its wide compositional range when plotted in some projections (again, see FeO vs. MgO, Fig. 4e), but in others the B appears to have two roughly linear segments of different slopes. This is particularly notable in graphs of CaO vs. MgO, and in S vs. MgO (Fig. 4), where the B trend has a steep positive slope to an MgO of about 17.6, above which the slope changes. This variation in trend appears not to be an analytical artifact, and therefore must be considered in petrogenetic modeling. Alternatively, the A group could be considered to include all beads with compositions containing MgO = 17.6 wt % or less. In this scheme the low-MgO end of the B trend becomes part of the A trend, and the remaining group B glasses are roughly linear in all projections.

While the A, B and C groups are fairly continuous in their major element oxide contents, they form more scattered groupings in their trace element compositions. Steele *et al.* (1992) analyzed 365 Apollo 15 green glass beads for trace elements using INAA and 52 of them further for major elements using an electron microprobe. These beads were obtained from NASA subsplits ,9012 and ,154 from breccia 15426. Steele's study confirmed Delano's definitions of the major groups

of green glasses, using this separate source for beads. They note that the B and C groups are fairly continuous when plotted in Sc vs. FeO space, but that the A glasses form parallel trends that are not continuous with the B and C glasses. In fact, when examined in detail, the A glasses are seen to consist of two distinct, non-overlapping groups according to their trace element compositions. Steele *et al.* (1992) called these groups hA (high-LREE) and lA (low-LREE). These groupings may correspond in major elements to a group of A glasses with detectable Cl content, and to a second group with low Cl content (Fig. 4). Galbreath *et al.* (1990) also note that, based on Co contents, the A glasses are distinct from the B and C glasses.

Shearer and Papike (1993) report that the chondrite-normalized REE contents of the A and B groups overlap, while the C has the lowest REE content. Chondrite-normalized REE profiles of the B glasses are fairly flat, with a small negative Eu anomaly, and their chondrite-normalized Ce content ranges from 4 to 8.5. This is in contrast to the Apollo 14B glasses, whose chondrite-normalized Ce ranges from 8 to 20. Elkins *et al.* (2000) showed that the Apollo 14B glasses had likely assimilated a small amount of KREEPy material, which is also evident in their elevated REE profiles; the Apollo 15 A, B, and C glasses, with their lower, flatter profiles, are unlikely to have assimilated any KREEPy material.

In Fig. 7 the complete 15 A-B-C data sets are shown in an olivine-clinopyroxene-quartz pseudoternary diagram. The Apollo 15 A-B-C compositions form trends moving roughly toward the quartz apex, which is consistent with melting on the olivine + orthopyroxene saturation boundary at progressively shallower depths (Stolper, 1980), and this interpretation is also consistent with the liquids being multiply-saturated with olivine and orthopyroxene. The movement of the olivine + orthopyroxene saturation boundary with pressure forms a key indication of pressures of formation, and is discussed further below.

When the compositions are plotted in an olivine + clinopyroxene + plagioclase pseudoternary (not shown), it is tempting to call on melting at the olivine-plagioclase-clinopyroxene invariant point as the origin of the trends. The glass data clusters strongly in one place on the diagram, with an average for all compositions of olivine=21%, clinopyroxene=53%, and plagioclase=26%, and a maximum range for each of these of only 2%. Though the glasses are multiply saturated with only olivine + orthopyroxene, the ternary compositions involving plagioclase could be explained by assuming that the aluminous phase had been completely

melted out of the source and therefore not on the liquidus of the final compositions. Despite the intriguing appearance of the trends in ternary space, we will demonstrate below that the B and C glasses could not have been formed by simple melting events.

The multiple saturation point and other constraints on models of formation

The Apollo 15C green glass has the highest Mg# of any picritic glass yet found on the moon, but it has the shallowest multiple saturation depth (compare in particular to the Apollo 14B green glass, with an Mg# of 64 and a multiple saturation depth of ~ 480 km). The related Apollo 15A green glass has a similar temperature of multiple saturation, but a depth of 440 km. The Apollo 15A composition used in our experiments is at the high Mg# end of the A group, and therefore not quite at the opposite extrema of the A-B-C trends from the 15C. The Apollo 15A experiments thus provide a crucial pressure and temperature constraint not only on the A group but also on the lowest-Mg# B glasses, whose almost identical compositions would yield almost identical multiple saturation information.

There is some discussion about the meaning of multiple saturation points among investigators. The multiple saturation point is postulated to represent the temperature and pressure of the liquidus assemblage from which the melt was segregated (Delano, 1986). If polybaric fractional melting formed the magma, then the multiple saturation point (MSP) represents a mean pressure of melts formed at both greater and shallower depths than the multiple saturation point.

The MSP shows the phases most recently in equilibrium with the liquid. The deepest calculated MSP in a given compositional group does not guarantee that the melt began its liquid line of descent at the calculated depth; parental liquids derived at greater depths may be missing from the data set. Nor does the MSP guarantee that the liquid formed from a source that contained only the liquidus phases at the MSP. The melt extent could have completely exhausted one or more phases from the solid assemblage, and thus the liquid will be in equilibrium with only the phases remaining in the solid, and those are the phases that will appear as the liquidus phases on either side of the MSP in pressure-temperature space.

To begin modeling, the direction of movement of liquid compositions along the compositional trends must be determined, and the multiple saturation points offer the first, clearest information on the directions of the processes. By their multiple saturation depths, the B and C trends are

constrained to start at the low Mg#-end of the B trend (deepest) and progress upward in both depth and Mg# to the high Mg#-end of the C trend (most shallow).

The A group is not so constrained. From the A multiple saturation point, the high Mg#-end of the A group was last in equilibrium with a solid assemblage at 440 km depth. No depth constraint exists for other A compositions. Because the A group does not form a distinct trend, it is likely to have formed over a limited depth range.

The Apollo 15 B-C glass trends cannot have been formed by simple melting or fractional crystallization

Arguments against a melting or fractional crystallization origin of the Apollo 15 B-C compositional trends were made by Dence *et al.* (1974), Stolper (1974), and Grove (1981), among others. There are two relatively simple arguments that rule out simple melting or fractional crystallization models. First, Delano (1986) and others have also pointed out that NiO content in these glasses is inconsistent with olivine fractionation: as olivine crystallizes out of a melt, Mg# of the remaining liquid falls, and so does NiO content, since NiO is compatible in olivine. In the Apollo 15 B-C glasses, NiO decreases with increasing MgO (Fig. 4i). This argument cannot be used on the group A glasses, since the NiO vs. Mg# relation is unclear.

The second argument against melting or fractional crystallization, pointed out by Stolper (1974) and Grove (1981) requires plotting the data on a ternary diagram with fayalite and forsterite as two components, and any third component. In Fig. 8 the Apollo A, B, and C trends are plotted on a fayalite + forsterite + quartz ternary, along with the Apollo 14B glasses, which are known to have formed by olivine fractionation plus minor assimilation. Fractional melting trends (which are fractional crystallization trends in reverse) form curves in this ternary, with the high-Mg# end of the curve pointing toward the source material that is melting. The radius of curvature of the trend is controlled by the Fe-Mg exchange coefficients of the phases present. The first melts have the lowest Mg#, and subsequent melts increase in Mg#. If the melting were continued until the entire source was molten, then the end of the trend of accumulated melts would correspond to the source composition. The curving trend for olivine melting from high silica toward high Mg# can be seen clearly in the Apollo 14B compositions. The Apollo 15B and C compositions clearly do not follow this pattern; in fact, they move toward higher silica and higher Mg# at the same time. Therefore, simple melting could not have formed the groups B and C glass trends.

Thermal constraints are also inconsistent with polybaric melting. According to the multiple saturation point, the beginning composition of the B trend was in equilibrium with olivine and orthopyroxene at 1520°C. If it rises and melts adiabatically from 2.2 to 1.3 GPa, it will undergo about 9% melting, assuming 1% melt production per kilobar of decompression (Longhi, 1992). The integrated heat of fusion at 1500°C is about 160 calories per gram, and the heat capacity C_p is 0.3 cal/°C (Longhi, 1992). Therefore the total temperature drop created by 9% of melting is $\Delta T = (0.09 * 160)/0.3 = 48°C$. While it is melting, the package of material is also rising along an adiabat, on which it cools by 1.5°C per kilobar, creating a total adiabatic temperature drop of 14°C. The source, and therefore its melt product, would be required to cool at least 62°C through the B and C trends. The multiple saturation data, however, shows that the end of the C trend is at about the same temperature as the beginning of the B trend (both are experimentally determined to be 1520°C).

One could argue that, at the extremum of experimental inaccuracy, the temperature of the 15A multiple saturation point might be 25°C higher and that of the 15C composition 25°C lower, giving a temperature drop over the B and C trend of 50°C, which would be almost permissive of the temperature drop required for polybaric melting. However, this also assumes that the mantle being melted is at the same temperature as the rising glass magma, that is, around 1500°C and therefore does not require any additional superheat to bring it to its solidus. It is generally agreed that the lunar mantle at this time and depth could not have been above about 1200°C (Solomon and Longhi, 1977; Spohn *et al.*, 2001), and the rising magma would then have required at least 300°C of superheat to bring the cumulate mantle to 1500°C. The Apollo 15 B-C glasses are therefore also precluded from being the result of any process in which heat and mass transfer are coupled, as in assimilation-fractional crystallization.

The A glass compositional variation may have been formed by melting

Although the B and C trends cannot have been formed by incremental melting over a small pressure range, the A trend may have been created by such a process.

The A glass compositions form a trend that is negatively correlated between SiO_2 and MgO (Fig. 4a), a relationship that is consistent with melting if the trend moves from high SiO_2 and low MgO to low SiO_2 and high MgO. The A glasses, however, form no clear trend in compositional space and, with only one multiple saturation point, there is no constraint on whether the A

glasses came from a single depth or a small range of depths. Thus far, all major element information is consistent with the formation of the A glasses by melt extraction from an olivine and orthopyroxene residue at a depth of about 440 km in the moon.

An assimilation model for the formation of the Apollo 15 A-B-C green glasses

Because thermal constraints make AFC unlikely as the formation process for the B and C trends, we turn to a model where the rising parental green glass magma is not responsible for donating the heat required to melt the cumulate, though the parental green glass melt does assimilate the melted cumulate. This is an assimilation process in which heat and mass transfer are decoupled. In terrestrial magmatic systems several investigators have suggested that heating, melting, and assimilation of surrounding country rock occurs through episodic replenishment of magma into a reservoir (Baker *et a*l., 1991; Gunnarsson *et al.*, 1998; Kinzler *et al.*, 2000). In these settings an initial influx of magma enters the reservoir, cools, crystallizes, and provides heat to melt the surrounding country rock. A fresh batch of deeply derived melt rises and mixes with the melted country rock present in the reservoir, forming the final magma for eruption. Such a process is what we envision to account for the green glass compositions trends.

It is clear, by drawing vectors along the B and C trends in compositional variation diagrams, what the range of possible compositions the assimilant melt can have. In Fig. 9 we show the possible range of assimilant melt compositions that could be used to form the A, B, and C compositional trends. The assimilant melts for the A and C trends are limited in their possible Mg#s by TiO_2 content; the A and C trends decrease steeply in Ti and thus the assimilant can only have a Ti content between the end of the data trend and where that vector intersects 0% TiO_2. (This is in contrast to the 14B green glasses, in which TiO_2 content increases as fractionation progresses, indicating that a high-Ti component was assimilated while olivine fractionation progressed.)

The B trend has no such TiO_2 constraint because TiO_2 data for the Bs, though scattered, seems to decline only slightly over the B trend. We allow the Mg#s of the possible B assimilant to range from 67 to 85. This Mg# range, and that constrained for the C trend by TiO_2 content, in turn limit the contents of the other major element oxides. Shearer and Papike (1993) assumed that the cumulate that melted to form the green glasses consisted of 80% olivine and 20% orthopyroxene, and that it melted in proportions equal to the normative mineralogy. These assumptions then

indicate that the cumulate source had an Mg# between 76 and 84. Though Shearer and Papike (1993) were using their data to form a petrogenetic model of batch melting, their assumptions and our own create similarly magnesian source regions.

It is simpler and therefore more compelling to conclude that the A glasses were formed by melting, and that a part of the A glasses formed the low Mg# progenitor that began the B trend. The A compositions are consistent with melting a single source extremely depleted in incompatible elements, except that Steele *et al.*, 1992, found that the trace element concentrations in the group A glasses fall into two non-overlapping groups. The assimilation that created the beginning of the B trend may have caused the bimodal trace element profile.

As was mentioned earlier, the glasses form a trend when plotted on an olivine-clinopyroxene-quartz pseudoternary (Fig. 7). The A and C glasses are seen to be in equilibrium with olivine and orthopyroxene from multiple saturation experiments, and the other glasses in the trends can also safely be assumed to be in equilibrium with olivine and orthopyroxene. These glasses therefore lie on the olivine + orthopyroxene saturation boundary in this ternary diagram. The olivine + orthopyroxene saturation boundary remains perpendicular to the olivine-quartz side of the ternary, and moves toward the olivine apex with increasing pressure (Stolper, 1980). The known pressures of multiple saturation points for these glasses can then be used to calibrate a barometer for glasses in equilibrium with olivine and orthopyroxene. Such a barometer is shown in Fig. 10.

Though the movement of the saturation boundary is not linear, depths of multiple saturation for other compositions can be approximated by interpolation and extrapolation. Using these techniques, the depths of the deepest glasses from the A, B, and C trends can be approximated as 2.3, 2.25, and 1.8 GPa, respectively (460, 450, and 360 km depth). Similarly, the ranges of possible assimilant melt compositions can be plotted, and their approximate depths found. The shallowest possible assimilant melt depth for the B and C trends are 1.3 and 0.6 GPa (260 and 120 km depth). This technique provides constraints on the depths over which the processes could occur, and it also shows that the possible assimilant melt compositions are all from shallower depths than the glass trends themselves. This implies that the assimilation trends are not created by combining two melts that came from similar depths, but rather by combining a

deep, original melt with a shallower secondary melt. This requires that the temperature profile of the moon at this time be highly irregular, with melting regions at a variety of depths.

Shearer and Papike (1993) showed that the rare earth element abundances of the A and B glasses are higher than those of the C glasses. In lunar petrogenesis, high rare earth element contents are linked to the KREEP component, the final few percentages of the lunar magma ocean. The KREEP component is often modeled to have crystallized in close proximity to the final high-Ti cumulates. None of the A, B, or C glasses mixed with compositions with significant Ti content. Therefore the A and B glasses either formed from a deep depleted silicate mantle cumulate with a small KREEP component but extremely low Ti content, or, intriguingly, they may have formed by melting a primordial lunar composition that had not differentiated, and therefore comes from below the original lunar magma ocean. The A glasses have only a very small Eu anomaly, also consistent with this possibility (Shearer and Papike, 1993). If this is the case, then the magma ocean may be constrained to a maximum depth of about 440 km.

Longhi (1992) noted that, to reach the 7-8% of Al_2O_3 present in these green glasses, all the pyroxene would have to have been exhausted from the residuum. Our shallow multiple saturation point for the A15 C shows that pyroxene was not exhausted from the residuum, which begs the question, where did the Al_2O_3 come from for these glasses? Plagioclase is only stable to about 8 kbar, which is about 160 km depth on the moon (and the Eu and Sr data of Shearer and Papike (1993) show that the B and C are not continuous trends if they are formed by plagioclase assimilation, since Eu and Sr are higher in the B glasses than in the C's; the two trends can be continuous only if the aluminum comes from elsewhere). Seifert and Ringwood (1988) have shown that spinel, the aluminous phase likely to be stable in this depth range, is not a liquidus phase in any of the green glass compositions. This may simply indicate that the spinel phase had been completely exhausted from the residuum that the green glasses last equilibrated with, but the lack of spinel on the liquidus lends support to the theory of Shearer and Papike (1993), that intercumulus melt, the last few percent of melt trapped in a cumulate as it settles and solidifies, could provide the aluminous component.

The cumulate melting experiments we carried out showed that at a temperature equivalent to the multiple saturation temperature of the glasses, the aluminous phase was exhausted from this possible cumulate composition, and resulting melts could not mix with green glass progenitors to

cause the groups B and C compositional trends. In this final model, though, the heat required to melt the cumulate does not come from the parental green glass magma, and so there are fewer temperature constraints on the cumulate melting process to create the assimilant.

Using cumulate compositions modeled by John Longhi (personal communication), we found we could create appropriate assimilants at appropriate depths. Using Longhi's modeled olivine, pigeonite, and plagioclase cumulate phase compositions for about 300 km depth, we find that the B trend can be created accurately by adding to a low-MgO B glass a melt of a cumulate consisting of 5% olivine, 77% pigeonite, and 18% plagioclase (or, an aluminous intercumulus melt). The B trend would require a large amount of this assimilant, which by the high-MgO end of the trend would make up about 40% of the final B glass by weight. For the C trend, we used Longhi's modeled cumulate phase compositions for about 260 km depth. The C trend can be created by adding to a low-MgO C glass a molten assimilant consisting of 25% olivine, 50% pigeonite, and 25% plagioclase (or aluminous intercumulus melt). The final, high-MgO green glass contains about 13% of this assimilant by weight.

In Fig. 11 we summarize the depth and temperature constraints from the Apollo 15 A-B-C and 14B glasses, as obtained from the olivine + clinopyroxene + quartz pseudoternary. The deepest glasses from the 14B, 15A, and 15B trends originated deeper than 400 km and hotter than 1500 °C. The deepest 15C glass originated at about 360 km. The assimilant magmas are also constrained in depth through their possible compositions. The shallowest possible assimilant melt, for the C glasses, might have come from 120 km, though it may have originated as deeply as 260 km. In either case this model implies a shallow, hot region in the moon at about 3.5 Ga. This shallow hot area is consistent with disruption of the selenotherm due to the giant impacts of the Late Heavy Bombardment (Elkins Tanton *et al.*, 2001).

The trends of the B and C glasses are consistent with formation of their assimilants by melting of a single source at, respectively, lower, and then higher temperatures, or their assimilants may have come from separate sources. By examining the possible assimilation depths for the B and C glasses, shown in Fig. 13, if the assimilant source melted at one pressure and formed liquids that mixed to form both the B and C trends, then the source was located at about 260 km depth. It is further possible that the elbows in the B trend, seen in Fig. 6, are caused by exhaustion of an

early component in the assimilant source. This early component could well have been an intercumulus melt high in Ca and S.

While the A14B glasses, originating at about 480 km depth, assimilated high-Ti and KREEPy material dissimilar from their own source, the A15 trends, originating between about 460 and 260 km, are formed by assimilating material from similar source regions: all the 15A-B-C glasses and their assimilants are in equilibrium with olivine + orthopyroxene. The distribution of Ti-rich and Ti-poor cumulates within the lunar mantle may be heterogeneous, or by the time the Apollo 15 glasses erupted their path of eruption may have been depleted in low-temperature high-Ti components. A depleted, olivine-rich melt channel to the surface is consistent with the C glasses' compositions being conserved over a passage from a minimum of 120 km depth to the surface.

Non-vesicular rims

Five beads from the groups A and B reanalyzed from slide 15426,72 have noticeable rims (none of the group C glasses observed in this slide have rims, but there are far fewer group C beads to observe). Beads 26A and 35A (Delano's personal notation from original photographs) have thick, non-vesicular agglutinate rims of heterogeneous composition, 20 to 100 microns thick. The beads themselves are spherical, with radii of about 150 and 40 microns, respectively. See Fig. 12 a-b. The compositions of the rims of the beads and of other soil components are given in Table 7. Both rims contain two distinct compositions of glass (low Ti and Ti ~5%), along with grains of olivine, clinopyroxene, iron sulfide, and anorthite. Gibbons and Horz (1976) describe lunar soil agglutinates as schlieren-rich, and containing plagioclase, pyroxene, and olivine fragments. These features can be seen in both rims. Basu and McKay (1985) remark that agglutinates often contain more than one glass composition, which can also be seen in Fig. 12 and in Table 7. These agglutinates may have adhered to the glass beads while the beads were still hot immediately following eruption, or they may have been heated and adhered during subsequent lunar gardening.

Vesicular rims and implication for eruption conditions

Vesicles inside green glass beads have been reported previously by a number of researchers, including Delano and Lindsley (1983), who found 24 vesicular glass beads in 5 grams of sample 15427. The two vesicles shown in figures in their paper have diameters of about 10 and 100

microns respectively, and are near the centers of the beads that contain them. Heiken *et al.* (1974) found large vesicles in a small fraction of glass beads from Apollo 17. In contrast, the vesicular rims found in this study are very thin patches on the exterior of the picritic glass beads, 10 to 20 microns thick, they have different compositions than the beads they are attached to, and they show no diffusion profiles with the interior bead.

Additional researchers have analyzed thin coatings on the outside of the glass beads for volatiles that may have driven the fire-fountaining hypothesized to be the process of eruption of the green glasses (Meyer *et al.*, 1975; Goldberg *et al.*, 1975; Butler, 1978, Fogel and Rutherford, 1995). Meyer *et al.* (1975) found a thin film of microscopic mounds on the surface of Apollo 15 green glass beads, consisting of condensates of Zn, Ga, Pb, Cu, Tl, S, F and Cl. Goldberg *et al.* (1975) found that the Apollo 15 green glasses have a layer less than 0.1 microns thick that contains up to 3000 ppm of fluorine, while typically lunar rocks contain only 50 to 100 ppm fluorine. Fluorine is thus a prime candidate for volatile propulsion during eruption.

We found four beads with partial vesicular rims: beads 80A, 84A, 155B, and 190B (Two are shown in Fig. 13). All the vesicular rims are extremely high in S (1000 to 2300 ppm) and contain as much as 420 ppm Ni (Table 7). The S content in particular makes the rim compositions distinctive from the glass beads they adhere to. There is no detectable P_2O_5, Cl, Zn, or Cu in the rims. This is of particular interest as Butler (1978) found that S and Zn were most concentrated in the surface coatings correlated with fire fountain eruption, and so these rims might reasonably be expected to contain high S and Zn. We analyzed soil components from around each of the vesicular rims, to rule out environmental contamination to explain the rim compositions. There is no relationship between rim compositions and the compositions of surrounding soil materials, and nor is there any relationship between the glass trends themselves and surrounding soil materials.

The vesicular rim glasses probably erupted simultaneously with the glass beads. We believe them to be consistent with the observations of Agrell *et al.* (1973) and Heiken *et al.* (1974), that smaller beads of green glass adhered to the outside of larger beads while still molten and in the process of eruption.

Many researchers have hypothesized that the glass beads were produced in fire fountain eruptions propelled by volatiles (for example, Ridley *et al.* 1973; Heiken *et al.* 1974; Delano,

1979). We suggest that the vesicular rims are large residues of the fluids that propelled the glass beads in their eruption, and adhered to the beads in the process. Thus they were not obtained by the beads from the soil of the moon, but rather from some deeper source, and therefore are an important clue to the process of fire fountain eruptions and potentially to the composition and location of the volatile propellants within the early moon.

The highest S content in the vesicular rims is 2300 ppm. An Apollo 15A green glass melt at 2.2 GPa is saturated with 2300 ppm sulfur (Holzheid and Grove, 2002), and 2.2 GPa is the depth of multiple saturation determined for a group A glass. The sulfur content of the vesicular rims is thus consistent with their origin at the same depth as the group A glasses. If the sulfur-rich rims have the same provenance as the group A beads, then the following scenario is suggested: the group A beads erupt in a fire fountain and remain in a hot vapor cloud for 5 – 10 minutes, enough time for their sulfur to volatilize (Arndt *et al.*, 1984; Arndt and Engelhardt, 1987; Delano *et al.*, 1994). As they fell out of the cloud, fresher beads of glass adhered to them. These fresher beads had not had time to devolatilize and formed vesicular rims on the older beads. As the beads fell from the vapor cloud, they rapidly cooled and quenched to glass. Further, because surface films are enriched in Cl, F, and Zn, along with S, and the vesicular rim glasses contain no Cl, F, or Zn, then these three elements must be far more volatile than sulfur.

Bead inclusion and implications for cooling rates

Fig. 12b shows bead 26A, surrounded by an agglutinate rim. This bead also has an included grain, which is in turn surrounded by a diffusion rim. The relationship between the inclusion, the diffusion rim, and the picritic glass bead provides constraints on the cooling time of the bead. The included bead is a HASP glass (high-alumina, silica-poor glass), as defined by Naney *et al.* (1976). Naney *et al.* found five such grains in Apollo 16 samples, and previous researchers found HASP glasses in the Apollo 14 returned samples (Brown *et al.* 1971; Finkelman 1973). Delano *et al.* (1983) described these HASP glasses as the products of fractional vaporization: at lunar conditions K_2O, Na_2O, SiO_2, and FeO are all volatile and subject to loss. Their loss creates the HASP composition, which is listed in Table 7.

The immediate questions surrounding the existence of this inclusion are: (1) Did the HASP composition contaminate the Apollo 15 glasses and cause their compositional trends? (2) Was the HASP inclusion inserted into 26A upon eruption, or was it carried to the surface from depth?

First, the composition of the HASP glass is not collinear with any of the A, B, or C trends; nor is it within the groupings formed by the other soil component; nor is it related compositionally to the vesicular rim glasses. Therefore we can confidently conclude that the HASP glass did not contaminate the Apollo 15 picritic glasses.

Uhlmann *et al.* (1974) studied the kinetics of cooling and crystal growth in various lunar glasses and basalts. They noted that the lower the viscosity of the liquid composition, the faster nucleated crystals would grow, and therefore the faster the bead must quench to glass to prevent visible crystal growth. The Apollo 15 A-B-C glasses all erupted at temperatures above their liquidus and are free of crystals, and their compositions indicate that as liquids they had very low viscosity ($10^{-0.5}$ Pas at 1450°C). Uhlmann *et al.* (1974) conducted experiments on an orange glass composition and found that it cooled at 10 to 60 degree/second. Because of their lower viscosity, the green glasses from this study would have to have cooled even faster to avoid growing crystals. The glass bead #26A needed to cool from approximately 1450 to 650°C at a maximum rate of 10 to 60 degrees/second to avoid growing crystals. We therefore conclude that the bead cooled in 10 to 80 seconds.

Using a simple diffusion equation, a distance of 10 microns (the width of the diffusion halo around the HASP glass), and a diffusion constant D of 10^{-6} to 10^{-7} cm^2/sec (LaTourette and Wasserburg, 1997), we find that the diffusion halo formed in only 1 to 2 seconds. The HASP bead was therefore engulfed by bead #26A during or after eruption, and the volatile-depletion hypothesis of Delano *et al.* (1983) is supported. Had the HASP bead been carried from depth, then it would have either formed a much larger halo, or diffused completely into the larger glass bead.

Conclusion

We concur with the work of previous researchers who had ruled out fractional crystallization and simple batch melting as processes to form the Apollo 15 B-C trends (e.g., Dence *et al.*, 1974; Stolper, 1974; Grove, 1981; Delano, 1979; Delano and Lindsley, 1982; Shearer *et al.*, 1996). We also demonstrate through thermal arguments that polybaric fractional melting is not the process that formed the B and C glasses, though it is possible that the A glasses are the result of a simple melting process. The trends of groups B and C can be modeled by assimilation of magma ocean

cumulates at depths between 400 to 120 km depth. This model is consistent with pressure, temperature, and compositional constraints.

A simple, consistent model for the Apollo 15 A, B, and C is that the A group formed by congruent melting over a small pressure range, and then an average composition from group A assimilated a separate melt to form the B trend, and a second assimilation process formed the C trend. In particular, Fig. 4a (SiO_2 vs. MgO) supports the supposition that the B assimilation trend begins at a central composition in the A trend, and that the C glasses are formed by assimilation of a composition at the high-Mg# end of the B glasses. In this model the assimilants are melted before mixing with the group B and C progenitor glasses, and thus heat and mass transfer are decoupled, in a process similar to one envisioned for some terrestrial systems (Baker *et al.*, 1991; Gunnarsson *et al.*, 1998; Kinzler *et al.*, 2000. The required assimilants are consistent with compositions and depths calculated for magma ocean cumulates by Longhi (personal communication).

Our reanalysis of the Apollo 15 groups A, B, and C green glasses confirms the work done in the 1970s, 80s, and 90s by Delano (1979, 1986, 1994). We add to the database analyses of P_2O_5, K_2O, Na_2O, S, and Cl, and find there is no detectable F or Zn in these glass beads. Our compositions are consistently offset from the analyses of Delano, particularly in CaO and Al_2O_3, which differ by 4.5% and 2.5%, respectively. These offsets are likely due to differences in materials used for standards and in the data reduction program, as well as differences between energy dispersive analysis, which Delano used, and wavelength dispersive analysis, which this study used. It was not possible for us to duplicate the standardization or data reduction techniques used by Delano, so it was not possible to quantify these effects.

We confirm that the distinctive compositional trends of the Apollo 15 green glasses are as reported by Delano (1986), and further, that they are not caused by any possible surface contamination, but instead reflect deep lunar magmatic processes.

Four of the glass beads from groups A and B have small patchy vesicular rims. These rims are 10 to 20 microns in width and contain abundant vesicles. They have higher S and Ni contents than the glasses they adhere to, though they have no detectable P_2O_5, Cl, Zn, or F. Their size, texture, and composition are consistent with being condensates from the fluid that propelled the initial fire fountain eruptions of the picritic glasses.

Acknowledgements

Our most heartfelt thanks to John Delano for his help and discussion. Many thanks also to Nick Ware at ANU. This research was supported by a NASA grant and by a National Defense Science and Engineering Graduate Fellowship.

References

Agrell S.O., Agrell J.E. and Arnold A.R. (1973) Observations on glass from 15425, 15426, 15427. *Proc. Lunar Planet. Sci. Conf.* **4**, 12-14.

Albee A.L. and Ray L. (1970) Correction factors for electron probe microanalysis of silicates, oxides, carbonates, phosphates, and sulfates. *Anal. Chem.* **42**, 1408-1414.

Apollo 15 Preliminary Examination Team (1972) The Apollo 15 lunar samples: A preliminary description. *Science* **175**, 363-375.

Armstrong, J.T. (1995) CITZAF – A package of correction programs for the quantitative electron microbeam x-ray-analysis of thick polished materials, thin-films, and particles. *Microbeam Anal.* **4**, 177-200.

Baker M.B., Grove T.L., Kinzler R.J., Donnelly-Nolan J.M., and Wandless G.A. (1991) Origin of compositional zonation (high-alumina basalt to basaltic andesite) in the Giant Crater lava field, Medicine Lake volcano, northern California. *J. Geophys. Res.* **96**, 21819-21842.

Basu A. and McKay D.S. (1985) Chemical variability and origin of agglutinitic glass. *Proc. Lunar Planet. Sci. Conf.* **16**, D87–D94.

Bence A.E and Albee A.L. (1968) Empirical correction factors for electron microanalysis of silicates and oxides. *J. Geol.* **76**, 382-403.

Brown R.W., Reid A.M., Ridley W.I., Warner J.L., Jakes P., Butler P., Williams R.J. and Anderson D.H. (1971) Microprobe analyses of glasses and minerals from Apollo 14 sample 14259. NASA TM X-58080, 89 p.

Butler P. Jr. (1978) Recognition of lunar glass droplets produced directly from endogenous liquids: The evidence for S-Zn coatings. *Proc. Lunar Planet. Sci. Conf.* **9**, 1459-1471.

Delano J.W. (1979) Apollo 15 green glass: Chemistry and possible origin. *Proc. Lunar Planet. Sci. Conf.* **10**, 275-300.

Delano J. W. (1986) Pristine lunar glasses: criteria, data, and implications. *Proc. Lunar Planet. Sci. Conf.* **17**, D201–D213.

Delano J.W. and Lindsley D.H. (1982) New data on the fractionation trend in the Apollo 15 volcanic green glasses: Groups B, C. *Proc. Lunar Planet. Sci. Conf.* **13**, 162-163.

Delano J.W. and Lindsley D.H. (1983) Mare glasses from Apollo 17: Constraints on the moon's bulk composition. *Proc. Lunar Planet. Sci. Conf.* **14**, B3–B16.

Delano J.W., Hanson B.Z. and Watson E.B. (1994) Abundance and diffusivity of Sulfur in lunar picritic magmas (abstract). *Proc. Lunar Planet. Sci. Conf.* **25**, 325-326.

Dence M.R., Grieve R.A.F. and Plant A.G. (1974) the Imbrium Basin and its ejecta. *Lunar Science* **5**, 165-167, Lunar Science Institute, Houston, Texas.

Elkins L.T., Fernandes V.A., Delano J.W. and Grove T.L. (2000) Origin of lunar ultramafic green glasses: Constraints from phase equilibrium studies, *Geochim. Cosmochim. Acta* **64** 2339-2350.

Elkins Tanton L.T., Hager B.H. and Grove T.L. (2001) Magmatic effects of the Late Heavy Bombardment. (abstract) *American Geophysical Union Abstracts*, Spring Meeting.

Elkins Tanton L.T., Van Orman J.A., Hager B.H. and Grove T.L. (2002) Reexamination of the lunar magma ocean cumulate overturn hypothesis: High-Ti cumulate sinking is unlikely. *Earth Planet. Sci.Lett.* in press.

Finkelman R.B. (1973) Analysis of the ultrafine fraction of the Apollo 14 regolith. *Proc. Lunar Planet. Sci. Conf.* **4**, 179–189.

Fogel R.A. and Rutherford M.J. (1995) Magmatic volatiles in primitive lunar glasses: 1. FTIR and EPMA analysis on Apollo 15 green and yellow glasses and revision of the volatile-assisted fire-fountain theory. *Geochim. Cosmochim. Acta* **59**, 201-215.

Galbreath K.C., Shearer C.K., Papike J.J. and Shimizu N. (1990) Inter- and intra-group compositional variations in Apollo 15 pyroclastic green glass. *Geochim. Cosmochim. Acta* **54**, 2565-2574.

Gibbons R.V. and Horz F. (1976) The chemistry of some individual lunar soil agglutinates. *Proc. Lunar Planet. Sci. Conf.* **7**, 405–422.

Goldberg R.H., Burnett D.S. and Tombrello T.A. (1975) Fluorine surface films on lunar samples: Evidence for both lunar and terrestrial origins. *Proc. Lunar Planet. Sci. Conf.* **6**, 2189–2200.

Grove T.L. (1981) Compositional variations among Apollo 15 green glass spheres. *Proc. Lunar Planet. Sci. Conf.* **12**, 935-948.

Grove T.L. and Vaniman D.T. (1978) Experimental petrology of very low Ti (VLT) basalts. In *Mare Crisium: The View from Luna 24* (R.B. Merrill and J.J. Papike, eds.) pp. 445-471. Pergamon Press, New York.

Grove T.L., Kinzler R.J. and Bryan W.B. (1990) 2. Natural and experimental phase relations of lavas from Serocki volcano. *Proceedings of the Ocean Drilling Program, Scientific Results,* **106/109**, 9-17.

Gunnarsson B., Marsh B.D. and Taylor H.P. Jr. (1998) Generation of Icelandic rhyolites: silicic lavas from the Torfajokull central volcano. *J Volcanol Geotherm Res* **83**, 1-45.

Heiken G.H., McKay D.S. and Brown R.W. (1974) Lunar deposits of possible pyroclastic origin. *Geochim. Cosmochim. Acta* **38**, 1703-1718.

Hess P. C. and Parmentier E. M. (1995) A model for the thermal and chemical evolution of the moon's interior: Implications for the onset of mare volcanism. *Earth Planet. Sci. Lett.* **134**, 501–514.

Kinzler R.J. and Grove T.L. (1992) Primary magmas of mid-oceanic ridge basalts 1. Experiments and methods. *Journal of Geophysical Research* **97/B5**, 6885-6906.

Kinzler R.J., Donnelly-Nolan J.M., and Grove T.L. (2000) Late Holocene hydrous mafic magmatism at the Paint Pot Crater and Callahan Flows, Medicine Lake Volcano, N. California and the influence of H2O in the generation of silicic magmas. *Contrib. Mineral. Petrol.* **138**, 1 - 16.

LaTourette T. and Wasserburg G.J. (1997) Self diffusion of europium, neodymium, thorium, and uranium in haplobasaltic melt: The effect of oxygen fugacity and the relationship to melt structure. *Geochim. Cosmochim. Acta* **61**, 755-764.

Longhi J. (1992) Origin of picritic green glass magmas by polybaric fractional fusion. *Proc. Lunar Planet. Sci.* **22**, 343-353.

Meyer Jr. C., McKay D.S., Anderson D.H. and Butler Jr. P. (1975) The source of sublimates on the Apollo 15 green and Apollo 17 orange glass samples. *Proc. Lunar Planet. Sci. Conf.* **6**, 1673–1699.

Naney M.T., Crowl D.M. and Papike J.J. (1976) The Apollo 16 drill core: Statistical analysis of glass chemistry and the characterization of a high alumina – silica poor (HASP) glass. *Proc. Lunar Planet. Sci. Conf.* **7**, 155-184.

Papike J. J., Ryder G. and Shearer C. K. (1998) Lunar Samples. In *Planetary Materials* (ed. J.J. Papike) Reviews in Mineralogy **36**. 5-1–5-224. Mineralogical Society of America, Washington D.C.

Ridley W.I., Reid A.M. and Warner J.L. (1973) Apollo 15 green glasses. *Phys. Earth Planet. Inter.* **7**, 133-136.

Ringwood A. E. and Kesson S. E. (1976) A dynamic model for mare basalt petrogenesis. *Proc. Lunar Sci. Conf.* **7**, 1697–1722.

Seifert S. and Ringwood A.E. (1988) The lunar geochemistry of chromium and vanadium. *Earth Moon Planet* **40**, 45-70.

Shearer C.K. and Papike J.J. (1993) Basaltic Magmatism on the moon: A perspective from volcanic picritic glass beads. *Geochim. Cosmochim. Acta* **57**, 4785-4812.

Shearer C.K., Papike J.J. and Layne G.C. (1996) Deciphering basaltic magmatism on the Moon from the compositional variations in the Apollo 15 very low-Ti picritic magmas. *Geochim. Cosmochim. Acta* **60**, 509-528.

Steele A.M., Colson R.O., Korotev R.L. and Haskin L.A. (1992) Apollo 15 green glass: Compositional distribution and petrogenesis. *Geochim. Cosmochim. Acta* **56**, 4075-4090.

Smith J.V., Anderson A.T., Newton R.C., Olsen E.J., Wyllie P.J., Crewe A.V., Isaacson M.S. and Johnson, D. (1970) Petrologic history of the moon inferred from petrggraphy, mineralogy, and petrogenesis of Apollo 11 rocks. *Proc. Apollo 11 Lunar Planet. Sci. Conf.*, 897-925.

Solomon S.C. and Longhi J. (1977) Magma oceanography: 1. Thermal evolution. *Proc. Lunar Planet. Sci. Conf.* **8**, 583-599.

Spohn T., Konrad W., Breuer D. and Ziethe, R. (2001) The longevity of lunar volcanism: Implications of thermal evolution calculations with 2D and 3D mantle convection models. *Icarus* **149**, 54-65.

Stolper E. (1974) Compositional variations in lunar ultramafic glasses. In *Lunar Science* **5**, 749-751. Lunar Science Institute, Houston, Texas.

Stolper E. (1980) A phase diagram for mid-ocean ridge basalts – preliminary results and implications for petrogenesis. *Contrib. Mineral. Petrol.* **74**, 13-27.

Taylor, S.R. and Jakes, P. (1974) The geochemical evolution of the moon. *Proc. Lunar Planet. Sci. Conf.* **5**, 1287-1305.

Uhlmann, D.R., Klein L. and Kritchevsky G. (1974) The formation of lunar glasses. *Proc. Lunar Planet. Sci. Conf.* **5**, 2317-2331.

Wagner T.P. and Grove T.L. (1997) Experimental constraints on the origin of lunar high-Ti ultramafic glasses. *Geochim. Cosmochim. Acta* **61**, 1315-1327.

Wood J.A., Dickey J.S., Marvin U.B. and Powell B.N. (1970) Lunar anorthosites and a gepphysical model of the moon. *Proc. Apollo 11 Lunar Planet. Sci. Conf.*, 965-988.

Appendix I: Compositions of 119 Apollo 15 green glasses, groups (G) A, B, and C. Sample number (S) from Delano (personal communication). Reported value is average of N analyses. One sigma population error is given on oxide wt% for major elements and ppm for trace elements (population error is standard deviation divided by the square root of the number of analyses).

			Major elements												Trace elements				One sigma population errors													
S	G	N	SiO_2	TiO_2	Al_2O_3	Cr_2O_3	FeO	MnO	MgO	CaO	Na_2O	K_2O	P_2O_5	Mg#	NiO	S	Cl	Cu	SiO_2	TiO_2	Al_2O_3	Cr_2O_3	FeO	MnO	MgO	CaO	Na_2O	K_2O	P_2O_5	NiO	S	Cl	Cu
2	A	4	45.55	0.39	7.48	0.48	19.67	0.26	17.54	8.41	0.19	0.02	0.01	61.4	159.9	193.3	22.4	0.0	0.088	0.018	0.036	0.012	0.110	0.011	0.036	0.034	0.016	0.005	0.009	0.002	0.001	0.001	0.000
3	A	4	45.71	0.43	7.30	0.49	19.85	0.25	17.39	8.37	0.20	0.02	0.01	60.9	168.9	197.5	15.3	0.0	0.173	0.018	0.057	0.020	0.127	0.003	0.050	0.057	0.012	0.003	0.005	0.002	0.001	0.001	0.001
4	A	5	45.81	0.36	7.46	0.49	19.57	0.28	17.36	8.42	0.22	0.02	0.01	61.3	226.8	261.4	50.0	0.0	0.088	0.013	0.027	0.014	0.114	0.007	0.027	0.024	0.021	0.002	0.008	0.001	0.002	0.001	0.001
6	A	5	45.75	0.36	7.40	0.50	19.60	0.26	17.50	8.46	0.15	0.02	0.01	61.4	168.1	198.3	11.5	0.0	0.075	0.005	0.010	0.017	0.123	0.016	0.013	0.043	0.016	0.004	0.007	0.001	0.001	0.000	0.000
7	A	5	45.46	0.42	7.35	0.55	19.85	0.24	17.57	8.41	0.13	0.02	0.00	61.2	221.2	202.1	479.2	0.0	0.076	0.031	0.076	0.026	0.076	0.015	0.034	0.024	0.010	0.002	0.000	0.001	0.000	0.001	0.001
10	A	2	45.63	0.41	7.33	0.50	19.65	0.23	17.60	8.40	0.22	0.03	0.00	61.5	232.8	239.5	60.1	0.0	0.130	0.013	0.065	0.006	0.120	0.012	0.090	0.015	0.034	0.007	0.005	0.001	0.001	0.004	0.001
13	A	5	45.94	0.37	7.22	0.48	19.65	0.25	17.48	8.40	0.19	0.02	0.00	61.3	205.1	149.3	20.2	0.0	0.068	0.002	0.051	0.016	0.154	0.012	0.033	0.013	0.023	0.002	0.000	0.001	0.001	0.001	0.000
14	A	5	45.82	0.38	7.52	0.52	19.53	0.27	17.27	8.48	0.19	0.01	0.01	61.2	167.1	163.7	43.3	0.0	0.063	0.010	0.036	0.010	0.142	0.011	0.021	0.025	0.028	0.003	0.007	0.001	0.000	0.003	0.001
15	A	6	45.65	0.38	7.39	0.53	19.77	0.27	17.31	8.48	0.21	0.02	0.01	60.9	179.5	221.8	71.8	0.0	0.129	0.011	0.020	0.014	0.057	0.006	0.038	0.030	0.016	0.003	0.007	0.001	0.000	0.002	0.001
16	A	5	45.75	0.41	7.31	0.49	19.77	0.26	17.39	8.40	0.20	0.02	0.00	61.1	217.0	219.6	69.9	0.0	0.039	0.014	0.032	0.023	0.131	0.014	0.026	0.029	0.017	0.006	0.002	0.001	0.001	0.002	0.001
17	A	5	45.78	0.40	7.34	0.48	19.76	0.25	17.38	8.41	0.18	0.01	0.00	61.1	178.9	237.3	33.6	0.0	0.057	0.020	0.025	0.027	0.015	0.014	0.032	0.045	0.012	0.003	0.002	0.001	0.000	0.002	0.001
18	A	4	45.68	0.38	7.29	0.49	19.74	0.27	17.51	8.39	0.22	0.01	0.00	61.3	208.4	204.2	52.8	0.0	0.071	0.024	0.059	0.024	0.046	0.014	0.070	0.021	0.026	0.005	0.001	0.001	0.001	0.002	0.002
19	A	4	45.72	0.44	7.25	0.50	19.85	0.25	17.42	8.41	0.14	0.01	0.00	61.0	197.6	172.2	89.6	0.0	0.046	0.037	0.052	0.021	0.077	0.008	0.022	0.034	0.014	0.004	0.000	0.000	0.000	0.003	0.001
22	A	6	45.90	0.39	7.37	0.49	19.55	0.26	17.34	8.50	0.18	0.01	0.01	61.3	146.7	143.1	36.6	0.0	0.079	0.015	0.060	0.014	0.049	0.007	0.047	0.020	0.008	0.002	0.006	0.001	0.000	0.001	0.001
24	A	4	45.92	0.38	7.55	0.50	19.11	0.28	17.48	8.58	0.17	0.02	0.00	62.0	194.0	196.7	73.4	0.0	0.164	0.012	0.025	0.003	0.293	0.003	0.091	0.014	0.027	0.003	0.000	0.001	0.001	0.003	0.001
26	A	7	45.81	0.38	7.36	0.49	19.73	0.27	17.27	8.44	0.22	0.02	0.00	60.9	162.5	239.7	88.0	0.0	0.066	0.007	0.023	0.007	0.087	0.008	0.023	0.015	0.012	0.002	0.000	0.001	0.001	0.001	0.000
27	A	2	45.63	0.36	7.38	0.48	19.84	0.25	17.36	8.43	0.26	0.01	0.00	60.9	201.5	211.4	64.3	0.0	0.260	0.018	0.060	0.041	0.040	0.007	0.015	0.015	0.031	0.001	0.003	0.001	0.000	0.004	0.000
31	A	5	45.83	0.39	7.50	0.52	19.35	0.25	17.55	8.49	0.09	0.02	0.00	61.8	177.5	287.8	103.8	0.0	0.091	0.024	0.014	0.021	0.109	0.005	0.022	0.034	0.012	0.003	0.000	0.001	0.001	0.003	0.000
32	A	7	45.90	0.35	7.39	0.53	19.72	0.27	17.18	8.49	0.13	0.03	0.00	60.8	211.6	325.5	4.5	5.0	0.080	0.007	0.095	0.011	0.062	0.010	0.029	0.019	0.014	0.002	0.000	0.001	0.000	0.000	0.000
34	A	4	45.80	0.36	7.29	0.51	19.86	0.28	17.35	8.45	0.08	0.02	0.01	60.9	188.7	240.8	0.0	0.2	0.065	0.020	0.040	0.015	0.114	0.018	0.039	0.020	0.025	0.004	0.005	0.002	0.000	0.000	0.000
35	A	3	45.86	0.35	7.34	0.53	19.72	0.28	17.27	8.52	0.10	0.02	0.00	60.9	214.5	275.9	2.2	0.0	0.034	0.003	0.023	0.012	0.163	0.022	0.041	0.050	0.013	0.002	0.000	0.001	0.003	0.000	0.000
37	A	6	45.92	0.34	7.25	0.55	19.74	0.26	17.38	8.45	0.08	0.01	0.01	61.1	206.5	263.1	34.4	8.9	0.061	0.008	0.029	0.021	0.042	0.007	0.020	0.031	0.019	0.002	0.004	0.001	0.000	0.001	0.000
38	A	4	45.77	0.36	7.31	0.57	19.89	0.25	17.35	8.38	0.10	0.02	0.00	60.9	194.7	171.6	44.3	19.7	0.043	0.010	0.085	0.020	0.036	0.021	0.046	0.034	0.010	0.002	0.003	0.002	0.001	0.003	0.001
39	A	4	45.92	0.37	7.47	0.53	19.48	0.26	17.37	8.53	0.07	0.01	0.00	61.4	175.6	294.3	0.0	51.9	0.039	0.015	0.039	0.029	0.155	0.012	0.044	0.038	0.018	0.002	0.001	0.001	0.001	0.000	0.000
40	A	4	45.88	0.37	7.36	0.54	19.66	0.25	17.35	8.47	0.09	0.02	0.01	61.1	176.8	190.7	67.5	33.5	0.070	0.010	0.024	0.012	0.184	0.015	0.040	0.030	0.009	0.001	0.007	0.001	0.000	0.001	0.001
43	A	5	45.78	0.34	7.25	0.54	19.91	0.26	17.43	8.40	0.08	0.01	0.00	60.9	206.6	171.3	29.3	3.7	0.048	0.017	0.017	0.008	0.047	0.009	0.022	0.037	0.024	0.001	0.000	0.001	0.000	0.001	0.000
44	A	4	45.85	0.35	7.24	0.54	19.92	0.27	17.35	8.36	0.09	0.01	0.00	60.8	187.2	266.4	44.4	2.5	0.131	0.033	0.049	0.024	0.198	0.003	0.043	0.036	0.018	0.002	0.003	0.001	0.000	0.002	0.000
45	A	5	45.73	0.38	7.29	0.55	19.95	0.28	17.35	8.40	0.05	0.01	0.01	60.8	185.5	252.7	37 6	5.7	0.061	0.020	0.020	0.013	0.069	0.013	0.025	0.024	0.019	0.003	0.004	0.001	0.001	0.002	0.000
47	A	5	45.89	0.37	7.49	0.52	19.69	0.27	17.16	8.46	0.12	0.02	0.02	60.8	194.8	214.1	22.8	10.3	0.021	0.010	0.030	0.019	0.077	0.012	0.038	0.033	0.022	0.002	0.011	0.001	0.001	0.001	0.001
48	A	5	45.57	0.43	7.43	0.55	19.62	0.24	17.56	8.47	0.11	0.02	0.00	61.5	223.5	211.2	439.4	0.0	0.031	0.044	0.034	0.019	0.230	0.015	0.022	0.025	0.018	0.002	0.000	0.001	0.000	0.002	0.000
50	A	5	45.77	0.41	7.47	0.51	19.70	0.23	17.33	8.47	0.07	0.03	0.00	61.1	185.5	198.3	416.3	3.1	0.047	0.023	0.037	0.014	0.042	0.009	0.092	0.012	0.007	0.002	0.000	0.002	0.000	0.002	0.000
52	A	5	45.82	0.38	7.31	0.56	19.78	0.25	17.37	8.41	0.07	0.02	0.03	61.0	168.6	169.1	18.8	12.9	0.082	0.016	0.036	0.027	0.105	0.010	0.027	0.045	0.011	0.004	0.015	0.001	0.000	0.001	0.001
56	A	4	45.90	0.35	7.37	0.55	19.69	0.26	17.33	8.44	0.07	0.02	0.01	61.1	194.8	280.6	19.8	1.6	0.030	0.019	0.017	0.035	0.068	0.014	0.009	0.027	0.023	0.002	0.007	0.001	0.001	0.001	0.000
57	A	4	45.74	0.39	7.22	0.54	19.99	0.28	17.35	8.37	0.09	0.02	0.01	60.7	184.3	199.9	0.8	18.6	0.099	0.019	0.074	0.021	0.070	0.012	0.017	0.040	0.016	0.002	0.006	0.002	0.001	0.000	0.001
58	A	4	45.71	0.36	7.45	0.56	19.88	0.25	17.22	8.44	0.08	0.03	0.02	60.7	190.1	218.3	49.2	12.4	0.070	0.011	0.037	0.005	0.027	0.008	0.025	0.018	0.016	0.002	0.014	0.001	0.001	0.003	0.001
60	A	5	45.94	0.38	7.20	0.52	19.80	0.27	17.34	8.40	0.12	0.02	0.01	61.0	185.2	177.1	41.3	8.5	0.030	0.021	0.045	0.010	0.198	0.012	0.029	0.017	0.007	0.003	0.011	0.002	0.001	0.002	0.000
62	A	4	45.79	0.39	7.47	0.52	19.76	0.26	17.25	8.44	0.10	0.02	0.01	60.9	169.7	168.1	22.7	21.6	0.061	0.014	0.043	0.012	0.038	0.015	0.023	0.025	0.013	0.003	0.013	0.001	0.001	0.001	0.001

S	G	N	SiO_2	TiO_2	Al_2O_3	Cr_2O_3	FeO	MnO	MgO	CaO	Na_2O	K_2O	P_2O_5	Mg#	NiO	S	Cl	Cu	SiO_2	TiO_2	Al_2O_3	Cr_2O_3	FeO	MnO	MgO	CaO	Na_2O	K_2O	P_2O_5	NiO	S	Cl	Cu
64	A	3	45.73	0.35	7.21	0.51	20.01	0.24	17.38	8.45	0.10	0.02	0.01	60.8	179.4	180.9	3.3	8.5	0.079	0.005	0.055	0.005	0.115	0.010	0.030	0.062	0.011	0.001	0.011	0.002	0.002	0.000	0.001
69	A	5	45.90	0.38	7.29	0.53	19.82	0.26	17.33	8.39	0.08	0.02	0.00	60.9	170.0	272.2	18.2	3.3	0.063	0.014	0.043	0.022	0.092	0.012	0.016	0.026	0.021	0.003	0.000	0.001	0.000	0.001	0.000
71	A	4	45.83	0.36	7.38	0.56	19.71	0.27	17.30	8.45	0.11	0.02	0.01	61.0	194.5	223.6	1.2	6.2	0.094	0.009	0.017	0.010	0.268	0.013	0.023	0.021	0.023	0.003	0.008	0.001	0.001	0.000	0.001
74	A	5	45.78	0.40	7.43	0.51	19.62	0.23	17.49	8.43	0.09	0.02	0.00	61.4	199.5	251.7	421.9	8.3	0.039	0.042	0.037	0.017	0.069	0.017	0.045	0.030	0.005	0.003	0.000	0.002	0.000	0.002	0.001
76	A	5	45.57	0.42	7.53	0.54	19.66	0.25	17.53	8.41	0.05	0.03	0.00	61.4	163.5	157 4	446.7	13.1	0.172	0.019	0.034	0.021	0.072	0.004	0.049	0.044	0.022	0.002	0.000	0.001	0.000	0.002	0.001
78	A	5	45.96	0.38	7.38	0.55	19.66	0.27	17.25	8.46	0.07	0.02	0.00	61.0	188.1	232.9	0.0	15.1	0.061	0.017	0.041	0.013	0.244	0.010	0.063	0.023	0.021	0.002	0.000	0 001	0.001	0.000	0.001
79	A	4	45.93	0.40	7.55	0.51	19.48	0.22	17.34	8.43	0.10	0.03	0.00	61.3	189.3	171.9	386.1	20.4	0.073	0.017	0.063	0.019	0.179	0.007	0.039	0.012	0.033	0.005	0.000	0.001	0.001	0.003	0.000
80	A	5	45.88	0.39	7.26	0.53	19.82	0.28	17.37	8.39	0.06	0.02	0.01	61.0	198.6	293.8	10.2	26.0	0.064	0.016	0.018	0.014	0.039	0.009	0.029	0.020	0.012	0.003	0.007	0.002	0.001	0.001	0.000
83	A	5	45.75	0.37	7.27	0.53	19.93	0.28	17.32	8.42	0.12	0.02	0.00	60.8	225.7	209.4	14.1	24.4	0.093	0.012	0.031	0.016	0.080	0.009	0.023	0.010	0.030	0.003	0.000	0.002	0.000	0.001	0.001
84	A	3	45.84	0.37	7.50	0.51	19.58	0.27	17.28	8.51	0.09	0.02	0.02	61.1	188.0	296.1	0.0	48.3	0.026	0.023	0.015	0.011	0.218	0.007	0.012	0.035	0.008	0.001	0.017	0.001	0.000	0.000	0.000
85	A	5	46.04	0.45	7.57	0.53	18.90	0.25	17.61	8.56	0.08	0.02	0.00	62.4	170.9	186.1	414.7	28.5	0.044	0.021	0.040	0.013	0.326	0 011	0.036	0.025	0.016	0 003	0 000	0.001	0.001	0.002	0.001
89	A	4	45.63	0.40	7.34	0.53	19.84	0.22	17.48	8.46	0.07	0.02	0.00	61.1	184.9	156.1	360.1	33.6	0.034	0.037	0.042	0.026	0.161	0.012	0.032	0.015	0.008	0.004	0.000	0.001	0.000	0.002	0.001
90	A	5	45.96	0.39	7.20	0.55	19.79	0.28	17.25	8.42	0.11	0.01	0.02	60.8	206.9	199.5	0.0	30.3	0.029	0.011	0.015	0.015	0.189	0.017	0.079	0.024	0.030	0.003	0.013	0.001	0.001	0.000	0.001
93	A	3	45.77	0.38	7.30	0.55	19.77	0.26	17.38	8.48	0.09	0.01	0.01	61.0	203.1	212.8	0.0	21.7	0.056	0.021	0.010	0.007	0.060	0.006	0.047	0.041	0.011	0.004	0.003	0.001	0.001	0.000	0.001
94	A	5	45.71	0.38	7.13	0.55	20.05	0.27	17.37	8.40	0.11	0.02	0.01	60.7	204.1	177.9	38.2	22.4	0.065	0.019	0.080	0.017	0.149	0.010	0.017	0.021	0.008	0.004	0.007	0.001	0.001	0.001	0.001
95	A	5	45.88	0.37	7.41	0.52	19.64	0.28	17.27	8.47	0.13	0.02	0.01	61.0	193.1	185.8	4.6	24.0	0.026	0.020	0.045	0.017	0.145	0.010	0.050	0.027	0.032	0.002	0.011	0.001	0.001	0.000	0.001
96	A	5	45.54	0.40	7.54	0.54	19.67	0.25	17.46	8.51	0.08	0.02	0.00	61.3	186.9	203.5	385.6	35.3	0.066	0.021	0.020	0.007	0.101	0.008	0.026	0.027	0.010	0.003	0.000	0.002	0.002	0.003	0.001
97	A	5	45.91	0.36	7.43	0.56	19.55	0.29	17.29	8.49	0.08	0.02	0.02	61.2	190.3	234.5	20.9	23.8	0.066	0.008	0.033	0.022	0.117	0.014	0.025	0.033	0.028	0.002	0.010	0.002	0.001	0.001	0.000
98	A	5	45.89	0.39	7.43	0.55	19.58	0.26	17.31	8.48	0.10	0.01	0.01	61.2	181.2	213.3	33.7	25.8	0.069	0.016	0.034	0.015	0.143	0.006	0.033	0.020	0.014	0.002	0.008	0.001	0.000	0.001	0.001
103	A	5	45.84	0.37	7.41	0.54	19.83	0.24	17.20	8.43	0.12	0.02	0.00	60.7	206.7	263.5	0.0	28.3	0.095	0.009	0.015	0.024	0.056	0.004	0.070	0.011	0.014	0.002	0.000	0.001	0.001	0.000	0.001
105	A	5	45.54	0.40	7.36	0.55	19.83	0.24	17.56	8.38	0.12	0.02	0.00	61.2	202.0	131.6	397.5	23.2	0.069	0.014	0.017	0.018	0.039	0.017	0.022	0.009	0.012	0.002	0.000	0.001	0.000	0.001	0.001
109	A	4	45.87	0.36	7.40	0.56	19.72	0.25	17.34	8.38	0.10	0.02	0.00	61.1	176.5	211.8	29.6	21.1	0.067	0.020	0.042	0.019	0.101	0.010	0.023	0.036	0.011	0.003	0.000	0.002	0.001	0.002	0.001
112	A	5	45.95	0.39	7.20	0.52	19.85	0.27	17.36	8.37	0.09	0.01	0.00	60.9	226.2	166.1	6.6	24.9	0.026	0.013	0.103	0.020	0.130	0.018	0.022	0.036	0.013	0.003	0.000	0.001	0.000	0.000	0.001
113	A	4	45.54	0.39	7.43	0.54	19.86	0.24	17.47	8.45	0.07	0.02	0.00	61.0	163.2	170.8	454.3	28.2	0.055	0.011	0.024	0.021	0.038	0.014	0.049	0.051	0.023	0.002	0.000	0.001	0.000	0.004	0.001
115	A	4	45.92	0.34	7.24	0.54	19.82	0.25	17.39	8.42	0.07	0.02	0.00	61.0	170.0	287.9	1.2	31.8	0.051	0.016	0.028	0.022	0.041	0.009	0.020	0.027	0.009	0.007	0.000	0.001	0.000	0.000	0.001
118	A	5	45.95	0.33	7.31	0.52	19.71	0.27	17.38	8.44	0.06	0.01	0.00	61.1	174.6	197.1	1.3	18.8	0.050	0.006	0.027	0.014	0.102	0.008	0.030	0.040	0.010	0.004	0.002	0.002	0.001	0.000	0.001
119	A	5	45.84	0.38	7.43	0.58	19.67	0.26	17.27	8.48	0.09	0.01	0.00	61.0	169.6	194.0	28.4	28.2	0.028	0.012	0.009	0.021	0.146	0.014	0.037	0.029	0.014	0.003	0.000	0.001	0.000	0.001	0.001
120	A	3	45.78	0.33	7.23	0.60	19.88	0.27	17.42	8.39	0.10	0.02	0.00	61.0	201.6	207.7	19.8	28.0	0.155	0.008	0.057	0.016	0.197	0.006	0.018	0.027	0.048	0.003	0.000	0.003	0.001	0.001	0.002
121	A	5	45.96	0.40	7.45	0.56	19.54	0.26	17.26	8.47	0.08	0.02	0.01	61.2	176.8	425.6	26.2	30.5	0.039	0.013	0.014	0.013	0.052	0.008	0.031	0.012	0.016	0.004	0.006	0.001	0.001	0.001	0.001
125	A	3	45.69	0.36	7.35	0.54	19.89	0.28	17.31	8.50	0.06	0.01	0.01	60.8	171.7	222.0	2.7	54.0	0.132	0.013	0.091	0.011	0.036	0.018	0.064	0.012	0.019	0.004	0.005	0.002	0.001	0.000	0.000
126	A	5	45.62	0.37	7.47	0.54	19.75	0.28	17.36	8.50	0.10	0.02	0.01	61.0	170.8	194.8	17.5	52.4	0.058	0.012	0.037	0.008	0.081	0.003	0.034	0.018	0.027	0.003	0.007	0.002	0.001	0.001	0.001
127	A	5	45.70	0.38	7.34	0.52	19.82	0.25	17.36	8.49	0.11	0.01	0.00	61.0	224.9	206.9	15.8	32.6	0.053	0.012	0.015	0.020	0.074	0.005	0.032	0.010	0.020	0.002	0.003	0.001	0.000	0.001	0.001
131	A	5	45.54	0.37	7.50	0.54	19.72	0.24	17.52	8.44	0.13	0.01	0.00	61.3	195.7	210.7	115.7	0.0	0.089	0.011	0.025	0.008	0.120	0.008	0.027	0.014	0.020	0.004	0.000	0.001	0.001	0.003	0.001
134	A	5	45.70	0.39	7.39	0.53	19.80	0.26	17.39	8.43	0.09	0.02	0.00	61.0	188.9	241.4	0.0	30.5	0.074	0.007	0.011	0.014	0.127	0.011	0.041	0.020	0.026	0.002	0.001	0.001	0.000	0.000	0.001
136	A	3	45.65	0.36	7.35	0.53	19.91	0.27	17.37	8.48	0.05	0.01	0.00	60.9	198.9	280.7	18.6	21.7	0.043	0.007	0.032	0.001	0.068	0.022	0.043	0.064	0.005	0.004	0.005	0.002	0.001	0.001	0.001
137	A	5	45.74	0.36	7.40	0.51	19.76	0.27	17.35	8.48	0.11	0.02	0.00	61.0	237.1	194.2	10.3	24.5	0.085	0.010	0.021	0.018	0.141	0.014	0.027	0.047	0.011	0.004	0.000	0.001	0.001	0.001	0.001
138	A	4	45.69	0.36	7.20	0.54	19.88	0.29	17.48	8.42	0.11	0.01	0.00	61.0	234.0	169.7	15.3	31.5	0.040	0.016	0.073	0.011	0.116	0.012	0.032	0.030	0.011	0.004	0.005	0.002	0.001	0.001	0.001
139	A	5	45.66	0.38	7.52	0.52	19.76	0.27	17.33	8.43	0.10	0.02	0.00	61.0	189.5	219.6	24.7	41.2	0.071	0.019	0.020	0.015	0.027	0.009	0.035	0.040	0.015	0.003	0.004	0.001	0.000	0.001	0.001
21	B	5	47.30	0.31	7.57	0.55	17.05	0.24	18.54	8.34	0.09	0.02	0.00	66.0	131.0	381.7	112.3	0.0	0.060	0.013	0.022	0.017	0.112	0.019	0.024	0.014	0.017	0.003	0.000	0.001	0.000	0.002	0.002
25	B	5	46.65	0.37	7.61	0.54	18.17	0.20	17.80	8.47	0.15	0.03	0.00	63.6	132.4	425.9	80.5	0.0	0.069	0.014	0.065	0.006	0.069	0.007	0.020	0.048	0.023	0.002	0.000	0.001	0.001	0.002	0.002
42	B	5	45.95	0.36	7.60	0.56	19.20	0.28	17.44	8.46	0.12	0.02	0.00	61.8	174.8	226.9	86.9	8.8	0.035	0.005	0.048	0.005	0.136	0.015	0.034	0.049	0.020	0.003	0.000	0.001	0.002	0.002	0.001
92	B	3	46.18	0.37	7.73	0.51	18.77	0.22	17.53	8.52	0.16	0.02	0.00	62.5	204.6	332.5	47.4	23.4	0.090	0.015	0.000	0.040	0.084	0.022	0.017	0.015	0.026	0.002	0.000	0.002	0.002	0.002	0.001
102	B	5	47.46	0.28	7.52	0.57	16.83	0.20	18.64	8.34	0.16	0.01	0.00	66.4	110.2	414.4	43.9	6.2	0.081	0.010	0.066	0.015	0.128	0.018	0.026	0.017	0.013	0.002	0.000	0.001	0.001	0.002	0.001

S	G	N	SiO_2	TiO_2	Al_2O_3	Cr_2O_3	FeO	MnO	MgO	CaO	Na_2O	K_2O	P_2O_5	Mg#	NiO	S	Cl	Cu	SiO_2	TiO_2	Al_2O_3	Cr_2O_3	FeO	MnO	MgO	CaO	Na_2O	K_2O	P_2O_5	NiO	S	Cl	Cu
111	B	5	46.36	0.40	7.48	0.54	18.69	0.21	17.55	8.56	0.17	0.02	0.00	62.6	162.2	458.5	58.8	14.4	0.124	0.008	0.186	0.010	0.223	0.007	0.057	0.039	0.015	0.002	0.000	0.001	0.001	0.001	0.000
117	B	5	47.20	0.30	7.60	0.54	17.33	0.18	18.39	8.32	0.12	0.02	0.00	65.4	134.6	385.7	51.4	40.5	0.062	0.019	0.026	0.015	0.078	0.007	0.030	0.010	0.013	0.003	0.000	0.000	0.002	0.002	0.001
122	B	5	46.15	0.39	7.68	0.52	18.71	0.24	17.55	8.60	0.15	0.02	0.00	62.6	170.5	391.7	144.7	42.8	0.147	0.009	0.031	0.017	0.193	0.007	0.023	0.031	0.021	0.003	0.000	0.001	0.001	0.003	0.000
129	B	5	46.22	0.44	7.63	0.53	18.66	0.26	17.55	8.57	0.12	0.02	0.00	62.6	167.0	317.8	29.0	9.0	0.032	0.015	0.020	0.014	0.180	0.009	0.039	0.022	0.012	0.002	0.000	0.002	0.000	0.002	0.001
155	B	5	46.98	0.39	7.66	0.54	17.40	0.27	18.19	8.41	0.15	0.02	0.00	65.1	104.1	384.0	0.0	16.1	0.019	0.007	0.021	0.016	0.078	0.010	0.046	0.024	0.012	0.003	0.000	0.001	0.001	0.000	0.001
173	B	4	46.75	0.42	7.64	0.52	17.85	0.24	17.98	8.44	0.14	0.01	0.01	64.2	147.3	371.8	0.0	11.2	0.028	0.007	0.039	0.020	0.050	0.002	0.073	0.009	0.012	0.006	0.008	0.003	0.001	0.000	0.001
182	B	5	46.44	0.38	7.63	0.57	18.41	0.21	17.67	8.55	0.12	0.02	0.00	63.1	174.8	461.2	55.9	6.6	0.154	0.016	0.133	0.011	0.069	0.010	0.031	0.022	0.015	0.004	0.000	0 002	0.001	0.002	0.000
185	B	5	46.31	0.41	7.72	0.52	18.44	0.27	17.62	8.59	0.09	0.02	0.00	63.0	164.0	386.9	59.1	15.7	0.042	0.008	0.019	0.020	0.145	0.008	0.032	0.009	0.013	0.003	0.000	0.002	0.002	0.002	0.001
190	B	4	45.92	0.47	7.72	0.51	19.01	0.25	17.42	8.54	0.13	0.02	0.00	62.0	158.7	484.6	2.5	23.9	0.083	0.022	0.030	0.022	0.097	0.015	0.033	0.030	0.021	0.005	0.000	0.002	0.001	0.000	0.001
204	B	5	46.35	0.49	7.66	0.54	18.43	0.25	17.51	8.59	0.16	0.02	0.00	62.9	151.2	465.4	39.0	8.7	0.060	0.011	0.084	0.015	0.113	0.014	0.033	0.022	0.014	0.004	0.000	0.001	0.001	0.001	0.001
205	B	5	45.84	0.47	7.66	0.49	19.15	0.27	17.41	8.51	0.18	0.02	0.00	61.8	172.9	325.4	17.1	1.7	0.045	0.012	0.035	0.016	0.082	0.011	0.034	0.021	0.016	0.002	0.000	0.002	0.001	0.001	0.000
211	B	4	46.09	0.43	7.71	0.54	18.90	0.25	17.43	8.48	0.15	0.02	0.00	62.2	170.2	420.4	30.2	6.2	0.041	0.007	0.051	0.008	0.163	0.006	0.023	0.017	0.012	0.001	0.001	0.002	0.002	0.001	0.001
213	B	2	45.94	0.42	7.58	0.48	19.17	0.25	17.33	8.59	0.21	0.02	0.01	61.7	170.1	368.8	18.1	9.6	0.025	0.000	0.080	0.032	0.180	0.004	0.035	0.030	0.025	0.000	0.015	0.005	0.001	0.001	0.001
221	B	4	45.75	0.45	7.57	0.55	19.27	0.25	17.55	8.47	0.11	0.02	0.00	61.9	183.2	253.0	16.1	4.6	0.072	0.007	0.040	0.019	0.091	0.011	0.005	0.010	0.005	0.005	0.001	0.002	0.002	0.001	0.000
228	B	4	45.72	0.44	7.71	0.52	19.37	0.25	17.38	8.46	0.14	0.01	0.00	61.5	164.2	229.3	43.0	6.0	0.030	0.016	0.047	0.028	0.078	0.008	0.039	0.025	0.020	0.003	0.000	0.003	0.001	0.002	0.001
251	B	5	47.33	0.41	7.50	0.50	16.97	0.24	18.57	8.32	0.15	0.01	0.00	66.1	145.0	354.4	7.5	19.1	0.023	0.004	0.031	0.026	0.036	0.008	0.034	0.032	0.020	0.003	0.004	0.003	0.002	0.000	0.001
256	B	5	46.58	0.42	7.60	0.52	18.05	0.27	17.90	8.49	0.16	0.01	0.00	63.9	105.6	350.0	0.0	13.3	0.103	0.018	0.061	0.015	0.112	0.013	0.032	0.030	0.020	0.004	0.000	0.003	0.001	0.000	0.001
278	B	5	46.03	0.41	7.52	0.53	19.08	0.27	17.56	8.45	0.14	0.02	0.00	62.1	196.7	377.3	2.0	13.1	0.022	0.019	0.039	0.008	0.065	0.012	0.036	0.007	0.012	0.002	0.000	0.002	0.001	0.000	0.001
289	B	5	46.56	0.33	7.67	0.57	18.16	0.20	17.87	8.44	0.19	0.02	0.00	63.7	129.4	353.4	11.2	16.0	0.077	0.011	0.056	0.014	0.056	0.007	0.016	0.040	0.008	0.003	0.000	0.002	0.001	0.000	0.001
327	B	5	46.35	0.45	7.76	0.53	18.47	0.26	17.54	8.50	0.12	0.02	0.01	62.9	145.5	382.1	11.3	10.3	0.070	0.020	0.039	0.012	0.126	0.013	0.048	0.027	0.030	0.003	0.005	0.002	0.001	0.001	0.001
334	B	4	47.35	0.40	7.57	0.53	16.87	0.24	18.56	8.36	0.12	0.01	0.00	66.2	103.0	340.3	32.4	5.3	0.077	0.005	0.017	0.017	0.144	0.010	0.034	0.044	0.019	0.002	0.000	0.001	0.000	0.002	0.000
335	B	4	46.73	0.40	7.57	0.50	18.06	0.23	17.91	8.44	0.14	0.01	0.00	63.9	161.9	401.3	0.8	14.7	0.049	0.013	0.094	0.034	0.054	0.016	0.011	0.034	0.024	0.002	0.000	0.003	0.001	0.000	0.001
340	B	3	45.93	0.45	7.62	0.53	19.12	0.26	17.47	8.47	0.13	0.02	0.00	62.0	194.3	428.9	9.4	10.2	0.021	0.016	0.069	0.006	0.115	0.008	0.020	0.029	0.005	0.004	0.000	0.003	0.001	0.001	0.001
351	B	5	46.60	0.38	7.73	0.54	18.08	0.24	17.81	8.45	0.14	0.02	0.00	63.7	153.6	365.6	115.5	15.8	0.136	0.011	0.022	0.022	0.173	0.012	0.034	0.028	0.018	0.001	0.000	0.002	0.000	0.002	0.001
387	B	5	46.35	0.46	7.73	0.50	18.58	0.23	17.49	8.54	0.11	0.02	0.00	62.6	170.6	463.4	5.6	3.1	0.131	0.009	0.009	0.018	0.056	0.015	0.024	0.023	0.021	0.002	0.000	0.001	0.000	0.000	0.000
390	B	5	45.85	0.43	7.60	0.54	19.22	0.27	17.45	8.51	0.11	0.02	0.00	61.8	218.8	357.4	0.0	4.4	0.048	0.016	0.035	0.008	0.067	0.008	0.024	0.033	0.022	0.002	0.000	0.001	0.001	0.000	0.000
392	B	5	47.58	0.31	7.50	0.54	16.86	0.20	18.62	8.27	0.11	0.01	0.00	66.3	108.7	393.1	55.1	5.5	0.082	0.019	0.048	0.008	0.100	0.008	0.029	0.037	0.016	0.003	0.001	0.002	0.001	0.001	0.001
402	B	3	46.94	0.41	7.65	0.52	17.48	0.26	18.15	8.41	0.17	0.01	0.00	64.9	152.0	359.6	83.2	13.0	0.146	0.021	0.043	0.020	0.151	0.006	0.101	0.054	0.024	0.004	0.000	0.001	0.002	0.003	0.002
412	B	3	47.20	0.39	7.62	0.55	17.09	0.23	18.46	8.30	0.16	0.02	0.00	65.8	107.2	428.4	18.7	1.2	0.099	0.017	0.015	0.023	0.048	0.015	0.047	0.058	0.008	0.002	0.000	0.001	0.001	0.001	0.000
418	B	5	45.96	0.43	7.64	0.49	19.14	0.25	17.50	8.42	0.16	0.01	0.00	62.0	182.4	343.5	28.8	4.3	0.048	0.015	0.098	0.020	0.086	0.008	0.014	0.021	0.011	0.002	0.000	0.002	0.001	0.001	0.000
434	B	5	46.07	0.39	7.69	0.54	18.88	0.25	17.50	8.50	0.16	0.02	0.00	62.3	188.5	344.4	57.1	5.6	0.042	0.015	0.034	0.007	0.029	0.010	0.036	0.027	0.022	0.003	0.000	0.002	0.001	0.003	0.001
443	B	5	46.12	0.38	7.72	0.52	18.85	0.20	17.55	8.51	0.13	0.02	0.00	62.4	155.8	329.5	6.6	2.2	0.173	0.014	0.026	0.024	0.029	0.007	0.048	0.041	0.015	0.003	0.000	0.001	0.001	0.000	0.000
116	C	5	47.80	0.33	7.48	0.52	16.59	0.24	18.59	8.33	0.11	0.02	0.00	66.6	111.5	476.5	0.0	23.3	0.118	0.009	0.036	0.018	0.033	0.014	0.024	0.030	0.012	0.005	0.000	0.001	0.001	0.000	0.002
175	C	5	47.79	0.31	7.48	0.55	16.63	0.24	18.55	8.31	0.12	0.01	0.00	66.5	71.3	439.1	13.1	3.8	0.048	0.013	0.052	0.023	0.087	0.011	0.039	0.043	0.016	0.002	0.000	0.001	0.001	0.001	0.000
246	C	4	47.54	0.35	7.60	0.56	16.66	0.24	18.56	8.33	0.15	0.01	0.00	66.5	90.5	488.3	11.4	3.6	0.027	0.016	0.056	0.016	0.104	0.008	0.038	0.028	0.022	0.002	0.000	0.002	0.002	0.001	0.000
270	C	5	48.16	0.31	7.50	0.54	16.18	0.24	18.60	8.35	0.13	0.01	0.00	67.2	89.9	472.6	0.3	8.0	0.072	0.014	0.029	0.023	0.145	0.005	0.048	0.006	0.016	0.002	0.000	0.001	0.002	0.000	0.000
295	C	5	47.69	0.33	7.54	0.55	16.65	0.24	18.49	8.34	0.15	0.02	0.00	66.4	100.8	396.1	6.2	6.0	0.161	0.007	0.027	0.013	0.143	0.012	0.059	0.037	0.013	0.002	0.000	0.001	0.001	0.000	0.000
359	C	5	48.48	0.29	7.53	0.54	15.95	0.23	18.50	8.35	0.11	0.01	0.00	67.4	85.4	494.6	39.9	1.5	0.058	0.013	0.022	0.013	0.133	0.014	0.047	0.032	0.019	0.004	0.000	0.001	0.001	0.002	0.000
436	C	5	48.41	0.21	7.46	0.52	16.12	0.23	18.60	8.37	0.07	0.01	0.00	67.3	59.1	506.5	22.7	6.8	0.100	0.019	0.030	0.011	0.048	0.011	0.027	0.027	0.011	0.002	0.000	0.001	0.001	0.001	0.000

Table and Figure Captions

Table 1. Experimental starting materials.

Table 2. Apollo 15C green glass phase equilibrium experiments. Phase proportions are determined by multiple linear regression of analyzed phases against starting compositions. Run product compositions are given in oxide wt%. Reported value is average of N analyses. Number after oxide is 1 standard deviation on the average and is in units of the last significant digit of the oxide wt%. Pressure is GPa, except when noted as "a" (atmosphere). Temperature in degrees C, run times in hours.

Table 3. A15A green glass phase equilibrium experiments. Notes are as in Table 2. Column marked "Fe %" gives percent of iron loss of experiment compared to starting material.

Table 4. Electron microprobe standards.

Table 5. Analytical statistics and precision.

Table 6. Cumulate mantle melting experiments. Data reported as in Table 2.

Table 7. Compositions of other materials from slide 15426,72. Oxides are reported in wt% and trace elements in ppm, each as an average of N analyses.

Figure 1. Possible formation processes for the Apollo 15 A-B-C picritic glasses discussed in this paper.

Figure 2. Phase diagram of Apollo 15C green glass synthetic analog. Experiment numbers are given next to the symbols.

Figure 3. Phase diagram of Apollo 15A green glass synthetic analog. Experiment numbers are given next to the symbols.

Figure 4. Compositional variation diagrams for the Apollo 15 A-B-C glasses, showing major element oxides in wt. % or trace elements in ppm vs. MgO in wt. %. Group A glasses with low Cl, filled circles; group A glasses with high Cl, empty circles; group B glasses, filled squares; group C glasses; empty triangles. Bars show +/- 2-sigma single bead population errors for each axis, and minimum detection limits for the y-axis are given.

Figure 5. Compositional variation diagrams showing data from Delano (1986) in solid symbols and reanalysis from this paper in unfilled symbols. Circles = group A; squares = group B; triangles = group C.

Figure 6. Compositional variation diagrams for the Apollo 15 A-B-C glasses, showing major oxides vs. Mg#. The Mg# diagram frequently makes all three groups appear continuous, but the MgO diagrams (Figure 4) show they are not.

Figure 7. Apollo 15 A-B-C glasses plotted on an olivine - clinopyroxene - quartz pseudoternary.

Figure 8. Fayalite - forsterite - quartz pseudoternary, showing the Apollo 15 A-B-C glasses and the Apollo 14B glasses. The Apollo 14B glass curve demonstrates the shape of olivine melting or fractionating; the Apollo 15 B and C glasses cannot be melting trends as they point to a source with olivine Mg# too low to be a part of the lunar mantle.

Figure 9. Compositional variation diagrams of the Apollo 15 A, B, and C showing possible compositions for assimilants.

Figure 10. Olivine - clinopyroxene - quartz pseudoternary showing the positions of the olivine - orthopyroxene saturation boundary as it moves with pressure, as based on experimental results. Bold lines: experimental multiple saturation depths; thin lines: estimates of other depths; shaded areas show range of possible assimilants in both composition and depth.

Figure11. Depth and temperature constraints from petrogenetic modeling of the Apollo 15 A,B,C and 14B picritic glasses.

Figure 12. Beads 26A and 35A, showing heterogeneous non-vesicular agglutinate rims.

Figure 13. Beads 80A and 84A, showing homogeneous vesicular partial rims.

Table 1. Experimental starting materials

	SiO_2	TiO_2	Al_2O_3	Cr_2O_3	FeO	MnO	MgO	CaO	Na_2O	K_2O	Tot	Mg#
A15A	46.01	0.42	7.93	0.46	18.88	0.24	17.58	8.48	0.00	0.00	100.00	62.39
A15C	48.29	0.23	7.77	0.55	16.12	0.19	18.27	8.59	0.00	0.00	100.00	66.89
Cumulate melting	45.76	0.07	10.27	0.00	12.74	0.00	21.17	9.83	0.17	0.00	100.01	74.76

Table 2. Apollo 15C green glass phase equilibrium experiments.

#	P	T	t	R^2	Prop	phase	N	SiO_2		TiO_2		Al_2O_3		Cr_2O_3		FeO		MnO		MgO		CaO		Total	K_D	Mg#
3	1 a	1420	3	0.50	99	glass	5	48.9	2	0.23	2	7.93	6	0.52	3	15.7	3	0.20	2	18.1	1	8.50	5	99.99		
					1	spinel	5	0.2	2	0.09	9	9.5	4	59.7	8	17.0	5	0.27	2	13.0	3	0.21	5	99.96	1.50	57.7
5	1 a	1390	4	0.44	99	glass	5	48.9	3	0.26	1	7.89	3	0.51	1	16.0	2	0.17	2	17.9	1	8.45	7	100.00		
					1	spinel	8	0.4	2	0.10	2	10.6	7	58.3	9	17.6	8	0.29	3	13.1	2	0.30	5	100.72	1.50	57.0
6	1 a	1370	3	0.02	96	glass	6	48.70	2	0.22	1	7.9	1	0.55	3	16.2	1	0.20	1	17.23	8	8.90	7	99.88		
					3	olivine	9	39.7	3	0.00	0	0.07	3	0.17	1	13.1	1	0.20	5	47.4	3	0.29	2	100.83	0.29	86.6
					1	spinel	3	0.6	1	0.12	0	10.2	3	54.9	3	20.6	2	0.17	4	11.7	2	0.33	5	98.62	1.87	50.4
8	2.0	1490	2	0.49	72	glass	12	46.5	2	0.33	1	9.8	1	0.39	2	17.8	3	0.25	12	13.7	2	11.04	8	99.82		
					28	opx	11	55.0	3	0.02	1	2.1	4	0.73	9	11.3	2	0.15	3	28.7	2	2.0	2	100.04	0.30	81.9
9	1.6	1440	3	0.25	69	glass	5	46.0	1	0.30	1	9.8	1	0.32	1	18.3	3	0.21	4	13.6	1	11.54	6	100.07		
					31	opx	6	54.4	3	0.03	1	1.9	2	0.74	5	11.49	6	0.13	1	28.4	2	1.90	5	98.97	0.30	81.5
10	1.3	1380	8	0.05	61	glass	5	46.5	3	0.37	2	11.13	4	0.28	1	17.6	2	0.30	2	11.71	2	11.5	1	99.46		
					8	olivine	5	38.1	5	0.00	0	0.11	5	0.20	2	20.6	4	0.19	4	40.5	5	0.5	1	100.14	0.34	77.8
					6	opx	3	54.5	1	0.00	0	2.8	7	0.9	1	12.5	1	0.17	5	27.3	4	1.92	9	100.07	0.30	79.6
					25	cpx	5	53.9	4	0.03	2	2.5	3	0.85	5	12.3	1	0.18	4	25.0	5	5.2	5	99.94	0.33	78.3
12	1.3	1450	3	0 16	84	glass	8	47.3	2	0.25	1	8.95	4	0.50	2	16.6	2	0.23	2	15.2	1	10.3	2	99.42		
					4	olivine	15	39.5	5	0.00	0	0.08	4	0.31	2	16.5	4	0.14	2	43.6	5	0.35	5	100.40	0.35	82.5
					12	opx	13	55.2	3	0.04	1	1.8	3	0.88	0	10.2	2	0.15	2	30.5	2	1.64	5	100.40	0.31	84.3
13	1.3	1470	4	0.01	89	glass	6	47.7	2	0.22	1	8.53	5	0.46	2	16.87	9	0.19	3	16.57	4	9.4	1	99.95		
					2	olivine	8	39.0	2	0.00	0	0.08	1	0.28	2	15.6	2	0.10	2	44.4	3	0.27	1	99.68	0.34	83.5
					9	opx	8	55.5	4	0.02	1	1.4	2	0.8	1	9.5	2	0.08	2	30.7	3	1.17	4	99.15	0.31	85.1
14	1.3	1490	2	0.04	97	glass	15	48.6	3	0.21	2	7.85	7	0.50	2	16.2	2	0.19	5	17.45	9	8.98	8	99.96		
					3	olivine	5	39.4	1	0.00	0	0.08	1	0.32	2	14.7	3	0.11	1	44.8	2	0.26	1	99.66	0.35	84.4
					0	opx	4	55.5	2	0.03	1	1.2	2	0.67	5	9.0	1	0.11	2	31.3	3	1.12	2	98.94	0.31	86.1
15	1.3	1510	3	0.02	96	glass	5	48.7	2	0.22	1	7.9	1	0.55	3	16.2	1	0.20	1	17.23	8	8.90	7	99.88		
					4	olivine	3	40.0	3	0.00	0	0.04	0	0.29	1	14.7	3	0.11	2	44.6	2	0.26	3	99.98	0.35	84.4
					0	opx	3	56.2	5	0.00	0	1.4	2	0.7	1	9.07	7	0.09	2	30.98	4	1.41	1	99.86	0.31	85.9
17	1.5	1530	2		100	glass	20	48.3	2	0.22	2	7.28	8	0.56	2	14.50	2	0.16	3	19.7	1	9.08	7	99.79		
18	1.1	1490	2.5	0.02	99	glass	20	48.0	2	0.24	2	7.79	6	0.59	2	15.90	1	0.17	2	17.9	1	8.63	7	99.25		
					1	ol	3	38.10	2	0.00	0	0.05	1	0.33	1	13.8	2	0.08	2	48.72	4	0.26	2	101.31	0.32	86.3
19	1.3	1360	5			glass	No analyzable glass; tiny interstitial areas only, modified by quench pyroxene																			
						olivine	7	38.1	5	0.02	1	0.06	1	0.10	1	23.8	4	0.18	3	36.9	3	0.36	3	99.55		73.4
						opx	1	52.9		0.05		3.59		0.66		13.7		0.16		26.2		2.67		99.89		77.4
						cpx	6	53.2	6	0.05	3	3.4	4	0.88	8	13.3	3	0.19	4	22.7	8	6.8	6	100.47		75.3
						spinel	3	0.0	0	0.10	2	39	2	26	2	21.5	3	0.14	4	13.0	3	0.4	4	100.34		51.8

Table 3. A15A green glass phase equilibrium experiments.

Experiments with known phase composition data

Run	P	T	t	cap.	R^2	Fe%	P	phase	N	SiO_2	TiO_2	Al_2O_3	Cr_2O_3	FeO	MnO	MgO	CaO	Total	K_D	Mg#
39	1 a	1408	0.5	Fe				glass	9	45.8 3	0.42 2	7.89 8	0.5 3	18.8 3	0.24 3	17.5 1	8.4 2	99.55		62.4
24	1.0	1412	2	Fe	6.2	12	89	glass	4	47.5 3	0.41 5	9.2 2	0.44 3	16.5 2	0.23 2	15.4 3	9.63 7	99.37		62.4
							9	olivine	4	39.3 1	0.00 0	0.00 0	0.27 5	17.4 4	0.15 1	44.0 2	0.39 1	101.43	0.37	81.8
26	2.5	1463	2.5	Fe				olivine	5	37.8 1	0.03 2	0.22 2	0.19 3	31.1 8	0.27 2	32.0 7	0.7 2	101.63		64.7
								garnet	4	41.0 3	0.54 6	22.1 6	1.0 1	16.7 3	0.32 2	13.9 4	6.7 2	102.23		59.7
35	2.0	1503	0.7	Fe	0	Tr.	89	glass	4	46.4 3	0.39 3	8.8 3	0.41 1	19.5 2	0.20 3	15.6 1	9.2 1	100.5		58.7
							6	olivine	4	39.2 2	0.00 0	0.13 2	0.25 3	19.2 1	0.16 3	42.4 1	0.39 1	101.70	0.36	79.7
							5	opx	3	54.6 8	0.04 1	2.3 7	0.40 5	11.8 2	0.13 2	28.4 4	2.7 4	100.44	0.33	81.2
38	1.5	1500	1	Fe	3.3	9	98	glass	5	47.0 1	0.41 5	8.31 7	0.48 1	17.3 2	0.26 2	17.5 1	8.7 2	99.92		64.3
							2	olivine		39.4 2	0.00 0	0.10 1	0.29 3	16.36 6	0.15 4	45.1 4	0.35 3	101.76	0.37	83.1
45	1.5	1485	1.1	C	2.7	8	96	glass	5	46.7 5	0.43 3	8.2 1	0.39 2	17.3 4	0.2 1	16.6 5	8.8 2	98.61		63.1
							4	olivine	3	39.2 1	0.01 1	0.04 3	0.25 2	16.5 2	0.17 4	44.1 5	0.37 4	100.66	0.36	82.6
53	1.5	1445	3.4	C				glass	4	46.9 4	0.51 3	9.1 1	0.39 1	16.0 2	0.16 3	15.5 3	9.7 1	98.25		63.4
								opx	3	54.1 3	0.06 1	1.9 1	0.39 4	11.4 4	0.17 2	27.5 2	3.00 9	98.49	0.40	81.1
								olivine	3										0.37	82.4
54	2.0	1515	1.3	C	1.9	7	95	glass		47.3 1	0.42 4	8.21 9	0.36 2	17.8 3	0.12 3	16.9 1	8.9 2	100.08		62.8
							4	olivine		39.7 5	0.00 0	0.1 1	0.20 5	16.63 8	0.15 3	44.6 1	0.35 2	101.68	0.35	82.7
69	2.5	1570	1.3	C	5.5	8	89	glass	2	46.7 7	0.53 1	8.99 1	0.28 1	18 1	0.09 4	14.98 1	8.6 6	98.39		59.4
							9	opx	2	53.71 4	0.00 0	2.73 9	0.39 1	10.56 1	0.12 1	29.84 7	1.98 8	99.30	0.29	83.4

Experiments with known phases

Run	P	T	Fe %	Cap.	Phases
25	2.0	1459	2.7	Fe	Glass, olivine, opx
30	1.5	1443	0.8	Fe	Glass, olivine, opx
34	2.0	1490	0.8	Fe	Glass, olivine, opx
51	1.0	1485	1.9	C	Glass
55, 65	2.5	1524	1	C	Glass, pyroxene, olivine, garnet
62	1.5	1460	1.5	C	Glass, olivine, opx
63	2	1556	1	C	Glass
64	2.5	1554	1	C	Glass, opx
67	1.5	1522	0.6	C	Glass
68	2.5	1530	1	C	Glass, pyroxene, garnet
72	1.0	1475	0.9	C	Glass, olivine

Table 4. Electron microprobe standards.

	SiO_2	TiO_2	Al_2O_3	FeO	MnO	MgO	CaO	Na_2O	K_2O	P_2O_5	Tot	Source
DJ 35 (synthetic diopside/jadeite)	56.88		8.82			12.10	16.83	5.36			99.99	
Alvin 1690-20 (MORB)	49.9	1.71	15.5	9.92	0	7.68	10.8	3.13	0.16	0.18	98.98	Grove *et al.* (1990)
70-002 (MORB)	49.6	1.2	15.8	8.98	0.17	8.66	11.9	2.67	0.1	0.12	99.20	Kinzler and Grove (1992)

Table 5. Analytical statistics and precision.

Comparison with Delano (1979, 1986) analyses	SiO_2	TiO_2	Al_2O_3	Cr_2O_3	FeO	MnO	MgO	CaO
Average difference between our data and Delano's data (wt %)	0.17	0.01	-0.34	-0.03	-0.04	0.05	0.25	-0.22
Avg. difference between our data and Delano's (percent of Delano's wt %)	0.37	3.69	-4.52	-4.93	-0.23	19.95	1.44	-2.55
Analytical precision								
1 σ standard deviation from microprobe counting statistics (%)	**0.16%**	7 - 9%	**0.66%**	7 - 9%	**0.68%**	10 - 12%	**0.31%**	**0.64%**
(Bold values are constant through all analyses)								
Microprobe x-ray counting times (seconds)	100	80	40	40	60	40	100	40
Minimum detectable limits (Major oxides in wt %, traces in ppm)	0.019	0.080	0.007	0.080	0.007	0.110	0.003	0.006
+/- 2 σ population st. dev. for single beads (Major oxides in wt %, traces in ppm)	0.12	0.05	0.09	0.08	0.2	0.04	0.1	0.1

Comparison with Delano (1979, 1986) analyses	Na_2O	K_2O	P_2O_5	NiO	S	Cl	Cu	Zn	F
Average difference between our data and Delano's data (wt %)									
Avg. difference between our data and Delano's (percent of Delano's wt %)									
Analytical precision									
1 σ standard deviation from microprobe counting statistics (%)	17 - 42%	27 - 60%	99%	12 - 18%	4 - 6%	40%	70%	99%	99%
(Bold values are constant through all analyses)									
Microprobe x-ray counting times (seconds)	5	80	40	300	300	40	300	300	300
Minimum detectable limits (Major oxides in wt %, traces in ppm)	0.300	0.450	0.990	0.150	0.050	0.990	0.700	0.990	0.990
+/- 2 σ population st. dev. for single beads (Major oxides in wt %, traces in ppm)	0.05-0.12	0.06	0.02	32-48	6	56	36		

Table 6. Cumulate mantle melting experiments.

Run	P	T	t	R^2	Prop.	phase	N	SiO_2		TiO_2	Al_2O_3	FeO	MgO	CaO	Na_2O	Total	K_D	Mg#
2	1.3	1400	2	0.12	77	glass	9	47.3	5	0.081	13.148	12.81	13.72	12.487	0.053	99.53		65.61
					23	olivine	6	39.5	4	0.000	0.101	13.73	46.14	0.401	0.000	99.83	0.32	85.69
3	1.3	1380	2	0.15	78	glass	4	47.1	1	0.000	13.245	12.01	13.827	12.51	0.021	98.64		67.22
					22	olivine	3	39.5	4	0.020	0.081	13.295	45.94	0.392	0.00	99.22	0.33	86.04
4	1.3	1360	5	0.26	69	glass	5	46.2	3	0.083	14.11	12.074	12.735	12.92	0.042	98.12		65.27
					21	olivine	5	34.9	2	0.000	0.081	14.51	44.23	0.413	0.00	94.11	0.35	84.41
					10	cpx	6	52.6	4	0.021	5.17	8.01	23.25	10.95	0.012	99.78	0.36	83.81
7	1.3	1420	2	0.17	88	glass	7	45.9	3	0.000	11.63	12.81	17.52	11.403	0.104	99.24		70.92
					12	olivine	13	40.4	4	0.000	0.092	11.72	47.85	0.381	0.021	100.37	0.34	87.91
11	1.3	1380				glass		48.2		0.1	12.5	10.8	15.4	13.0	0.0	100.02		71.74

Table 7. Compositions of other materials from slide 15426,72.

Sample	Grp	N	SiO_2	TiO_2	Al_2O_3	Cr_2O	FeO	MnO	MgO	CaO	Na_2O	K_2O	P_2O_5	Tot	Mg#	NiO	S	Cl	Cu
Vesicular rim analyses																			
Rim on 84	A	3	46.95	0.36	8.30	0.53	17.80	0.22	16.68	8.79	0.21	0.029	0.000	100	62.6	280	1768	32	68
Rim on 80	A	5	45.46	0.51	11.14	0.48	16.32	0.18	15.84	9.62	0.23	0.043	0.000	100	63.4	423	2317	194	56
Rim on 190	B	5	46.10	0.39	8.32	0.56	18.21	0.19	17.16	8.79	0.18	0.023	0.000	100	62.7	271	959	41	60
Rim on 155	B	3	45.07	0.52	8.09	0.50	19.33	0.20	17.17	8.67	0.26	0.030	0.000	100	61.3	318	2129	144	37
Agglutinate glasses																			
Rim on 35	A	2	45.75	0.38	7.36	0.54	19.47	0.23	17.60	8.38	0.14	0.026	0.000	100	61.7	90	1976	92	23
Rim on 35	A	4	44.67	5.33	9.24	0.32	20.49	0.18	8.73	10.20	0.45	0.158	0.090	100	43.2	42	2489	54	14
Agglutinate glass (photo 17)		1	45.80	0.68	8.18	0.47	19.60	0.23	16.11	8.77	0.06	0.035	0.000	100	59.4	134	871	0	0
Agglutinate glass (photo 17)		1	45.55	1.62	8.59	0.42	19.57	0.27	14.54	8.94	0.21	0.083	0.108	100	57.0	97	1046	0	122
Rim on 26	A	1	44.17	5.11	9.75	0.28	20.36	0.27	9.35	9.63	0.57	0.229	0.180	100	45.0	23	2113	0	0
Agglutinate glass (photo 23)		3	44.50	4.84	10.33	0.26	19.56	0.27	9.29	9.87	0.53	0.220	0.219	100	45.8	19	1869	0	183
Yellow agglutinate (photo 28)		2	44.61	4.81	10.35	0.28	19.41	0.25	9.83	9.68	0.44	0.177	0.123	100	47.4	15	668	0	138
Yellow agglutinate (photo 31)		4	44.71	4.64	10.30	0.26	19.60	0.25	9.72	9.73	0.39	0.196	0.133	100	46.9	5	906	0	162
Agglutinate glass near 190	B	2	45.96	5.02	9.97	0.28	19.10	0.26	9.54	9.44	0.28	0.107	0.032	100	47.1	6	22	0	299
HASP glass inclusion in bear #26A		1	36.09	0.83	17.41	0.01	16.46	0.17	13.47	15.49	0.00	0.002	0.000	100	59.3	577	30	0	90
Other soil materials																			
Yellow glass (photo 17)		3	43.23	3.36	8.08	0.57	22.18	0.27	13.64	8.22	0.29	0.064	0.044	100	52.3	104	878	0	2
Yellow glass (photo 17)		2	46.91	3.38	11.82	0.24	16.41	0.20	10.81	9.77	0.36	0.101	0.000	100	54.0	24	0	0	29
Brown glass inclusion (photo 17)		2	44.99	0.36	7.28	0.49	20.57	0.26	17.48	8.46	0.06	0.015	0.000	100	60.2	195	220	0	0
Glass chip (photo 23)		1	45.39	0.36	7.16	0.51	20.31	0.23	17.86	8.09	0.04	0.018	0.000	100	61.0	167	295	0	0
Glass chip (photo 23)		1	45.72	0.28	7.68	0.53	19.53	0.25	17.30	8.59	0.02	0.025	0.000	100	61.2	242	192	0	218
Dark brown grain (photo 28)		3	43.31	3.53	8.46	0.59	21.94	0.30	12.81	8.69	0.20	0.061	0.049	100	51.0	59	973	0	33
Yellow glass (photo 36)		4	43.32	3.63	8.59	0.54	21.84	0.29	12.78	8.49	0.34	0.074	0.043	100	51.0	58	1044	0	45
Yellow glass (photo 10)		4	44.75	4.53	10.37	0.29	19.64	0.24	9.69	9.65	0.43	0.197	0.145	100	46.8	0	1115	0	37
Glass chip near 190	B	1	48.39	0.26	7.60	0.47	16.19	0.23	18.21	8.54	0.04	0.025	0.000	100	66.7	86	349	0	246
Glass chip near 190	B	1	46.46	0.31	7.60	0.51	19.16	0.25	16.95	8.66	0.02	0.017	0.000	100	61.2	145	596	0	50
Glass chip near 190	B	1	45.98	4.63	10.57	0.24	19.32	0.24	7.31	10.45	0.81	0.278	0.163	100	40.3	0	0	0	148
Glass chip near 155	B	1	46.14	0.30	7.65	0.49	19.51	0.24	17.03	8.56	0.04	0.010	0.000	100	60.9	151	257	0	0
Glass chip near 155	B	1	45.83	3.97	6.09	0.43	19.18	0.29	10.75	13.20	0.01	0.022	0.166	100	50.0	0	957	0	70
Glass chip near 155	B	1	44.95	4.54	10.60	0.10	18.82	0.28	6.88	12.91	0.42	0.075	0.305	100	39.4	0	2410	0	0
Glass chip near 155	B	1	46.31	0.43	6.97	0.48	18.68	0.23	18.60	8.19	0.08	0.012	0.000	100	64.0	81	243	0	0
Glass chip near 84	A	1	45.93	0.32	7.79	0.45	19.58	0.20	17.15	8.48	0.05	0.021	0.000	100	61.0	147	160	0	0
Glass chip near 84	A	1	45.60	0.44	7.21	0.49	19.15	0.25	18.33	8.42	0.04	0.031	0.000	100	63.0	121	262	0	91
Glass chip near 84	A	1	51.88	1.70	1.62	0.61	15.84	0.29	20.16	7.87	0.00	0.002	0.000	100	69.4	14	61	0	252
Glass chip near 80	A	1	47.24	0.30	7.79	0.53	17.07	0.28	18.24	8.37	0.13	0.012	0.000	100	65.6	130	495	0	176
Glass chip near 80	A	1	46.08	0.33	7.56	0.46	19.33	0.25	17.26	8.47	0.20	0.028	0.000	100	61.4	290	304	0	0
Glass chip near 80	A	1	45.85	0.29	7.45	0.53	19.61	0.26	17.56	8.38	0.01	0.024	0.000	100	61.5	193	204	0	100
Glass chip near 80	A	1	49.24	0.52	10.30	0.61	18.44	0.30	7.64	12.82	0.09	0.018	0.000	100	42.5	0	576	0	0
Glass chip near 80	A	1	45.78	0.36	7.43	0.54	20.02	0.26	17.17	8.33	0.05	0.025	0.000	100	60.5	264	209	0	0

Processes in the lunar cumulate mantle considered for formation of the Apollo 15 A-B-C compositional trends

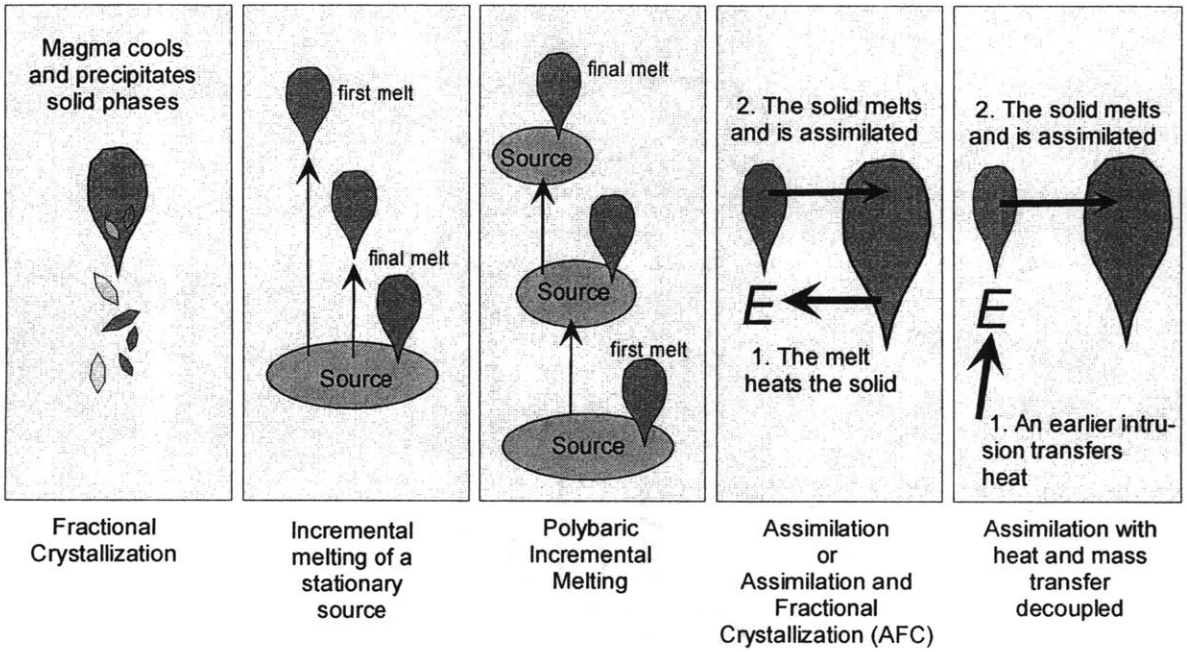

Figure 1

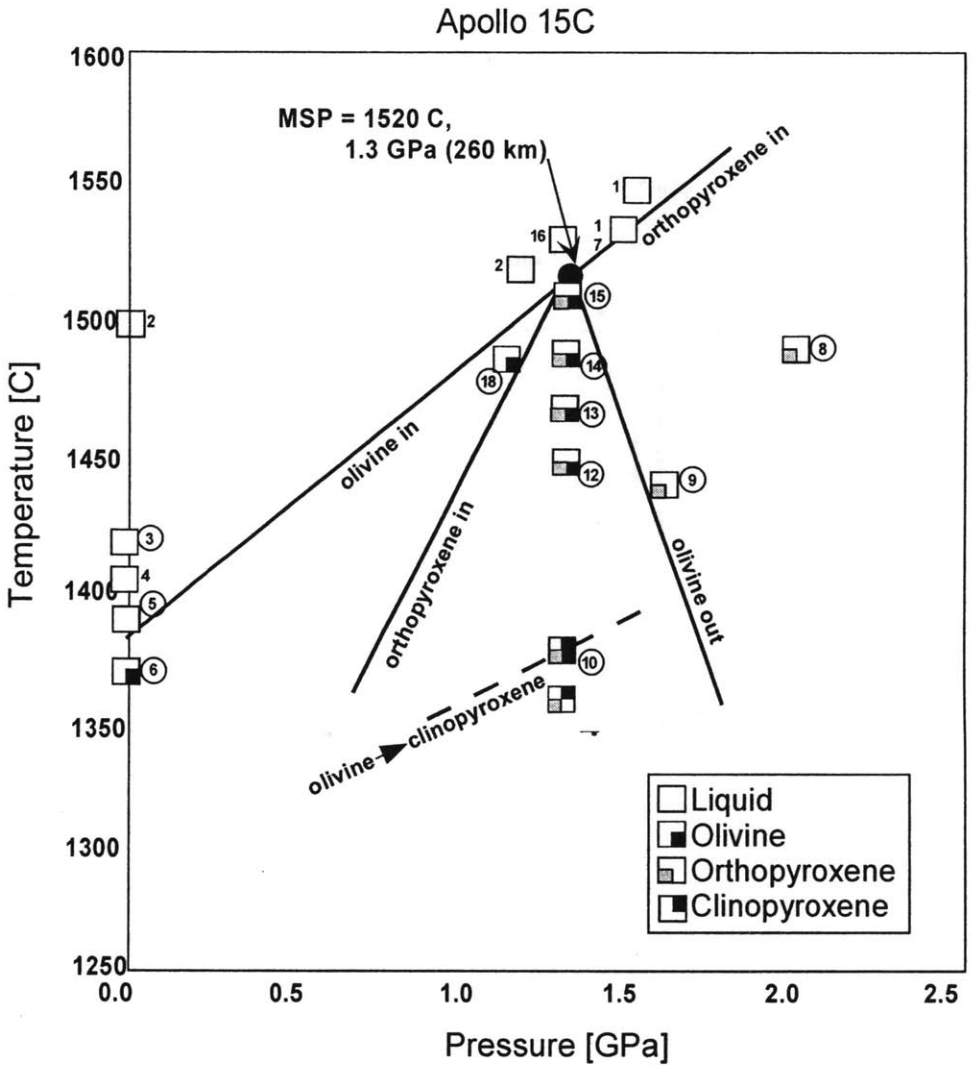
Apollo 15C
MSP = 1520 C,
1.3 GPa (260 km)
orthopyroxene in
olivine in
orthopyroxene in
olivine out
olivine→clinopyroxene
Liquid
Olivine
Orthopyroxene
Clinopyroxene
Temperature [C]
Pressure [GPa]
1600
1550
1500
1450
1400
1350
1300
1250
0.0
0.5
1.0
1.5
2.0
2.5

Figure 2.

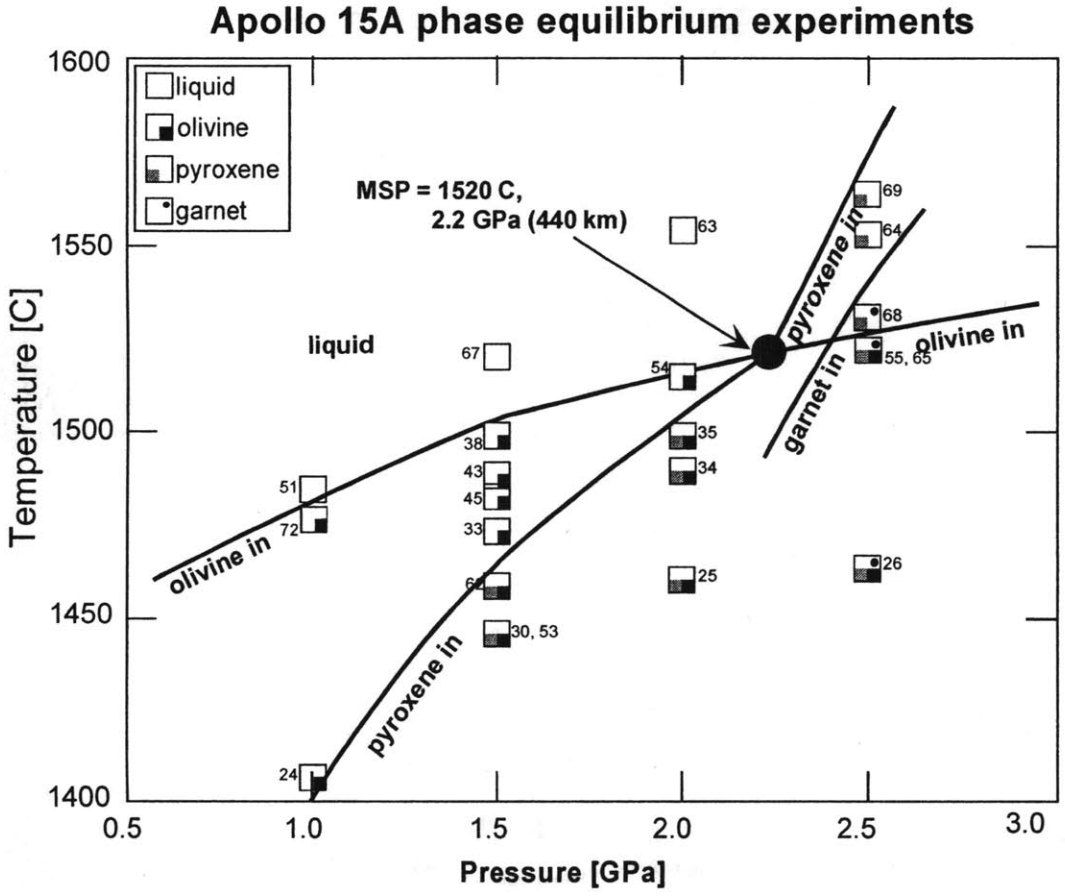
Apollo 15A phase equilibrium experiments
liquid
olivine
pyroxene
garnet
MSP = 1520 C,
2.2 GPa (440 km)
liquid
olivine in
pyroxene in
garnet in
olivine in
pyroxene in
Temperature [C]
Pressure [GPa]
1600
1550
1500
1450
1400
0.5
1.0
1.5
2.0
2.5
3.0
63
69
64
68
55, 65
67
54
35
34
38
43
45
33
51
72
25
26
60
30, 53
24

Figure 3

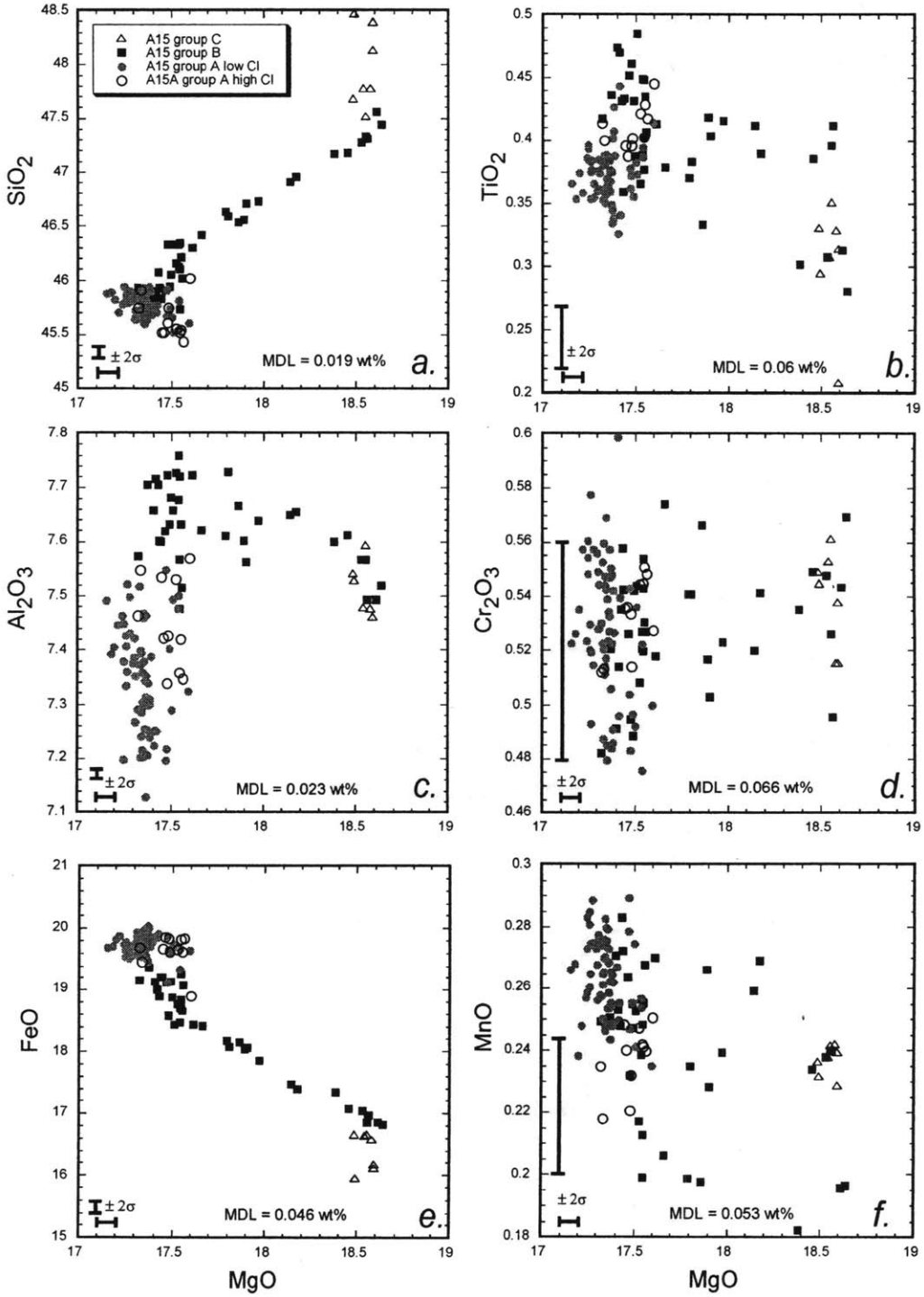
A15 group C
A15 group B
A15 group A low Cl
A15A group A high Cl
SiO2
MDL = 0.019 wt%
a.
TiO2
MDL = 0.06 wt%
b.
Al2O3
MDL = 0.023 wt%
c.
Cr2O3
MDL = 0.066 wt%
d.
FeO
MDL = 0.046 wt%
e.
MnO
MDL = 0.053 wt%
f.
±2σ
MgO
MgO

Figure 4a

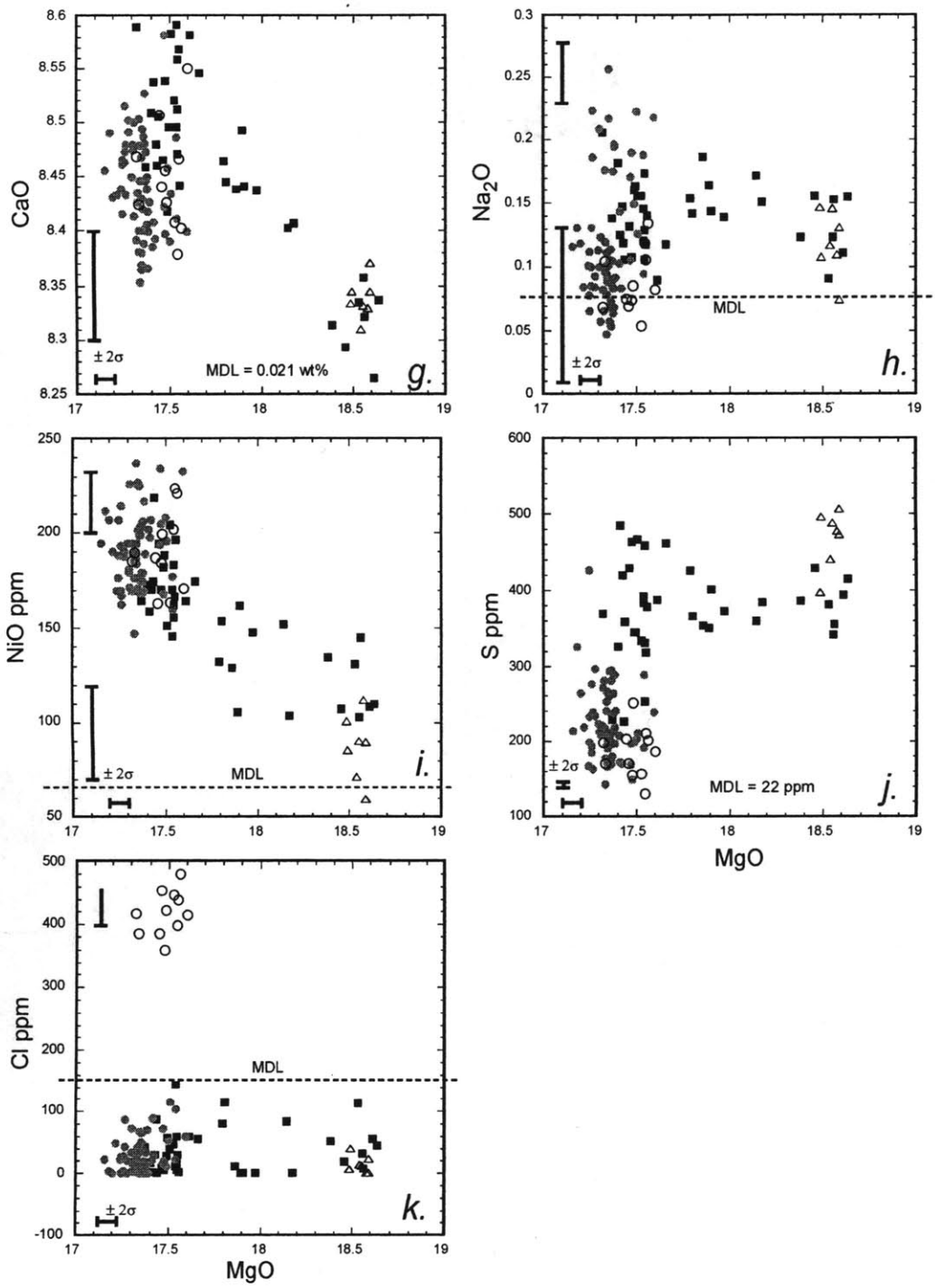
CaO
MDL = 0.021 wt%
± 2σ
g.
Na_2O
MDL
h.
NiO ppm
i.
S ppm
MDL = 22 ppm
j.
Cl ppm
k.
MgO
MgO

Figure 4b

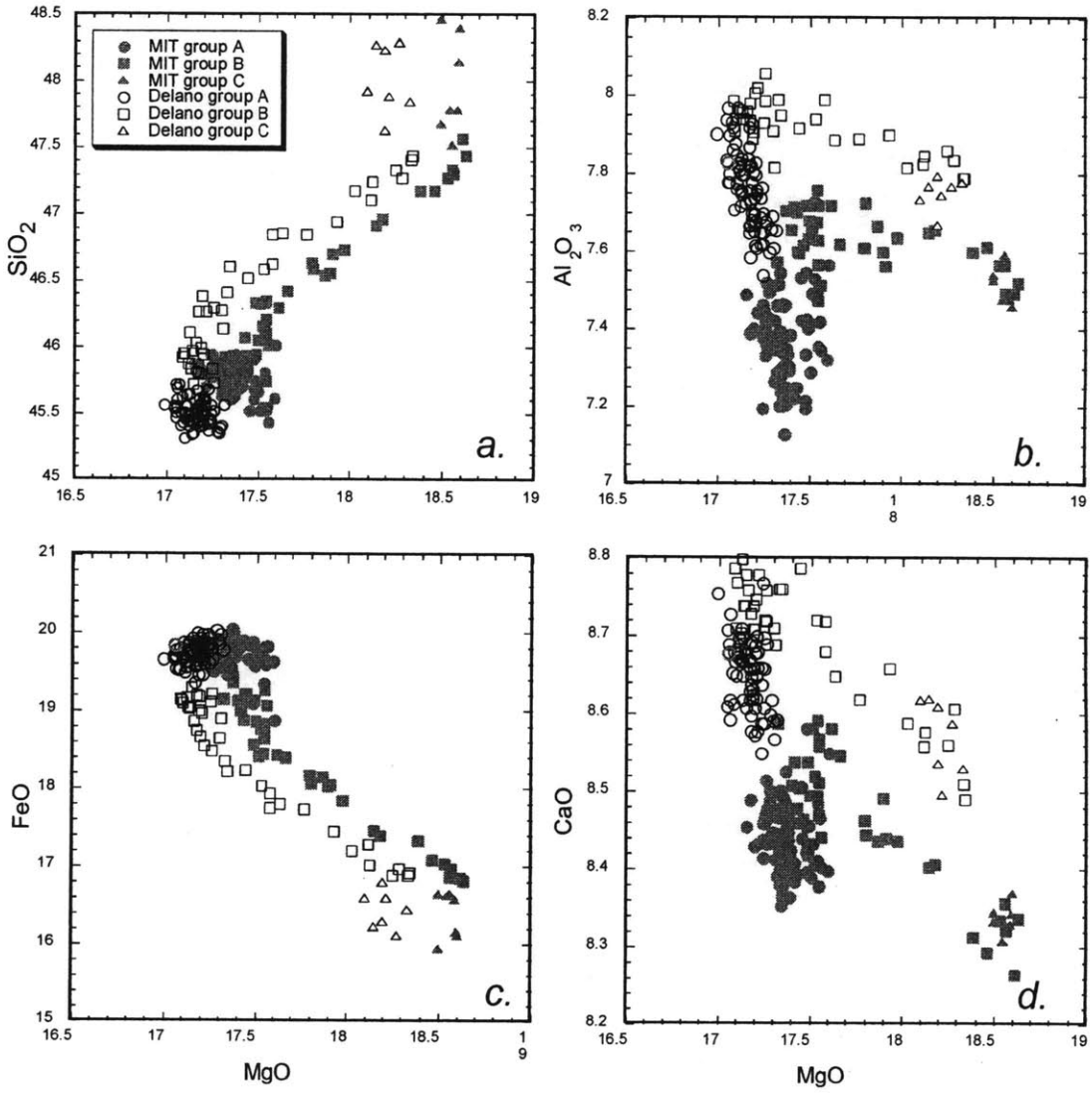
MIT group A
MIT group B
MIT group C
Delano group A
Delano group B
Delano group C
a.
b.
c.
d.
SiO2
Al2O3
FeO
CaO
MgO
MgO

Figure 5.

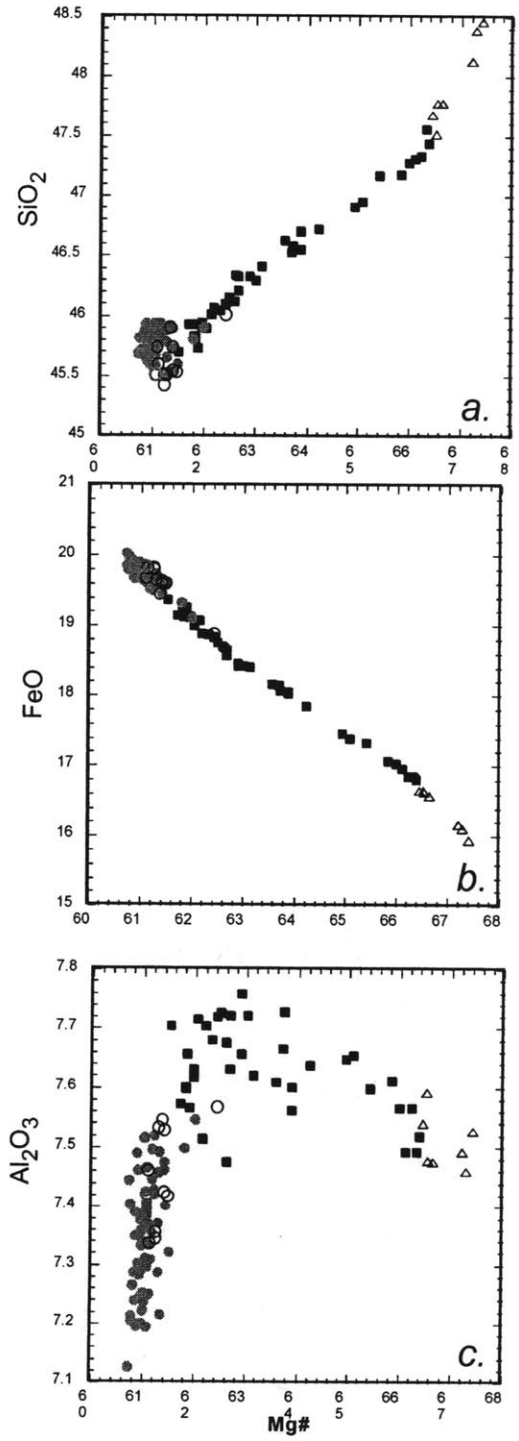

Figure 6.

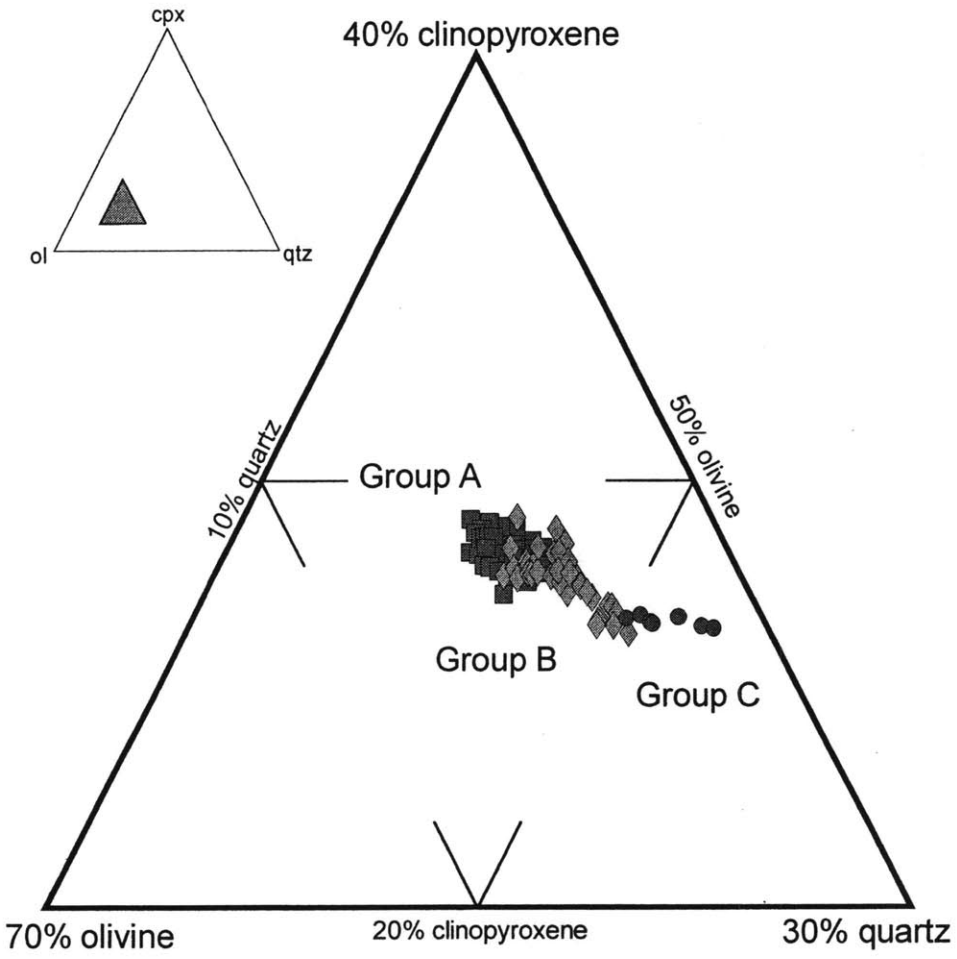
cpx
ol
qtz
40% clinopyroxene
10% quartz
50% olivine
Group A
Group B
Group C
70% olivine
20% clinopyroxene
30% quartz

Figure 7.

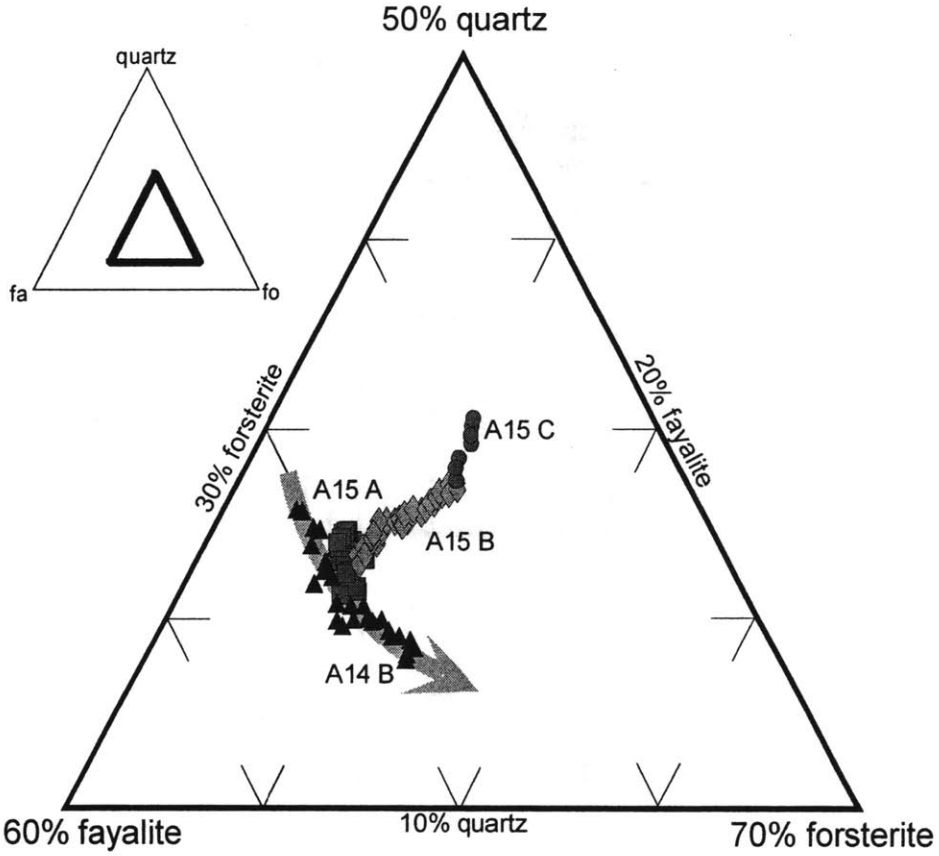
50% quartz
quartz
fa
fo
30% forsterite
20% fayalite
A15 C
A15 A
A15 B
A14 B
60% fayalite
10% quartz
70% forsterite

Figure 8.

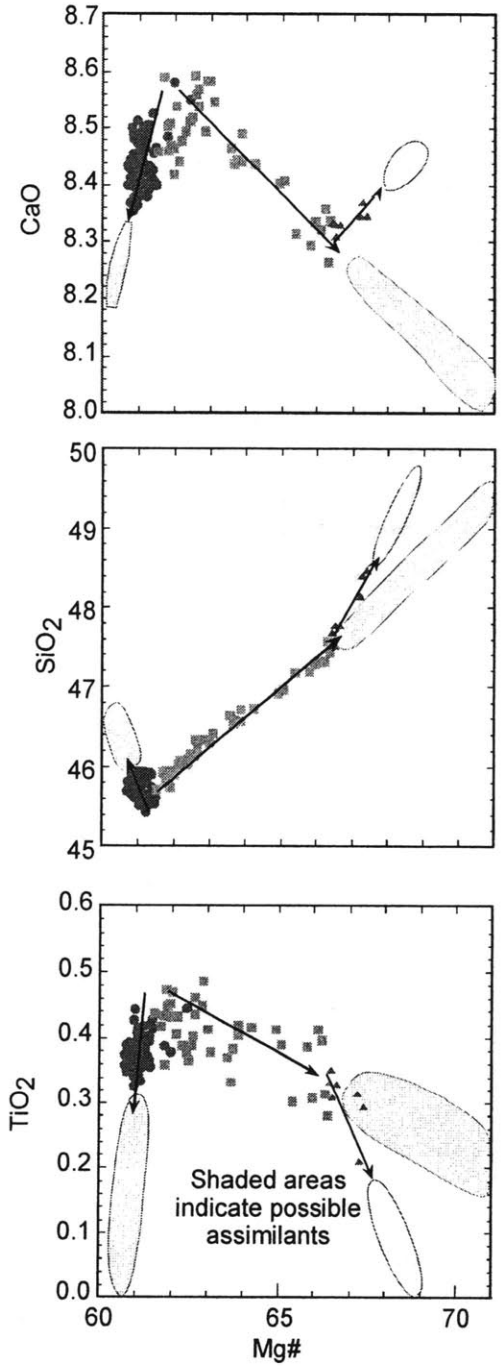
8.7
8.6
8.5
8.4
8.3
8.2
8.1
8.0
CaO
50
49
48
47
46
45
SiO2
0.6
0.5
0.4
0.3
0.2
0.1
0.0
TiO2
Shaded areas
indicate possible
assimilants
60
65
70
Mg#

Figure 9.

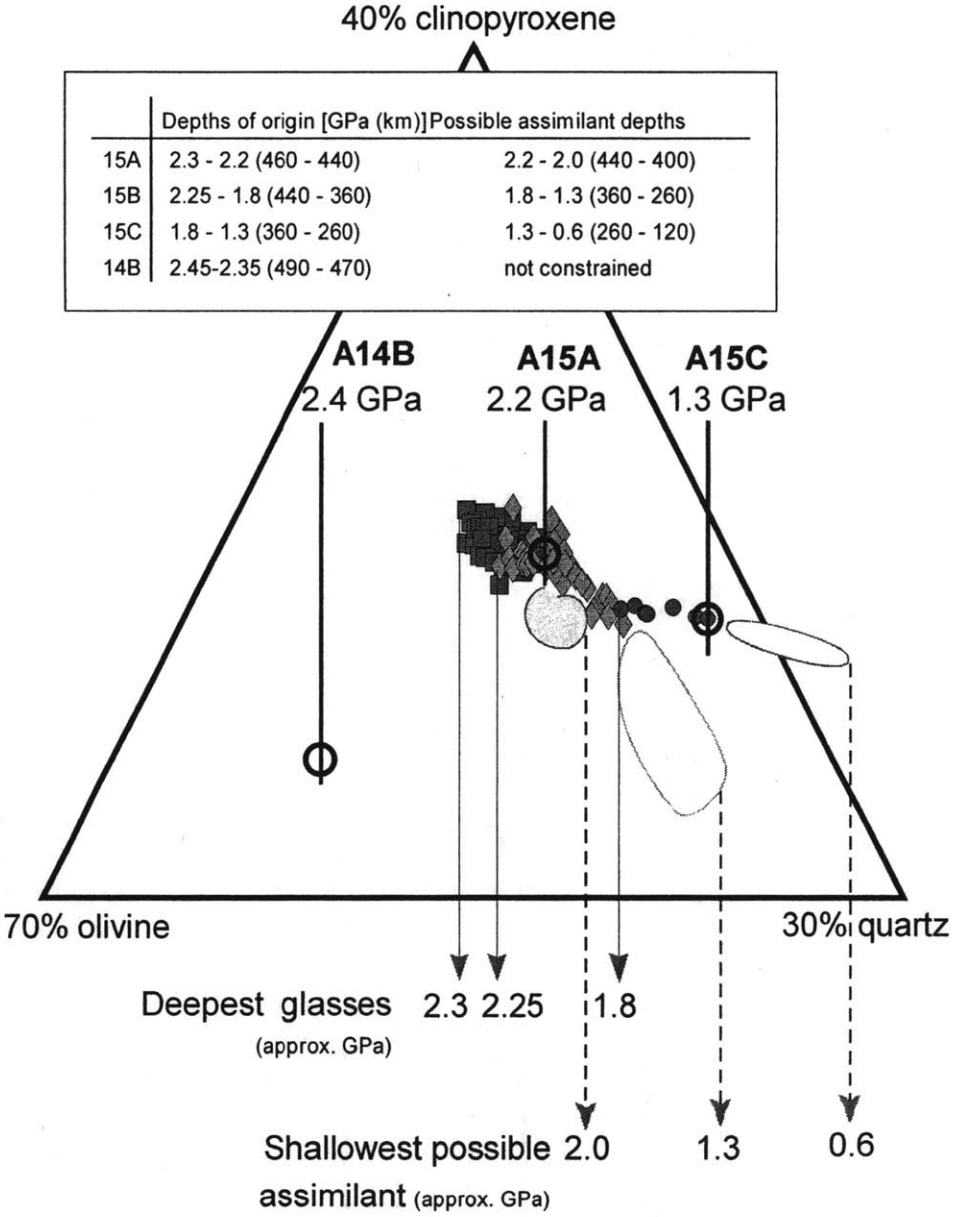
40% clinopyroxene
Depths of origin [GPa (km)]
Possible assimilant depths
15A
2.3 - 2.2 (460 - 440)
2.2 - 2.0 (440 - 400)
15B
2.25 - 1.8 (440 - 360)
1.8 - 1.3 (360 - 260)
15C
1.8 - 1.3 (360 - 260)
1.3 - 0.6 (260 - 120)
14B
2.45-2.35 (490 - 470)
not constrained
A14B
2.4 GPa
A15A
2.2 GPa
A15C
1.3 GPa
70% olivine
30% quartz
Deepest glasses
(approx. GPa)
2.3
2.25
1.8
Shallowest possible
assimilant (approx. GPa)
2.0
1.3
0.6

Figure 10.

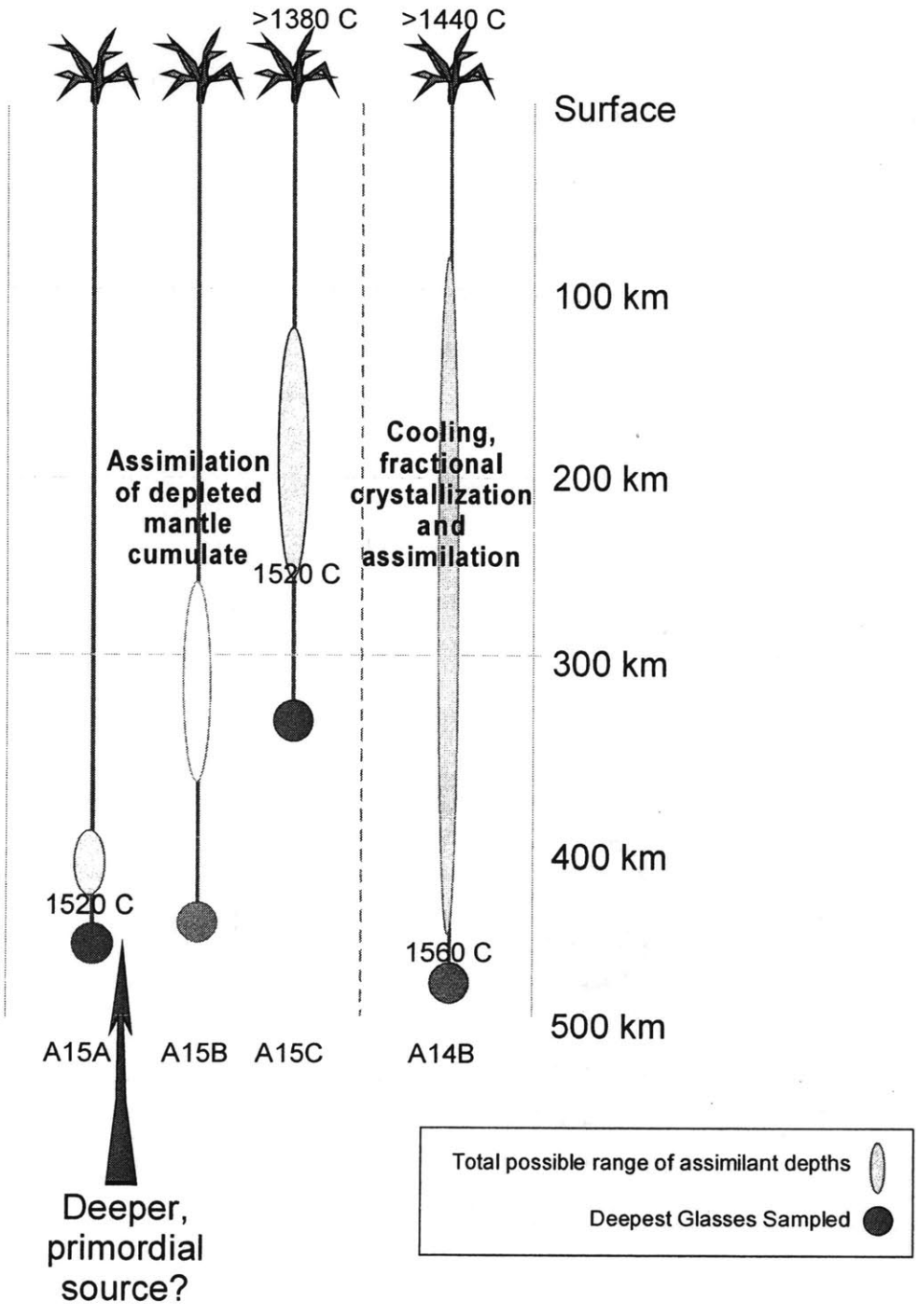
>1380 C
>1440 C
Surface
100 km
200 km
300 km
400 km
500 km
Assimilation of depleted mantle cumulate
Cooling, fractional crystallization and assimilation
1520 C
1520 C
1560 C
A15A
A15B
A15C
A14B
Deeper, primordial source?
Total possible range of assimilant depths
Deepest Glasses Sampled

Figure11.

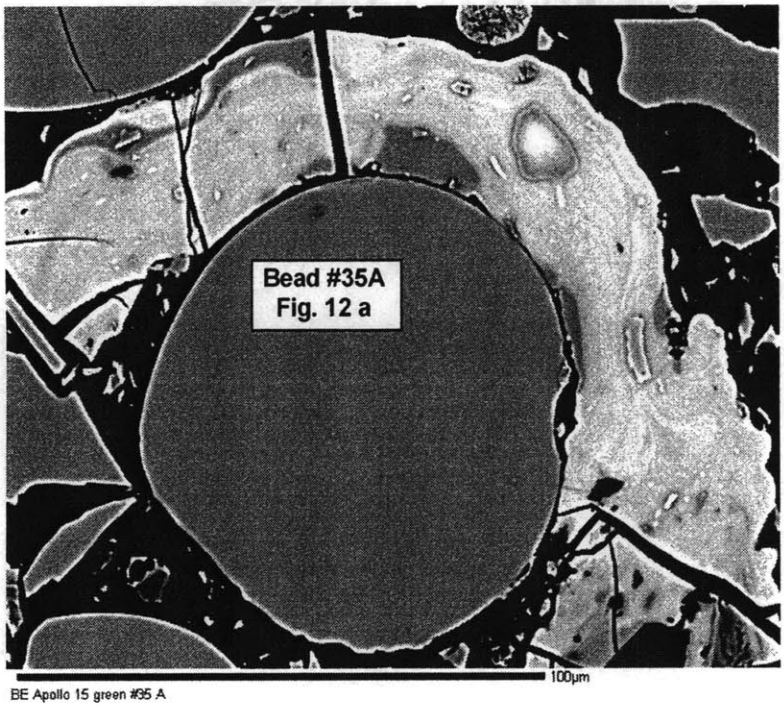
Bead #35A
Fig. 12 a
100µm
BE Apollo 15 green #95 A

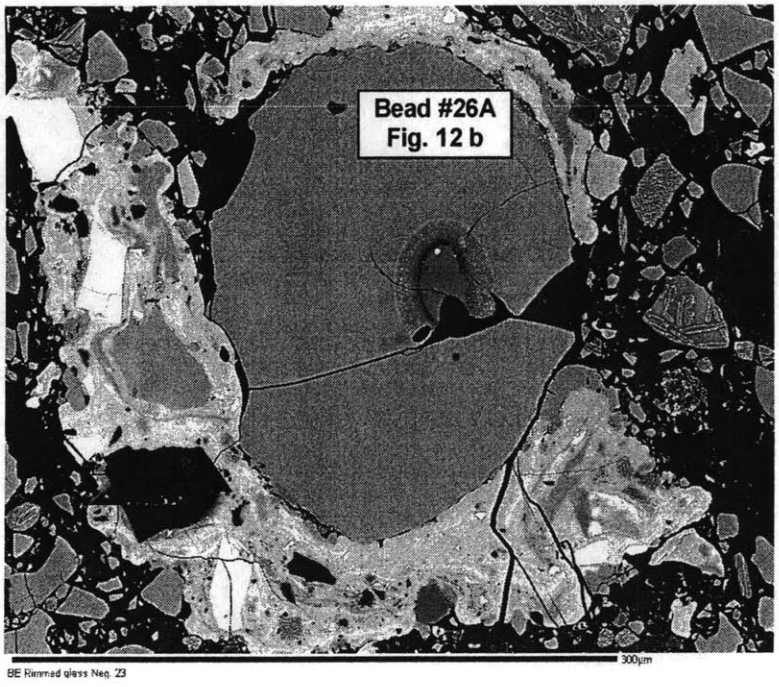
Bead #26A
Fig. 12 b
300µm
BE Rimmed glass Neg. 23

Figure 12.

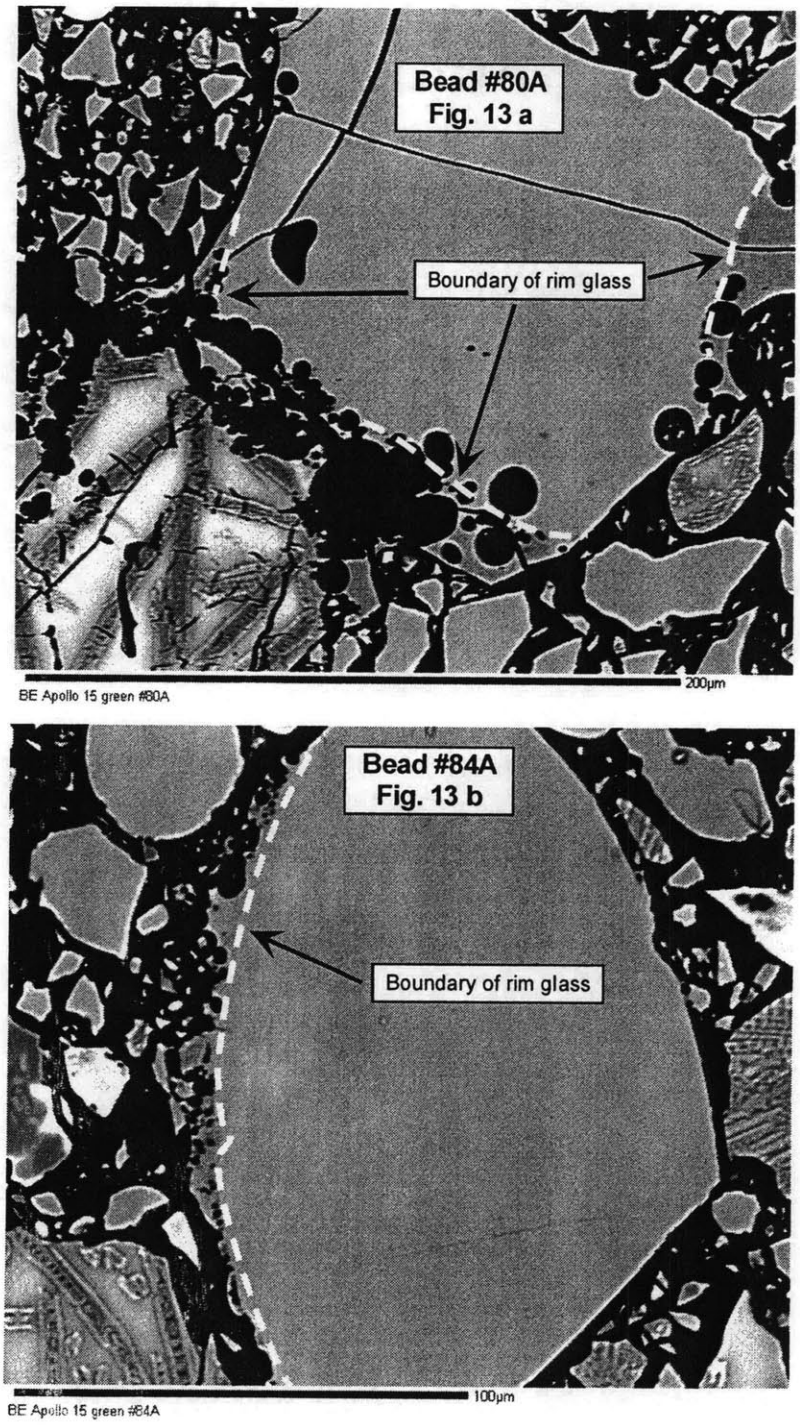
Bead #80A
Fig. 13 a
Boundary of rim glass
200µm
BE Apollo 15 green #80A
Bead #84A
Fig. 13 b
Boundary of rim glass
100µm
BE Apollo 15 green #84A

Figure 13.

Ch. 7. Reexamination of the lunar magma ocean cumulate overturn hypothesis: melting or mixing is required

Elkins Tanton, L.T., J. A. Van Orman, B. H. Hager, and T. L. Grove, Reexamination of the lunar magma ocean cumulate overturn hypothesis: Melting or mixing is required, *Earth and Planetary Science Letters* 196, 239-249, 2002.

Abstract

There is a long-standing hypothesis that the last fraction of the lunar magma ocean crystallized into a layer of dense, Ti-rich cumulate minerals at shallow depths (~100 km) early in the moon's history. Many questions remain about the stability of these high-Ti cumulates. It has been suggested that the cumulates subsequently sank deep into the moon because of gravitational instability, but high-Ti material is required at shallower depths by 3.5 Ga to create the high-Ti mare basalts and picritic glasses. The high-Ti material may have re-erupted from depth, or some or all of it may have remained at shallow depths throughout lunar history. Data on phase stabilities, bulk compositions, densities, and temperatures of melting and crystallizing in addition to results from numerical modeling suggest that the high-Ti cumulates would sink only under highly specific conditions. Five scenarios for sinking high-Ti cumulate materials are examined, and only two are found plausible. In particular, it is found that simple sinking of solidified high-Ti cumulates is unlikely because the temperature at which the cumulates solidify is low, and viscosity under these conditions is very high. It is, however, possible that high-Ti cumulates mixed with a substantial fraction of olivine would have viscosity low enough to allow them to sink as solids. Further, because clinopyroxene and ilmenite melt in a ratio of 2:1, remelted high-Ti cumulates would be negatively buoyant and sink as liquids, percolating downward through the underlying mantle and beginning to recrystallize ilmenite at 200 km depth, making a hybrid, heterogeneous mantle.

Introduction

The moon's interior is thought to consist of cumulate zones produced by early (~4.55 Ga) magma ocean differentiation. Models of lunar magma ocean crystallization [1, 2, 3, 4] suggest that the deepest cumulates (300 to 400 km) are primarily mafic, olivine +/- low-calcium pyroxene that crystallized near or sank to the base of the magma ocean, while the uppermost cumulates are primarily plagioclase, which floated upward and formed an anorthositic crust. Highly fractionated, late-stage liquid was trapped between the deep mafic cumulates and the anorthositic crust. Depending on the model composition used, ilmenite begins to crystallize from the late stage liquid when 89 – 95% of the magma ocean has solidified [personal communication with Paul Hess and John Longhi]. Depending on the thickness of anorthosite crust assumed, ilmenite crystallization would therefore begin at a depth between 150 and 100 km at a temperature between 1180 and 1125°C [2, 5]. Crystallization of ilmenite + clinopyroxene ± plagioclase would continue until KREEP, the final liquid differentiate, crystallizes beneath the

anorthositic crust. The KREEP model age of 4.42 Ga [6] is thought to mark the completion of magma ocean crystallization.

Once crystallized, the high–Ti cumulates would have a density of 3700 - 3800 kg/m^3, compared to the underlying olivine + pyroxene mantle density of about 3300 kg/m^3. Ringwood and Kesson [1] proposed that because the solid ilmenite + clinopyroxene cumulate layers were denser than the underlying, less evolved olivine- and pyroxene-bearing cumulates, the ilmenite + clinopyroxene cumulates sank into the underlying cumulate pile after crystallization. If the high-Ti component sank into the deep moon, then the question of how and where the high-Ti picritic glasses and mare basalts obtained their titanium component remains. Ringwood and Kesson [1] and other investigators [e.g., 2, 3, 7] hypothesized that the sunken high-Ti cumulates subsequently remelted and contributed to the formation of high-Ti mare basalts and picritic glasses. Other investigators have challenged the hypothesis of deeply foundered, remelted high-Ti cumulates on the basis that high-Ti melts are not buoyant below 200 - 300 km depth in the moon [8,9] (as shown in Fig. 1); paradoxically, the multiple saturation depths for the high-Ti picritic glasses are all below this depth limit. Because of the difficulty of eruption from their depths of multiple saturation, we believe the multiple saturation points are recording different information for the high-Ti glasses than they do for the low-Ti picritic compositions.

The multiple-saturation depths and saturation phases of picritic glasses and mare basalts contain clues about the location of high-Ti material in the moon. Eight experimental multiple saturation points are shown in Fig. 2. Experimentally-determined multiple saturation points indicate the approximate depth and temperature of melt segregation from its source, and the phases at multiple saturation are thought to indicate the residual source mineralogy. The mare basalts thus far investigated all have multiple saturation points shallower than 300 km depth, while the picritic glasses all have origination depths greater than 250 km. The green glass multiple saturation points indicate a source mineralogy of olivine + orthopyroxene, and so, surprisingly, do the high-Ti glasses: none of the high-Ti glasses yet studied has ilmenite on its liquidus at any pressure. If the high-Ti glasses were the result of deep remelting of sunken high-Ti cumulates [e.g., 1], then each should show high-Ti cumulate mineralogy on its liquidus. The absence of ilmenite on the liquidus of any of the high-Ti compositions means either that the melt fraction was high enough to exhaust the high-Ti phase in the source, or that the Ti content was added as a later solid assimilant, which would not be reflected in experimental phase equilibrium results.

The green glass compositions also provide evidence for the spatial distribution of Ti in the moon. The compositional trends of the Apollo 14B green glasses show increasing titanium from assimilation simultaneous with fractional crystallization of olivine. Therefore the Apollo 14B data require high–Ti material for assimilation shallower than their depth of multiple saturation (480 km)[10] at between 3 and 4 Ga.

Questions remain, however, about the processes of high–Ti cumulate redistribution; most importantly, whether it is possible for solid or liquid cumulates to sink. Zhong *et al.* [7] suggested that the high-Ti cumulates sank to the core-mantle boundary, and then rose, melted, and erupted at the time of mare basalt genesis. This mechanism would probably leave high-Ti material at shallow mantle depths to accommodate the picritic glass compositional trends, and could nicely explain the predominance of mare basalts on the near side of the moon, but questions remain about re-erupting dense high-Ti liquids, and, more importantly, about the initial fall of the cumulates.

In this study we examine several processes that may have allowed the shallow, late-crystallizing high-Ti material to sink into the deep moon. Using finite element numerical fluid dynamic models of the moon's interior and data on phase stability, bulk compositions, densities, and temperatures of melting and crystallizing, we show that the conditions that would allow high-Ti cumulates to sink are restrictive. Five scenarios are examined, and only two are found likely to allow significant volumes of high-Ti material to relocate deeper into the moon.

Models

Addressing the possibility of sinking solids or downward-percolating liquids requires models of the host mantle density and viscosity, the high-Ti cumulate mineralogy, density, liquidus and solidus temperatures, and viscosity, as well as expressions for density as a function of depth and composition for liquids. These parameters allow us to answer simple questions of comparisons, such as, at 90 km depth, will a late magma ocean liquid be negatively buoyant with respect to the lunar mantle? To look further at the complex dynamic problem of flowing solid materials, a numerical code is required, such as the finite element fluid dynamical code used in this paper.

The density of the lunar mantle as a function of depth is calculated using the cumulate pile models of Hess and Parmentier [2] and Snyder *et al.* [3]. For the mantle cumulates we calculated the weighted average density of the phases thought to be present at each depth by finding the

phase composition in equilibrium with the modeled Mg# for each depth, and then estimating the density of each phase. This yielded a model curve of mantle density with depth just after crystallization of the magma ocean. We removed the spike of dense high-Ti cumulate from its original position under the light anorthosite crust to make the data interpretation clearer (it is indisputable that the solid high-Ti cumulate compositions modeled by Hess and Parmentier [2] and Snyder *et al.* [3] are denser than any possible underlying mafic mantle cumulates). No correction for pressure is included, as the densities of the solid phases under consideration increase by only a few percent over the pressure range of interest [11].

The densities of model lunar magmas, magma ocean liquids, and cumulate remelts are calculated as a function of composition, temperature, and pressure. The density at 0.1 MPa was calculated using the method of Lange and Carmichael [12]. For each of the liquids considered, the density as a function of pressure was then calculated using a third-order Birch-Murnaghan equation of state following Delano [13].

Circone and Agee [8] determined the density vs. pressure relationship experimentally for a high-Ti lunar glass, and found Ti content to be a determining variable in the density relationship. Our calculations closely match their experimental results. For the very low Ti Apollo green glasses, the equation of state determined by Miller *et al.* [14] for a komatiite liquid, with K = 25 GPa and K' = 5, matches our Birch-Murnaghan calculation as well as the green glass density curve determined by Longhi [15].

Fig. 1 shows the multiple saturation points, liquid density curves, and mantle cumulate curves plotted on axes of density vs. pressure (and corresponding depth in the moon). This presentation of the data aids in determining the gravitational stability of a given material in comparison to the hypothesized lunar cumulate mantle. All the liquid compositions are buoyant compared to the mantle at shallow depths, and all the liquid compositions cross the mantle curves at some depth and become negatively buoyant. The green glasses are buoyant at their depths of multiple saturation, but each high-Ti glass is more dense than the lunar mantle at its depth of multiple saturation. The high-Ti magmas could never have risen and erupted if formed in entirety at their depths of multiple saturation.

To model the fluid dynamics of the lunar interior, more specifically, the onset of Rayleigh-Taylor instability (formation of falling or rising diapirs because of a density contrast between

layers), we use a version of the finite element code ConMan [16] that includes compositionally and thermally driven convection, and a stress-dependent viscosity.

Stress-dependent rheology is particularly important when modeling the formation of instabilities: nascent instabilities quickly build up stress while deforming, thereby lowering their viscosity and enabling flow. This feedback process speeds the fall of instabilities significantly when compared to simple temperature-dependent rheology. Though the extrapolation of the stress dependence of viscosity from laboratory to planetary scales is an inexact science, addition of stress dependence to the viscosity law only increases the likelihood of the model predicting that the high-Ti cumulate fell into the deeper moon, and therefore the inclusion of stress-dependence is doubly important for modeling this process. The viscosity law used depends on stress, temperature, and depth:

$$\eta = \eta_o \left[\frac{\sigma_o}{\sigma}\right]^2 \exp\left[\frac{E+vz}{R(T+T_o)} - \frac{E+vz_o}{R(1+T_o)}\right] \qquad (1)$$

where η_0, σ_0, T_0, and z_0 are reference values of viscosity, stress, temperature and depth, respectively, E is the activation energy for solid-state creep, and v scales viscosity to depth. E is set to create an order of magnitude change in viscosity for each 100 degree change in temperature, and v is set to create a factor of five total viscosity change across the depth of the model. Because an accurate viscosity law for ilmenite + pyroxene is not known, in these models it is assumed to follow the same law as olivine. This is a generous assumption: pyroxene is stiffer than olivine [17, 18, 19], and a higher viscosity caused by pyroxene in the cumulate would inhibit the formation and sinking of cumulate diapirs.

Thermal convection is governed by the Rayleigh number :

$$Ra = \frac{\rho g \alpha \Delta T h^3}{\eta_o \kappa} = 38{,}000 \qquad (2)$$

where α is thermal expansivity, κ is thermal diffusion, ρ is a characteristic density, ΔT is the temperature change over the model box, and h is a characteristic length. Convection due to the negative buoyancy of the high-Ti cumulate is controlled by the compositional Rayleigh number

$$Rac = \frac{\Delta\rho g h^3}{\eta_o \kappa} = Ra \frac{\Delta\rho}{\rho \alpha \Delta T} = -100,000 \quad (3)$$

where $\Delta\rho$ is the difference in densities between the compositions. The numerical model, which is 260 by 260 km, is illustrated in Fig. 3, and model parameters are given in Table 1. The boundary conditions for each model are the same: free-slip in the horizontal along the top boundary, free-slip in the vertical along the side boundaries, and a flow-through bottom boundary. The bottom of the KREEP layer is also constrained to be a free-slip boundary with no flow-through.

We ran a large suite of models, and report four here. For each of the models, the top 15 elements (60 km) are anorthosite crust, which is modeled with an initial viscosity 100 times that of the mantle. The next layer is 3 elements (12 km) of KREEP. This is probably a significant overestimate of the thickness of the KREEP layer, but numerical considerations require that at least three elements be used in each material. A thicker KREEP layer will only facilitate descent of the high-Ti layer. The initial viscosity of the KREEP layer is 100 times less than the mantle. Below the KREEP layer are 5 elements (20 km) of high-Ti cumulate. The initial viscosity for the high-Ti layer and the initial temperature conditions are varied among the models. The remainder of the model box is made up of 43 elements (170 km) of silicate mantle.

Three numerical model runs describe the parameter space of high-Ti cumulate descent. In the simplest model, Moon20, the entire model box begins at 1400 °C, and the high-Ti cumulate and the silicate mantle begin with the same initial viscosity. This is an extreme and unrealistic model: there is no conductive cooling of the surface, and no allowance for the relative stiffness of pyroxene in comparison to olivine. The high-Ti cumulate forms diapirs that sink to 260 km depth by about 25 Ma (shown in Fig. 3a). This is the sinking behavior found in previous models of cumulate overturn, but we found this behavior only in this extreme model. Note that for the hot initial condition assumed, a real high-Ti cumulate layer would be fully liquid and positively buoyant, not negatively buoyant, as in the calculations.

A second model, Moon21, starts with this same 1400 °C initial condition (no conductive cooling), but with the initial viscosity of the high-Ti layer 10 times that of the silicate mantle, to approximate the stiffer rheology of pyroxene in the cumulate layer as compared to the olivine-dominated mantle. In this model the high-Ti cumulate layer never forms instabilities and does

not fall. This model was designed to test the effects of a higher-viscosity pyroxene cumulate, and we found that if the mineralogy of the cumulate layer raises its viscosity an order of magnitude above that of olivine under the same conditions, then cumulate sinking is halted.

In a third model, Moon22, the most realistic starting conditions are used, and high-Ti cumulate sinking did not occur. To crystallize, the ilmenite + clinopyroxene cumulate must be below 1150 °C [5, 20], and so with the uncooled initial conditions used in models Moon20 and Moon21 the high-Ti cumulate would still be liquid, and this liquid would be positively buoyant. In this model, Moon22, the model box is cooled conductively until the bottom of the high-Ti layer reaches 1170 °C (a value probably still above the solidus of the material, but chosen to facilitate flow by providing the minimum viscosity). With a cooled start, using the olivine viscosity law for the high-Ti cumulates, no instabilities form. The stationary cumulate layers are shown in Fig. 3b. With the conductively cooled starting condition, instabilities do not form until the background viscosity (the starting viscosity of the mantle and high-Ti cumulate) is lowered to 10^{16} Pas at the start of the model run.

In a variation of this most realistic model, Moon22, the lower boundary of the high-Ti layer was perturbed to form a nascent instability. This is an important test, since Conrad and Molnar [21] demonstrated that, especially with stress-dependent viscosity, the time of development of instabilities is strongly controlled by initial perturbations. For this test we placed a hanging bulge of cumulate in the center of the model box 24 km wide and 20 km at its deepest point was added to the existing 20-km thick high-Ti cumulate layer. Though this central bulge created a very sluggish material flow downward beneath its center, encouraging growth of the instability, the material was stiff enough that over 500 Ma no instability formed and none of the high-Ti cumulate fell.

The existence of a lubricating, liquid KREEP layer above the high–Ti cumulate helps the Rayleigh-Taylor instability to develop [22], but as KREEP has a solidus only slightly cooler than the high–Ti solidus, and the KREEP will be closer to the cold surface of the moon, it is unlikely that the KREEP layer will stay liquid long enough to facilitate the instability. To maximize the possibility of instability, the KREEP layer in this model is given a viscosity 100 times less than background. Still, no instabilities are formed, and the cumulate layer is frozen at its depth of formation.

Discussion

There are several possible mechanisms that could allow redistribution of high-Ti liquids or solids into underlying cumulates. The most commonly suggested process for moving high–Ti material into the deep moon is the sinking of solid high-Ti ilmenite + pyroxene cumulates as instabilities from their depth of crystallization [e.g., 1, 2, 7]. We find this process unlikely due to viscosity constraints. Attempting to find a process that does allow high-Ti material to move more deeply into the moon, we then investigate models that attempt to lower the viscosity of the solid cumulate (models 2 and 5), and models in which a heavy liquid may be negatively buoyant with respect to the lunar mantle, and sink through percolative flow (models 3 and 4).

(1) Could the solid ilmenite + pyroxene cumulate layer sink via a Rayleigh-Taylor instability?

No. Numerical models demonstrate that the process becomes a race to form Rayleigh–Taylor instabilities in the high-Ti cumulate before it freezes in place. We find that under realistic initial conditions, taking into account the temperature at which high-Ti cumulates become negatively buoyant, and even with a perturbed lower boundary, the viscosity is too high to allow high-Ti cumulates to fall.

To allow instabilities to form, the high-Ti material must be hot enough that its viscosity allows it to flow. Using the viscosity law shown above, we found that instabilities would not form until the shallow moon was ~1300 °C, hot enough that the cumulate would be well above its solidus, and therefore no longer gravitationally unstable at shallow depths. This is the falling behavior described in previous models of cumulate overturn, but we found this behavior only in this high-temperature model without solidus and density constraints. Previous investigators have simplified this problem by modeling without conductive cooling and temperature-dependent viscosity constraints, and that is why some papers have shown instabilities forming and falling on appropriate time scales. It is common to simplify a modeling problem by using constant viscosity, but in this case, with a near-surface material having a low solidus temperature, more realistic modeling is necessary.

(2) Could the ilmenite + clinopyroxene cumulate sink as a solid if it were heated radiogenically?

No. Radiogenic heating of the high–Ti layer would not lower its viscosity and allow it to fall; the numerical models examined above assume the high–Ti layer is just below its solidus, and so any heating will simply melt it. Radiogenic heating in the KREEP layer would keep it liquid

longer, but if the top of the high–Ti cumulate were at 1200°C (and the cumulate were somehow still solid) then viscosities would be such that not even a liquid KREEP layer would lubricate sufficiently to allow the cumulate to fall.

(3) Could a late–stage liquid from magma ocean crystallization become negatively buoyant?

No. At the point when ilmenite appears on the liquidus and begins to crystallize, the late–stage liquid has only about 6% TiO_2, and would not be negatively buoyant at any depth above 250 km (see Fig. 2). It is not possible to sink a late–stage magma ocean liquid.

(4) If the ilmenite + clinopyroxene cumulate could be remelted, would that secondary liquid sink?

Yes. Radiogenic heating or shock heating from giant impacts could raise the ilmenite + clinopyroxene cumulate above its solidus and produce a dense liquid. Several experimental studies [e.g., 5, 23] have demonstrated that clinopyroxene and ilmenite melt in a ratio of ~2:1, resulting in a liquid with about 33% ilmenite at maximum. Such a liquid would be negatively buoyant with respect to mafic mantle cumulates at depths below 20-80 km, depending on the mantle composition used, making it a good candidate for carrying a high–Ti component deeper into the moon (Fig. 1). The bulk of the ilmenite + pyroxene cumulate probably crystallized between 60 and 100 km, and thus it is likely that any radiogenic remelting (for example, from the Procellarum KREEP terrane [24]) would occur in a region of negative buoyancy and any resulting high-Ti liquid would be denser than the surrounding lunar mantle. The giant impacts of the late heavy bombardment then could have shock-melted any remaining shallow portions of high-Ti cumulate.

The ilmenite + clinopyroxene cumulate is likely to have also contained plagioclase. The composition studied by Van Orman and Grove [5] contained 7% plagioclase by mass. When fully molten, the density of their high-Ti cumulate is about 3040 kg/m^3 at one atmosphere. This composition will be negatively buoyant with respect to the cumulate models of Hess and Parmentier [2] and Snyder *et al.* [3] at between 140 and 200 km. These depths are probably too great to be helpful in high-Ti migration; the bulk of the ilmenite probably crystallized at shallower levels, and remelting mechanisms such as impact or radiogenic heating probably also occurred more shallowly. However, if the melting extent is small enough that clinopyroxene or, better yet, ilmenite is not exhausted, then the liquid would still be negatively buoyant at its likely

source depths. On the other hand, if the source contained more than 7% plagioclase, then obtaining a negatively buoyant liquid by remelting is increasingly unlikely.

Downward liquid flow through percolation would likely be fast enough to create a hybrid mantle for later remelting, in part because of the very low viscosity of clinopyroxene-ilmenite melt. Using percolation theory from Wark and Watson [25], we find that a matrix grain diameter of 0.1 cm and porosity of 1% results in a melt velocity of 0.4 cm/yr. If the porosity is 5%, the melt velocity rises to 9 cm/yr. Because melt velocity scales with the square of the grain size, larger grains in the matrix will significantly speed the downward liquid flow.

The steep liquidus of the ilmenite + pyroxene liquid would cause ilmenite to begin crystallizing at ~1200°C and less than 200 km depth [5, 20]. At shallow depths, the liquid will also most likely crystallize olivine and dissolve pyroxene. At greater depths, the liquid will be in its pyroxene primary phase volume, and will dissolve olivine and crystallize pyroxene. This makes possible the formation of a heterogeneous, hybrid mantle from downward flow of high–Ti liquids. If the liquid did percolate downward at 9 cm/year, then it would have reached 200 km depth in about 2 million years. This timing is adequate to account for the onset of high-Ti mare basalt eruptions, which began near the end of the late heavy bombardment [6].

(5) Could the cumulate composition reasonably be modeled in another way, that would allow it to fall as a solid?

Maybe. Recognizing the viscosity limitations of the ilmenite + pyroxene cumulate, Van Orman and Grove [5] suggested that mixing olivine-rich cumulate with the high-Ti cumulate could lower its viscosity enough to allow the formation of instabilities. If the late–stage magma ocean liquid entrained and assimilated 10 - 20% olivine from deeper cumulates, then the change in bulk composition would alter the liquidus relations in such a way that ilmenite would no longer crystallize; instead, spinel would be the titaniferous phase. The solidus temperature of this material would be higher, allowing a negatively buoyant cumulate layer to form while the layer remained hot, and had lower viscosity. MELTS [26] predicts that the solidus of this new cumulate would be about 115°C higher (1240°C at 100 km depth) than the original ilmenite + clinopyroxene cumulate, leading to a reduction in viscosity by about a factor of 30. The density contrast between the new cumulate and the underlying mantle would be about half of what it was with the ilmenite + clinopyroxene cumulate, but the decrease in density is small compared to the sharp viscosity reduction. (It is interesting to note that Wagner and Grove [9] found

orthopyroxene + olivine + spinel, not ilmenite, on the liquidus of the Apollo 14 black glass.) According to our numerical models, if the viscosity law for the spinel + clinopyroxene + olivine cumulate is similar to an olivine law, and the cumulate layer is at or above 1240°C, then it is tantalizingly close to conditions necessary to form a sinking instability. If the MELTS calculation is incorrect and ilmenite crystallizes rather than spinel, the resulting solid will be even denser and more likely to fall. Solomatov and Stevenson [27] have suggested that, while crystallizing, a magma ocean would simultaneously be convecting. Even sluggish, local convective currents may be enough to mix olivine into the ilmenite + pyroxene cumulate in quantities sufficient to allow the dense layer to flow and fall.

Longhi (personal communication) suggested that entrainment of plagioclase was as likely as entrainment of olivine into the late-stage liquid. Using the results of Philpotts *et al.* [28], an interesting scenario can be constructed from this suggestion. Philpotts *et al.* [28] found that when a basaltic magma was only 25% crystallized, structural chains of plagioclase and pyroxene had formed a solid three-dimensional network, through which the remaining liquid was strained. The pyroxene made the chains negatively buoyant in the liquid, and this structure actually caused the plagioclase to fall, not rise to the surface. If this happened at any point in the final crystallization of the lunar magma ocean, there would be several important results: (1) plagioclase would be trapped at depth in the moon, and the crustal highlands component may not represent the vast majority of the aluminous lunar component, as has previously been supposed; (2) the final magma ocean liquids would be further depleted in pyroxene component, and therefore enriched in ilmenite; (3) this ilmenite-enriched final liquid would be equally unlikely to fall through gravitational instability when solidified, because it will be resting on a very stiff network of plagioclase and pyroxene; and (4) the final solids will produce even denser liquids if remelted by a later event, making percolative downward flow of a high-Ti liquid even more likely.

Conclusions

We suggest that mass movement of a solid high–Ti cumulate from the shallow into the deep moon is unlikely, due to viscosity and temperature constraints.

A remelted ilmenite + clinopyroxene liquid (scenario 4) is negatively buoyant even at shallow depths and will sink. Falling high-Ti liquids from remelted cumulates would hybridize the lunar mantle as deeply as 300 km. Remelting the cumulate layer by giant meteorite bombardment may

be a more viable mechanism than remelting by radioactive heating. Their rate of radioactive heat production is highest early in the moon's history, so while radioactive heat may have kept the high-Ti cumulates molten for longer, it is a poor candidate for later remelting. The giant impacts of the late heavy bombardment, however, were sufficient to remix and remelt high-Ti cumulates [29].

The most likely cumulate to sink as a solid is the result of late–stage magma ocean liquids assimilating 10 - 20% olivine before crystallizing (scenario 5). This material would form sinking diapirs, leaving a fraction of the high–Ti cumulate at shallow depths. A lunar mantle with varying Ti content at depths shallower than 560 km is consistent with the timing and composition of lunar glasses, and is permitted by rheological constraints.

These two mechanisms, a remelted high-Ti cumulate percolating downward as a liquid, and a solid high-Ti cumulate mixed with olivine foundering as a solid, may both have occurred. Some early cumulate may have sunk as a solid, and later cumulate may have been remelted in the late heavy bombardment and sunk as a liquid.

Acknowledgments

The authors thank John Longhi, Marc Parmentier, and Kevin Righter for constructive and thoughtful reviews. This work was supported by NASA, a National Defense Science and Engineering graduate fellowship, and an Amelia Earhart graduate fellowship.

References

[1] A.E. Ringwood, S.E. Kesson, A dynamic model for mare basalt petrogenesis, Proc. Lunar Planet. Sci. Conf. 7 (1976) 1697–1722.

[2] P.C. Hess, E.M. Parmentier, A model for the thermal and chemical evolution of the moon's interior: Implications for the onset of mare volcanism, Earth Planet. Sci. Lett. 134 (1995) 501-514.

[3] G.A. Snyder, L.A. Taylor, C.R. Neal, A chemical model for generating the sources of mare basalts: Combined equilibrium and fractional crystallization of the lunar magmasphere, Geochim. Cosmochim. Acta 56 (1992) 3809-3823.

[4] J. Longhi, Magma oceanography – 2. Chemical evolution and crustal formation, Proc. Lunar Planet. Sci. Conf. 8 (1977) 600-.

[5] J.A. Van Orman, T.L. Grove, Origin of lunar high-titanium ultramafic glasses: Constraints from phase relations and dissolution kinetics of clinopyroxene-ilmenite cumulates, Meteorit. Planet. Sci. 35 (2000) 783-794.

[6] L.E. Nyquist and C.-Y. Shih, The isotopic record of lunar volcanism, Geochim. Cosmochim. Acta 56 (1992) 2213-2234.

[7] S. Zhong, E.M. Parmentier, M.T. Zuber, A dynamic origin for the global asymmetry of lunar mare basalts, Earth Planet. Sci. Lett. 177 (2000) 131-140.

[8] S. Circone, C.B. Agee, Compressibility of molten high-Ti mare glass: Evidence for crystal-liquid density inversions in the lunar mantle, Geochim. Cosmochim. Acta 60 (1996) 2709-2720.

[9] T.P. Wagner, T.L. Grove, Experimental constraints on the origin of lunar high-Ti ultramafic glasses, Geochim. Cosmochim. Acta 61 (1997) 1315-1327.

[10] L.T. Elkins, V.A. Fernandes, J.W. Delano, and T.L. Grove, Origin of lunar ultramafic green glasses: Constraints from phase equilibrium studies, Geochim. Cosmochim. Acta 64 (2000) 2339-2350.

[11] J.D. Bass, Elasticity of minerals, glasses, and melts, in T.J. Ahrens, ed., Mineral physics and crystallogaphy: A handbook of physical constants, American Geophysical Union, Washington D.C. (1995) 45-63.

[12] R.A. Lange, I.S.E. Carmichael, Densities of Na_2O-K_2O-CaO-MgO-FeO-Fe_2O_2-Al_2O_2-TiO_2-SiO_2 liquids: new measurements and derived partial molar properties, Geochim. Cosmochim. Acta 51 (1987) 2931-2946.

[13] J.W. Delano, Buoyancy-driven melt segregation in the earth's moon, 1. Numerical results., Proc. Lunar Planet. Sci. Conf. 20 (1990) 3-12.

[14] G.H. Miller, E.M. Stolper, T.J. Ahrens, The equation of state of a molten komatiite 1. Shock wave compression to 36 GPa, J. Geophys. Res. 96 (1991) 11831-11848.

[15] J. Longhi, Origin of picritic green glass magmas by polybaric fractional fusion, Proc. Lunar Planet. Sci. Conf. 22 (1992) 343-353.

[16] S.D. King, A. Raefsky, B.H. Hager, ConMan: Vectorizing a finite element code for incompressible two-dimensional convection in the Earth's mantle, Phys. Earth Planet. Int. 59 (1989) 195-207.

[17] S.H. Kirby, A.K. Kronenberg, Deformation of clinopyroxenite: evidence for a transition in flow mechanisms and semi-brittle behavior, J. Geophys. Res. 89 (1984) 3177-3192.

[18] J.W. Delano, Chemistry and liquidus phase relations of the Apollo 15 red glass: Implications for the deep lunar interior, Proc. Lunar Planet. Sci. Conf. 11 (1980) 251-288.

[19] M. Bystricky and S. Mackwell, Creep of dry clinopyroxene aggregates. J. Geophys. Res. 106 (2001) 13443-13454.

[20] P.C. Hess, M.J. Rutherford, H.W. Campbell, Ilmenite crystallization in nonmare basalt: Genesis of KREEP and high-Ti mare basalt, Proc. Lunar Planet. Sci. Conf. 9 (1978) 705-724.

[21] C.P. Conrad and P. Molnar, The growth of Rayleigh-Taylor-type instabilities in the lithosphere for various rheological and density structures. Geophys. J. Int. 129 (1997) 95-112.

[22] L.T. Elkins Tanton, Bradford H. Hager, Melt intrusion as a trigger for lithospheric foundering and the eruption of the Siberian flood basalt, Geophys. Res. Lett. 27 (2000) 3937-3940.

[23] B.A. Wyatt, The melting and crystallization behavior of a natural clinopyroxene-ilmenite intergrowth, Contrib. Mineral. Petrol. 61 (1977) 1-9.

[24] L.A. Haskin, The Imbrium impact event and the thorium distribution at the lunar highlands surface, J. Geophys. Res. 103 (1998) 1679-1689.

[25] D.A. Wark, E.B. Watson, Grain-scale permeabilities of texturally equilibrated, monomineralic rocks, Earth Planet. Sci. Lett. 164 (1998) 591-605.

[26] M. S. Ghiorso, R.O. Sack, Chemical mass transfer in magmatic processes IV. A revised and internally consistent thermodynamic model for the interpolation and extrapolation of liquid-solid equilibria in magmatic systems at elevated temperatures and pressures, Contrib. Mineral. Petrol. 119 (1995) 197-212.

[27] V.S. Solomatov, D.J. Stevenson, Suspension in convective layers and style of differentiation of a terrestrial magma ocean, J. Geophys. Res. 98 (1993) 5375-5390.

[28] A.R. Philpotts, C.M. Brustmas, J. Shi, W.D. Carlson, C. Denison, Plagioclase-chain networks in slowly cooled basaltic magma, Am. Mineral. 84 (1999) 1819-1829.

[29] L.T. Elkins Tanton, B.H. Hager, T.L. Grove, Magmatic effects of the lunar late heavy bombardment, in preparation.

[30] T.L. Grove, D.T Vaniman, Experimental petrology of very low Ti (VLT) basalts, in R.B. Merrill, J.J. Papike, eds., Mare Crisium: The View From Luna 24, Pergamon Press, New York (1978) 445-471.

[31] H.K. Chen, D.H. Lindsley, Apollo 14 very low titanium glasses: Melting experiments in iron-platinum alloy capsules, J. Geophys. Res. 88 (1983) B335-342.

[32] D.H. Green, A.E. Ringwood, W.O. Hibberson, N.G. Ware, Experimental petrology of the Apollo 17 mare basalts, Proc. Lunar Sci. Conf. (1978) 871-893.

Table and Figure Captions

Table 1. Numerical model parameters.

Fig. 1. Lunar depth vs. density curves for liquid compositions and two lunar mantle models [2, 3]. The vertical scale shows pressure in GPa and corresponding depth in the moon. High-density spikes above 100 km representing solidified high–Ti cumulates have been removed from the mantle models. Multiple saturation points are are plotted at their experimental pressure and calculated density (A15C Green = Elkins Tanton and Grove, in preparation; A17 VLT = [22]; A15A Green = Grove, unpublished; A14 VLT = [23]; A14B Green = [10]; A14 Black = [9]; A17 Orange = [24]; A15 Red = [25]). The black glass density curve is from [8]. The green glass density curve is from [15], and our calculations. Other liquid curves calculated as described in text.

Fig. 2. Pressures and temperatures of multiple saturation for the eight picritic glass compositions listed in Fig. 1. High-Ti compositions are shown with filled circles, and low-Ti compositions with empty circles.

Fig. 3. Results of numerical models of solid high-Ti cumulate instabilities. Fig. 3a shows the only model in which instabilities formed. Overturn progressed only under entirely unrealistic conditions, where no surface cooling occurred and the temperature of the cumulates was above their solidus. Fig. 3b shows the results of more realistic starting conditions, where as a starting condition the model was conductively cooled until the high-Ti cumulate layer was at its solidus.

Table 1. Numerical model parameters

h	height and width of model box	260 km
ρ	reference mantle density	3250 kg/m^3
$\Delta\rho$	difference between cumulate and mantle densities	-400 kg/m^3
ΔT	temperature across the model box	1400 °C
η_0	reference viscosity	1.00E+20 Pas
α	thermal expansivity	3E-05 /°
κ	thermal diffusivity	1E-06 m^2/s
e	number of elements in model box, in each dimension	67

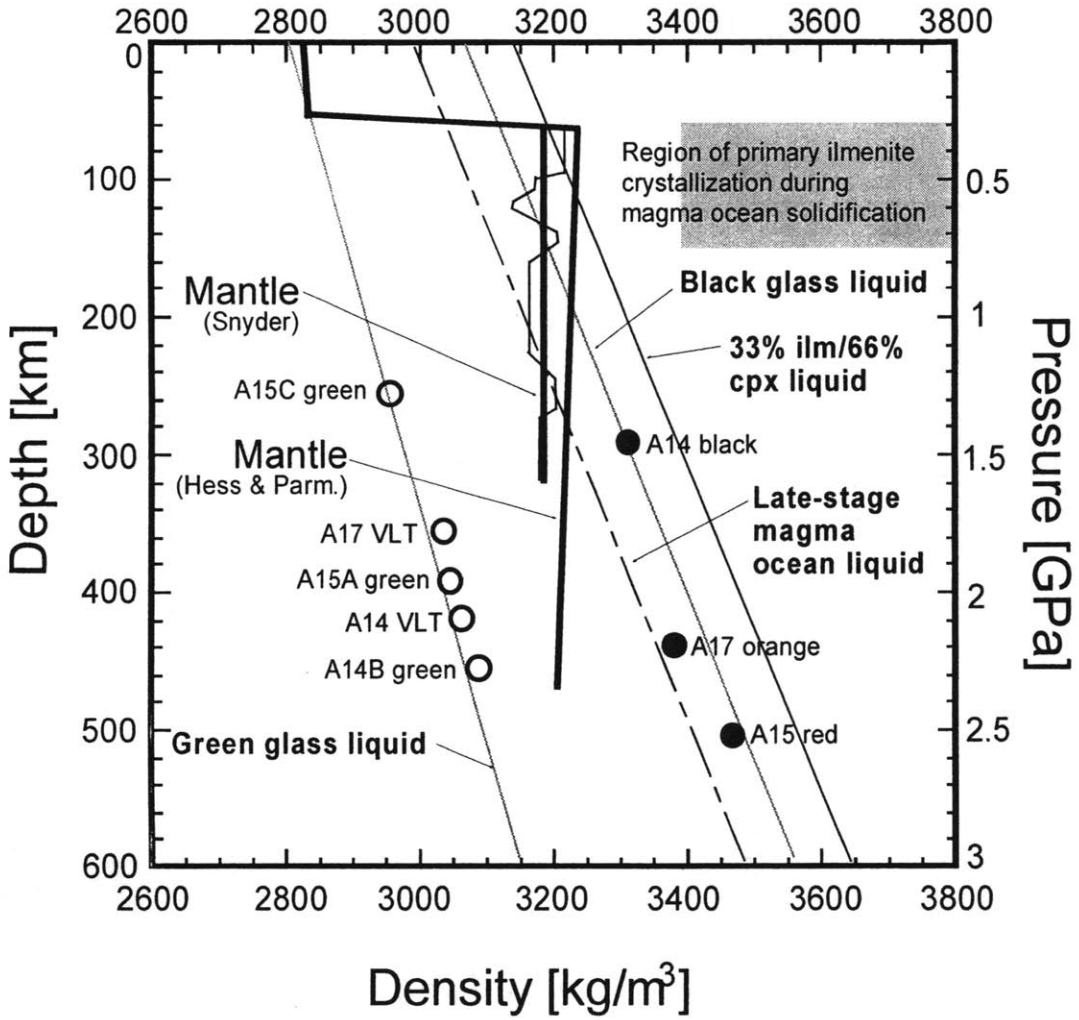
2600
2800
3000
3200
3400
3600
3800
0
100
200
300
400
500
600
Depth [km]
0.5
1
1.5
2
2.5
3
Pressure [GPa]
Density [kg/m3]
Region of primary ilmenite crystallization during magma ocean solidification
Black glass liquid
33% ilm/66% cpx liquid
Late-stage magma ocean liquid
Mantle (Snyder)
Mantle (Hess & Parm.)
A15C green
A17 VLT
A15A green
A14 VLT
A14B green
Green glass liquid
A14 black
A17 orange
A15 red

Figure 1

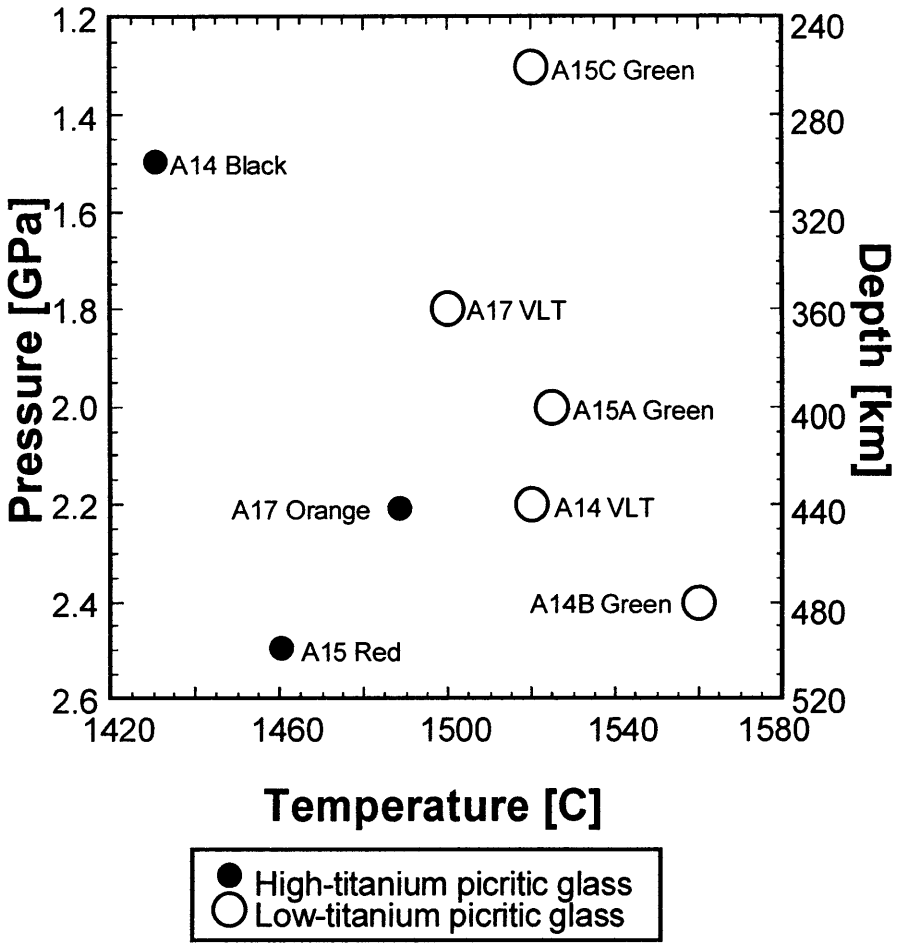
1.2
1.4
1.6
1.8
2.0
2.2
2.4
2.6
Pressure [GPa]
240
280
320
360
400
440
480
520
Depth [km]
A15C Green
A14 Black
A17 VLT
A15A Green
A17 Orange
A14 VLT
A14B Green
A15 Red
1420
1460
1500
1540
1580
Temperature [C]
High-titanium picritic glass
Low-titanium picritic glass

Figure 2

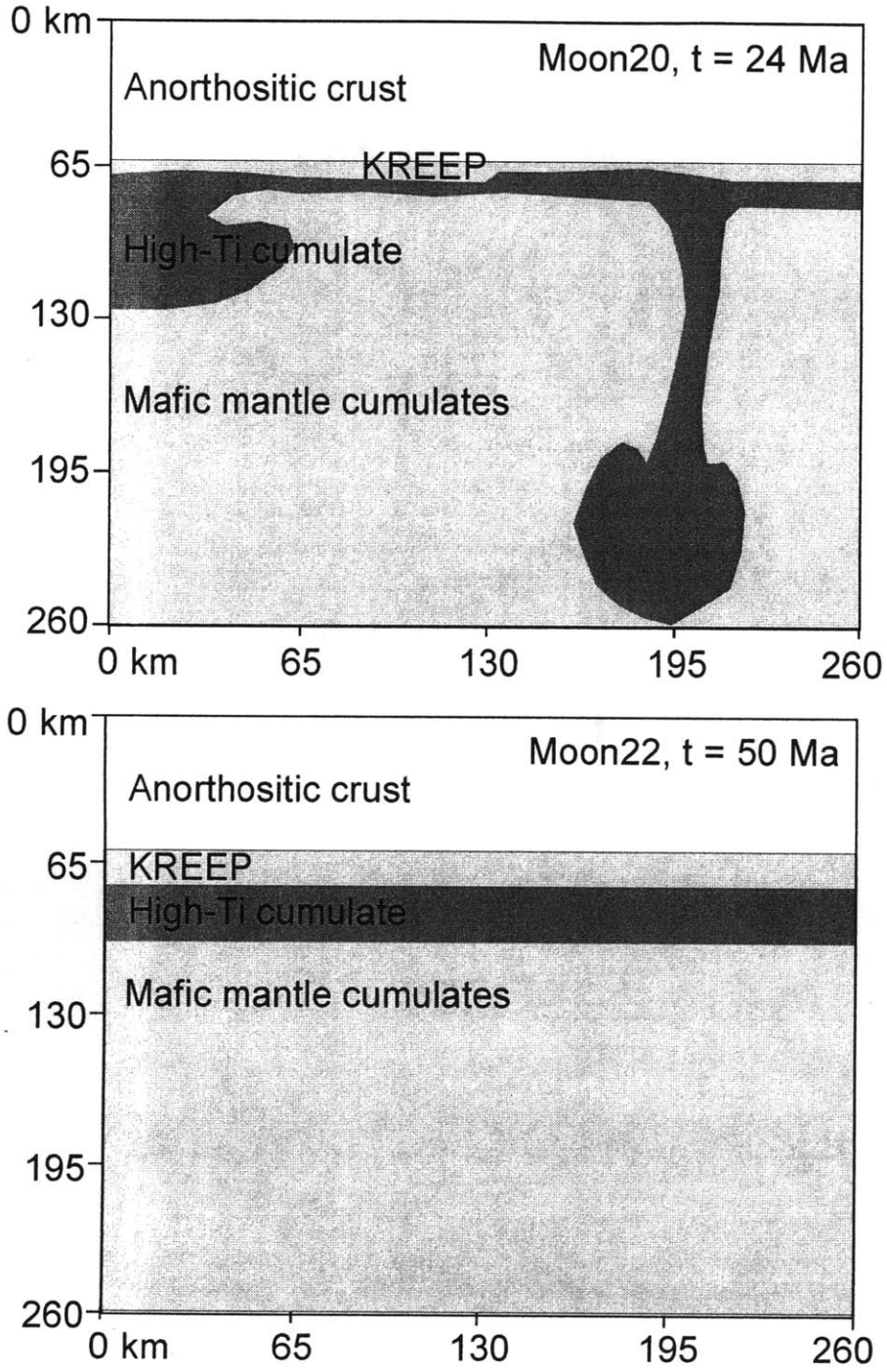
0 km
Moon20, t = 24 Ma
Anorthositic crust
65
KREEP
High-Ti cumulate
130
Mafic mantle cumulates
195
260
0 km
65
130
195
260
0 km
Moon22, t = 50 Ma
Anorthositic crust
65
KREEP
High-Ti cumulate
130
Mafic mantle cumulates
195
260
0 km
65
130
195
260

Figure 3

Ch 8. Magmatic effects of the lunar late heavy bombardment

Abstract

We present a model for impact-induced volcanism on the Moon. Magma can be produced in two stages: first, crater excavation can depressurize the column beneath the crater to the point that material is moved above its solidus and melts; and second, after excavation the lithosphere rises isostatically, warping the lithosphere-mantle boundary into a dome and initiating convection, in which adiabatic melting can occur. The first process, in-situ decompression melting, produces by far the largest volume of melt of the two stages and is consistent with the volumes of mare basalt seen in lunar basins. Lunar conditions are such that convection in the lithospheric dome can continue for up to 350 Ma. The longevity of magma production can account for high alumina and high titanium magma production on the Moon, and part of the longevity of lunar magmatism.

Introduction

Large volumes of mare basalts are visible on the surface of the Moon, preferentially lying in large impact basins. The processes of formation and eruption of these basalts are not well established, though it is recognized that eruptions peaked in the Imbrian Period (3.85 – 3.2 Ga), and that the majority of the basalts lie on the near side. It has been suggested that crustal thickness explains why so little basalt erupted onto the far side: the density of liquid basalt at pressures corresponding to the bottom of the crust are greater than that of the crustal rocks, so eruption is suppressed by gravitational density stability (Solomon, 1975). The existence of a relationship between impact basins and mare basalt eruptions has been suggested by many investigators. In particular, large impacts are thought to have removed enough of the low-density crustal lid that heavier, liquid mare basalts could erupt. Zhong *et al.* (2000) further suggested that heating late cumulates at depth in the Moon would result in a mode 1 eruption, which could cause the preferential appearance of mare basalts on the near side.

We present a model for melt creation under near side lunar basins that is triggered by the impacts themselves. There are two stages in the impact process that can create basalt magmas: 1. Excavation from the impact causes instantaneous decompression melting beneath the impact site, which can allow material to melt in-situ through decompression; and 2. Isostatic rebound of the lithosphere underlying the impact site can create a dome in the lithosphere-mantle boundary, which induces convection due to the resulting horizontal temperature gradients, and upwelling of mantle material in these convective cells can melt adiabatically. (See Figure 1.) Melting different cumulate compositions and interaction of melts with solid cumulates can result in the

range of mare basalt and picritic glass compositions sampled from the Moon, including the aluminous, KREEP, and high-Ti basalts. The thinned crust, disturbed selenotherm, and brecciated lithosphere could facilitate eruption.

We find, based on analysis of mare basalt and picritic glass multiple saturation points, that a lithospheric thickness of 250 km and a mantle potential temperature of 1450 °C are the most realistic model for the Moon between 4.0 and 3.5 Ga. This impact model is consistent with gravity models of the lunar crust under the large basins and with petrologically constrained models of temperature and depth of mare basalt origin. Specifically, we attempt to explain the volume and longevity of mare basalt volcanism, along with the pattern of eruptions of varying compositions through time. The aluminous and KREEP basalts appear, from returned samples, to have erupted earlier than the high-Ti basalts and picritic glasses, which in turn erupted before the low-Ti basalts and picritic glasses. (See Figure 2.)

Models

Constraints on lithospheric thickness and mantle temperature

As in any model addressing basalt genesis, bringing the required volume of mantle material above its solidus is the heart of the problem. The higher the mantle potential temperature, the deeper mantle melting can begin, and the larger the resulting volume of magma. Similarly, melting is facilitated by a thin lithosphere; the thinner the lithosphere, the lower the pressure of the top of the mantle, and thus lower temperatures will produce melting.

We define the lithosphere as material cooler than 1000 °C, and the mantle as the cumulates that underlie the lithosphere. In this model, the lower lithosphere will be made of magnesian cumulates, and the top of the lithosphere is the anorthositic crust. Following the models of Ringwood and Kesson (1976) and Hess and Parmentier (1995), we model late-stage high-titanium cumulates and KREEP material in a layer between 60 and 80 km depth (Figure 3).

In this model we use mantle potential temperatures of 1350°C and 1450°C. These temperatures are consistent with the experimentally determined multiple saturation points of mare basalts and picritic glasses, as discussed below. In the in-situ decompression melting models, stage 1 of melting, lithospheres 200, 250, 300, and 350 km thick are used. We find that a 250 km thick lithosphere is most consistent with mare basalt multiple saturation points, and use only that thickness in the numerical models of convection under the craters. A lithosphere of 250 km is at

4.0 to 3.5 Ga also roughly consistent with the lunar thermal evolution models of Solomon and Longhi (1977) and Spohn *et al.* (2001).

Crater models

The evolution of the shape of craters, from the first seconds after impact, through isostatic rebound at thousands of years after impact, is controversial. Because material excavated from the crater is thrown farther than any possible radius of inward flow, depressurization will result no matter the magnitude of lateral crater collapse. This simple assumption removes the importance of some of the controversy over the possibility of instantaneous lateral resurge filling the crater and disallowing in-situ melting; if the mass has been ejected from the crater, then a mass deficiency exists for the lithosphere in the region of the crater, and our modeled processes will proceed.

Our models are based on the results of O'Keefe and Ahrens (1999, 1993) and Cintala and Grieve (1998); see Figure 4. The maximum depth of excavation equals 0.15R, where R is the radius of excavation. The value 0.15R is also the maximum isostatic uplift of the bottom of the lithosphere under the crater. The radius of the final crater, such as those measured on the Moon by Wilhelms (1987), is about 1.9R.

The complex crater depth profile, D_C, of O'Keefe and Ahrens (1999) is closely fit by the following expression, where R is the radius of excavation of the crater, r is the radial distance from the center of the crater, all in km. This profile is shown in Figure 4.

$$D_C = R\left(\frac{0.2r^3}{R^3} + \frac{0.022}{\frac{r}{R} + 0.1} - 0.22\right) \qquad (1)$$

When integrated, this profile yields the following expression for excavated crater volume, V:

$$V_C = 0.11\pi R^3 \qquad (2)$$

This excavated volume is matched by the total ejecta volume obtained by integrating the following expression for ejecta blanket thickness, D_E as a function of distance from the crater's outer edge:

$$D_E = \frac{0.34R^{4.24}}{r^{3.5}} \quad (3)$$

This crater depth profile is used in both the in-situ decompression melting model and the formation of the lithospheric dome for subsequent convective melting.

The resulting volumes are in agreement with the ejecta law given in Housen, Schmidt and Holsapple (1983), and crater profiles are roughly in agreement with Melosh (1989) and Cintala and Grieve (1998).

Modeling melt volumes

Shock melt from impact

Shock melting from the energy of impact was not modeled in this study. A 300-km radius crater makes about 10^5 km^3 of shock melt, and a 100-km radius crater about 10^4 km^3 of melt, from the results of Pierozzo *et al.* (1997) and Tonks and Melosh (1993). Because the surface of the planet is different compositionally from its interior, shock melts are generally compositionally distinct from adiabatic melts, and would not be mistaken for them, and so are not included in total volumes of basaltic melt produced by impacts in this study. Another effect of shock melt may be important, though, and that is its ability to mix with rising decompression melts to produce a range of mare basalt compositions. Shock melt from a large lunar basin is likely to contain aluminous, high titanium, and KREEP components, and thus may be an important contributor through melt mixing to the observed range of mare basalt compositions.

Stage 1: In-situ decompression melting

At the time of impact, material at the impact site is ejected, and within a certain additional radius, material is melted (shock melt) or disrupted and heated by shock. In giant craters the volume of material heated but not melted may be considerable, but this heating process is not considered in this model. For simplicity, a conductive selenotherm through the lithosphere culminating at an adiabatic asthenosphere is assumed to remain in place after excavation.

Excavation of the crater reduces pressure in the material beneath the crater by an amount equal to the lithospheric pressure of the material excavated. (See Figure 5.) The greatest pressure release is over the interval from 0.2R to 0.4R, and pressure release declines to zero at the crater rim (and pressure can increase outside the rim due to new deposits). This lowering of pressure effectively moves the solidus deeper into the lunar mantle material, in some cases causing it to cross the selenotherm and create melt. A general equation for in-situ decompression melt was created by integrating the area of intersection between the solidus and selenotherm around the axis of symmetry of the crater. The parameters used in the equations are given in Table 1.

A critical parameter is β, the melt fraction per degree between solidus and liquidus. This can be calculated using C_p, the heat capacity of the silicate cumulates, and H_f, the heat of fusion of the silicate cumulates, as follows:

$$\beta = \frac{df}{dT} = \frac{C_P}{H_f} = 0.003 \frac{wt\%}{^\circ} \tag{4}$$

Based on this $\frac{df}{dT}$ and the maximum decompression created by any impact modeling, the maximum melt percent of a parcel of mantle in the in-situ melting model is 6%.

The selenotherm is modeled as a straight, conductive profile through the lithosphere from the surface to the adiabatic potential temperature at the base of the lithosphere, and as an adiabat through the mantle. The following expressions describe the selenotherm in the lithosphere, which is conductive, and in the mantle, where it is adiabatic:

$$Lithospheric\_selenotherm = T_A = z\left(\frac{T_p}{d} + a\right) \tag{5}$$

$$Mantle\_selenotherm\_(adiabatic) = T_B = az + T_p \tag{6}$$

A solidus for mantle material can be expressed as follows, and subsequently as it appears following excavation of the crater:

$$Solidus = sz + s_o \tag{7}$$

$$Solidus\_following\_crater\_excavation = T_C = s(z + D_C) + s_o \tag{8}$$

Where the expression for the crater profile, D_C, is given by equation 1 above.

The integration is performed in two parts, one from the intersection of the solidus and the adiabat (z_l, where equation T_B equals equation T_C) upward to the base of the lithosphere (where the selenotherm changes slope and becomes conductive), and the second from the base of the lithosphere to the intersection between the solidus and the conductive selenotherm (z_u, where equation T_A equals equation T_C). The maximum interval of melting between the solidus and selenotherm is found over the area of greatest excavation. As the radius increases toward the edge of the crater the solidus effectively moves up, following the crater floor, and the melting interval decreases. (See Figures 1 and 5.) The final equation for in-situ melt is given as:

$$F = 2\pi\beta\left[\int_{d}^{z_l}\int_{0}^{R} r\left(T_B - T_C\right)drdz + \int_{z_u}^{d}\int_{0}^{R} r\left(T_A - T_C\right)drdz\right] \tag{9}$$

This equation for F is easily integrated, and the result is an equation for in-situ melt as a function of R, d, s, a, s_o, and T_p.

Stage 3: Adiabatic melting in convection currents

The excavated crater profile shown in Figure 3 is not in isostatic equilibrium; the thinned lithosphere has a gravitational driving force to rise and form a dome in the lithosphere-mantle boundary. The process of forming a dome may occur virtually instantaneously, when the lithosphere behaves as a liquid due to the intense shock of the impact. Alternatively, the lithosphere may rebound isostatically over approximately the next 10^4 years. Clear evidence for such domes under basins on the Moon is shown in gravity models for the Moon (Wieczorek and Phillips, 1999; Neumann *et al.*, 1996; Bratt *et al.*, 1985).

This dome necessarily creates a horizontal temperature gradient at its edge, a driving force for convection. The convection is calculated numerically using an spherical axisymmetric version of the finite element code ConMan (King *et al.*, 1990), called NewScam, and any resulting melt is

calculated with a post-processor routine using the parameters given in Table 1. We ran a large suite of test models to ensure that the code was correctly calculating the convective flow, and to ensure that the grid had sufficient resolution to avoid numerical defects.

Thermal convection is governed by the Rayleigh number:

$$Ra = \frac{\rho g \alpha \Delta T h^3}{\eta_o \kappa} \tag{10}$$

where α is thermal expansivity, κ is thermal diffusivity, ρ is a characteristic density, ΔT is the temperature change over the model box, h is a characteristic length and η_o is a reference viscosity. The compositional Rayleigh number controls convection due to the negative buoyancy of the high-Ti cumulate

$$Ra_{comp} = \frac{\Delta \rho g h^3}{\eta_o \kappa} = Ra\left[\frac{\Delta \rho}{(\rho \alpha \Delta T)}\right] \tag{11}$$

where $\Delta\rho$ is the difference in densities between the compositions. Viscosity is first calculated using the following non-Newtonian law:

$$\eta_{nonN.} = \eta_o \exp\left(\frac{E + vz}{T + T_o} - \frac{E + vz_o}{1 + T_o}\right) \tag{12}$$

where η_o, z_o, and T_o are reference values for viscosity, depth, and temperature, respectively; E is the activation energy, set such that a 100°C change in mantle temperature creates a factor of ten change in viscosity, and v is the reference volume, set such that a 33 kb change in pressure also creates a factor of ten change in viscosity. The second invariant of the stress tensor is given as:

$$Secinv = 0.5\left(\sigma_{rr}^2 + \sigma_{\tau\tau}^2 + \sigma_{\Phi\Phi}^2\right) + \sigma_{r\tau}^2 \tag{13}$$

If the second invariant of the stress tensor is non-zero, then viscosity is recalculated using the following two non-Newtonian laws in this order:

$$\eta_{stress} = \left(\frac{\sigma_o^2}{2(Secinv)^2} \right)^{0.25}$$ Stress-weighting law (14)

$$\eta = \eta_{stress} \left(\frac{\sigma_o^{0.66} \eta_{nonN}^{0.33}}{2(Secinv)^{0.66}} \right)^{0.75}$$ Strain-weighting law (15)

where σ_o is the reference value for stress. A list of key variables is given in Table 1.

A starting condition for each model runs was created by using an erfc cooling law to make a cooled lithosphere of the required depth with a lithospheric dome with maximum uplift equal to 0.15 times the crater excavation radius.

For each of the models, the top 15 elements (60 km) are anorthosite crust, which is modeled with an initial viscosity 100 times that of the mantle. To test how changes in lithospheric geometry (isostatic uplift and later convection) affects the hypothesized high-titanium cumulate, it is included in the numerical model (for further description of this model, see Elkins Tanton *et al.* (2002b)). After the anorthosite crust, the next layer is 3 elements (12 km) of KREEP. This is probably a significant overestimate of the thickness of the KREEP layer, but numerical considerations require that at least three elements be used in each material. The initial viscosity of the KREEP layer is 100 times less than the mantle. Below the KREEP layer are 5 elements (20 km) of high-Ti cumulate. The remainder of the model box is made up of 77 elements (308 km) of silicate mantle. The KREEP and high-Ti layers are removed within the radius of excavation of the crater the models with crater radii greater than 100 km, because the KREEP and high-Ti layers would be significantly disturbed or melted by craters of these sizes. For these large craters, the high-Ti cumulate is retained outside the crater radius.

The boundary conditions for each model are the same: free-slip in the horizontal along the top boundary, free-slip in the vertical along the side boundaries, and a flow-through bottom boundary.

Results

In-situ melt:

In-situ decompression melt is the largest contributor to melt created by lunar impacts. It constitutes between 98 and 100% of the melt created in this model, but the in-situ melting occurs instantaneously, in a geological sense, after the impact. The longevity of magmatism is entirely the province of later convective melting under the crater.

In almost every case, the mantle potential temperature and selenotherm used in these models would create extant mantle melt before crater excavation. The total volume of this existing melt is calculated under the area that the crater will later excavate, and it is included in the total in-situ decompression melt. The extant melt makes up between 0 and 54% of the total in-situ melt volume. Table 2 lists total melt for the in-situ stage, and breaks down this total into extant melt and melt created by the impact process. These totals are listed for mantle potential temperatures of 1350 and 1450 °C, for lithospheric thicknesses of 200, 250, 300, and 350 km, and for craters with excavation radii of 50, 100, 200 and 300 km.

The impact-generated mafic mantle melts originate from between 190 and 390 km depth when the mantle potential temperature is 1350 °C, and from 150 and 560 km for a mantle potential temperature of 1450 °C. In each case, the upper bound varies with lithospheric thickness.

Convective melt

From the start of each of the numerical model runs, mantle material flows upward in the center of the dome and flows out and down at the edges. In terrestrial models, stress-dependent rheology is important in modeling this process: instabilities are eventually pulled off the rim of the lithospheric dome, and nascent instabilities quickly build up stress while deforming, thereby lowering their viscosity and enabling downward flow (Elkins Tanton and Hager, 2002). This feedback process speeds the fall of instabilities significantly when compared to simple temperature-dependent rheology. On the Moon, velocities and stresses are low. No instabilities are pulled off the crater rims, and slow convection continues long after it would have ceased on the Earth. We previously modeled this process in Cartesian coordinates with a non-Newtonian viscosity law, and in an axisymmetric model with a Newtonian viscosity law, and find that results are not changed significantly by a non-Newtonian viscosity law and axisymmetric geometry. Velocity and stress are low on the Moon, and the convective melt process is not

significantly controlled by either non-Newtonian viscosity or planetary curvature for the parameters assumed here.

The maximum mantle velocity in any of the numerical convection runs is about 1 mm/year. In the case of the largest impact and the longest convective movement, some mantle materials are melted by 20% at the conclusion of the process. This is the maximum melting extent.

Convective melt totals are given in Table 2. Although they total only 1 or 2% of the total melt produced by the cratering process, convective melting continues for many millions, and in some cases, hundreds of millions of years after initial impact. Figure 6 shows the duration and volume of melt production for models with a 250 km thick lithosphere. When the mantle potential temperature is 1350 °C, the largest crater (R = 300 km) produces melt for about 150 Ma after impact. When the mantle potential temperature is 1450 °C, however, melting continues for about 330 Ma after impact.

None of the numerical convection models mobilized any solid KREEP or high-Ti cumulate. We conclude that these materials, if they remained at 60 to 80 km depth at the time of the late heavy bombardment, were incorporated into mare basalts and picritic glasses only through assimilation by existing magmas, or by mixing after having been melted by the initial impact.

Discussion

Nyquist and Shih (1992) have shown that the earliest mare basalts are aluminous, KREEP-rich, and high-titanium. Though in-situ decompression itself does not move any KREEP or high-Ti cumulate above its liquidus, if it lay at the depths modeled here (between 60 and 80 km depth), these cumulates would have been melted by initial shock impact in craters with excavation radii larger than 150 km. The resulting melt may have percolated downward in the Moon (Elkins Tanton *et al.*, 2002b) to make a hybrid mantle, or it may have risen, but in either case it was available to mix with rising decompression mantle melts to create KREEP and high-Ti mare basalts. Similarly, aluminous upper lithosphere and crust may have melted and mixed with rising mafic decompression melts to create high-alumina basalts.

The data of Nyquist and Shih (1992) also show that mare basalt volcanism lasted from 4.0 to at least 3.0 Ga. The longevity of melt production by the convective phase of these models (up to 350 Ma for one basin), given the range of time over which the large basins formed, is consistent with the aluminous and high titanium basalt flux, and perhaps some of the low titanium basalts.

Melt production from this process would last from before 4.0 Ga to about 3.5 Ga. Though by far the largest volume of basalt is produced by the initial in-situ decompression melting, later eruptions will cover the initial volumes, and dates are more likely to be obtained from these later eruptions.

Advocates for minimal lithospheric thinning under craters argue that the subsequent lack of a dome in the lithosphere-mantle boundary will create little convective melt. For the models described here, the lithospheric dome that results from isostatic compensation is assumed to have a maximum height of 0.15R, which is the same as the maximum depth of the crater following excavation. It is likely, though, that the lithospheric dome is shallower than the original crater depth, that is, that isostatic uplift does not completely return the planet's surface to flatness. On the Moon, however, the craters seen today remain depressed, but gravity modeling over lunar basins also shows domes in the crust with heights that are approximately 10% to 24% of the excavation radii of the craters above them (Wieczorek and Phillips, 1999; Neumann *et al.*, 1996; Bratt *et al.*, 1985). Shallower domes create less driving force for convection in the mantle, and therefore create less convective melt. If the height of the lithospheric dome is reduced to 0.10 R, then melt volumes are reduced by about 30%. If the height is further reduced to 0.05 R, then melt volumes are reduced by about 60%. These circumstances do not invalidate our model, but reduce the likelihood that the model creates uninterrupted melt production from 4.0 to 3.0 Ga.

South Pole Aitken, the huge and extremely ancient basin on the far side of the Moon, does not contain basalt fill (Pieters *et al.*, 1997). This could be because the basin formed long after magma ocean crystallization at a time when either the mantle was not hot enough to support impact-induced volcanism, or the lithosphere was too thick. A lithosphere 500 to 600 km thick (the 1000 °C isotherm at that depth) would be sufficient to suppress impact-induced volcanism.

Solomon and Head (1980) produced data necessary to calculate the volumes of mare basalt fill of lunar basins. Volumes from their data are plotted along with predicted volumes from these models in Figure 7. This figure shows modeled melt volumes for mantle potential temperatures of 1350 and 1450 °C, assuming that 10% of melt produced actually erupts. Six of the lunar basins are well modeled by a mantle potential temperature of 1450 °C, and the remaining two by the lower potential temperature.

These models are also consistent with the pressures and temperatures of multiple saturation for the mare basalts and picritic glasses. Figure 8 shows multiple saturation points for low- and

high-Ti mare basalts and picritic glasses. The mare basalts lie along the mafic cumulate solidus, and the picritic glasses scatter above the solidus. This scatter is consistent with convective movement above the solidus as well as percolative flow and reequilibration. The picritic glasses imply a mantle potential temperature of about 1450 °C, and the boundary between the source depths of the glasses and the basalts may imply a lithospheric thickness of about 250 km.

Under the impact basins the selenotherm is perturbed significantly, due to depressurization and due to isostatic uplift and rise of the hot mantle (Figure 8). The model depth range of melting for the 1450 °C mantle, from 150 and 560 km, is consistent with the depth of formation of all but the very shallowest mare basalts. Superheat from rising and stalling magmas from deeper in the Moon, and possibly heat of fusion from crystallization of the same, produces adequate heat to create the shallowest mare basalts.

The implications of this model, then, are that the deepest melts from both the in-situ and convective processes are picritic glasses. The mare basalts were formed either by simply melting the lithosphere (with its potentially varied lithologies), or they are the products resulting from picritic glass-like magmas interacting with the lithosphere on their way to the surface. Lithospheric interactions could include fractionation or assimilation of shock melt or solid cumulates. The order of eruption, with the most primitive, lowest titanium magmas last, is analogous to Earth processes in which early injections of magma heat, assimilate and mix with crustal components (here, lithospheric components), and the last eruptions come through a clean magma conduit and so retain their primitive, pristine compositions (Baker *et al.*, 1991; Gunnarsson *et al.*, 1998; Kinzler *et al.*, 2000).

Conclusions

The late heavy bombardment is sufficient to create the volumes and a large portion of the duration of mare basalt eruptions seen on the Moon. The process of impact-induced volcanism can create a variety of magmatic compositions, probably including the aluminous, KREEP, high-Ti, and some low-Ti glass and basalt compositions. The impact model results and a compilation of multiple saturation points are consistent with the following lunar conditions at 4.0 – 3.5 Ga: the potential temperature of the lunar mantle at 300 – 500 km depth was about 1450 °C, and the nearside lunar lithosphere is 200 – 300 km thick.

The model implies that deep magmas are picritic glasses, and that mare basalts originated in a cooler lithosphere. This lithosphere was heated and partly melted by impact processes. Only the shallowest mare basalts could not be produced directly by this process; they require the superheat and possibly heat of fusion of stalled, cooling magmas from deeper in the Moon.

Acknowledgments

This work was supported by a NASA grant, by a National Defense Science and Engineering graduate fellowship, and an Amelia Earhart graduate fellowship. Special thanks to Marc Parmentier for his insights into the in-situ depressurization melting process.

References

Baker M.B., Grove T.L., Kinzler R.J., Donnelly-Nolan J.M., and Wandless G.A. (1991) Origin of compositional zonation (high-alumina basalt to basaltic andesite) in the Giant Crater lava field, Medicine Lake volcano, northern California. *J. Geophys. Res.* 96, 21819-21842.

Bratt S.R., S.C. Solomon, J.W. Head, C.H. Thurber (1985) The deep structure of lunar basins: Implications for basin formation and modification. *J. Geophys. Res.* **90**, 3049-3064.

Chen H.K., J.W. Delano, and D.H. Lindsley (1982) Chemistry and phase relations of the VLT volcanic glasses from Apollo 14 and Apollo 15. *J. Geophys. Res.* 87, A171-A181.

Chen H.K. and D.H. Lindsley (1983) Apollo 14 very low titanium glasses: Melting experiments in iron-platinum alloy capsules, *J. Geophys. Res.* 88, B335-342.

Cintala M.J. and R.A.F. Grieve (1998) Scaling impact melting and crater dimensions: Implications for the lunar cratering record. *Meteor. Planet. Sci.* 33, 889-912.

Delano J.W. (1980) Chemistry and liquidus phase relations of the Apollo 15 red glass: Implications for the deep lunar interior, *Proc. Lunar Planet. Sci. Conf. 11*, 251-288.

Elkins L.T., V.A. Fernandes, J.W. Delano, and T.L. Grove (2000) Origin of lunar ultramafic green glasses: Constraints from phase equilibrium studies, *Geochim. Cosmochim. Acta* 64, 2339-2350.

Elkins Tanton L.T. and B.H. Hager (2002) Giant meteorites can cause flood basalts: A viable mechanism. Submitted to *Earth Planet. Sci. Lett.*

Elkins Tanton L. T., N. Chatterjee, and T.L. Grove (2002a) Constraints on lunar differentiation from the Apollo 15 green picritic glasses, submitted to *Meteoritics and Planetary Science.*

Elkins Tanton, L.T., J. A. Van Orman, B. H. Hager, and T. L. Grove (2002b) Reexamination of the lunar magma ocean cumulate overturn hypothesis: Melting or mixing is required, *Earth and Planetary Science Letters* 196, 141-151.

Green D.H., A.E. Ringwood, N.G. Ware, W.O. Hibberson, A. Major, E. Kiss (1971a) Experimental petrology and petrogenesis of Apollo 12 basalts. *Proc. Lunar Sci. Conf.* 2, 601-615.

Green D.H., N.G. Ware, W.O. Hibberson, A. Major (1971b) Experimental petrology of Apollo 12 mare basalts, Part 1, sample 12009. *Earth Planet. Sci. Lett.* 13, 85-96.

Green D.H., A.E. Ringwood, W.O. Hibberson, N.G. Ware (1975) Experimental petrology of Apollo 17 mare basalts. *Proc. Lunar Sci. Conf.* 6, 871-893.

Grove T.L. and D.T Vaniman (1978) Experimental petrology of very low Ti (VLT) basalts, in R.B. Merrill, J.J. Papike, eds., *Mare Crisium: The View From Luna 24*, Pergamon Press, New York, 445-471.

Gunnarsson B., Marsh B.D. and Taylor H.P. Jr. (1998) Generation of Icelandic rhyolites: silicic lavas from the Torfajokull central volcano. *J Volcanol Geotherm Res* 83, 1-45.

Head, J.W. III and L. Wilson (1992) Lunar mare volcanism: Stratigraphy, eruption conditions, and the evolution of secondary crusts. *Geochim. Cosmochim. Acta* 56, 2155-2175.

Hess P.C. and E.M. Parmentier (1995) A model for the thermal and chemical evolution of the moon's interior: Implications for the onset of mare volcanism, *Earth Planet. Sci. Lett.* 134, 501-514.

Hodges E.N. and I. Kushiro (1974) Apollo 17 petrology and experimental determination of differentiation sequences in model Moon compositions. *Proc. Lunar Sci. Conf.* 5, 505-520.

Housen K.R., R.M. Schmidt and K.A. Holsapple (1983) Crater ejecta scaling laws: Fundamental forms based on dimensional analysis. *J. Geophys. Res.* 88, pp 2485-2499.

Kesson S.E. (1975) Mare basalts: Melting experiments and petrogenetic interpretations. *Proc. Lunar Sci. Conf.* 6, 921-944.

King S.D., A. Raefsky, B.H. Hager (1990) ConMan: Vectorizing a finite element code for incompressible two-dimensional convection in the Earth's mantle, *Phys. Earth Planet. Int.* 59, 195-207.

Kinzler R.J., Donnelly-Nolan J.M., and Grove T.L. (2000) Late Holocene hydrous mafic magmatism at the Paint Pot Crater and Callahan Flows, Medicine Lake Volcano, N. California and the influence of H2O in the generation of silicic magmas. *Contrib. Mineral. Petrol.* **138**, 1 - 16.

Longhi J., D. Walker, T.L. Grove, E.M. Stolper, J.F. Hays (1974) The petrology of Apollo 17 mare basalts. *Proc. Lunar Sci. Conf.* 5, 447-469.

Melosh, H.J. (1989) *Impact cratering: A geological process*, Oxford University Press, Oxford and New York, 245 pp.

Neumann G.A., M.T. Zuber, D.E. Smith, F. G. Lemoine (1996) The lunar crust: Global structure and signature of major basins. *J. Geophys. Res.* 101, 16841-16843.

Nyquist L.E. and C.-Y. Shih (1992) The isotopic record of lunar volcanism, *Geochim. Cosmochim. Acta* 56, 2213-2234.

O'Keefe, J.D. and T.J. Ahrens (1993) Planetary cratering mechanics. *J. Geophys. Res.* 98, 17011-17028.

O'Keefe, J.D. and T.J. Ahrens (1999) Complex craters: Relationship of stratigraphy and rings to impact conditions. *J. Geophys. Res.* 104, 27,091-27,104.

Pierozzo E., A.M. Vickery and H.J. Melosh (1997) A reevalution of impact melt production. *Icarus* 127, 408-423.

Pieters C.M., S. Tompkins, J.W. Head, and P.C. Hess (1997) Mineralogy of the mafic anomaly in the Southy Pole-Aitken basin: Implications for excavation of the lunar mantle. *Geophys. Res. Lett.* 24, 1903-1906.

Ringwood A.E. and S.E. Kesson (1976) A dynamic model for mare basalt petrogenesis, *Proc. Lunar Planet. Sci. Conf. 7*, 1697–1722.

Solomon S.C (1975) Mare volcanism and lunar crustal structure. *Proc. Lunar Planet. Sci. Conf. 6*, 1021–1042.

Solomon S.C. and J.W. Head (1980) Lunar mascon basins: Lava filling, tectonics, and evolution of the lithosphere. *Rev. Geophys. Space Phys.* 18, 107-141.

Solomon S.C. and Longhi J. (1977) Magma oceanography: 1. Thermal evolution. *Proc. Lunar Planet. Sci. Conf.* **8**, 583-599.

Spohn T., Konrad W., Breuer D. and Ziethe, R. (2001) The longevity of lunar volcanism: Implications of thermal evolution calculations with 2D and 3D mantle convection models. *Icarus* **149**, 54-65.

Tonks W.B. and H.J. Melosh (1993) Magma ocean formation due to giant impacts. *J. Geophys. Res.* 98, 5319-5333.

Wagner T.P. and Grove T.L. (1997) Experimental constraints on the origin of lunar high-Ti ultramafic glasses. *Geochim. Cosmochim. Acta* **61**, 1315-1327.

Walker D, J. Longhi and J.F. Hays (1972) Experimental petrology and origin of Fra Mauro rocks and soil. *Proc. Lunar Planet. Sci. Conf.* 3, 797-817.

Walker D., J. Longhi, E.M. Stolper, T.L. Grove, J.F. Hays (1975) Origin of titaniferous lunar basalts. *Geochim. Cosmochim. Acta* 39, 1219-1235.

Walker D., J. Longhi, E.M. Stolper, T.L. Grove, J.F. Hays (1976) Differentiation of an Apollo 12 picritic magma. *Proc. Lunar Planet. Sci. Conf.* 7, 1365-1389.

Walker D., J. Longhi, A.C. Lasaga, E.M. Stolper, T.L. Grove, J.F. Hays (1977) Slowly cooled microgabbros 15555 and 15065. *Proc. Lunar Planet. Sci. Conf.* 8, 1521-1547.

Wieczorek M.A. and R.J. Phillips (1999) Lunar multiring basins and the cratering process. *Icarus* 139, 246-259.

Wilhelms D.E. (1987) *The geologic history of the moon.* USGS Prof. Paper 1348.

Zhong S., E.M. Parmentier, M.T. Zuber, A dynamic origin for the global asymmetry of lunar mare basalts, *Earth Planet. Sci. Lett.* 177 (2000) 131-140.

Table and Figure Captions

Table 1. Parameters used in in-situ and convective melt calculations.

Table 2. Melt volume totals for all stages of melt production. For stage 1, in-situ decompression melting, the total melt volume is given and also broken into the fraction extant beneath the lithosphere before impact, and the fraction created by crater excavation and attendant decompression. In-situ totals are shown for 200, 250, 300, and 350 km lithospheres, and for craters with excavation radii of 50, 100, 200, and 300 km. Convective melt totals (stage 2 of melting) are included for a 250 km lithosphere only. These model volumes are shown for mantle potential temperatures of 1350 and 1450 °C.

Figure 1. Schematic description of melt production by giant impact. Each image shows a cross-section through the Moon from the surface to the cumulate mantle, and from the axis of impact on the left to an arbitrary distance on the left. The melt-producing steps modeled in this study are: 1. In-situ decompression melting following crater excavation, and 2. Adiabatic decompression melting in convective currents under a rebounded lithosphere.

Figure 2. Approximate mare basalt flux over time, from 1 to 4.5 Ga, after Head and Wilson (1992). Dated samples of highlands, mare basalt, and picritic glasses, showing relationship of erupted composition with time, after Nyquist and Shih (1992).

Figure 3. Thermal and compositional model used in melt volume calculations for both in-situ decompression and convective melting. For in-situ decompression melting, lithospheric thicknesses of 200, 300, and 350 km are also used.

Figure 4. Model of crater profiles used in melt modeling. Adapted from O'Keefe and Ahrens (1999, 1993) and Cintala and Grieve (1998).

Figure 5. The process of in-situ decompression melting. Excavation of the crater leaves the selenotherm in place, but moves the solidus deeper into the Moon because of depressurization in the column under the excavated crater (arrow at top). The movement of the solidus creates a larger melting interval between the solidus and selenotherm.

Figure 6. Durations and volumes of melt production. Both figures are for 250 km lithospheres. The top figure shows results for both in-situ decompression melting and later convective melting for a mantle potential temperature of 1350 °C; the bottom figure shows results for a mantle potential temperature of 1450 °C. Each figure shows results for craters with radii of excavation as shown: 50, 100, 200, and 300 km. If lunar conditions are reasonably well-modeled by a 1450 °C mantle, then the results in the lower figure and the cratering rates of the late heavy bombardment could produce mare basalt eruptions from 4.0 to 3.0 Ga.

Figure 7. Comparison of melt volumes predicted by this study with mare basalt volumes after Solomon and Head (1980) and crater radii after Wilhelms (1987). It is assumed that 10% of the modeled melt produced erupts and the lunar lithosphere is 250 km thick. The dark line shows results with a mantle potential temperature of 1450 °C, and the lighter line shows 1350 °C.

Figure 8. Conditions in the lunar mantle circa 3.5 Ga, as inferred from the multiple saturation points of picritic glasses and mare basalts. The model solidus and selenotherm are shown, along with the alteration of the selenotherm caused by giant impact (the result of decompression and later mantle rise into a lithospheric dome). Multiple saturation points references are as follows: Luna 24, 17 VLT, Grove and Vaniman (1978); 70215, 70017, Longhi *et al.* (1974); 15065, 15555, Walker *et al.* (1977); 12009, Green *et al.* (1971b);

14072, Walker *et al.* (1972); 15016, Kesson (1975), Hodges and Kushiro (1974); 74275, Green *et al.* (1975); 12002, Walker *et al.* (1976); 12022, Green *et al.* (1971a); 14 black, Wagner and Grove (1997); 15C, 15A, Elkins Tanton *et al.*, (2002a); 14 VLT, Chen and Lindsley (1983), Chen *et al.* (1982); 74220, Walker *et al.* (1975); 14B, Elkins *et al.* (2000); 15 red, Delano (1980).

Table 1. Parameters used in melt volume calculations

Constants used in melt volume calculations		
s	slope of solidus	0.75 °/km
h_o	maximum crater excavation depth = 0.15R	km
R	radius of excavation of the crater	50, 100, 200, 300 km
s_o	solidus temperature at 1 atmosphere	1150°
T_p	mantle potential temperature	1350 or 1450 °C
d	lithospheric thickness	200, 250, 300, or 350 km
a	slope of the adiabat	0.17 °/km
C_P	heat capacity of silicates	1256.1 J/°kg
H_f	heat of fusion of silicates	418,700 J/kg
β	frac. of melt produced per deg. above solidus, df/dT	0.003 wt%/°
Variables used in in-situ melt volume calculations		
z	depth, 0 at original land surface	km
r	radial distance from crater center	km
$D_C(r)$	crater excavation depth	km
$T_A(z)$	geotherm in the lithosphere	°
$T_B(z)$	geotherm in mantle	°
$T_C(z)$	solidus after crater excavation	°
z_u	where T_A and T_C cross: shallowest limit of melt region	km
z_l	where T_B and T_C cross: deepest limit of melt region	km
F	volume of melt	km^3
Constants used in numerical modeling of convection		
h	height and width of model box	400 km
ρ	reference mantle density	3300 kg/m^3
$\Delta\rho$	difference between high-Ti cumulate and mantle densities	-400 kg/m^3
ΔT	temperature across the model box	1350 or 1450 °C
η_o	reference viscosity	10^{20} Pas
α	thermal expansivity	3×10^{-5} /°
σ_o	reference stress	1.6×10^{13} Pa
κ	thermal diffusivity	10^{-6} m^2/s
e	number of elements in model box, in each dimension	100
Ra	Rayleigh number	1.4×10^5
Ra_{comp}	Compositional Rayleigh number	-3×10^5

Table 2. Total melt volumes from model.

		Mantle T_p = 1350							Mantle T_p = 1450						
		In-Situ				Convective		Total	In-Situ				Convective		Total
lith thick d [km]	crater radius r_o [km]	In-situ impact melt [km^3]	Extant melt [km^3]	Impact frac. of total in-situ	Total in-situ melt [km^3]	Total convective melt	Convect. frac. of final total	melt	In-situ impact melt [km^3]	Extant melt [km^3]	Impact frac. of total in-situ	Total melt [km^3]	Total convective melt	Convect. frac. of final total	melt
200	50	8.6E+04	6.1E+04	0.59	1.5E+05				4.3E+05	3.3E+05	0.56	7.6E+05			
	100	4.1E+05	2.4E+05	0.63	6.5E+05	(not			1.8E+06	1.3E+06	0.58	3.2E+06	(not		
	200	2.2E+06	9.7E+05	0.69	3.1E+06	modeled)			8.5E+06	5.3E+06	0.61	1.4E+07	modeled)		
	300	6.2E+06	2.2E+06	0.74	8.4E+06				2.2E+07	1.2E+07	0.64	3.4E+07			
250	50	3.6E+04	2.3E+04	0.61	5.9E+04	5.1E+02	0.01	6.0E+04	3.1E+05	2.4E+05	0.56	5.4E+05	2.6E+03	0.00	5.5E+05
	100	1.9E+05	9.2E+04	0.67	2.8E+05	3.9E+03	0.01	2.8E+05	1.3E+06	9.5E+05	0.59	2.3E+06	1.9E+04	0.01	2.3E+06
	200	1.1E+06	3.7E+05	0.75	1.5E+06	3.2E+04	0.02	1.5E+06	6.4E+06	3.8E+06	0.63	1.0E+07	1.3E+05	0.01	1.0E+07
	300	3.5E+06	8.3E+05	0.81	4.3E+06	1.1E+05	0.02	4.4E+06	1.7E+07	8.5E+06	0.66	2.5E+07	3.4E+05	0.01	2.6E+07
300	50	7.2E+03	3.0E+03	0.71	1.0E+04				2.1E+05	1.6E+05	0.57	3.6E+05			
	100	4.7E+04	1.2E+04	0.80	5.9E+04	(not			9.2E+05	6.2E+05	0.60	1.5E+06	(not		
	200	3.9E+05	4.8E+04	0.89	4.3E+05	modeled)			4.5E+06	2.5E+06	0.64	7.0E+06	modeled)		
	300	1.4E+06	1.1E+05	0.93	1.6E+06				1.2E+07	5.6E+06	0.68	1.8E+07			
350	50	0	0	0					1.2E+05	8.9E+04	0.58	2.1E+05			
	100	0	0	0		(not			5.7E+05	3.6E+05	0.61	9.3E+05	(not		
	200	2.8E+04	0	1.00	2.8E+04	modeled)			2.9E+06	1.4E+06	0.67	4.4E+06	modeled)		
	300	2.3E+05	0	1.00	2.3E+05				8.2E+06	3.2E+06	0.72	1.1E+07			

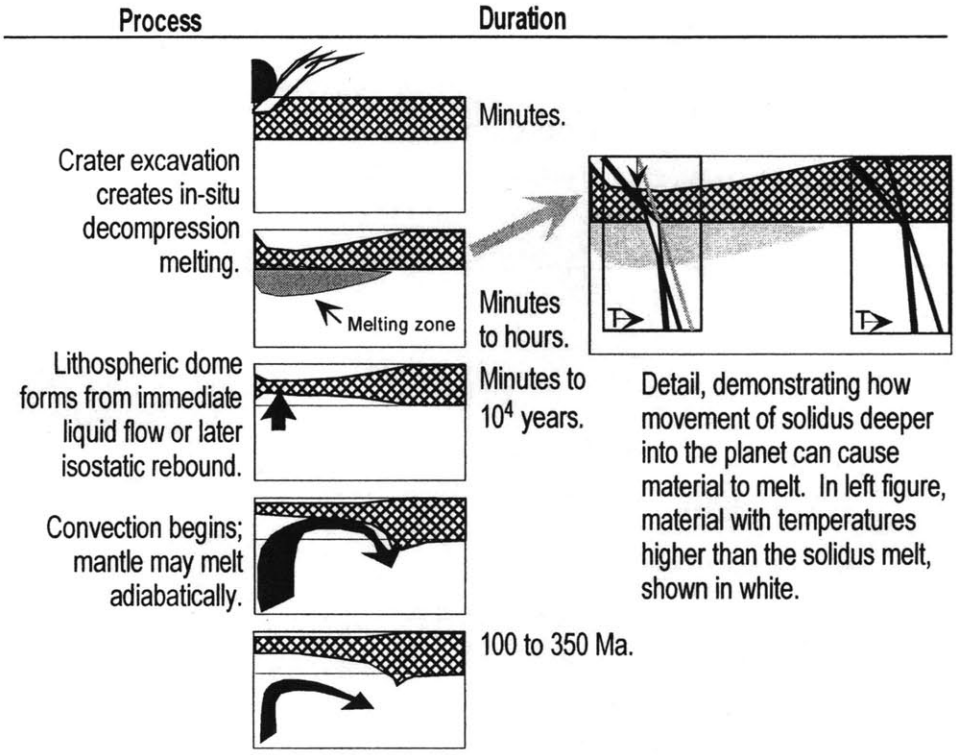
Process
Duration
Minutes.
Crater excavation creates in-situ decompression melting.
Melting zone
Minutes to hours.
Lithospheric dome forms from immediate liquid flow or later isostatic rebound.
Minutes to 10^4 years.
Convection begins; mantle may melt adiabatically.
100 to 350 Ma.
Detail, demonstrating how movement of solidus deeper into the planet can cause material to melt. In left figure, material with temperatures higher than the solidus melt, shown in white.

Figure 1

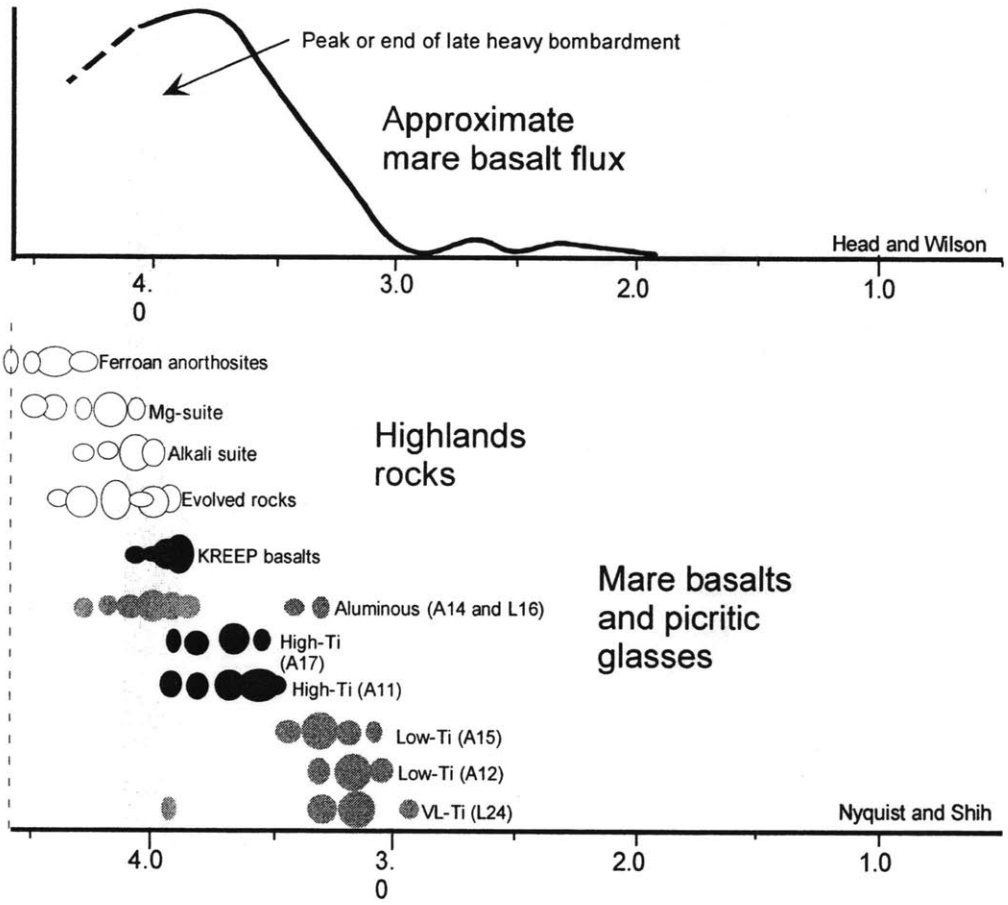
Peak or end of late heavy bombardment
Approximate
mare basalt flux
Head and Wilson
4.
0
3.0
2.0
1.0
Ferroan anorthosites
Mg-suite
Alkali suite
Evolved rocks
Highlands
rocks
KREEP basalts
Aluminous (A14 and L16)
High-Ti
(A17)
High-Ti (A11)
Mare basalts
and picritic
glasses
Low-Ti (A15)
Low-Ti (A12)
VL-Ti (L24)
Nyquist and Shih
4.0
3.
0
2.0
1.0

Figure 2

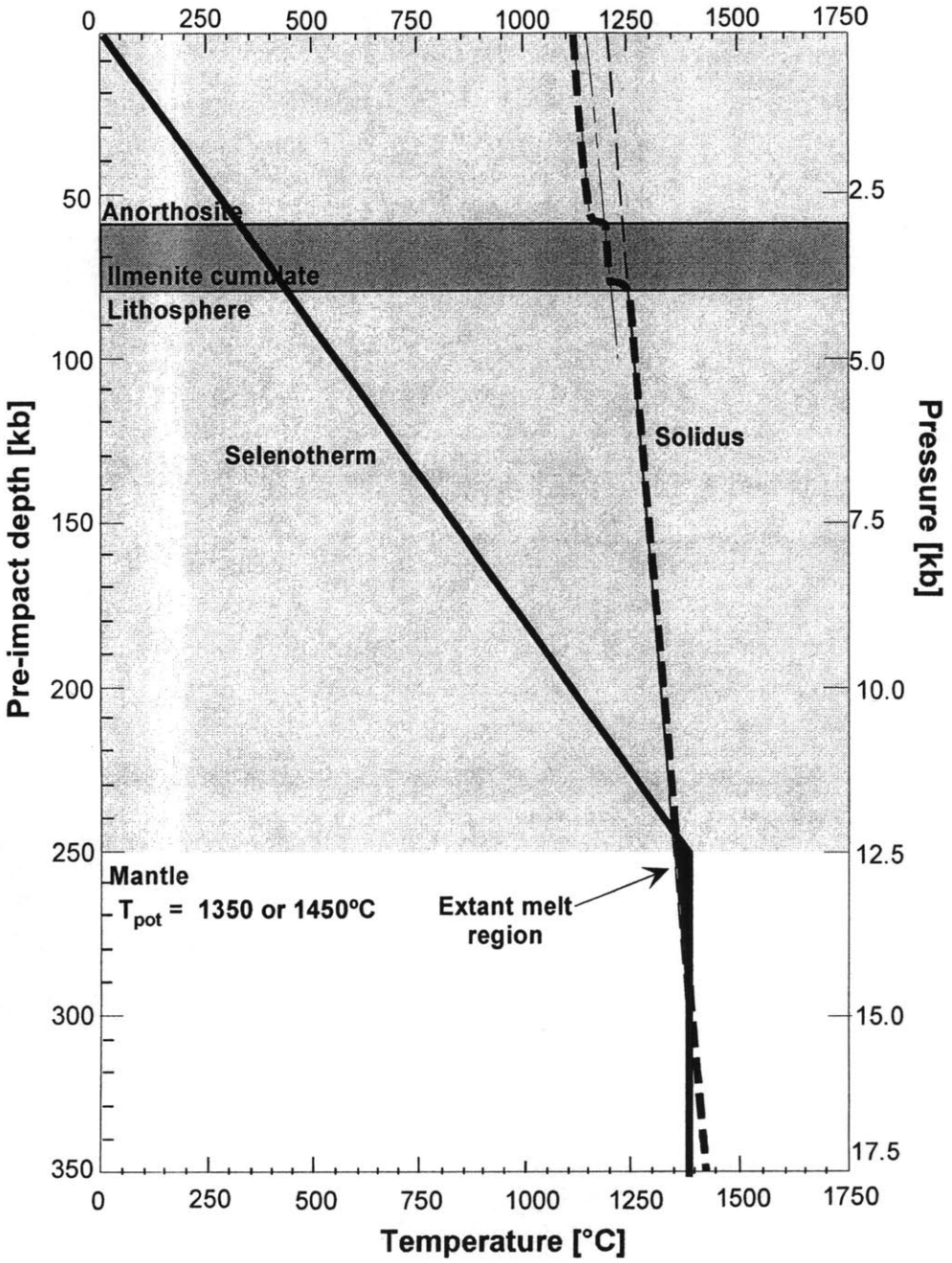
0
250
500
750
1000
1250
1500
1750
50
100
150
200
250
300
350
2.5
5.0
7.5
10.0
12.5
15.0
17.5
Anorthosite
Ilmenite cumulate
Lithosphere
Selenotherm
Solidus
Mantle
T_{pot} = 1350 or 1450°C
Extant melt region
Pre-impact depth [kb]
Pressure [kb]
Temperature [°C]

Figure 3

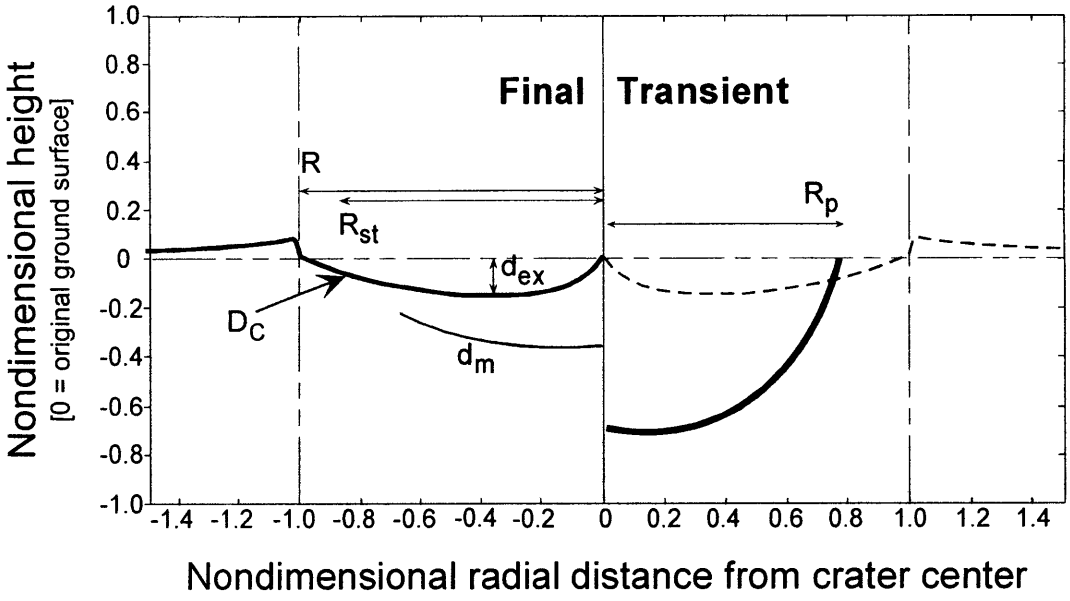
Final
Transient
R
R_{st}
R_p
d_{ex}
D_C
d_m
Nondimensional height
[0 = original ground surface]
Nondimensional radial distance from crater center
1.0
0.8
0.6
0.4
0.2
0
-0.2
-0.4
-0.6
-0.8
-1.0
-1.4 -1.2 -1.0 -0.8 -0.6 -0.4 -0.2 0 0.2 0.4 0.6 0.8 1.0 1.2 1.4

Figure 4

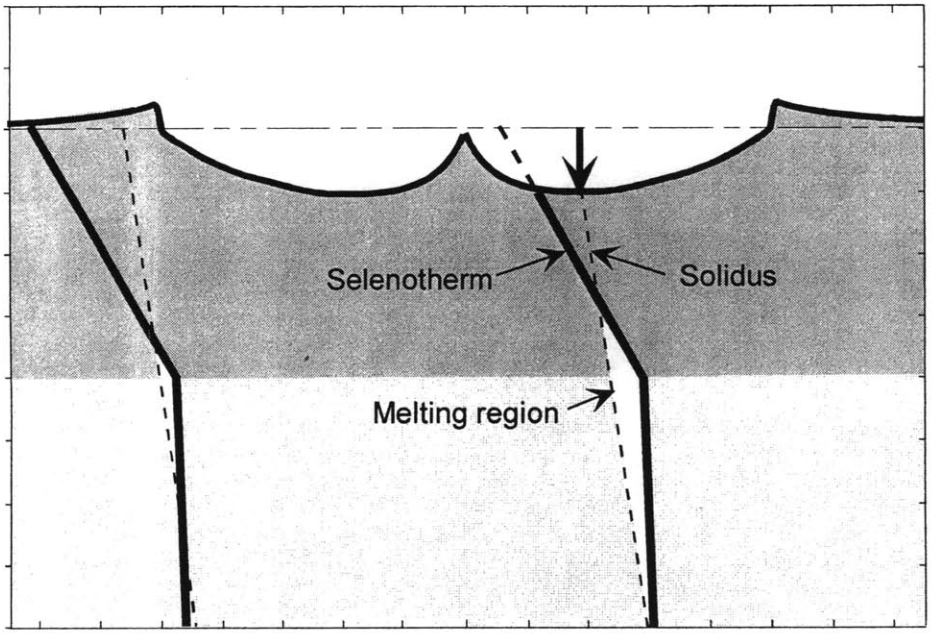

Before excavation:
small volume of existing melt

After excavation:
Selenotherm remains in place
while material is depressurized

Figure 5

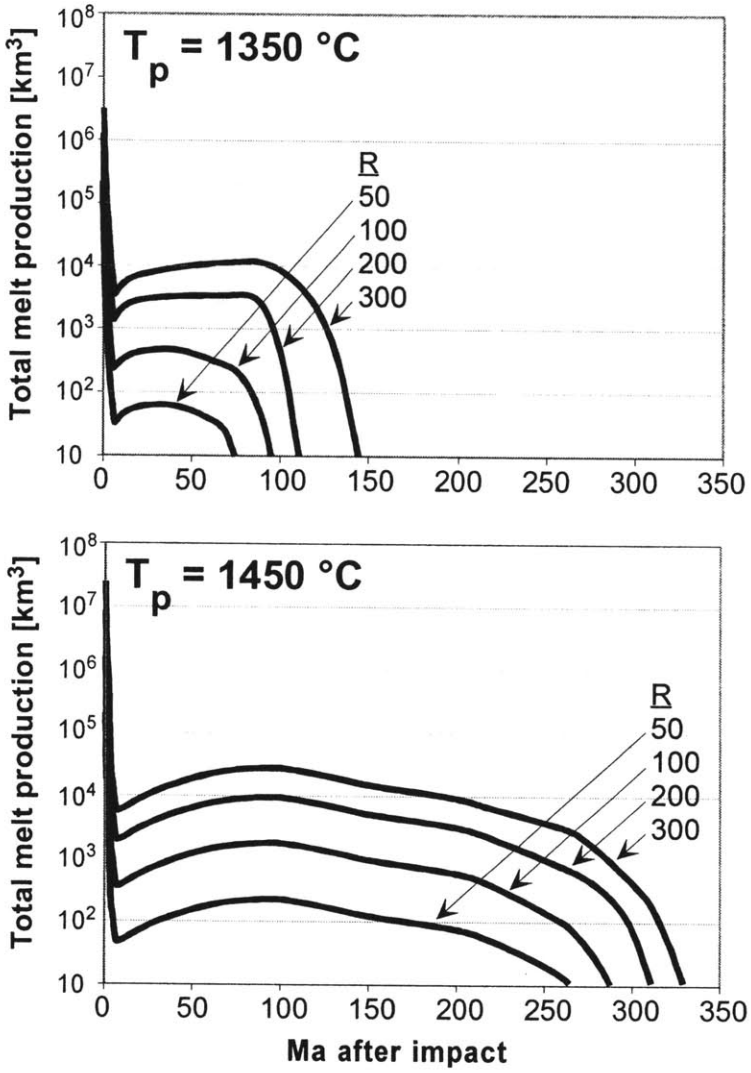
T_p = 1350 °C
Total melt production [km³]
R
50
100
200
300
T_p = 1450 °C
Total melt production [km³]
R
50
100
200
300
Ma after impact

Figure 6

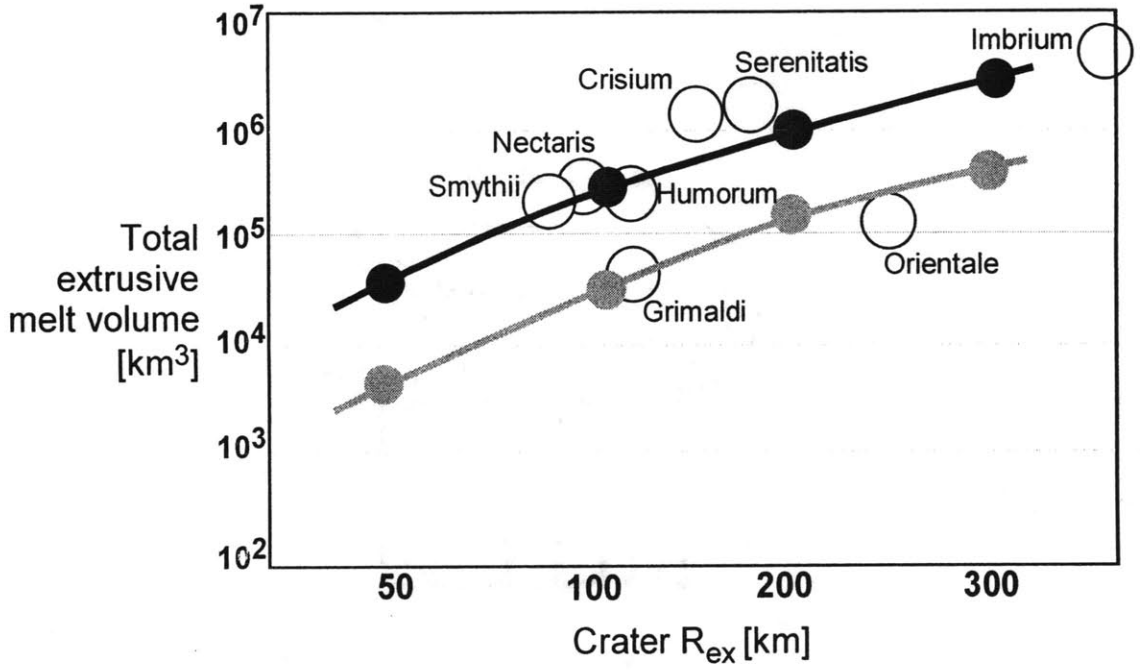
Total extrusive melt volume [km3]
10^7
10^6
10^5
10^4
10^3
10^2
Imbrium
Serenitatis
Crisium
Nectaris
Smythii
Humorum
Orientale
Grimaldi
50
100
200
300
Crater R_ex [km]

Figure 7

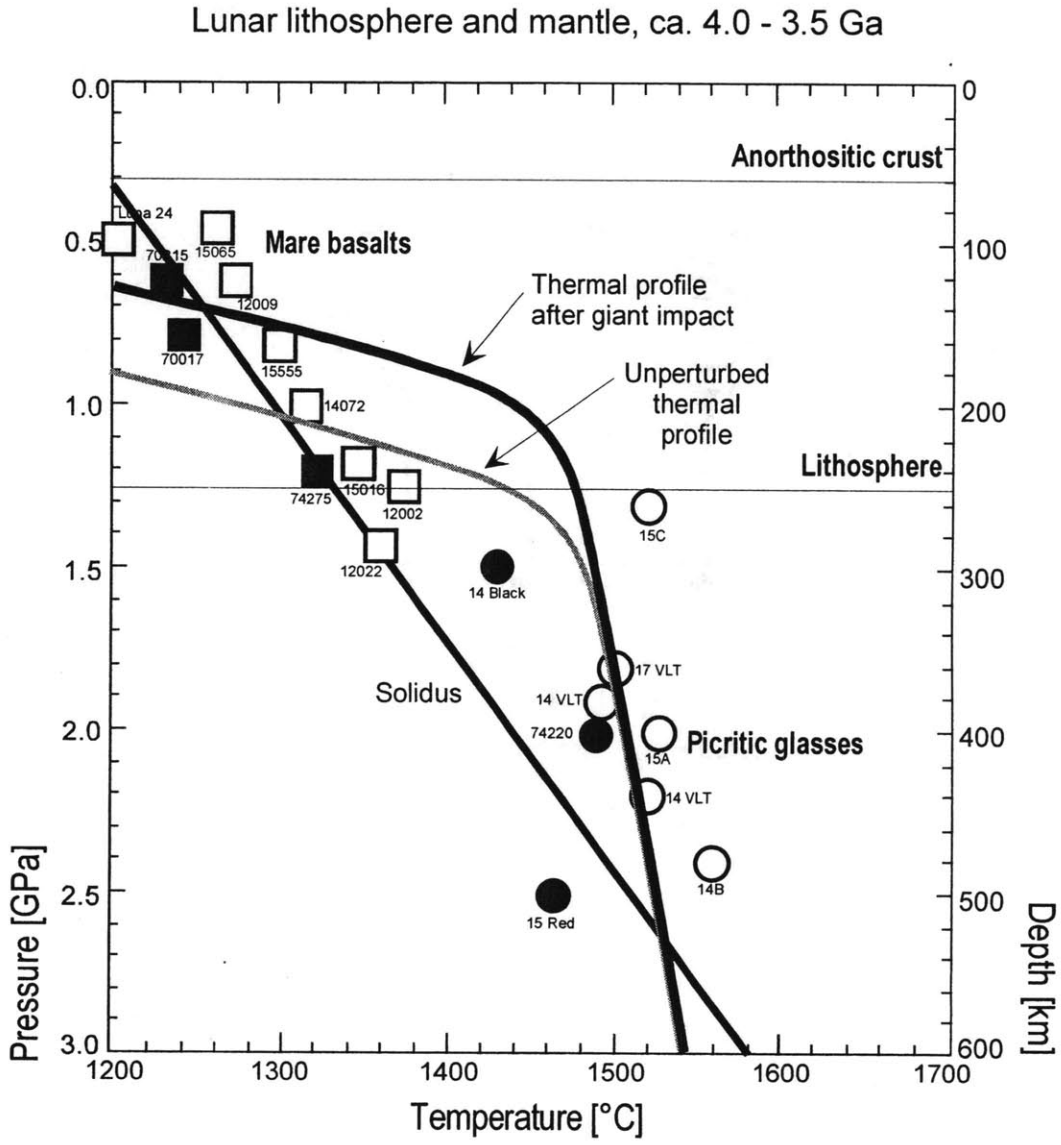

Figure 8

4935-11